

**Study of Fast Photo-physical Processes in Heterogeneous
Environments to Semiconductor Nanomaterials**

BY

SOMNATH KOLEY

CHEM11201304002

National Institute of Science Education and Research

Bhubaneswar, Odisha-752050

*A thesis submitted to the
Board of Studies in Chemical Sciences
In partial fulfilment of requirements
For the degree of*

DOCTOR OF PHILOSOPHY

of

HOMI BHABHA NATIONAL INSTITUTE





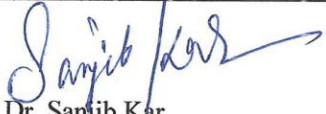



May, 2017

Homi Bhabha National Institute¹

Recommendations of the Viva Voce Committee

As members of the Viva Voce Committee, we certify that we have read the dissertation prepared by Mr. Somnath Koley entitled "Study of Fast Photo-physical Processes in Heterogeneous Environments to Semiconductor Nanomaterials" and recommend that it may be accepted as fulfilling the thesis requirement for the award of Degree of Doctor of Philosophy.


Chairman	 Prof. Alagar Srinivasan	Date: 22.02.2018
Guide/convenor	 Dr. Subhadip Ghosh	Date: 22.02.2018
External examiner	 Prof. Anindya Datta	Date: 22/02/2018
Member 1-	 Dr. Moby Sarkar	Date: 22/02/2018
Member 2-	 Dr. Sanjib Kar	Date: 22/02/2018
Member 3-	 Dr. Abdur Rahaman	Date: 22.02.2018

Final approval and acceptance of this thesis is contingent upon the candidate's submission of the final copies of the thesis to HBNI.

I hereby certify that I have read this thesis prepared under my direction and recommend that it may be accepted as fulfilling the thesis requirement.

Date: 22/2/2018

Place: Bhubaneswar


(Dr. Subhadip Ghosh)
Guide

¹This page is to be included only for final submission after successful completion of viva voce.

STATEMENT BY AUTHOR

This dissertation has been submitted in partial fulfillment of requirements for an advanced degree at Homi Bhabha National Institute (HBNI) and is deposited in the Library to be made available to borrowers under rules of the HBNI. Brief quotations from this dissertation are allowable without special permission, provided that accurate acknowledgement of source is made. Requests for permission for extended quotation from or reproduction of this manuscript in whole or in part may be granted by the Competent Authority of HBNI when in his or her judgment the proposed use of the material is in the interests of scholarship. In all other instances, however, permission must be obtained from the author.

Somnath Koley

DECLARATION

I, hereby declare that the investigation presented in the thesis has been carried out by me. The work is original and has not been submitted earlier as a whole or in part for a degree / diploma at this or any other Institution / University.

Somnath Koley

List of Publications

Journal

1. Probe Dependent Solvation Dynamics Study in a Microscopically Immiscible Dimethyl Sulfoxide–Glycerol Binary Solvent. Kaur,H.;[†]**Koley, S.**;[†]Ghosh; S.*J. Phys. Chem. B*, **2014**, *118*, 7577-7585. [[†] Equal Contribution]
2. *Probe Dependent Anomalies in Solvation Dynamics of Coumarin Dyes in Dimethyl Sulfoxide-Glycerol Binary Solvent: Confirming the Local Environments are Different for Coumarin Dyes. **Koley, S.**; Kaur, H.; Ghosh, S. *Phys. Chem. Chem. Phys.***2014**, *16*, 22352-22363.
3. *Study of Microheterogeneity in Acetonitrile–Water Binary Mixtures by using Polarity -Resolved Solvation Dynamics.**Koley, S.**; Ghosh,S.*ChemPhysChem***2015**, *16*, 3518 – 3526.
4. *Diffusion Assisted Bimolecular Electron Injection to CdS Quantum Dots: Existence of Different Regimes in Time Dependent Sink Term of Collins–Kimball Model. Bhowmik, A.;Kaur, H.; **Koley, S.**; Jana, S.;Ghosh, S. *J. Phys. Chem. C* **2016**, *120*, 5308–5314.
5. *Study of Diffusion Assisted Bimolecular Electron Transfer Reactions: CdSe/ZnS Core Shell Quantum Dot Acts as an Efficient Electron Donor and Acceptor. **Koley, S.**; Panda, M. R.; Ghosh, S. *J. Phys. Chem. C***2016**, *120*, 13456-13465.
6. *The Study of Electron Transfer Reactions in a Dendrimaric Assembly: Proper Utilization of Dendrimer Fluorescence. **Koley, S.**; Ghosh; S. *Phys. Chem. Chem. Phys.* **2016**, *18*, 24830-24834.

7. *A Deeper Insight into an Intriguing Acetonitrile–Water Binary mixture: Synergistic effect, Dynamic Stokes Shift, Fluorescence Correlation Spectroscopy, and NMR Studies. **Koley, S.**; Ghosh; S. *Phys. Chem. Chem. Phys.*, **2016**, *18*, 32308-32318.
8. *Encapsulation and Residency of a Hydrophobic Dye within the Water Filled Interior of a PAMAM Dendrimer Molecule. **Koley, S.**; Ghosh; S. *J. Phys. Chem. B***2017**, *121*, 1930-1940.
9. Spectroscopic and Calorimetric Studies of Molecular Recognitions in a Dendrimer–Surfactant Complex. **Koley, S.**; Panda, M. R.; Bharadwaj, K.; Ghosh; S. *Langmuir*, **2018**, *34*, 817–825.
10. Probing of Reorganization Dynamics within the Different Phases of Thermotropic Liquid Crystals. Panda, M. R.[†]; **Koley, S[†]**; Mishra K.; Ghosh; S. *Chemistry Select*, **2018**, *3*, 1551-1560.
11. An Approach to a Model Free Analysis of Excited-State Proton Transfer Kinetics in a Reverse Micelle. Singh, S.[†]; **Koley, S[†]**; Mishra K.; Ghosh; S. *J. Phys. Chem. C*, **2018**, *122*, 732–740.

* pertaining to the present thesis; [†] Equal Contribution

Conferences

1. Presented poster in “National Symposium of Radiation and Photochemistry” (**NSRP-2015**) at Indian Institute of Technology Kanpur.
2. Presented poster titled “Photoinduced Electron transfer from PAMAM Dendrimer to 2,4-Dinitrotoluene” in “Recent Advances in Molecular Spectroscopy” (**RAMS-2016**) at University of Hyderabad.
3. Delivered a short talk on “Probing the PAMAM Dendrimer and its Soft Assemblies” in Inter IISER Chemistry Meet (**IICM-2017**) at Indian Institute of Science Education and Research (IISER) Bhopal.

Somnath Koley

Dedicated to... ..

My Parents

ACKNOWLEDGEMENTS

It gives me immense pleasure to express my cordial gratitude and regards to my supervisor Dr. Subhadip Ghosh, for his constant support and guidance. His scientific insights, modern thinking, professionalism and valuable suggestions have made this work possible and will keep inspiring me in future. I really feel lucky and grateful to work with him.

I would like to thank my thesis monitoring committee members Prof. A. Srinivasan, Dr. Moley Sarkar, Dr. Sanjib Kar and Dr. Abdur Rahaman for their support and suggestions during the tenure of my PhD. I want to extend my gratitude and thankfulness to other teachers in School of Chemical Sciences, NISER, under whom I did my course-works. I would also like to thank the non-teaching staffs and support members of NISER for their direct or indirect supports which I availed for my thesis work.

I would like to acknowledge my seniors and lab members for their co-operation and working with them in the lab have been a great pleasure. I am particularly thankful to Sudhirda, Tapasda and Basuda my seniors in the department who helped me a lot during learning new instruments and techniques. I want to thank my present lab members Manas, Kiran, Krishna, Siddharth and Dushali for their support and enjoyable company.

I sincerely thank NISER for financial support and research infrastructure.

Finally, I owe my heartfelt gratitude to my parents and my elder sister for their sacrifice, constant support and encouragement during the course of my studies.

Somnath Koley

CONTENTS

	Page No.
SYNOPSIS	15
List of Schemes	25
List of Figures	27
List of Tables	37
Chapter 1	
Introduction	
1.1 Binary Solvent Mixture	41
1.1.1 Properties and Solvation Behaviour	41
1.1.2 Microheterogeneity and Composition Dependent Fluctuation within a Binary Mixture	43
1.2 Dendrimers	45
1.2.1 Structure, properties and applications	45
1.2.2 Changes in Structure and Properties with Physiological Conditions	48
1.2.3 Photophysical Studies on Dendrimers	48
1.2.4 Intrinsic Fluorescence of PAMAM Dendrimer	49
1.3 Quantum Dots	50
1.3.1 General Properties and Applications	50
1.3.2 Types of Metal Chalconide Quantum Dot	52
1.3.3 Study of Photoinduced Electron Transfer with QDs	53
1.4. Objective behind the thesis	54
Chapter 2	

Instrumentation and Methodologies

2.1. Instrumental Techniques Used	56
2.1.1. Steady State Spectra	56
2.1.2. Time Resolved Fluorescence Measurements	57
2.1.2.1. Basic Principle of Time Correlated Single Photon Counting Technique	58
2.1.2.2. Data fitting and deconvolution procedure	59
2.1.2.3. Construction of Time Resolved Emission Spectra and measurement of Solvation Dynamics	60
2.1.3. Time Resolved Fluorescence Anisotropy and Rotational Dynamics	62
2.1.4. Fluorescence Correlation Spectroscopy and Translational Diffusion Measurements	64
2.1.5. Cyclic Voltammetry measurement and Free Energy Calculation	68
2.2 Materials and Sample Preparation	68

Chapter 3

Composition Dependent Multiple Anomalies in the Solvation Dynamics of Coumarin Dyes in Dimethyl Sulfoxide– Glycerol Binary Solvent Mixture

3.1 Introduction	69
3.2 Composition Dependent Solvation Dynamics Study	72
3.3. Rotational Dynamics Study: Specific Solute-Solvent Interaction	81
3.4. Conclusion	86

Chapter 4

Study of Microheterogeneity in Acetonitrile –Water Binary Mixture

4.1. Introduction	88
4.2. Results and Discussions	91
4.2.1 Polarity Resolved Study	91
4.2.1.1. Steady State Spectra and Preferential Solvation Analysis	92
4.2.1.2. Time Dependent Dynamic Stokes Shift and Solvation Dynamics Study	95
4.2.1.3. Time Resolved Fluorescence Anisotropy Study	101
4.2.2. Nonexponential relaxation of C343: Powerlaw dependence and Simultaneous Stabilization of two forms in the binary mixture	104
4.2.3. Fluorescence correlation spectroscopy (FCS) study of translational diffusion	108
4.2.4. Synergistic Solvation behaviour in ACN-WT Binary Mixture	110
4.2.5. ¹ H NMR study in ACN-WT binary mixture	116
4.3. Conclusion	120

Chapter 5

Fluorescence Probing of PAMAM Dendrimer Interior

5.1. Introduction	122
5.2. Sample Preparation and Evidence for <i>Host-Guest</i> Complex Formation	125
5.3. Results and Discussions	127
5.3.1. Study of Red Edge Excitation Shift (<i>REES</i>) using Intrinsic Fluorescence Of <i>dendrimer</i>	127

5.3.2. Molecular Recognition Study of <i>C153-Dendrimer</i> Complex	130
5.3.3. Study of <i>C153</i> Fluorescence from the <i>Dendrimer-C153</i> complex as a Function of the Medium <i>pH</i>	132
5.3.4. <i>Rotational Anisotropy</i> Study of <i>Dendrimers</i> Alone and <i>C153</i> attached to the <i>Dendrimer</i>	134
5.3.4.1. <i>Rotational Diffusions study of Dendrimer using its Intrinsic Fluorescence</i>	135
5.3.4.2. Rotational Diffusion of <i>C153</i> Attached to a Dendrimer Molecule	139
5.3.5. <i>FCS</i> Study of Translational Diffusion of <i>C153-Dendrimer</i> Complex	141
5.3.6. Interaction of <i>Dendrimer</i> with a Hydrophilic Dye <i>Coumarin 343</i>	143
5.4. Conclusion	145

Chapter 6

Study of Electron Transfer Reactions in a Dendrimeric Assembly: Proper Utilization of Dendrimer Fluorescence

6.1. Introduction	146
6.2. Results and Discussions	148
6.2.1. Photophysical Study on PAMAM Dendrimer in Methanol	148
6.2.2. Fluorescence Quenching of Dendrimer in Presence of DNT	149
6.2.3. Evidence of Host-Guest Complex Formation: Isothermal Titration Calorimetry Study	152
6.2.4. Electron Transfer Rate and Chemical Driving Force	154
6.2.5. Understanding the PET Mechanism: Role of Tertiary Amines of Dendrimer	156
6.3. Conclusion	157

Chapter 7

Diffusion Assisted Bimolecular Electron Transfer with Quantum Dots

7.1. Introduction	159
7.2. Results and Discussions	164
7.2.1. Core Type Quantum Dots	164
7.2.1.1. Sample Characterization, Optical and Band Properties	164
7.2.1.2. Quenching Experiment and Fitting Models	166
7.2.1.2.1. Fitting to the steady state data	166
7.2.1.2.2. Fitting to the time resolved data	171
7.2.1.3. The Factors Affecting the ET Kinetics	173
7.2.2. Core-Shell Type Quantum Dot	177
7.2.2.1. Sample characterizations	177
7.2.2.2. Calculation of Band Positions and Free Energy	178
7.2.2.3. Energy Band Alignments, Steady State Fluorescence and Lifetime Quenching and Stern-Volmer Plots	179
7.2.2.4. Fitting of QD-NMA quenching data using SQCK model	184
7.2.2.5. Fitting of <i>QD-DNT</i> quenching data using modified <i>SV</i> equation	186
7.3. Conclusion	189
REFERENCES	190

SYNOPSIS

Chapter 1: Introduction

Soft molecular interactions are crucial for governing most of the chemical and dynamical processes undergo in solution.¹ These interactions including hydrophobic, electrostatic, hydrogen bond interactions, are important for many vital processes like solubilising of reactant molecules in a solvent, micellization of surfactant molecules and scaffolding of supramolecular assemblies are few examples.²⁻⁴ Availability of modern laser with wonderful time resolution has enabled researchers studying the kinetics within the molecular assemblies down to a sub-ten picosecond time scale.⁵ In this introductory chapter of the proposed thesis the basic aspects of the molecular spectroscopy along with the recent development for the exploration of complex chemical and biological systems are discussed. The works are discussed here include dynamics in binary systems and dendrimers and electron transfer kinetics in nanoparticles. All these studies are closely connected to my thesis works.

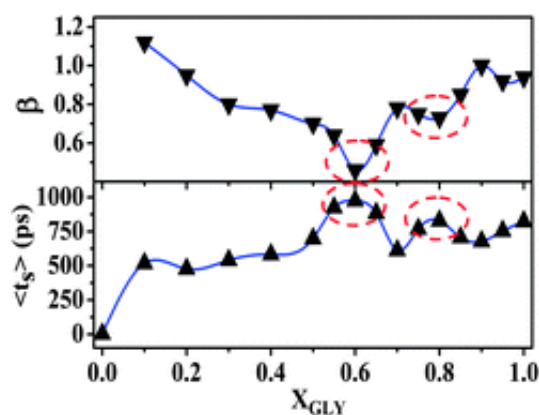
Chapter 2: Instrumentation and Adopted Methodologies

This chapter mainly discusses the experimental section for the work presented in the thesis. The details of the instrumental techniques used in this study, *viz.* steady-state and time resolved fluorescence, fluorescence anisotropy and translational diffusion measurements are discussed along with the instruments used. The detailed calculation and the principle of the adopted methodologies such as solvation dynamics,⁶ diffusion dynamics (translational and rotational)⁷⁻⁸ and photoinduced electron transfer kinetics⁹ are discussed in this chapter.

Chapter 3: Composition Dependent Multiple Anomalies in the Solvation Dynamics of Coumarin Dyes in Dimethyl Sulfoxide–Glycerol Binary Solvent Mixture¹⁰

Solvation dynamics of coumarin dyes in dimethyl sulfoxide (DMSO)–glycerol (GLY) binary mixtures were studied across the GLY concentrations. Three coumarin dyes with widely different hydrophobicities were used for probing the entire polarity regions of this solvent mixture. Multiple anomalous concentration regions with significantly slow solvation times were detected from all three coumarin dyes. However, their precise positions and number of anomalous points were found to be probe molecule dependent. The solvation dynamics of the moderately hydrophobic dye coumarin 480 maintain a plateau region with a similar solvation time (~ 550 ps) until X_{GLY} (the mole fraction of glycerol) reaches 0.5, followed by a sudden slowdown at two concentration region (to ~ 975 ps at $X_{\text{GLY}} \sim 0.6$ and to ~ 828 ps at $X_{\text{GLY}} \sim 0.8$) on the addition of more GLY to the mixture. For very high GLY-content samples ($X_{\text{GLY}} > 0.85$), the solvation times remain similar on further changes of the GLY concentrations. The solvent correlation function was found to be non-exponential in nature and the deviation of the exponent from unity nicely correlated with the slowdown of solvation time. In contrast to C480, the most hydrophobic dye coumarin 153 shows a linear increase of solvation time in the DMSO–GLY mixture, with increase in GLY concentration, except for the concentration region, $X_{\text{GLY}} \sim 0.45$ – 0.55 (peak at 0.5), where a substantial slowdown of the solvation time is observed. The highly hydrophilic probe coumarin 343 demonstrates multiple concentration regions ($X_{\text{GLY}} \sim 0.05$ – 0.10 , 0.25 – 0.35 and 0.55 – 0.65) where the solvation dynamics are significantly retarded. The presence of probe dependent anomalies in the DMSO–GLY mixture is a clear indication that the locations of probe molecules within this solvent mixture are different. We assume that the composition dependent slowing-down of the solvation time could be a reflection of several phenomena, including the inherent inhomogeneity, intriguing structural transformations in the DMSO–GLY

mixture, percolation among DMSO molecules and network structure formation, where DMSO:GLY complexes contribute to the dynamical features.

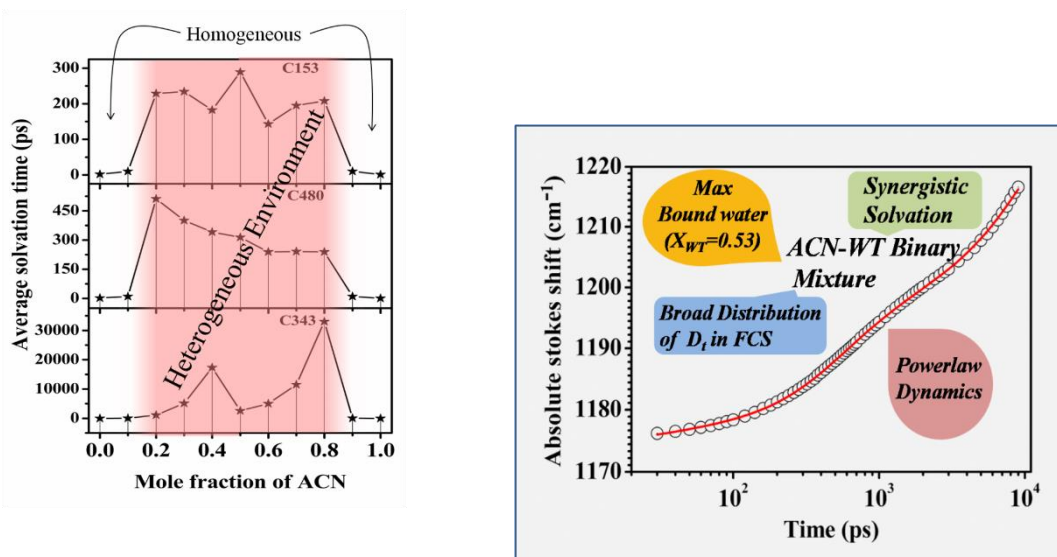


Average solvation time and deviation of non-ideality parameter in a single frame as a function of mole fraction of glycerol.

Chapter 4: Study of Microheterogeneity in Acetonitrile –Water Binary Mixture^{11,12}

The microheterogeneity of acetonitrile-water (ACN-WT) binary mixture has been studied by using several techniques such as Time Dependent Dynamic Stokes Shift (TDDDS), synergistic effect, fluorescence correlation spectroscopy (FCS) and nuclear magnetic resonance (NMR) spectroscopy. Synergism of a binary mixture refers to some unique changes of the physical and thermodynamic properties of the solvent mixture, originating from the interactions among its co-solvents, which are absent within the pure co-solvents. Synergistic solvation of a binary mixture is likely to be fundamental for greater stabilization of an excited state solute dipole; at least to some extent greater as compared to one stabilized by any of its co-solvents alone. In a composition dependent study using three coumarin dyes it has been observed that the solvation time was retarded to a large extent in the composition range of 0.2 to 0.8 mole fraction of acetonitrile. This has been assigned as microheterogeneous region and a diffusion assisted process which retard the solvation dynamics to a large extent. On further study with fluorescence correlation spectroscopy

(FCS) we observed that, unlike the translational diffusion coefficient (D_t) of a dye molecule within a pure solvent, which remains the same irrespective of the location of the dye molecule inside the solvent, a broad distribution among the D_t values of a dye molecule is obtained from different locations within the ACN–WT binary mixture. Lastly our ^1H NMR study in the ACN–WT binary mixture shows the existence of strong hydrogen bond interactions among the cosolvents in the ACN–WT mixture and quantitative information about the water bound to the acetonitrile molecule have been inferred. Our results provide a deeper insight and concrete evidence in favour of the proposed microheterogeneity range of the binary

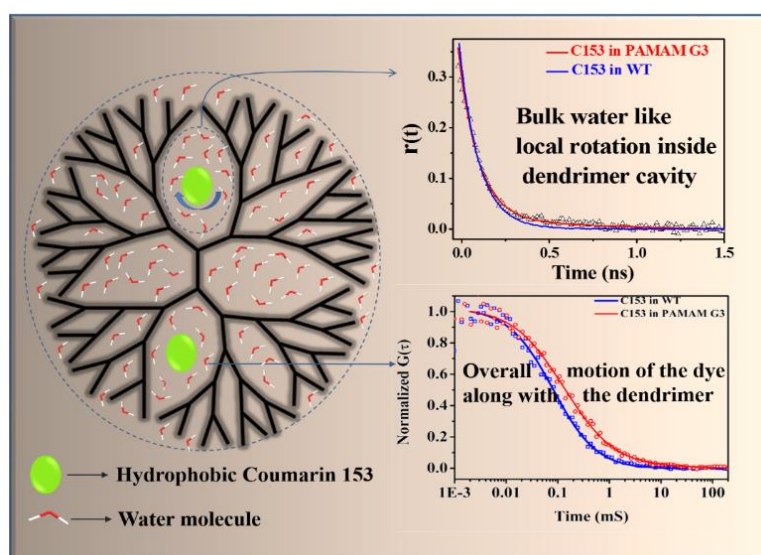


Depiction of the homogeneous and microheterogeneous environment with the mixture composition in the binary mixture (left) and the insights obtained from various spectroscopic studies (right).

Chapter 5: Fluorescence Probing of PAMAM Dendrimer Interior¹³

Tightly confined water within a small droplet behaves differently from bulk water. This notion is obtained based on the several reports that show unusual behaviors of water droplet residing at the core of a reverse micelle. In this study we have shown a well known hydrophobic dye coumarin 153 (C153) prefers to reside at the water rich region inside dendrimer molecule. Optical density (OD) measurement at the absorption peak of C153

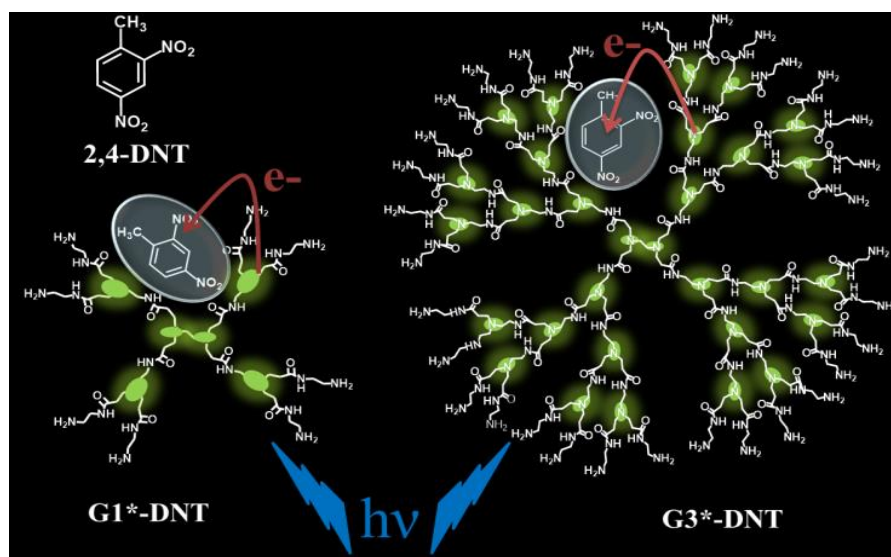
shows C153 is almost insoluble in bulk water but highly soluble in aqueous dendrimer solution. OD of C153 increases many-folds in the latter case as compared to the OD in bulk water. Most interesting observation we found when we compared the data from fluorescence correlation spectroscopy (FCS) with fluorescence anisotropy decay of C153 in aqueous dendrimer solution. FCS measurement reveals a much slower translational diffusion time (τ_D) of C153 attached to a dendrimer molecule as compared to the τ_D of free C153 in bulk water in the absence of dendrimer. Slower τ_D in former case is commensurate with the size of the dendrimer molecule. This is possible only when C153 is encapsulated by the dendrimer molecule. Contrary to the FCS study, fluorescence anisotropy decay of C153 in water remains largely invariant after addition of dendrimer. This can happen if the bulk-water like environment at C153 surroundings is preserved within the C153-dendrimer complex. This supports our intuitive expectation that C153 resides within the water-rich peripheral cavities inside a dendrimer molecule; as a more expected binding of C153 to the hydrophobic core of dendrimer may not be possible due to an inadequate size of the dendrimer core.



Schematic representation for the residency of the hydrophobic dye molecule inside water filled cavity of the dendrimer.

Chapter 6: Study of Electron Transfer Reactions in a Dendrimeric Assembly: Proper Utilization of Dendrimer Fluorescence¹⁴

In this chapter we have studied how the intrinsic fluorescence of the dendrimer can be utilised for potential application such as sensing of nitroaromatic compounds via electron transfer process. The effect of generation of dendrimer on encapsulation and electron transfer has been studied extensively. The association constant and the chemical driving force (free energy) for electron transfer was found to be very different for two different generation of dendrimer which leads to generation dependent quenching phenomena. Careful examination confirmed that the tertiary amine centres acting as novel photo-redox centre and trapping of quencher molecules within the dendrimer cage helps electron transfer process to take place through an expeditious route.

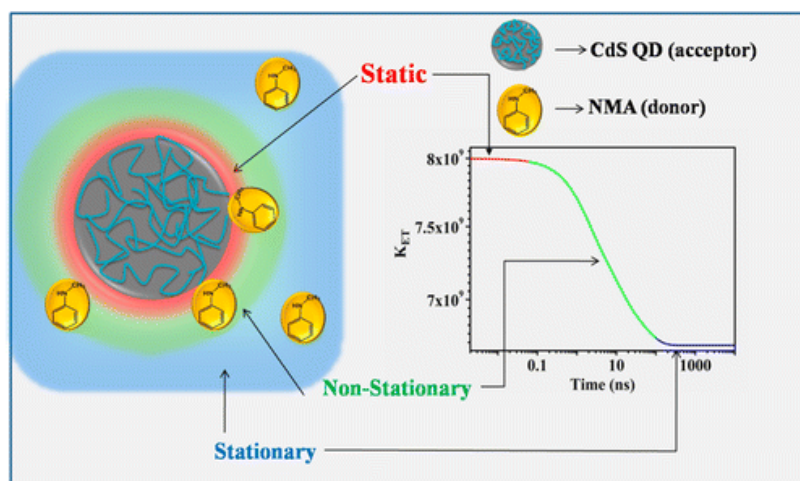


Schematic representation for trapping of 2,4-dinitrotoluene in two generations of PAMAM dendrimers and photoinduced electron transfer.

Chapter 7: Diffusion Assisted Bimolecular Electron Transfer with Quantum Dots^{15,16}

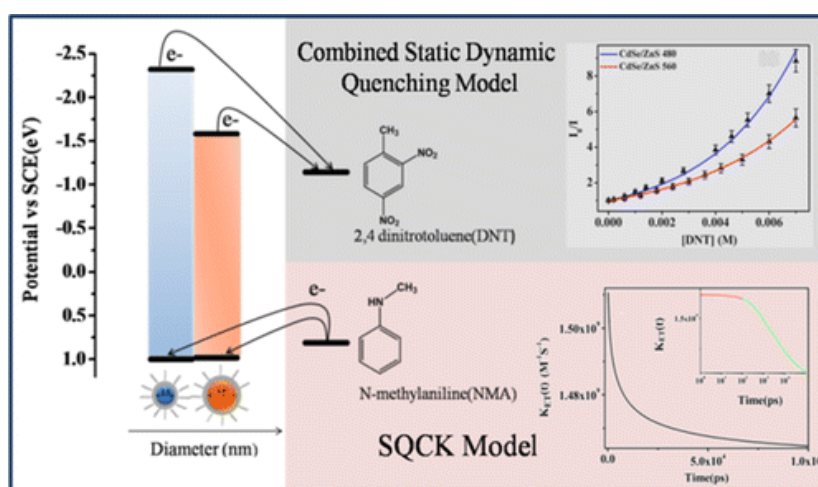
The diffusion assisted electron transfer process has been studied with two types of quantum dot which exhibited different phenomena:

(a) Core type quantum dot: Excited state lifetime and steady state fluorescence of a series of core type CdS quantum dots (QDs) with different sizes in toluene were quenched by electron donor molecule *N*-methyl aniline (NMA). Static quenching Collins–Kimball (SQCK) diffusion model enabled convincing fittings to the steady-state and time-resolved data using nearly a same set of parameters, only after considering the presence of inherent quencher sites statistically distributed over the quantum dot surface. Electron injection rate shows strong chemical driving force dependency. QD with largest dimension (~ 5.4 nm) used in this study exhibits a slightly higher chemical driving force ($-\Delta G^0 = 0.80$ eV) of electron transfer as compared to that ($-\Delta G^0 = 0.79$ eV) obtained for the smallest size QD (~ 3.8 nm). However, such a small change in driving force causes nearly ~ 3 times acceleration of the ET rate coefficient ($k_0 = 8.30 \times 10^9 \text{ M}^{-1} \text{ s}^{-1}$) within the larger size QD as compared to that ($k_0 = 2.74 \times 10^9 \text{ M}^{-1} \text{ s}^{-1}$) observed in smaller size QD. The time evolution of the sink term obtained from the Collins–Kimball fitting of ET kinetics shows different regimes of the kinetics (static and nonstationary as shown figure below).



(b) Core-Shell quantum dot: Excited-state lifetimes and steady-state emission of two different size CdSe/ZnS core–shell quantum dots (QDs) in toluene were quenched by an electron donor molecule *N*-methyl aniline (NMA) and an electron acceptor molecule 2,4-

dinitrotoluene (DNT) in two separate sets of experiments. Static quenching Collins-Kimball (SQCK) diffusion model enabled a conclusive fitting only to the electron transfer (ET) kinetics of QD-NMA pairs. However, for QD-DNT pairs, a clear break down of SQCK model was observed. Interestingly, when we considered a QD-to-DNT static complex formation, we observed even a classic Stern–Volmer (SV) fitting equation can provide an adequate fitting to the ET kinetics. ET kinetics we studied here are strongly controlled by the chemical driving forces (ΔG). For example, electron injection rates (by NMA) to the two QDs with core dimensions ~ 3.4 nm (QD560) and ~ 2.5 nm (QD480) were found to be similar ($\sim 1.50 \times 10^9$ – 1.60×10^9 $M^{-1} S^{-1}$), which is nicely correlated with their nearly same values of the chemical driving force ($-\Delta G \sim 0.18$ – 0.19 eV) associated with their ET reactions. Conversely, electron donating rates (to DNT) of the same two QDs are found to be $\sim 7.0 \times 10^9 M^{-1} S^{-1}$ (QD480) and $\sim 3.7 \times 10^9 M^{-1} S^{-1}$ (QD560), respectively, for QD480 and QD560, which is again congruent to their chemical free energy changes ($-\Delta G_{QD480-DNT} \sim 1.18$ eV and $-\Delta G_{QD560-DNT} \sim 0.44$ eV). A nonadiabatic sink term of ET kinetics from QD-NMA pair shows distinct regimes associated with the ET reaction (i.e., static, nonstationary, and stationary).



References:

- [1] Claessens, C. G.; Stoddart, J. F. Review Commentary—Interactions in Self-Assembly. *J. Phys. Org. Chem.* **1997**, *10*, 254-272.
- [2] Nandi, N.; Bhattacharyya, K.; Bagchi, B. Dielectric Relaxation and Solvation Dynamics of Water in Complex Chemical and Biological Systems. *Chem. Rev.* **2000**, *100*, 2013-2046.
- [3] Pal, S. K.; Zewail, A. H. Dynamics of Water in Biological Recognition. *Chem. Rev.* **2004**, *104*, 2099-2124.
- [4] Bhattacharyya, K. Solvation Dynamics and Proton Transfer in Supramolecular Assemblies. *Acc. Chem. Res.* **2003**, *36*, 95-101.
- [5] Lakowicz, J. R. In Principles of Fluorescence Spectroscopy; Ed.; Springer: New York, 2006.
- [6] Maroncelli, M.; Fleming, G. R. Picosecond Solvation Dynamics of Coumarin 153: The Importance of Molecular Aspects of Solvation. *J. Chem. Phys.* **1987**, *86*, 6221-6239.
- [7] Horng, M. L.; Gardecki, J. A.; Maroncelli, M. Rotational Dynamics of Coumarin 153: Time-Dependent Friction, Dielectric Friction, and Other Nonhydrodynamic Effects. *J. Phys. Chem. A* **1997**, *101*, 1030-1047.
- [8] Haustein, E.; Schwille, P. Fluorescence Correlation Spectroscopy: Novel Variations of an Established Technique. *Annu. Rev. Biophys. Biomol. Struct.* **2007**, *36*, 151-169.
- [9] Marcus, R. A. Electron Transfer Past and Future. *Adv. Chem. Phys.* **1999**, *106*, 1-6.
- [10] Koley, S.; Kaur, H.; Ghosh, S. Probe Dependent Anomalies in Solvation Dynamics of Coumarin Dyes in Dimethyl Sulfoxide-Glycerol Binary Solvent: Confirming the Local

Environments are Different for Coumarin Dyes. *Phys. Chem. Chem. Phys.* **2014**, *16*, 22352—22363.

[11] Koley, S.; Ghosh, S. Study of Microheterogeneity in Acetonitrile–Water Binary Mixtures by using Polarity -Resolved Solvation Dynamics. *ChemPhysChem* **2015**, *16*, 3518 – 3526.

[12] Koley, S.; Ghosh, S. A Deeper Insight into an Intriguing Acetonitrile–Water Binary mixture: Synergistic effect, Dynamic Stokes Shift, Fluorescence Correlation Spectroscopy, and NMR Studies. *Phys. Chem. Chem. Phys.*, **2016**, *18*, 32308-32318.

[13] Koley, S.; Ghosh, S. Encapsulation and Residency of a Hydrophobic Dye within the Water Filled Interior of a PAMAM Dendrimer Molecule. *J. Phys. Chem. B* **2017** (DOI: 10.1021/acs.jpcc.6b10176).

[14] Koley, S.; Ghosh, S. The Study of Electron Transfer Reactions in a Dendrimaric Assembly: Proper Utilization of Dendrimer Fluorescence. *Phys. Chem. Chem. Phys.* **2016**, *18*, 24830-24834.

[15] Bhowmik, A.; Kaur, H.; Koley, S.; Jana, S.; Ghosh, S. Diffusion Assisted Bimolecular Electron Injection to CdS Quantum Dots: Existence of Different Regimes in Time Dependent Sink Term of Collins–Kimball Model. *J. Phys. Chem. C* **2016**, *120*, 5308–5314.

[16] Koley, S.; Panda, M. R.; Ghosh, S. Study of Diffusion Assisted Bimolecular Electron Transfer Reactions: CdSe/ZnS Core Shell Quantum Dot Acts as an Efficient Electron Donor and Acceptor. *J. Phys. Chem. C* **2016**, *120*, 13456-13465.

List of Schemes

		Page No.
1. Scheme 1.1.	Timescales of light absorption and different fast processes	40
2. Scheme 1.2.	Simplified presentation of preferential and synergistic solvation around a solute dipole by a binary mixture formed by two counterparts A and B.	42
3. Scheme 1.3.	Schematic representation of an amine terminated PAMAM dendrimer molecule with ethylenediamine core. Different generation have been depicted with different colour.	47
4. Scheme 1.4.	Simplified diagram for the band alignment and exciton generation of a spherical quantum dot upon photoexcitation.	51
5. Scheme 2.1.	Schematic representation of a reverse mode TCSPC.	59
6. Scheme 2.2.	(A) Schematic diagram of solvation dynamics around a solute dipole, (B) time resolved emission spectra (TRES), (C) wavelength dependent fluorescence lifetime decay.	62
7. Scheme 2.3.	Pictorial presentation for the fluorescence anisotropy process (left). Right sided picture demonstrates the experimental setup for time resolved anisotropy measurement.	63
8. Scheme 2.4.	Schematic representation of a confocal microscope.	65
9. Scheme 2.5.	Development of the autocorrelation curve in FCS.	66
10. Scheme 3.1.	Chemical Structure of the coumarin dyes used in this study.	71
11. Scheme 4.1.	Chemical Structure of the coumarin dyes used in polarity resolved study.	91
12. Scheme 4.2.	Chemical structure of the dyes used for synergism analysis.	111

13. **Scheme 5.1.** Chemical structures of *PAMAM* dendrimers (*G1* & *G3*) and coumarin dyes used in this study. The ethylenediamine core of the dendrimers has been identified by red colour. 124
14. **Scheme 5.2.** *pH* dependent protonation of primary and tertiary amine centers of *dendrimer-G1* in aqueous solution. 125
15. **Scheme 5.3.** (A) *MM2* (*molecular mechanics*) optimised structure of *PAMAM dendrimer-G3* in the presence of ~200 water molecules.⁷⁹ (B) One cavity of the *dendrimer* has been magnified for the inspection of cavity size, which shows the average diameter of these water rich cavities is ~1.3 nm. Therefore *C153* with a size of ~0.8 nm can easily be accommodated within the cavity. Water molecules are not shown for clarity. 140
16. **Scheme 6.1.** Schematic representation of the photoinduced electron transfer from *PAMAM* dendrimer to 2,4-DNT. 147
17. **Scheme 7.1.** Schematic representation for diffusion assisted bimolecular reaction between quantum dot and organic molecule. 160

List of Figures

	Page No.
1. Figure 3.1. Picosecond lifetime decay profile of C480 in DMSO-GLY binary mixture at $X_{\text{GLY}} \sim 0.5$ monitored at different emission wavelengths. Black circles represent the instrument response function and the solid lines represent the best fit of the experimental data.	73
2. Figure 3.2. (A) Time resolved emission spectra of C153 in DMSO-GLY binary mixture at $X_{\text{GLY}} \sim 0.5$. (B) Decay of solvent correlation function $C(t)$ for C153 in DMSO-GLY binary mixture at $X_{\text{GLY}} = 0.1$ (red), 0.2 (green), 0.4 (cyan), 0.5 (magenta), 0.7 (dark cyan) and 1.0 (orange).	74
3. Figure 3.3. Plot of average solvation time as a function of mole fraction of glycerol for (A) C153, (B) C480 and (C) C343.	76
4. Figure 3.4. Variation of average solvation times (lower panel) and β value (upper panel) as a function of mole fraction of glycerol in DMSO-GLY binary mixture.	77
5. Figure 3.5. Decay of rotational correlation function $r(t)$ of C153 in DMSO-GLY binary mixture with $X_{\text{GLY}} = 0.1$ (Red), 0.4 (Blue), 0.6 (Cyan), 0.8 (Magenta).	81
6. Figure 3.6. The left panel shows the plots of viscosity normalized average rotational times of coumarin dyes as a function of X_{GLY} . The right panel show the log-log plots of the average rotational relaxation times vs medium viscosity at unit temperature of coumarin dyes in DMSO-GLY mixture	83

across the composition under the hydrodynamic boundary conditions.

7. **Figure 4.1.** Steady state emission spectra of three coumarin dyes in ACN-WT binary mixtures of different compositions. The inset shows the plot of absorption and emission maxima as a function of ACN mole fraction. 92
8. **Figure 4.2.** The left panel represents the decay of solvent correlation function $C(t)$ for (A) C153, (B) C480 and (C) C343 in ACN-WT binary mixtures with $X_{ACN}=0.2$ (red line), $X_{ACN}=0.3$ (green line), $X_{ACN}=0.4$ (blue line), $X_{ACN}=0.5$ (cyan line), $X_{ACN}=0.6$ (magenta line), $X_{ACN}=0.7$ (pink line), and $X_{ACN}=0.8$ (wine line). The right panel shows the plots of average solvation time $\langle\tau_s\rangle$ as a function of X_{ACN} for (D) C153, (E) C480, (F) C343, respectively. The vertical for clear understanding of the mole fraction values. 97
9. **Figure 4.3.** Comparison of the decay curve of solvent correlation function $C(t)$ with time evolution of fwhm of TRES (Γ curve) in ACN-WT mixture for (A) C153 at $X_{ACN}=0.5$, (B) C480 at $X_{ACN}=0.2$ and (C) C343 at $X_{ACN}=0.8$. For better comparison, we normalised the Γ curve [$\Gamma(t) = \frac{fwhm(t) - fwhm(\infty)}{fwhm(0) - fwhm(\infty)}$] in a similar manner of normalising $C(t)$ [$=(v_t - v_\infty)/(v_0 - v_\infty)$] curve. Good correlation between long components of Γ curve and $C(t)$ curve was found only in the case of C343, indicating a diffusion 100

assisted solvation kinetics for this dye.

10. **Figure 4.4.** (A) log-log plot of rotational relaxation time (τ_{rot}) of C480 (blue) and C343 (green) in ACN-WT binary mixture as a function of medium viscosity within slip and stick boundary condition. C153 exhibited same trend as C480 and hence not shown for clarity. (B) Plot of viscosity normalized rotational time (τ_{rot}/η) of C153 (red), C480 (blue) and C343 (green) as a function of X_{ACN} within the binary mixture. 103
11. **Figure 4.5.** Powerlaw fitting to the Stokes Shift data for C343 in equimolar ACN-WT mixture. 105
12. **Figure 4.6.** Time resolved area normalized emission spectra (TRANES) of C343 in ACN-WT ($X_{WT} \sim 0.5$) binary mixture. An isoemissive point at 20475 cm^{-1} is clearly visible as shown in the inset of the figure. 107
13. **Figure 4.7.** Distributions of diffusion coefficients as obtained from FCS measurements for (A) DCM in ACN-WT ($X_{WT} = 0.51$) binary mixture; (B) DCM in neat ACN; (C) R6G in ACN-WT ($X_{WT} = 0.51$) binary mixture and (D) R6G in neat WT. 109
14. **Figure 4.8.** Plots of (A) absorption maxima, (B) emission maxima and (C) molar electronic transition energy of DCM in ACN-WT binary mixture as a function of mole fraction of water. 114
15. **Figure 4.9.** Plots of (A) absorption maxima, (B) emission maxima and (C) molar electronic transition energy of 4-AP in ACN-WT binary mixture as a function of mole fraction of water. 115

16. **Figure 4.10.** Plots of (A) absorption maxima, (B) emission maxima and (C) molar electronic transition energy of *C343* in *ACN-WT* binary mixture as a function of mole fraction of water. 115
17. **Figure 4.11.** Plots of (A) absorption maxima, (B) emission maxima and (C) molar electronic transition energy of *R6G* in *ACN-WT* binary mixture as a function of mole fraction of water. 115
18. **Figure 4.12.** (A) Chemical shift data for the O-H proton of water in the binary mixture at different compositions and (B) Chemical shift data for the C-H proton of acetonitrile in the binary mixture at different compositions. 118
19. **Figure 4.13.** Observed chemical shifts of *C-H* proton of *ACN* (A) and *O-H* proton of water (B) as a function of composition ratio in *ACN-WT* mixture. The red line in figure B represents the best fitting using Eqs 4.6 and 5.7. (C) Plot of fraction of water bound to acetonitrile as a function of water mole fraction within the binary mixture. 120
20. **Figure 5.1.** Photographs were taken under UV illumination (~365 nm) for (A) *C153* in water and (B) *C153* in aqueous solution of *dendrimer-G3* (~0.1 mM). A strong fluorescence only from the latter solution was observed under same excitation power. 126
21. **Figure 5.2.** Absorption spectra of *C153* saturated water in the absence (black curve) and presence of ~0.05 mM (green curve), 0.1 mM (blue curve), and 0.2mM (red curve) *dendrimer-G3* 126

respectively ($pH \sim 9.6$).

22. **Figure 5.3.** Absorption spectrum of *dendrimer-G3* (black) in water. 128
Excitation (dotted lines) and emission (solid lines) spectra of
dendrimer-G1 (blue) and *dendrimer-G3* (red) in water.
23. **Figure 5.4.** Emission spectra of aqueous (A) *dendrimer-G1* and (A) 128
dendrimer-G3 at different excitation wavelengths.
24. **Figure 5.5.** Initial portion of the fluorescence lifetime decay profiles of 131
C153 in aqueous *dendrimer-G1* at different emission
wavelengths. No detectable rise component was found at red
emission ($\sim 640\text{nm}$) wavelength after reconvolution with
excitation lamp profile.
25. **Figure 5.6.** (A) Plot of fluorescence quantum yield (ϕ) of *C153* in 133
aqueous *dendrimer-G3* solution as a function of medium pH .
(B) Plot of pH of aqueous *dendrimer-G3* solution as a
function of HCl/dendrimer mole ratio. Two end points were
detected during the titration due to the stepwise protonation
to the primary amine centres first (at HCl/dendrimer ~ 32)
and followed by tertiary amine centres (at HCl/dendrimer
 ~ 62). This figure shows a nice correlation of end points with
the number of primary and tertiary amines present in
dendrimer-G3.
26. **Figure 5.7.** Decay of rotational correlation function $r(t)$ with time for 136
dendrimer-G1 and *dendrimer-G3* in water utilising the
intrinsic fluorescence of *dendrimer*. Solid lines represent the

- fitted curves.
27. **Figure 5.8.** Dynamic light scattering (*DLS*) study of sizes of the *dendrimer-G3* complex in water at different *pHs*. 138
28. **Figure 5.9.** Rotational anisotropy decay curves for *C153* in aqueous ~ 0.2 mM *dendrimer-G3* solution (black curve). Red line represents the best fitting to the experimental decay curve. The blue line has been simulated using the reported rotational correlation time of *C153* in bulk water from Ref 211. The simulated curve is plotted with a viscosity ~ 1.15 times higher (to make a same viscosity with ~ 0.2 mM aqueous *dendrimer-G3* solution) with respect to the viscosity of neat water, to compare these two curves at isoviscous condition. 139
29. **Figure 5.10.** Normalized autocorrelation curves for *C153* in water (blue) and *C153* in aqueous *dendrimer-G3* solution (red). *pH* of the aqueous *dendrimer* solution is ~ 9.6 . 143
30. **Figure 5.11.** Fitted lines of the rotational correlation function $[r(t)]$ of *C343* in ~ 0.2 mM aqueous *dendrimer* solution at different medium *pHs*. The inset depicts the average rotational time of *C343* (black points) and *C153* (red points) as a function of medium *pH*. Samples were excited at 445 nm and emission was collected at the emission peak positions. 144
31. **Figure 6.1.** Steady state spectra of *PAMAMdendrimer-G3* in methanol: absorption (blue dashed line); excitation (green line, 148

monitored at emission peak); and emission (red line, excited at excitation spectrum). Black dashed line represents the absorption spectrum of *DNT* in methanol.

32. **Figure 6.2.** Quenching of steady state fluorescence and lifetime of *PAMAMdendrimerG1* (upper panel) and *PAMAMdendrimerG3* (lower panel) in presence of *DNT* in methanol. (C) and (F) represent the lifetime (blue) and steady state (red) *SV* plots for *G1* and *G3 PAMAM dendrimers* respectively. $I(\tau)$ & $I_0(\tau_0)$ are the steady state intensities (*lifetimes*) of dendrimers in the presence & absence of quencher molecule. 150
33. **Figure 6.3.** *SV* plots of lifetime quenching for *PAMAMdendrimerG1* (blue) and *G3* (red). Solid lines represent linear fit of the experimental data points. 151
34. **Figure 6.4.** ITC raw data of heat change during titration of *DNT* with (A) *G1* and (C) *G3PAMAM dendrimers* in methanol. (B) and (D) are the analysis of the data and blue line represents conclusive fitting with one site binding model. 153
35. **Figure 6.5.** Fitting of the steady state S-V plots using equation 6.1 for (A) *G1-DNT* pair and (B) *G3-DNT* pair. 154
36. **Figure 6.6.** Cyclic voltammetry curves for (A) *G1* and (B) *G3PAMAM dendrimers* (represented vs. Ag/AgCl reference electrode). 156
37. **Figure 6.7.** Fluorescence lifetime of the dendrimer after addition of 2,4-DNT in presence of 1(N) HCl solution. 157
38. **Figure 7.1.** Left panel: Transmission electron microscopy images of 165

- CdS quantum dots: (A) CdS440, (B) CdS460, and (C) CdS480. Right panel: Corresponding size distribution histograms of (D) CdS440, (E) CdS460 and (F) CdS480.
39. **Figure 7.2.** Fitted auto correlation curves for CdS440 (blue), CdS460 (green) and CdS480 (red) in toluene. 165
40. **Figure 7.3.** (a) Energy band alignment diagram of *QD-NMA* pairs used in this study. (b) Absorption spectra of *NMA* (black solid line), *CdS440* (3.8 nm, blue dotted line), *CdS460* (4.5 nm, green dotted line) and *CdS480* (5.4 nm, red dotted line). Corresponding emission spectra of the *QDs* are shown in solid lines (same colors with absorption spectra). 166
41. **Figure 7.4.** (A) Steady state emission spectra and (B) lifetime decay profile of CdS440 in toluene at various *NMA* concentrations. Excitation wavelength = 375 nm. 167
42. **Figure 7.5.** Steady state S-V plots of *QD-NMA* pairs. SQCK fittings for CdS440 (blue), CdS460 (green) and CdS480 (red) are shown by the solid lines. 167
43. **Figure 7.6.** Time evolution of experimentally measured survival probability due to ET process only CdS440 at various quencher concentrations. Red lines represent the SQCK fittings. 172
44. **Figure 7.7.** Time evolution of the rate coefficient of electron transfer from *NMA* to three different size *QDs* (obtained from SQCK fittings). The insets show the same plots in log scale (time axis): static (red line) and non-stationary (green line) 174

regimes are clearly visible within the plot.

45. **Figure 7.8.** Plot of $\ln k_{\text{ET}}$ as a function of $1/T$ (Arrhenius plot) for the three QD-NMA pairs. Red lines are the linear fit to the experimental data (blue solid balls). Activation energies were calculated from the slope of the fitted lines and equation 7.10. 175
46. **Figure 7.9.** Fitted auto correlation curves for *CdSe/ZnS480* (blue) and *CdSe/ZnS560* (red) in toluene. 178
47. **Figure 7.10.** (A) Energy band alignment of the *QD-NMA* and *QD-DNT* redox pairs. (B) Absorption spectra (solid lines) for *DNT* (black), *NMA* (cyan), *QD480* (blue), *QD560* (red) and emission spectra (dotted lines) for *QD480* (blue), *QD560* (red). 180
48. **Figure 7.11.** Left panel shows steady state emission spectra of *CdSe/ZnS480* in toluene at (A) various *NMA* concentrations and (B) various *DNT* concentrations. Right panel depicts fluorescence lifetime decay profile for *CdSe/ZnS480* in toluene at (C) various *NMA* concentrations and (D) various *DNT* concentrations. Excitation wavelength = 375 nm. 181
49. **Figure 7.12.** Left panel shows the steady state Stern-Volmer plots for (a) *QD-DNT* pairs (the solid lines showing the best fits by eq. 7) and (b) *QD-NMA* pairs (the solid lines showing SQCK fittings). Right panel represents the corresponding time resolved *SV* plots for (c) *QD-DNT* pair and (d) *QD-NMA* pair, respectively. Solid lines represent linear fit of the data 182

and the error bar represents the error limit in the experimental data points.

50. **Figure 7.13.** Time evolution of the rate coefficient $[k(t)]$ for QD-NMA pair. As both the QDs (QD480 & QD560) exhibited similar kind of dependency of ET rate with time, therefore only one data has been shown. Inset shows the different regimes (red-*stationary* and green- non-stationary) of the electron transfer process. 185
51. **Figure 7.14.** Plot of $(I_0/I_c) / (1+k_D[C])$ as a function of quencher concentration $[C]$ for (A) CdSe/ZnS480-DNT pair and (B) CdSe/ZnS560-DNT pair. 188

List of Tables

		Page No.
1. Table 3.1.	Decay parameters of solvent correlation function for the coumarin dyes in DMSO-GLY binary mixture.	78
2. Table 3.2.	Rotational relaxation parameters for coumarin dyes in DMSO-GLY mixture.	85
3. Table 4.1.	Parameters of preferential solvation of all three coumarin dyes in ACN-WT binary mixture.	94
4. Table 4.2.	Decay parameters of $C(t)$ of coumarin dyes in ACN-WT binary mixtures at different mole fractions of acetonitrile (X_{ACN}).	98
5. Table 4.3.	Comparison of the long component obtained from the solvent correlation function i.e. $C(t)$ and that from the decay of FWHM of TRES i.e. Γ in case of C343 in some of the ACN-WT mixtures.	100
6. Table 4.4.	Fitting parameters of time resolved fluorescence anisotropy decays of coumarin dyes in ACN-WT mixtures at different mole fractions of acetonitrile (X_{ACN}).	102
7. Table 4.5.	Ground (μ_g) and excited state (μ_e) dipole moments and their differences ($\Delta\mu_{g-e}$) for the dye molecules used in this study.	112
8. Table 5.1.	Emission maxima (λ_{em}^{max}) for dendrimer intrinsic fluorescence different excitation wavelengths (λ_{ex}) and corresponding of <i>dendrimer-G1</i> and <i>dendrimer-G3</i> in aqueous solution.	129

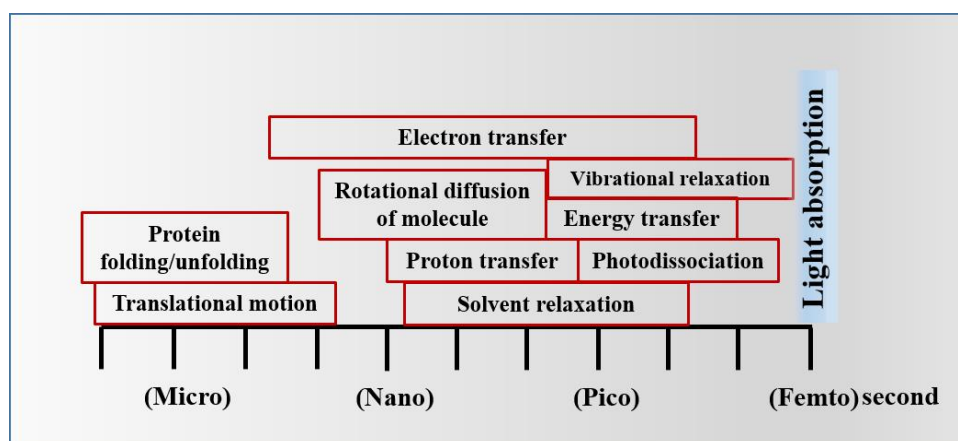
9. Table 5.2.	<i>Wobbling-in-cone</i> model parameters obtained from the fittings of <i>rotational anisotropy</i> decays of <i>dendrimer</i> molecules utilizing their intrinsic fluorescence.	137
10. Table 5.3.	<i>pH</i> dependency of fast (τ_{short})& slow (τ_{long}) <i>rotational anisotropy</i> decay components and the corresponding sizes of <i>C153-dendrimer(G3)</i> complex (as obtained from Stokes Einstein equation assuming τ_{long} originates due to the overall rotation of the complex).	138
11. Table 5.4.	Parameters obtained from the fittings of <i>FCS</i> autocorrelation curves for the translational diffusion of <i>C153</i> in aqueous <i>dendrimer-G3</i> solution (~ 0.1 mM) at different <i>pHs</i> .	142
12. Table 6.1.	Thermodynamic parameters associated to the binding of <i>DNT</i> to G1 and G3 <i>PAMAM</i> dendrimers obtained from ITC measurements.	153
13. Table 6.2.	Calculated parameters associated with the electron transfer in the present system.	155
14. Table 7.1.	SQCK time resolved [$S_q(t)$] and steady-state S-V fitting parameters of <i>QD-NMA</i> pairs [using equations 7.6-7.9 with $k_D(t)$ from equation 7.3 & k_0 from equation 7.5]. τ_q^{neat} is the <i>QD*</i> lifetime in neat <i>NMA</i> . $R_{\text{tr}}(R_{\text{ss}})$ is the reaction radius (<i>R</i>) obtained from time-resolved (steady-state) SQCK fitting. Unit of <i>R</i> and <i>a</i> is nm.	173

15. Table 7.2.	Temperature dependent electron transfer rate constants and calculated activation energy for the three quantum dots in toluene. $k_{ET}=k_0$ in SQCK fittings.	176
16. Table 7.3.	SQCK fitting parameters of time resolved $S_q(t)$ and steady-state SV plots of <i>QD-NMA</i> and <i>QD-DNT</i> pairs.	186
17. Table 7.4.	Rate coefficients (k_D) and association constants (K_S) of <i>QD-DNT</i> pairs. The value of K_S obtained from the fitting of steady state SV plot using Eq 7 (where k_D value was obtained from lifetime SV fitting and kept fixed in Eq 7).	187

Chapter 1

Introduction

Soft molecular interactions (non-covalent interactions such as hydrophobic, electrostatic and hydrogen bond interactions) are crucial for governing most of the chemical reactions and dynamical processes undergo in solution phase¹⁻¹¹. A number of experimental and computational studies have been reported during the last few decades to understand the nature of non-covalent interactions and how do they affect a chemical process in a supramolecular assembly and biological systems¹²⁻²⁷. Availability of laser with excellent time resolution has revolutionized the modern science by enabling the possibility of studying molecular interactions in real time. Light absorption takes place in femtosecond (10^{-15}) timescale where a molecule absorb the light energy and get excited from the ground state to the excited state. According to Kasha's rule radiative emission occurs mostly from the lowest vibrational level of the first excited state to the ground state with same spin multiplicity (i.e. fluorescence radiation will be observed from $S_1 \rightarrow S_0$ electronic transition. Immediately after electronic excitation of a molecule by a short laser pulse, the excited state of the molecule can be deactivated through a number of fast photophysical phenomena. These include photodissociation, charge transfer, energy transfer, hydrogen bond formation, molecular motion, conformational change etc. (Scheme 1.1).²⁸



Scheme 1.1. Timescales of light absorption and different fast processes.

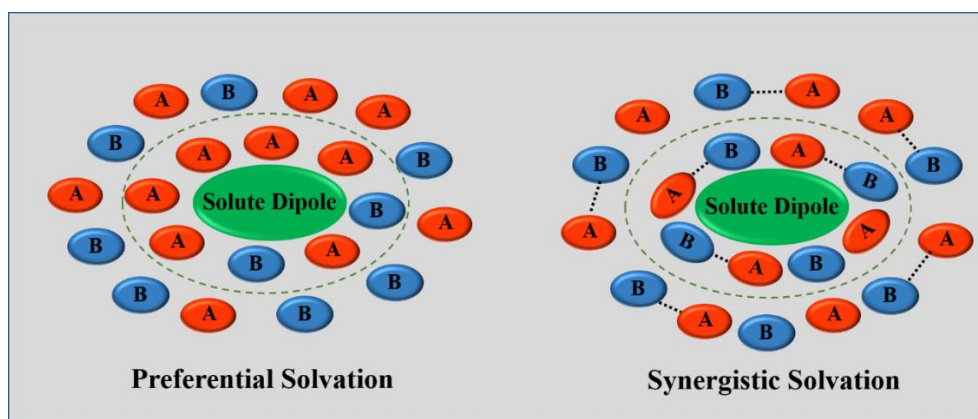
The investigation of the specific interactions and associated timescales provides insight to a number of fundamental processes like, solvent reorganization around a solute molecule dynamic heterogeneity in quasi confined medium, micellization of surfactant molecules, scaffolding of supramolecular assemblies etc.^{12-15,22} In this introduction chapter a brief overview on recent development in the topics closely resembled with my thesis work is provided. I shall first introduce the physical and chemical properties of the systems followed by the ultrafast spectroscopic studies reported in recent years and scope of these studies in a broader sense.

1.1 Binary Solvent Mixture

1.1.1 Properties and Solvation Behaviour

Binary solvent mixture, is important by its own right, is extensively used in chemical industries and laboratories for its widespread application (viz. as a reaction medium, chromatographic separation, biomolecule stabilization, solubilisation of drugs and other organic molecules, as a cryoscopic agent etc.).²⁹⁻³³ Interesting non-linear physical properties are commonly observed in binary liquid. Bulk physical properties such as dielectric constant, viscosity, refractive index, enthalpy of mixing etc., often exhibit non-linear behaviour with change in the composition of the binary solvent mixture.³⁴⁻⁴¹ All these facts drew a considerable attention to the researchers to explore the microscopic and dynamical properties of solvent mixtures by several theoretical, computational and experimental approaches.⁴²⁻⁴⁵ Spectroscopic measurement using an organic dye molecule provides a closer view of the solvent structure and in most of the cases the structure of the solvent mixture in the immediate vicinity of the dye molecule are found to be different compared to the bulk solvent structures, which rules out the assumption that mixed solvent systems can be considered as homogeneous dielectric continuum medium.⁴⁶⁻⁴⁷ For a solute molecule in a mixed solvent

system can be solvated non-preferentially or preferentially (by one of the component of the solvent mixture extensively) depending upon the interactions between solute and solvent counterparts. In absence of any specific solute-solvent interaction, enrichment of polar counterpart around the polar solute dipole can also occur by the virtue of electrostatic interaction between the oppositely polarised dipoles. This type of non-specific preferential solvation is completed through dielectric enrichment.⁴⁸ The dielectric enrichment model has been successfully applied mostly for the mixture of non-polar and polar binary solvent mixtures. But the solute-solvent interaction in a binary mixture depends on the interaction between the two solvent counterparts. For strongly interacting binary solvent mixture (polar-polar binary mixture) a different phenomenon apart from the preferential solvation can occur, which is called synergistic solvation (Scheme 1.2). In case of synergistic solvation two interacting solvent counterparts together solvate the solute dipole rather than solvation by the one type of solvent molecules.⁴⁹



Scheme 1.2. Simplified presentation of preferential and synergistic solvation around a solute dipole by a binary mixture formed by two counterparts A and B.

1.1.2 Microheterogeneity and Composition Dependent Fluctuation within a Binary Mixture

While the mixture of nonpolar and polar solvent is predominated by preferential solvation behaviour, mixture of two polar solvent produce a more complicated solvent structure. In case of aqueous binary mixture of an amphiphilic cosolvent, two opposing effects contribute simultaneously. One is the stabilisation of the solvent structure by favourable interaction of the amphiphile hydrophilic portion with the water molecules via hydrogen bond formation, and the destabilization effect comes from the hydrophobic solvation and thereby disruption of the water structure is observed. This phenomena is called “*Janus Effect*” named after Greek god Janus having two faces in opposite directions.⁵⁰⁻⁵²In the later effect the hydrophobic parts undergo self-aggregation via dipole-dipole interaction and hence a microstructure is formed within the medium and this causes composition dependent fluctuation and Microheterogeneity in a binary mixture.⁵⁰⁻⁵² A large number of reports can be found in literature, where exploration of exact solvent structure and mode of interaction in binary mixtures are emphasized through various theoretical and experimental approaches. Among the aqueous binary mixtures DMSO-water, acetonitrile-water, ethanol-water, tert-butanol-water and dioxane-water mixture are prevalent within the recent reports.⁵¹⁻⁵⁵During past few decades the researchers were found to be more concerned about the static solvent structure and macroscopic physical properties of the binary solvents. In an early work, Leung and co-workers studied aqueous DMSO system with neutron scattering and X-ray studies as a function of solvent composition and temperature.⁵³They observed a strong hydrogen bond and dipole interactions within the binary solvent mixture which induce a cryoprotective property by inhibiting the hexagonal lattice formation of water at low temperature.⁵³ The hydrogen bonding between DMSO and water molecule was further supported by molecular dynamics simulation studies, where 1DMSO:2H₂O complex was observed for some solvent compositions with maximum non-ideal behaviours within the binary mixture.⁵⁴

Solvation dynamics (i.e. the reorganization of solvent molecule around a solute dipole) controlled by the structure of the solvent network immediately after the solute probe, provides valuable information regarding the composition dependent anomalies in a binary mixture.⁵⁶⁻⁵⁸ Skaf and co-workers studied solvation dynamics of coumarin 153 in DMSO-water binary mixture using computer simulation, varying the solvent composition.⁵⁷ They found non monotonous change in solvation times with slowest dynamics at 33 mole percent of DMSO.⁵⁷ The result is well supported by the recent study of solvation dynamics of coumarin 480 using fluorescence upconversion technique by Sarkar and coworkers.⁵⁸ Bagchi and coworkers studied solvation dynamics of tryptophan in DMSO-water mixture and found two anomalous regimes, one at 10-15 mole percentage and other at 40-50 mole percentage of DMSO.⁵¹ They attributed the first one due to the percolation among the DMSO molecules and the later one is due to the presence of 1:2 and 2:1 complexes of DMSO and water molecule within the mixture.⁵¹ Aqueous DMSO is known for effect on protein structures and conformations as revealed by molecular dynamics simulation and fluorescence correlation spectroscopy studies.⁵⁹⁻⁶⁰ The studies mostly indicate a significant change in protein conformation at low DMSO concentration. At 10-15% mole fraction of DMSO the protein (lysozyme) remains partially unfolded and with increasing in further DMSO content, a collapsed state of the protein is stabilised.

Alcohol-water mixture is one of the extensively studied binary mixture and known to possess heterogeneity at microscopic level. Guo et al first evidenced the structure and incomplete mixing of methanol and water at microscopic scale with X-ray emission spectroscopy.⁶¹ With longer chain alcohols (ethanol, tert-butanol) inhomogeneity were detected at the intermediate composition ranges and formation of alcohol clusters has been established by various approaches.⁵²

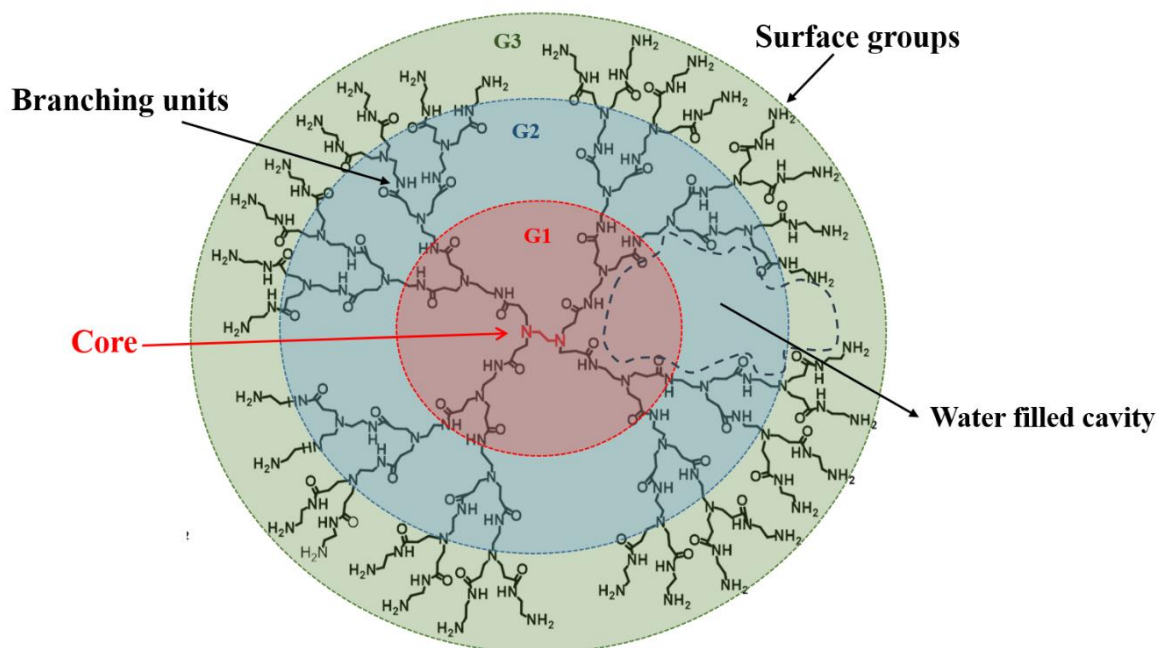
Binary mixture of DMSO and glycerol drew attention to the researchers recently for the application of this mixture for viscosity dependent studies on bimolecular reactions.⁶²⁻⁶³ As DMSO and glycerol have almost similar physical properties (like dielectric constants, refractive indexes, densities), it was assumed that DMSO and glycerol can be mixed in any proportion to achieve the desired viscosity in between 2.2 cP (viscosity of DMSO) and 1400 cP (viscosity of glycerol) without changing the physical parameters. However, presence of the microscopic inhomogeneity of DMSO-GLY mixture has found this assumption to be oversimplified. Rasul et al. reported that DMSO has antagonistic effect on the cryoprotective property of glycerol.⁶⁴ In a recent FCS study of translational diffusion for various polarity coumarin dyes in DMSO-GLY mixture by Bhattacharyya et al. revealed two distinct environments within this binary mixture where the translational diffusion of the dye molecules are widely different, one of which is found to be neat DMSO like and the other is bulk like.⁶⁵ This fact was further supported by a probe dependent solvation and rotational dynamics study in DMSO-GLY binary mixture by Ghosh et al.⁶⁶ A strong probe dependency of solvation dynamics was found in case of DMSO-GLY binary mixture which is absent in neat solvents (like monohydric alcohol, glycerol, DMSO etc.) of other homogeneous binary mixture (DMSO-WT).

All the above discussion elucidates the non-ideal behaviour of the binary mixture and unpredictable composition dependent dynamical fluctuations. In a major part of the thesis a deeper analysis of binary mixture by probing the microenvironment has been provided using different spectroscopic methods. The origin of slow dynamics, which is a matter of debate during the last two decades, has also been explored and a comprehensive explanation is provided.

1.2 Dendrimers

1.2.1 Structure, properties and applications

Dendrimers, a special kind of synthetic branched polymer have been in spotlight from the time of its discovery in 1980s.⁶⁷ Unique architecture and versatile applications of dendrimer have drew attention to the researchers.⁶⁷⁻⁷¹ Dendrimer structure possesses a highly symmetric structure around its core, monodisperse in nature and nanometer scale dimension. Internal cavities of dendrimer serve as binding site for drug molecules (Scheme 1.3). Apart from drug delivery dendrimers are also used for biomimicry and cellular applications.⁷¹ Repetitive branching units around the hydrophobic core determines the size of this macromolecule (referred as generation of dendrimer). On the other hand surface groups of the dendrimer determines the charge of this molecules. Following established synthetic routes, all the aforementioned parameters (size, charge etc.) can be tuned as per the requirement. Among the dendrimer molecules, Poly(amidoamine) [popularly known as PAMAM] dendrimer, synthesized by Tomalia and coworkers, is most extensively studied.⁷¹ PAMAM dendrimers are known to mimic the globular proteins such as insulin, cytochrome c, haemoglobin.⁷¹ The higher generation dendrimer possess the size of biological cell membrane or lipid bilayer membrane act as the essential mimic for those systems. Another important aspect of the dendrimer is solubilizing drug molecule and delivery to desired location.⁷² Binding property of dendrimer was well explored by Turro and his coworkers where they found the encapsulation capability of a hydrophobic dye Nile red by PAMAM dendrimer increased drastically with increase in the hydrophobic chain length at the dendrimer core.⁷²



Scheme 1.3. Schematic representation of an amine terminated PAMAM dendrimer molecule with ethylenediamine core. Different generation have been depicted with different colour.

Dendrimers act as a nano-envelope for the synthesis of metal nanoparticles where it hosts the metal ions inside the architecture and in-situ reduction gives rise to individual metal nanoparticles without any aggregation. Crooks and coworkers observed the formation of Cu nanoclusters within a dendrimer envelope. This method is further modified and the synthesized nanoparticles have been applied widely such as homogeneous catalysis, plasmonic and semiconductor materials. Electron transfer processes in dendritic architecture has been studied extensively as incorporation of redox centre in dendrimer mimics the redox enzymes that take part in many important phenomena in biology. A number of model systems studied e.g. heme-protein, iron-sulphur protein and metalloprotein by modifying the dendrimer core by zinc-porphyrin, Fe_4S_4 cluster and transition metal complexes respectively.⁷⁶⁻⁷⁸ Those model systems were successfully able to mimic the biological systems that take part in the electron transfer process in living systems.

1.2.2 Changes in Structure and Properties with Physiological Conditions

Last couple of decades the dendrimer have witnessed the extensive studies on structure and its behavior at different physiological conditions, such as medium pH, effect of solvents and salts etc.⁷⁹⁻⁸⁶ Goddard and coworkers studied a number of properties of PAMAM dendrimers by molecular dynamics simulation. They found a substantial increase in the size and void area inside the macromolecule with increase in the dendrimer generation from 1 to 11 but at the same time the surface area per unit amine was found to be significantly reduced⁸⁰. Dendrimers are known to undergo conformational fluctuation with variation of medium pH and ionic strength. High pH and high ionic strength of the medium lead the dendrimer to form a “dense core structure”, and in low pH condition the reverse phenomena was observed (“dense shell structure” is formed)⁸⁴⁻⁸⁵. However incongruity found between the reports regarding pH dependent size change (swelling effect). Some early simulation reported considerable swelling of the dendrimer at low pH, which contradicted the result obtained from SNAS experiment where almost no change of the dendrimer size was observed^{79,86-87}. The recent atomistic MD simulation study by Goddard and his coworkers supported the concept of pH dependent conformational fluctuation rather than a size change which is in agreement with other experimental observations⁸⁸.

1.2.3 Photophysical Studies on Dendrimers

As discussed in the previous section, dendrimer has been extensively explored with various experimental techniques and computational studies to understand the structure, properties and dynamics under different physiological conditions. Fluorescence spectroscopy has been successfully used to study the microenvironment of a supramolecular system. Several effort of fluorescence probing has been attempted to explore the dendrimer interior by using various well-known fluorescent probes such as pyrene, ANS, 2-naphthol, porphyrin etc⁸⁹⁻⁹³. Pistolis

and coworkers studied the PAMAM dendrimer by probing pyrene fluorescence where they noted the ratio of first to third vibrational peaks which they correlated with micropolarity inside the dendrimer.⁸⁹ They observed the decrease in micropolarity with increase in generation size of the dendrimer, because of less penetration of water molecule with increasing branching. While they observed a great protection of the probe molecule in water for larger generation, on the other hand they found the pyrene fluorescence to be quenched by the tertiary amine group present within the dendrimer.⁸⁹ The binding capacity of a dye molecule in dendrimer has also been studied and it was found to be dependent of medium pH. A weaker binding was found with decreasing the pH, which has been attributed to the electrostatic effect, hydrogen bonding efficiency as well as the dendrimer structure fluctuation.⁹³ However fluorescence probe technique has been found problematic in some cases such as incomplete encapsulation of the dye by the dendrimer, quenching of dye fluorescence by tertiary amine groups of the dendrimer which leads to artifact in the measurement. The problems coming from quenching of pyrene fluorescence and interference from background fluorescence from dendrimer itself has been reported both by Pistolis and Turro groups while studying the pyrene fluorescence by steady state and time resolved fluorescence spectroscopy, respectively.^{89,91}

1.2.4 Intrinsic Fluorescence of PAMAM Dendrimer

As described earlier section that the PAMAM dendrimer possess some intrinsic fluorescence and appears as background noise against the fluorescence from the encapsulated dye (especially for the dyes which absorb in the UV region).⁹⁴⁻⁹⁵ Trucker and coworkers found that the intrinsic fluorescence of PAMAM dendrimer can provide some crucial information about the structural rigidity and microenvironment of the molecule as analysed by intrinsic fluorescence lifetime of five different generation of PAMAM dendrimer.⁹⁵ Later, Imae group extended this utilization of intrinsic fluorescence and studied effect of different physiological

conditions on dendrimer fluorescence.⁹⁴ Their studies revealed that the fluorescence of PAMAM dendrimer is strongly dependent on medium pH and an enhancement of both steady state fluorescence intensity and excited state lifetime with decrease in pH.⁹⁵ The actual reason of the origin of fluorescence has not yet been very clear although a number of studies on dendrimeric and similar hyperbranched polymeric system indicated that the branched tertiary amine groups are responsible for the strong photoluminescence in these type of systems⁹⁶⁻⁹⁹ Bard and coworkers have concluded that the surface functional groups of the dendrimer play an important role in the origin of fluorescence which contradicts to the report by Imae and her coworkers¹⁰⁰ where they found same type of emission of behavior with different surface groups at same physiological condition and thereby Imae et al concluded that the backbone rather, than the surface groups plays crucial role in the origin of fluorescence.⁹⁴

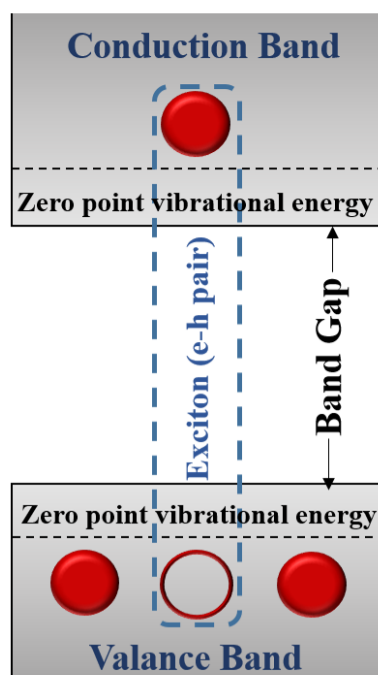
The above discussion suggests that dendrimers possess novel optical properties and ability to interact many organic molecules by the virtue of its unique architecture. In this thesis work these properties of dendrimer have been utilized which provided a crucial information which is hitherto unknown, as well as new applications involving dendrimer has been explored.

1.3 Quantum Dots

1.3.1 General Properties and Applications

The demand of clean energy require the development of quantum dot based photovoltaic devices where solar energy is converted into electrical energy.¹⁰¹⁻¹⁰⁴ Quantum dot nanomaterials are gaining popularity because their unique photocatalytic and fluorescence properties such as high emission quantum yield, high extinction coefficient, tuneable optical and electrical properties, etc. makes the material suitable for the optoelectronic, photocatalytic applications as well as biomarker in biological applications.¹⁰⁵⁻¹⁰⁶ Although different types of nanomaterials with small size (2-10nm) are referred as quantum dots such

as gold, silver, carbon and silicon based nanomaterials, the most extensively studied are metal chalconides, because of optimised synthetic routes wide range of materials can be prepared covering almost the entire visible and NIR region.¹⁰⁷ Quantum dots possess unique optical properties which is intermediate between the bulk material and individual molecules. As the size of the molecule is decreased below the exciton Bohr radius, which is the average distance between the electron in the conduction band and the corresponding hole in the valance band, the electron is said to be confined in a small quantum space.¹⁰⁸ This phenomena is called quantum confinement effect and this phenomena have direct correlation with the optical and band edge properties when the nanocrystal interacts with light.



Scheme 1.4. Simplified diagram for the band alignment and exciton generation of a spherical quantum dot upon photoexcitation.

Upon excitation with a laser of suitable energy the electron in valance band reaches to the conduction band and leaves a hole in the valance band. This electron and hole pair together is called exciton (Scheme 1.4). After residing for some time the exciton recombines releasing a

radiative energy (fluorescence). With decreasing the size of the nanocrystal the energy gap between the valance and conduction band increases and consequently the recombination energy increases which leads to emission to the blue end for the smaller sized particle compared to the larger one.

1.3.2 Types of Metal Chalconide Quantum Dot

(a) Core type: Quantum dots derived from single component of metal (e.g cadmium, lead, zinc) and chalconides (e.g. sulphur, selenium, tellurium) are called core type QDs. This includes a wide variety of QDs whose spectrum covers entire visible region. These materials have narrow emission properties than the corresponding bulk materials and high emission quantum yield. The surface of the quantum dots are often capped with organic surfactant molecules bring photostablity and help solublizing the quantum dot in solution phase. The common capping agents are hexadecylamine (HDA), Trioctylphosphine oxide (TOPO), 3-mercaptopropionic acid (MPA) etc.

(b) Core-Shell Type: Core type QDs although exhibited good emission yield, often suffer from photostability issue. The main problem with cadmium containing QD is the release of toxic Cd^{2+} and therefore making the material unsuitable for biological uses. Covering the QD surface with a wider band gap material provide a remedy to these problems. For example the core-shell CdSe/ZnS QDs (where CdSe acts as smaller band gap material at core and ZnS as larger band gap material in the shell) exhibits better photostability, narrower emission spectrum and reduces cytotoxicity as compared to the core only CdSe QDs.¹⁰⁹

(c) Alloyed Qunatum Dots: The change in the optical and band edge properties requires the change in the size of the particle as stated above. Recent advancements show that the optical properties can be tuned without changing thesize of the material. The QD can be

alloyed with one extra component of either metal or chalcogenide and changing the composition can modulate the optical and band edge properties of the alloyed QDs.¹¹⁰

1.3.3 Study of Photoinduced Electron Transfer with QDs

Semiconductor quantum dots are used as the building blocks in optoelectronic devices, LEDs and solar cells.¹¹¹⁻¹¹³ For all these applications photoinduced electron transfer (PET) is a fundamental process which controls the efficiency of the quantum dot sensitized devices. Designing suitable donor-acceptor pair would enable the efficient PET and thereby improve the performance of the devices. Several contributions have been made by Kamat and his coworkers where they studied PET from QDs to a numerous semiconductor materials.^{101,114} In a seminal work they studied PET from different sized (diameter of 2.8, 3.3, 4.0 and 4.2 nm) photoexcited CdSe quantum dots to various metal oxide nanoparticles (SnO₂, TiO₂, ZnO). Their finding showed a strong chemical driving force dependency of electron transfer from a single quantum state to a continuum electron accepting state of metal oxides.¹¹⁴ Another important work worth mentioning here is the interfacial electron transfer from CdS QD to the rhodamine B molecule attached to the surface of the QDs where an ultrafast electron transfer component of 12 ps was observed by Lian and his coworkers.¹¹⁵ Their work was a good approach towards the utilization of multiple exciton generation process which is essentially beneficial to the device performance. In a recent work by Tachiya and coworkers found that the number of attached dye molecule to a quantum dot surface or quantum rod surface follows a poisson type distribution and influences the energy transfer rate from QD to the attached dye molecules.¹¹⁶

A molecular level understanding is still demanding in the field to understand the factors affecting the electron transfer process. The effects include chemical driving force, electronic coupling parameter, and presence of surface traps (which actually reduce the transfer

efficiency by capturing the excitons). In this thesis the charge transfer kinetics with different types of quantum dots have been studied the role possible factors affecting the electron transfer process has been examined thoroughly.

1.4. Objective behind the thesis

In this thesis work, we have studied several fast photochemical process viz. excited state solvation dynamics, solute diffusion dynamics (rotational and translational) and photoinduced electron transfer in different systems. The systems studied include microheterogeneous binary systems to nanostructured assembly (dendrimer) and semiconductor quantum dots. The studied systems and processes although differ widely but in all the cases fast spectroscopic methods were employed to investigate the microenvironment and dynamics occurring within the system. We have investigated two type of binary solvent mixtures that are of potential applications and interesting non-ideal physical properties. Solvation dynamics in the studied binary solvent systems was found to be strongly dependent on the physical nature of the probe molecules which is absent in neat solvents. Probe dependent solvation dynamics in a system reflects the inherent inhomogeneity and presence of domain of widely varying polarity region. For a particular probe molecule, the solvation dynamics showed a non-monotonous composition dependent fluctuation in solvation time which arises due to non-ideal mixing and different microenvironment in the immediate vicinity of the probe molecule than the bulk. We have thoroughly investigated the origin of slow dynamics and both solute-solvent and solvent-solvent interaction was found to be the retardation factor of the solvation phenomena. We have probed the heterogeneity in the interior of dendrimer, a hyperbranched nanosized polymer, by utilizing its intrinsic fluorescence and probing solvatochromic dye molecules. We have shown how a hydrophobic dye molecule can reside inside the water filled cavity of the dendrimer molecule and exhibits water like photophysical behaviour, which was hitherto unknown. Poly(amidoamine) (PAMAM) dendrimer molecule

possess a significant amount of intrinsic fluorescence which we have utilised to study photoinduced electron transfer to electron deficient nitroaromatic compound 2,4-Dinitrotoluence (DNT). The generation dependent quenching phenomena was adequately explained by difference in host-guest interaction between dendrimer-DNT pairs and the chemical driving force for electron transfer process. Quantum dot nanocrystals (QDs) exhibits interesting size dependent optical and band edge phenomena which are being utilised extensively for solar cell designing. We have modelled the electron transfer process between core and core-shell type quantum dots of different sizes and organic donor or acceptor molecules in solution phase. We have fitted our data with a modified Collins-Kimball model and it was found that several factors are affecting the ET kinetics such as, the mutual diffusion of donor and acceptor, chemical driving force and surface traps on QDs.

Chapter 2

Instrumentation and Methodologies

In this chapter we will describe the basic working principle of the instruments used for various spectroscopic studies, data analysis techniques, sample preparation and the adopted methodologies such as solvation dynamics, rotational anisotropy and fluorescence correlation spectroscopy.

2.1. Instrumental Techniques Used

A number of instrumental techniques has been used for this thesis work. This section describes the details of the techniques and methods used extensively to carry out the works. As fluorescence based techniques have been used extensively, the basic instrumentation and working principles have been provided. The other instruments we have used for supporting the fluorescence data are ^1H NMR, isothermal titration calorimetry (ITC) and viscosity measurement setup. ^1H NMR spectra were recorded in Bruker 400 MHz NMR spectrometer. ITC experiments were performed by using MicroCal ITC200 (Malvern Instruments) calorimeter and the data was analysed by MicroCal Origin software provided within the instrument. Viscosity of the samples were measured in a Brookfield DV-II+ Pro cone and plate viscometer having temperature controller.

2.1.1. Steady State Spectra

Steady state absorption spectra were collected in Perkin-Elmer Lambda 750 spectrophotometer able to scan UV-Vis to NIR region. The maximum resolution of the instrument in UV-Vis region is ~ 0.17 nm and minimum measurable optical density is ~ 0.005 . Steady state fluorescence spectra were recorded using Perkin Elmer LS55 fluorescence spectrometer with a contentiously powered xenon lamp as excitation source. The emitted fluorescence was collected with a photomultiplier tube (Hamamatsu; R-928F) photodetector at

the perpendicular direction with respect to the excitation light. The stability of the measured intensity was checked with stable solution of coumarin dye during the course of measurements. For each sample average value from three measurements was taken for analysis.

2.1.2. Time Resolved Fluorescence Measurements

Time resolved data provides numerous information related to the dynamic properties of the system in contrary to the steady state data where the information is obtained from only equilibrium state. In a typical time resolved experiment we measure the time dependent population of a fluorophore in the first excited state. The population in the excited state of a molecule is related to the radiative and non-radiative rate constants as the following equation,¹¹⁷⁻¹¹⁸

$$-\frac{dn(t)}{dt} = (k_r + k_{nr})n(t) \dots\dots\dots(2.1)$$

$n(t)$ is the number of molecules present in the excited state at a particular time t and decreases with time progression. We can not see the molecules directly rather the time dependent intensity denotes the population and exhibits an exponential decay with time as

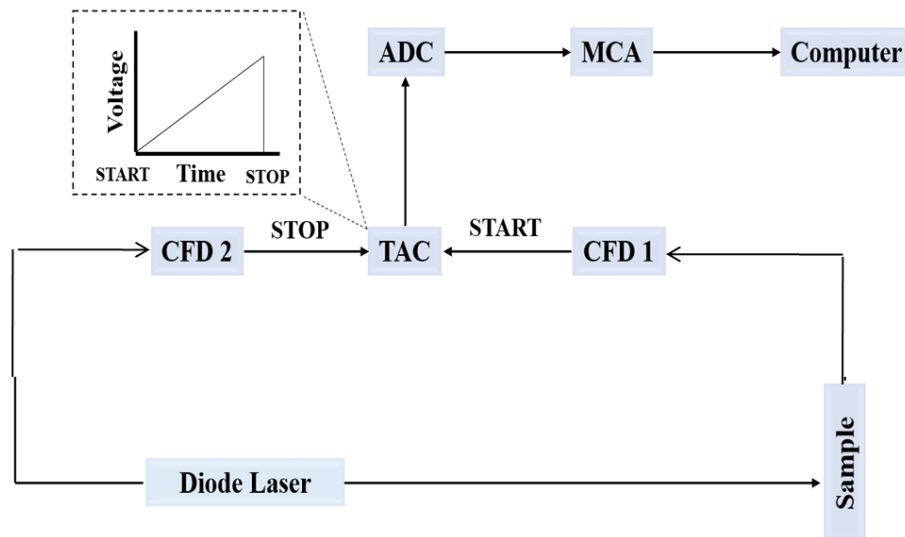
$$I(t) = I_0 \exp (-t/\tau) \dots\dots\dots(2.2)$$

Where τ is the fluorescence lifetime of the molecule and is the inverse of the total decay rate (combination of radiative and non-radiative rate) and I_0 is the fluorescence intensity immediate after the laser excitation. It is worth mentioning in this context that fluorescence is a random event and different molecules emit with different lifetimes. So, in ensemble average measurement we actually observe the statistical average of the times that different molecules spend in the excited state. We have measured the fluorescence lifetime by using Time

Correlated Single Photon Counting (TCSPC) technique with Edinburgh OB920 time resolved spectrometer, the details of which is given in the following section.

2.1.2.1. Basic Principle of Time Correlated Single Photon Counting Technique

The basic principle of the TCSPC technique is to measure the time gap between emission from the sample immediately after excitation by a short laser pulse. For our study we have used the picosecond lasers of wavelengths ~375nm, 405nm and 445nm having pulse width of ~90 ps as measured by full width of the half maxima (FWHM) the instrument response function (IRF) using a scatterer ludox solution. The working principle with basic instrumentation is provided in the flowing schematic diagram. The excitation pulse is divided into two parts, one is directly connected to the detector by a constant fraction discriminator (CFD) which computes accurately the arrival time of the first photon. Another CFD is connected to the emission channel where the photon emitted from the sample upon laser excitation is detected. Nowadays almost all the instruments operates under “reverse mode” where the emitted pulse from the sample induce a START pulse to the CFD connected to the and the excitation pulse is guided to another CFD as STOP pulse.¹¹⁷ The time gap between the START and STOP pulse is accurately measured and a voltage ramp is generated proportional to the time gap with an electronics called time to amplitude converter (TAC). The voltage is amplified to a considerable extent with a programmable gain amplifier (PGA). The unwanted voltages come as noise can be eliminated by a window discriminator and the main signal is converted to numerical values by analog-to-digital converter (ADC). The above cycle is repeated to a several thousands to times and collected into a multichannel analyser (MCA). This leads to the formation of a histogram of photon counts at y-axis and time delay at x-axis. The scheme represented below is the basic instrumentation of the TCSPC setup (Scheme 2.1)



Scheme 2.1. Schematic representation of a reverse mode TCSPC.

2.1.2.2. Data fitting and deconvolution procedure

For the measurement of the lifetime of a fluorophore having decay time longer than the excitation pulse, the measured intensity decay is the convolution with the lamp function. So, to take out the real fluorescence lifetime deconvolution of the data is required with the lamp profile which is acquired as IRF as discussed above. Each excitation pulse can be assumed to be a series of δ -function and excites an impulse response from the sample. The function is proportional to the intensity and each express an exponential decay, sum of which represents the overall TCSPC data. This fact can be expressed mathematically as,

$$R(t') = \int_0^{t'} I(t)P(t' - t)dt \dots \dots \dots (2.3)$$

Where $R(t')$ is the fluorescence intensity at time t' , $I(t)$ is the intensity of the excitation light at time t and $P(t'-t)$ is the response function of the instrument. For a single exponential decay the $P(t'-t)$ term can be replaced by $[\exp\{-(t'-t)/\tau\}]$ and the equation becomes

$$R(t') = \exp(-t' / \tau) \int_0^{t'} I(t) \exp(-t / \tau) dt \dots \dots \dots (2.4)$$

The deconvolution is performed following iterative non-linear least square method. The requirement for the applicability of the least square method is to have a sufficient number of experimental data points free from systematic error. R(t') and I(t) can be obtained experimentally and the deviations are taken for every points and χ^2 is calculated which represents the goodness of fit. The process is repeated through iteration until a negligible change in χ^2 is obtained between two successive iterations. A χ^2 value between 1.00 and 1.20 represents a good fit of the experimental data.

2.1.2.3. Construction of Time Resolved Emission Spectra and measurement of Solvation Dynamics

The steady state and time resolved fluorescence data can be combined to obtain the time resolved emission spectra (TRES) as prescribed by Maroncelli and Fleming.¹¹⁹ The fluorescence lifetime is obtained at regular interval (10 nm) covering the whole emission spectra. Time integrated intensity is obtained as follows,

$$A(\lambda) = \frac{I_{ss}(\lambda)}{\int_0^{\infty} \sum_i a_i \exp(-t / \tau)} \dots \dots \dots (2.5)$$

Where A(λ) is the intensity integral, I_{ss}(λ) is the steady state intensity and τ is the fluorescence lifetime. Wavelength dependent fluorescence intensity thus obtained by multiplication of integral function with lifetime function as,

$$I(\lambda, t) = \frac{I_{ss}}{\sum_i a_i \tau_i} \sum_i a_i \exp(-t / \tau) \dots \dots \dots (2.6)$$

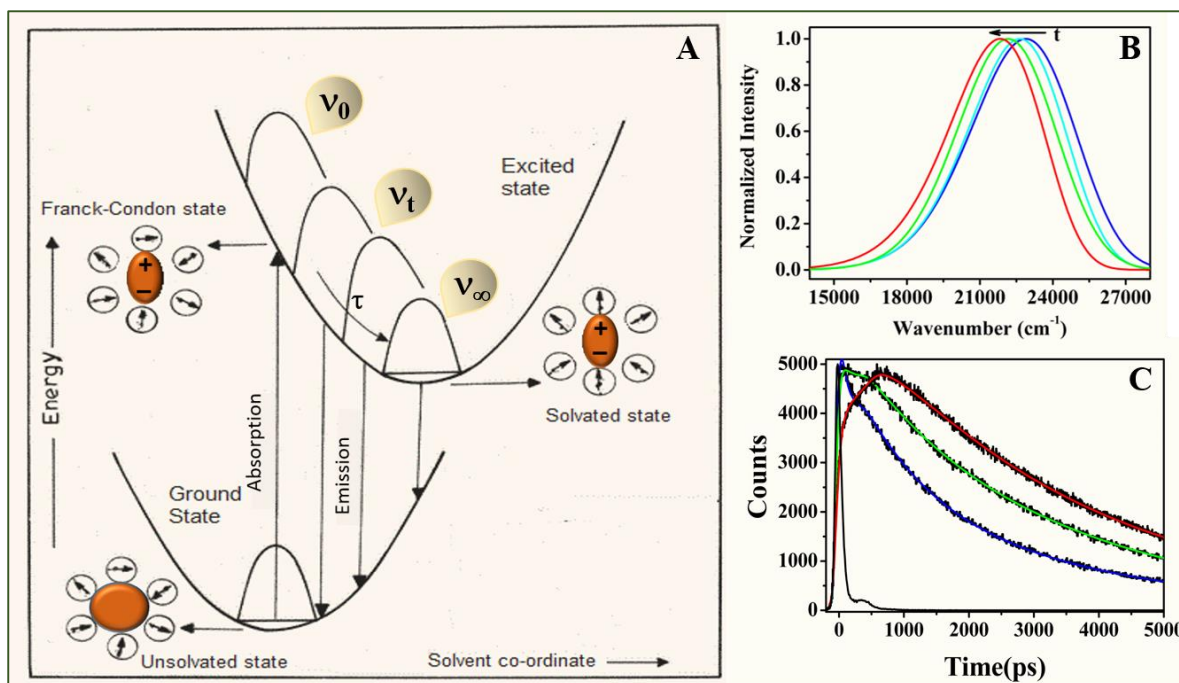
Once the time dependent emission spectra is obtained, the exact emission peak frequency can be obtained by the lognormal fitting of the experimental data points.

The time dependent emission energies thus obtained can be utilised for the study of excited state solvation dynamics as proposed by Fleming and coworkers by using time dependent dynamic stokes shift (TDDSS) method.¹¹⁹ The solvation dynamics refers to the reorientation of polar solvent molecules around a solute dipole excited by using an ultrashort laser pulse. For the study of solvation dynamics a molecule is chosen which has a low ground state dipole moment but after electronic excitation a significant increase in dipole moment. The solvent molecule remain in a random manner when the solute probe remains in ground state but the excited state solute drives the solvent molecules to reorient in order to stabilize the excited dipole. (Scheme 2.2.A) This stabilization of solute dipole by solvent dipoles leads to time dependent decrease in energy of the excited state and that is reflected by the red shift in the emission spectra what is known as dynamic stokes shift (Scheme 2.2.B). At blue range of the emission spectra the emission thus come from the unsolvated state whereas at the red end the fluorescence originates from the solvated state continue shifting till the solvation gets completed. This fact is clearly reflected in the fluorescence lifetime decay of the probe molecule where at blue end a sharp decay is observed while at the red end a rise component followed by the decay is observed (Scheme 2.2.C). The time evolution of solvation dynamics is presented by the decay of solvent correlation function $C(t)$, constructed from the peak frequencies measured at different time as the following equation,

$$C(t) = \frac{\nu(t) - \nu(\infty)}{\nu(0) - \nu(\infty)} \dots\dots\dots(2.7)$$

Where $\nu(0)$ and $\nu(\infty)$ are the emission energies of the excited state dipole at the time zero (when solvation process has not started), time infinity (completion of the solvation process).

$\nu(t)$ represents the emission energy at any intermediate time. The $C(t)$ decays in an exponential manner with time and the solvation time can be obtained by an exponential fit to the experimental data points.



Scheme 2.2. (A) Schematic diagram of solvation dynamics around a solute dipole, (B) time resolved emission spectra (TRES), (C) wavelength dependent fluorescence lifetime decay; at the blue emission spectra the lifetime decay exhibits only decay (represented by the blue fitted line) whereas at the red end a significant rise followed by the decay is observed (represented by the red fitted line).

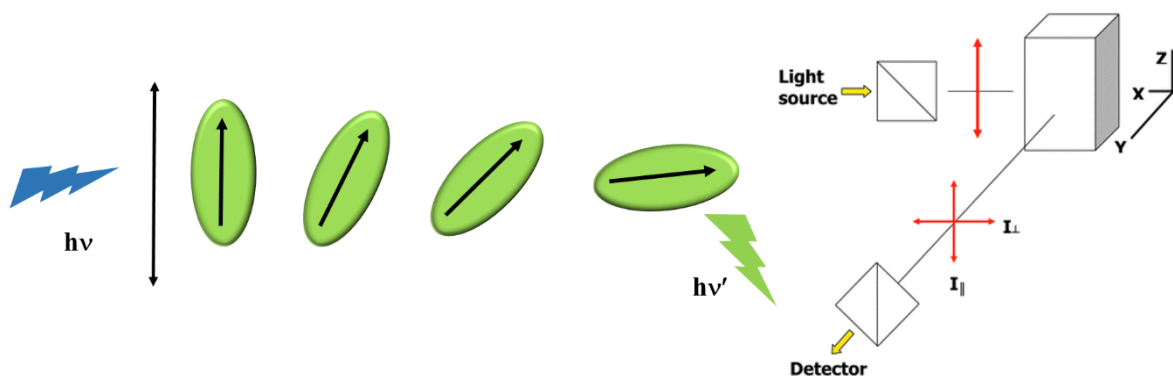
2.1.3. Time Resolved Fluorescence Anisotropy and Rotational Dynamics

Fluorescence anisotropy decay refers to the depolarisation of the emitted light from an ensemble of fluorophores after excitation with a polarised light. Most of the fluorophore absorbs light in the parallel direction to the excitation source and since the molecules are not static in solution but undergo Brownian motion to align in another direction as shown in the scheme (Scheme 2.3). By monitoring the emission at the parallel and perpendicular direction

with respect to the excitation polariser it is possible to detect the timescale of molecular rotation provided the excited state lifetime of the dye is in the same timescale of the rotational time or higher (Scheme2.3). The rotational correlation function is determined as the following equation,¹¹⁷

$$r(t) = \frac{I_{\parallel}(t) - GI_{\perp}(t)}{I_{\parallel}(t) + 2I_{\perp}(t)} \dots\dots\dots(2.8)$$

Where I_{\parallel} and I_{\perp} are the fluorescence intensities at parallel and perpendicular directions of the polarizer. G is the instrumental correction factor which is obtained from tail matching method by using a dye, which rotates freely within the conventional solvents (such as *C153* in methanol).¹¹⁷



Scheme 2.3. Pictorial presentation for the fluorescence anisotropy process (left). Right sided picture demonstrates the experimental setup for time resolved anisotropy measurement.

For a simple fluorophore having only one type of depolarisation the rotational correlation function is given as,

$$r(t) = r_0 \exp(-t / \tau_r) \dots\dots\dots(2.9)$$

where r_0 is the initial anisotropy and can vary from -0.2 to 0.4 depending on the angle between excitation and emission dipole. τ is the rotational time of the fluorophore in that

particular solution.¹¹⁷ From the rotational time a number of information can be extracted as the rotation of a molecule depends upon the viscosity of the medium and the size and the shape of the fluorophore. This fact is correlated by Stokes-Einstein-Debye equation,

$$\tau_r = \frac{4\pi\eta r_h^3}{3kT} \dots\dots\dots(2.10)$$

Where η is the viscosity of the medium, r_h is the hydrodynamic radius of the rotating fluorophore, k is the Boltzman constant and T is the experimental temperature.

2.1.4. Fluorescence Correlation Spectroscopy and Translational Diffusion Measurements

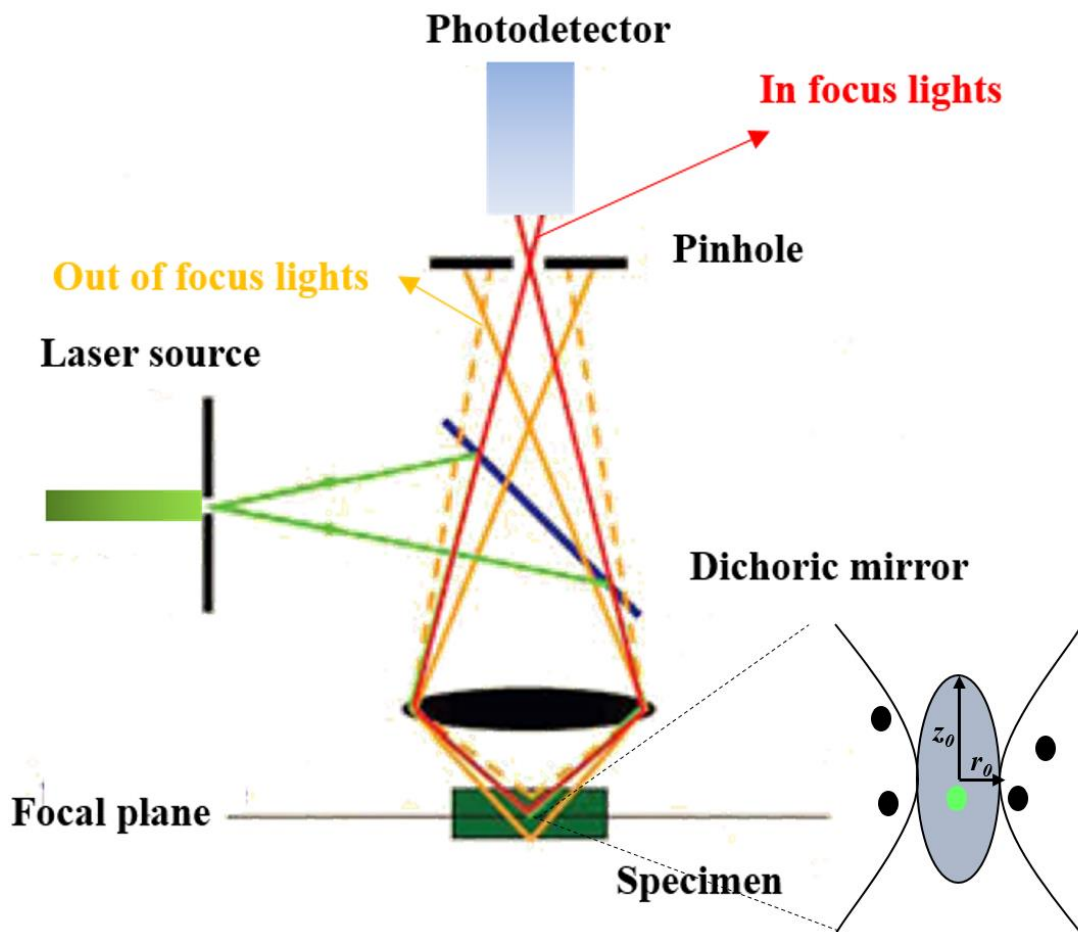
Fluorescence correlation spectroscopy (FCS) has been proved to be a convenient technique to study the behaviour of single molecules at high temporal resolution.^{117,120-121} Contrary to the other ensemble average fluorescence based techniques FCS does not deal with fluorescence intensity but the fluctuation of fluorescence intensity of a fluorophore within a small Gaussian volume due to Brownian motion. The factors that will affect the fluctuation in fluorescence intensity will be reflected in FCS technique such as number of molecules, local concentration, diffusion coefficient, binding and unbinding kinetics. FCS technique was first described by Webb and coworkers to study the drug binding and unbinding kinetics to DNA.¹²² Today the technique has been developed to high level of precision and sophistication by using ultrasensitive detectors and using fluorescent molecule of high quantum yield. The work is accomplished by using a confocal microscope the schematic diagram of which is given in the figure below. In short an intense laser pulse is focused towards the sample after being reflected by a dichroic mirror followed by passing through an objective lens (Scheme 2.5). The fluorescence reflected parallel to the excitation light is transmitted to through the same dichoric mirror. The parallel fluorescence beam is focused

through an aperture called confocal pinhole which is adjusted in such a way that only the focused beam will pass through it. The other defocused lights will not be transmitted through pinhole and thus it is called the heart of the confocal microscope.

The quantification of FCS is performed by autocorrelation analysis. A small fluctuation in fluorescence intensity signal in a three dimensional Gaussian confocal volume is recorded.

The normalized autocorrelation function $G(\tau)$ is given by the following equation,¹²¹

$$G(\tau) = \frac{\langle \delta F(t) \cdot \delta F(t + \tau) \rangle}{\langle F(t) \rangle^2} \dots\dots\dots(2.11)$$



Scheme 2.4. Schematic representation of a confocal microscope.

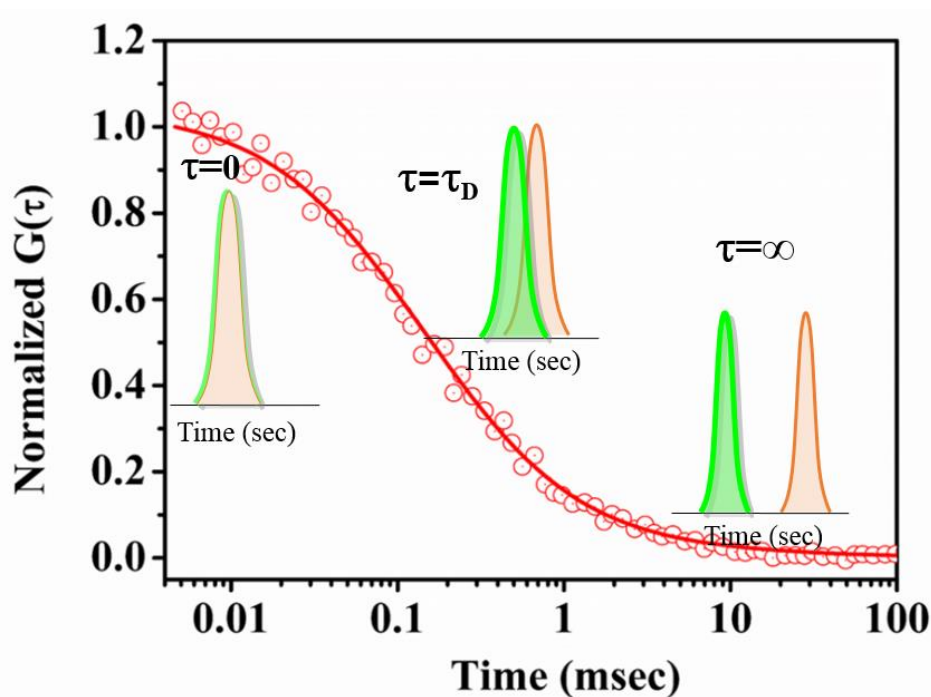
Where $F(t)$ is the fluorescence intensity and $\delta F(t)$ is the fluctuation in the intensity at any time t and is given by,

$$\delta F(t) = F(t) - \langle F(t) \rangle \dots \dots \dots (2.12)$$

where,

$$\langle F(t) \rangle = \frac{1}{T} \int_0^T F(t) dt \dots \dots \dots (2.13)$$

and $F(t+\tau)$ is the intensity emitted from the fluorophore after a time delay τ after the laser excitation. Initially created photon burst is copied and the copy signal undergoes spectral diffusion with time (as τ progresses). The overlap between the initial signal and the copy signal reduces with time and at that lead to the decay in the autocorrelation function as given in the figure below (Scheme 2.5).



Scheme 2.5. Development of the autocorrelation curve in FCS.

For the free diffusion of a single particle in a Gaussian confocal volume the autocorrelation curve yields,

$$G(\tau) = \frac{1}{V_{eff} \cdot \langle C \rangle} \left(\frac{1}{1 + \frac{\tau}{\tau_D}} \cdot \frac{1}{\sqrt{1 + \left(\frac{r_0}{z_0}\right)^2 \cdot \frac{\tau}{\tau_D}}} \right) \dots\dots\dots(2.14)$$

The first term, i.e. $(1/V_{eff} \cdot \langle C \rangle)$ is amplitude of the correlation curve $(G(0))$, which actually represents the inverse of the number of particle present in confocal volume. $r(0)$ is called the transverse radius (radius towards the lateral axis) and $z(0)$ is the radius towards axial direction of the confocal volume. The diffusion time of the fluorophore in the confocal volume can be obtained by fitting the autocorrelation curve by the function stated in the above equation considering additional contribution from the triplet state of the molecule and the equation becomes,

$$G(\tau) = \left(1 - T + T \exp - \frac{\tau}{\tau_{triplet}} \right) \frac{1}{N} \left(\frac{1}{1 + \frac{\tau}{\tau_D}} \cdot \frac{1}{\sqrt{1 + \left(\frac{r_0}{z_0}\right)^2 \cdot \frac{\tau}{\tau_D}}} \right) \dots\dots\dots(2.15)$$

Once the diffusion time is obtained, diffusion coefficient (D) is obtained by using the following equation as, $\tau_D = r_0^2 / 4D$. Diffusion coefficient depends on a number of physical parameters such as medium viscosity, molecular weight of the diffusing molecule which can be calculated accurately by this method.¹²¹

2.1.5. Cyclic Voltammetry measurement and Free Energy Calculation

Cyclic voltammetry experiments were performed in a 25ml electrochemical cell with three electrodes configuration in Metrohm-Autolab instrument. Electrode Potentials in aqueous solution were recorded with respect to Ag/AgCl electrode in 0.1 M KCl solution. Platinum wire electrode and platinum rotating disc working electrode were used as counter and reference electrode respectively.

The chemical driving force or the free energy for electron transfer was calculated by employing Rehm-Weller equation as,

$$\Delta G_{ET} = E_{D/D^+} - E_{A/A^-} - E_{00} - \frac{e^2}{\epsilon r_{D-A}} \dots\dots\dots(2.16)$$

Where E_{D/D^+} and E_{A/A^-} are the oxidation potential of the electron donor and reduction potential for the electron acceptor respectively. E_{00} is incorporated to consider the photoinduced reaction and is the energy required for ground state to excited state transition and obtained from the intersection of the excitation and emission spectra. e is the electronic charge, ϵ is the dielectric constant of the medium and r_{D-A} is the donor to acceptor distance.

2.2 Materials and Sample Preparation

Laser grade fluorescent dyes used in this study were purchased from Exciton and used without further purification. Quantum dots and dendrimer samples were purchased from Sigma-Aldrich. Other chemicals like N-methylaniline, 2,4-dinitrotoluene, HPLC grade solvents used in the thesis works were purchased from Sigma-Aldrich. NMR solvents were purchased from Acros Organics. Spectroscopic measurements were performed in sealed quartz cuvettes. The dye solutions were kept for several hours after preparation prior to optical measurements to ensure complete dissolution.

Chapter 3

Composition Dependent Multiple Anomalies in the Solvation Dynamics of Coumarin Dyes in Dimethyl Sulfoxide– Glycerol Binary Solvent Mixture

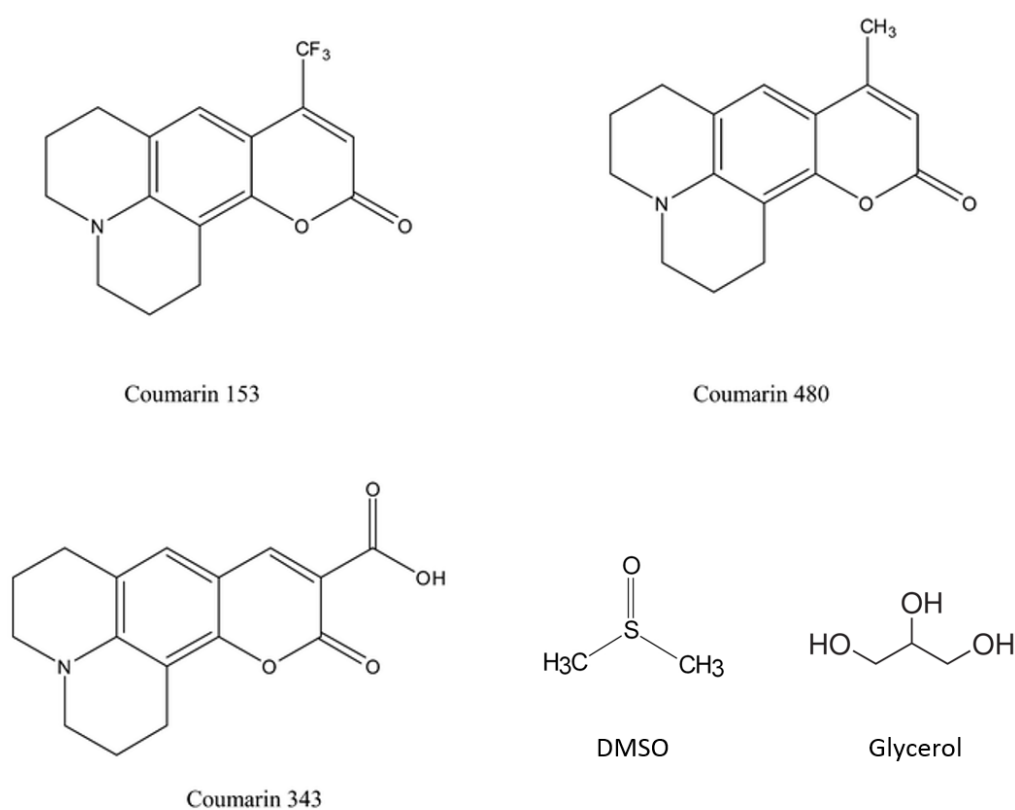
3.1 Introduction

Customizing solvent polarity is of great importance in controlling solution phase chemical reactions and dynamical processes. The solubility of a nonpolar (or polar) solute in a nonpolar (or polar) solvent can be high, even without much disturbing the solvent clusters.¹²³ However, when a polar (or nonpolar) solute is mixed with a nonpolar (or polar) solvent, the solubility of the solute decreases. The strong associations among the polar solute molecules (or polar solvent molecules) show little tendency to interact with a nonpolar solvent (or nonpolar solute).¹²³ Therefore, the solubility of a specific substrate in a reaction mixture can be controlled by customizing the solvent polarity on mixing two solvents with broadly different polarities. The binary solvent of a mixture of polar protic and amphiphilic solvent proves to be of great use in chromatographic separation, solubility, elementary chemical reactions, protein folding, and in other numerous biological reactions. The simultaneous presence of hydrophobic and hydrophilic groups in a binary solvent makes its physical properties highly sensitive toward the solvent composition.⁵⁰⁻⁵² Binary solvents where DMSO is a cosolvent are also well-studied; their versatile applications are well tested in drug discovery processes, as a cryoprotector, and due to the antagonistic effect on the structure of proteins.^{53-54,62-66} Aqueous DMSO solutions shows a composition dependent non-monotonous dynamical feature. At least two anomalous regions are observed with significant deviations in most of their physical properties: one at ~30–40 mole percentage DMSO, and another at a lower concentration range, ~10–15% as studied by both experimental as well as computational studies.^{51,54,57-59} In a recent simulation, Bagchi and coworkers studied the anomalous behavior of protein (lysozyme) structure fluctuations in aqueous DMSO

solvent.¹²⁴ They observed that at 10–15 mole% DMSO, native lysozyme transforms to a partially unfolded state. Further increases of the DMSO concentration (to 15–20 mole%) leads to a collapsed state, before it transforms into a completely unfolded state at very high DMSO concentrations. In an experimental UV circular dichroism study, Bhattacharjya et al. observed, at low DMSO concentrations (<6 mole%), an initiation of transition from the native state to a partially unfolded state of lysozyme, which was essentially subsequently completed at 18 mole% of DMSO concentration.¹⁷ They interpreted this observation as a potential consequence of the preferential binding of organic co-solvent to the hydrophobic residues of lysozyme.¹²⁵ Using molecular dynamics simulation with a polarizable force field, Head-Gordon and coworkers studied the molecular response of hydration water at the peptide (N-acetyl-leucine-methylamide, NALMA) surface in the presence of DMSO and GLY.¹²⁶ They observed an increase of hydration number in the glycerol solution, while the same decreases in the neat DMSO solution. Interestingly, in the presence of both the co-solvents, the water dynamics around NALMA are suppressed compared to neat water. Gögelein et al. experimentally determined the effect of GLY and DMSO on the phase behavior of lysozyme.¹²⁶ When GLY and DMSO are added, they observed experimentally that the fluid-solid transition was shifted to the lower temperature. Their observation was also supported by theoretical calculations based on the thermodynamic perturbation theory and on the Derjaguin–Landau–Verwey–Overbeek model.¹²⁷

Among several binary solvents, DMSO–GLY mixtures at correct ratios have emerged as an important candidate for their uses: as a medium to study the viscosity effect on bimolecular processes, in the partial disruption of protein structure, and as a cryo-protective agent.⁶²⁻⁶⁴ In a recent work, Bhattacharyya and coworkers studied spatially resolved FCS to measure the translational diffusion of coumarin dyes in DMSO–GLY binary mixtures. They observed two microscopically distinguishable environments within the mixture: one neat DMSO-like

region, while the other is bulk like.⁶⁵This fact was further supported by Kaur et al where the solvation dynamics was found to be strongly probe dependent. The solvation dynamics of a hydrophilic dye (coumarin 343) in DMSO–GLY (XDMSO ~ 0.89) mixture is completed with a much slower timescale (>12 ns) compared to the solvation time (~100 ps) obtained from a hydrophobic dye coumarin 153.⁶⁶Keeping all the aforementioned facts in mind we plan to study the composition dependent behaviour of this particular binary mixture to recheck the assumption of homogeneous mixing of DMSO and glycerol at any proportion. Our approach is to study the solvation and diffusion dynamics by using solvatochromatic probes (Scheme 3.1) across the composition range which also covers a wide viscosity range also (from 2.2cP to 1400 cP).



Scheme 3.1. Chemical structure of the coumarin dyes and solvents used in the polarity resolved study.

3.2 Composition Dependent Solvation Dynamics Study

Composition dependent steady state behaviour of DMSO-GLY binary mixture has been studied by Kaur et al for the calculation of preferential solvation parameters.⁶⁶ The index of preferential solvation in this binary mixture was found to be negative which indicates a much complicated behaviour of the mixture.⁶⁶ GLY molecules have three hydroxyl groups, which are strongly involved in hydrogen bond formation with dye molecules in DMSO-GLY mixtures. Apart from the hydrogen bond forming ability, GLY molecules possess a hydrophobic backbone that can easily bind with any hydrophobic surface. Solvation dynamics in neat glycerol is hydrogen bond assisted and thus requires local rearrangements of GLY molecules around the excited dipole of the solute molecule. The slow relaxation of GLY molecules within neat GLY makes the entire solvation time much slower (~ 500 – 1000 ps) compared to the bulk water (\sim few ps).¹²⁸⁻¹³⁰ In contrast to the GLY, DMSO is known as a fast solvent. The typical solvation time within this solvent is only ~ 3 ps.¹³¹ In this work, the solvation dynamics of coumarin dyes in DMSO-GLY mixtures at different ratios were studied, utilizing a diode laser with limited time resolution (~ 70 ps), although this meant that a part of the solvation dynamics which falls in the ultrafast region (< 30 ps) cannot be detected by our setup. The solvation time was obtained by employing the time-dependent dynamic Stokes shift (TDDSS) technique, which directly quantifies the time evolution of the solvation energy of the excited dipole. TDDSS was obtained from the steady state emission spectrum and the time-resolved parameters were reconstructed as described by Maroncelli and Fleming.¹¹⁹ shows the fluorescence lifetime decays of C480 in DMSO-GLY binary mixtures at 0.5 mole fraction of GLY. The lifetime transients at the blue wavelengths were adequately fitted with only decay components, *i.e.*, at $X_{\text{GLY}} \sim 0.6$, the lifetime decay of C480 at the extreme blue-end (440 nm) consists of 580 ps (47%) and 4640 ps (53%) decay components. This is in contrast to the red-end emission (560 nm), where a 4790 ps decay is preceded by a

distinct growth component of 860 ps (Figure 3.1). The blue-end emission is obtained from the unsolvated state, where the excited state population can be either directly funneled to the ground state (as a blue emission) or converted to a solvated state before it actually reaches the ground state. On the other hand, a red-end emission originates from the solvated state, where the population enrichment (“growth”) occurs at an initial time, due to excited state solvation, which is followed by an exponential decay at a longer time. Decay at the blue end and growth at the red end emissions are a clear indication of solvation dynamics taking place within the medium.

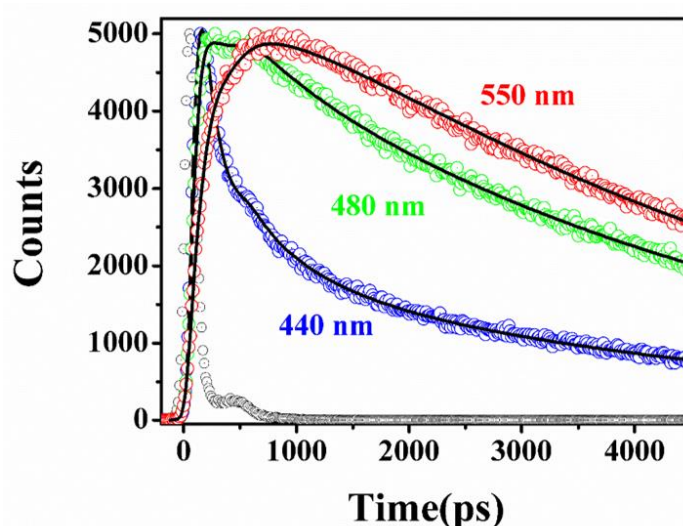


Figure 3.1. Picosecond lifetime decay profile of C480 in DMSO-GLY binary mixture at $X_{\text{GLY}} \sim 0.5$ monitored at different emission wavelengths. Black circles represent the instrument response function and the solid lines represent the best fit of the experimental data.

The time progression of the solvation process is described by a correlation function, $C(t)$ $[(\nu_t - \nu_\infty)/(\nu_0 - \nu_\infty)]$, constructed from the emission energies of the excited dipole immediately after excitation [*i.e.*, at time zero (ν_0)], at a particular time t (ν_t), and after a long time (ν_∞) when the solvation process has come to its end.¹¹⁹ Time-dependent emission energies were obtained from constructing the time dependent emission spectra (TRES) as described in the literature.¹¹⁹ Figure 3.2 shows the time resolved emission spectra (TRES) of

C153 in DMSO–GLY binary mixtures at ($X_{\text{GLY}} \sim 0.5$) and solvation correlation functions $[C(t)]$ of C153 at different compositions in the binary mixture. The $C(t)$ curves at different solvent compositions vary widely from each other as can be seen in figure 3.2. The $C(t)$ curves obtained from C153 and C343 were adequately fitted with a bi-exponential decay function [equation 3.1., $\beta = 1$]. However for C480, the initial time evolution of the solvent correlation function is fitted with an exponential decay, and the latter part becomes diffusion assisted, which can be better appreciated by introducing a stretched exponential fitting parameter within the fitting function (equation 3.1).¹³²

$$C(t) = a_1 e^{-(t/\tau_1)} + a_2 e^{-(t/\tau_2)^\beta} \dots\dots\dots(3.1)$$

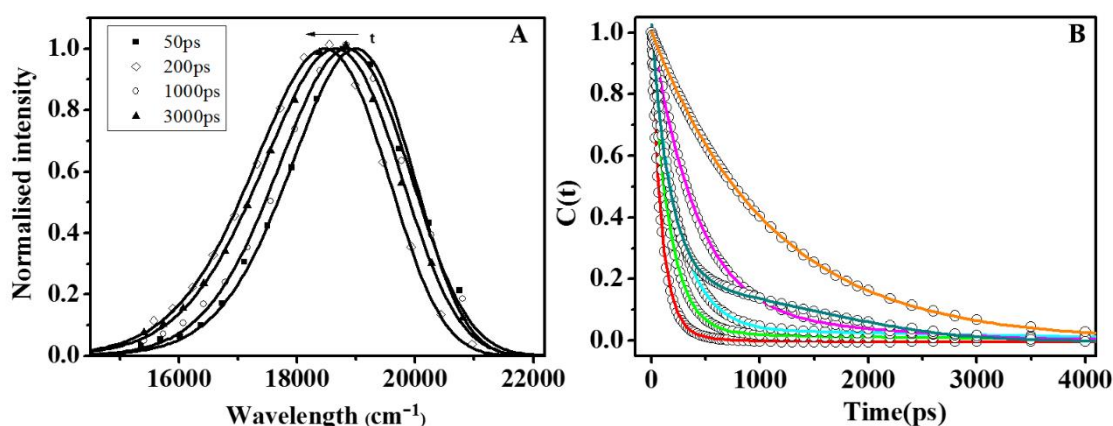


Figure 3.2. (A) Time resolved emission spectra of C153 in DMSO-GLY binary mixture at $X_{\text{GLY}} \sim 0.5$. (B) Decay of solvent correlation function $C(t)$ for C153 in DMSO-GLY binary mixture at $X_{\text{GLY}} = 0.1$ (red), 0.2 (green), 0.4 (cyan), 0.5 (magenta), 0.7 (dark cyan) and 1.0 (orange).

The non-exponential decay of $C(t)$ of C480 at a longer time might be a reflection of multiple relaxation channels, which is quite possible as at a longer time, the moderately hydrophobic dye C480 starts diffusing and experiences heterogeneous micro-domains across the DMSO–

GLY mixture. In the case of the other two dyes: C153 (highly hydrophobic) and C343 (highly hydrophilic), diffusion of the excited dipole is unlikely, which is why a simple bi-exponential decay function can successfully fit the solvent correlation curves obtained from these two dyes. The uses of a similar stretched exponential function has been employed in a recent simulation study of the solvation dynamics in DMSO–water mixture by Bagchi and coworkers.⁵¹ They found a hybrid fitting function with a relatively slow stretched exponential decay, which was preceded by an initial Gaussian type decay in the ultrafast time region, was required for an adequate fitting of the solvation correlation curves obtained from the DMSO–water mixtures.⁵¹ The initial sub-100 fs Gaussian type decays in the solvation dynamics were revealed in experimental studies on several fast liquids, including water, DMSO, and acetonitrile.¹²⁹⁻¹³¹ In our study, owing to the limited time resolution, we can only detect the latter part (>30 ps) of the solvation dynamics. Therefore, incorporation of Gaussian function, which accounts for sub-100 fs dynamics, is meaningless in our study. Thus, we used a combination of a fast exponential decay, together with the stretched exponential function at a longer time, which could reasonably account for the entire solvation dynamics obtained from C480 in DMSO–GLY mixtures (equation 3.1).

The solvation times differ widely with varying the composition of the binary mixture non-monotonously. The solvation dynamics in neat DMSO is completely ultrafast (~ 3 ps), but become more than two orders of magnitude slower on the addition of an insignificant amount of GLY ($X_{\text{GLY}} \sim 0.1$).¹³¹ The magnitude of slowdown is at the maximum in the case of C343 and minimum for C153 (Table 3.1, Figure 3.3). Several probe dependent anomalous concentration regions are detected within this solvent mixture, where the solvation dynamics become significantly slow. Among all the coumarin dyes studied here, C343 reported the maximum deviation (>10 -fold) in solvation time in the DMSO–GLY mixtures from $\sim 23\ 030$ ps (at $X_{\text{GLY}} \sim 0.05$) to ~ 2130 ps (at $X_{\text{GLY}} \sim 0.8$), while C480 shows only ~ 2 -fold deviation between the fastest

(~ 476 ps at $X_{\text{GLY}} \sim 0.2$) and slowest (~ 974 ps at $X_{\text{GLY}} \sim 0.6$) solvation time across the entire GLY concentration range within the DMSO–GLY mixtures (Table 3.1, figure 3.3). Not only in their magnitudes (*i.e.*, between the fastest and slowest solvation times) are they probe dependent, but also the precise positions of these anomalous concentration regions are not the same for every probe molecule. For instance, C153 exhibits an almost linear increase in the average solvation time ($\langle \tau_s \rangle \sim 102$ ps to 946 ps) with increases in the GLY concentrations ($X_{\text{GLY}} \sim 0.1$ to 0.9) within the solvent mixture; except in one concentration region, $X_{\text{GLY}} \sim 0.45$ – 0.55 , where the solvation time deviates non-monotonically to a slower dynamics (~ 745 ps, Figure 3.3). This is in contrast to the most hydrophilic dye C343, where the solvent response progresses non-monotonically on the gradual addition of GLY to the DMSO–GLY mixture. At least three (instead of one with C153) slow dynamics regions are detected, with two prominent slowdowns centred at $X_{\text{GLY}} \sim 0.05$, 0.3 and one relatively weak slowdown centred at $X_{\text{GLY}} \sim 0.6$ (Figure 3.3).

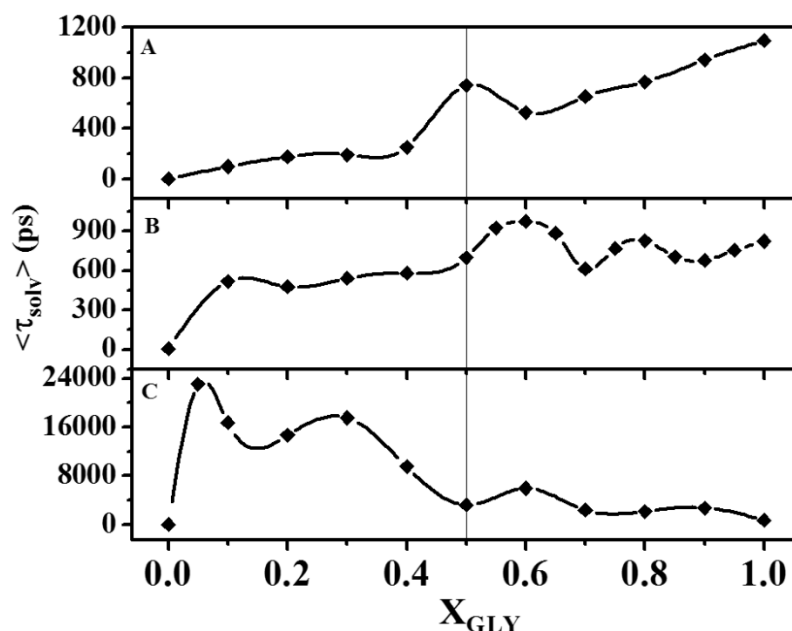


Figure 3.3. Plot of average solvation time as a function of mole fraction of glycerol for (A) C153, (B) C480 and (C) C343.

In the case of the moderately hydrophobic dye C480, solvent relaxation in the DMSO–GLY binary solvent is found to be non-exponential and diffusion assisted at longer times. Such a non-exponential behaviour of solvent relaxation could be a reflection of the non-Markovian character of the friction present within the relaxing solvent molecules, as well as the dynamical heterogeneity inside the solvent mixture.¹³³ The β value in equation 3.1 bears the nonideality character of the solvent mixture, which fluctuates in the range of 0.46–1.2 ($X_{\text{GLY}} \sim 0.6$ –0.1) in the DMSO–GLY mixtures when C480 is used as a solvatochromic probe (Table 3.1). The dynamical deviation of the average solvation times and changes in the β values with changing the X_{GLY} can identify the anomalous ranges simultaneously in a single frame (Figure 3.4). Any deviation of β values from unity represents the non-exponentiality of the dynamical process.⁵¹ Non-exponentiality is a reflection of the heterogeneity of the solvent mixture. One can also study the solvent inhomogeneity in terms of β values as a function of X_{GLY} , which provides the same feature that we came across from the dynamical deviation of $\langle \tau_{\text{solv}} \rangle$ (Figure 3.4). Two anomalous ranges of solvation dynamics of C480 in DMSO–GLY mixtures (across all the GLY concentrations) are captured together by low β values, as well as by long $\langle \tau_{\text{solv}} \rangle$ values.

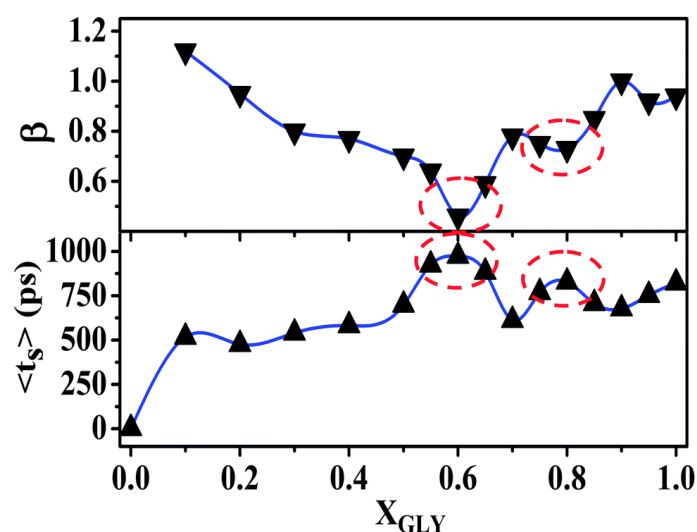


Figure 3.4. Variation of average solvation times (lower panel) and β value (upper panel) as a function of mole fraction of glycerol in DMSO-GLY binary mixture.

Table 3.1 Decay parameters of solvent correlation function for the coumarin dyes in DMSO-

Probe	X _{GLY}	Δv_{obs}^a (ν_0) cm^{-1}	Decay parameters of C(t),		$\langle \tau \rangle_{\text{solv}}$ (ps)
			τ_1^b (a_1) (ps)	τ_2^b (a_2) (ps)	
C153	0.1	210(19030)	88 (0.92)	257 (0.08)	102
	0.2	225(18916)	160 (0.97)	720 (0.03)	177
	0.3	291(18938)	195 (0.45)	195 (0.55)	195
	0.4	323(18860)	256 (0.60)	256 (0.40)	256
	0.5	270(18766)	420 (0.92)	4485 (0.08)	745
	0.6	350(18792)	395 (0.97)	4850 (0.03)	529
	0.7	325(18765)	435 (0.95)	4850 (0.05)	656
	0.8	354(18770)	680 (0.98)	5200 (0.02)	770
	0.9	367(18845)	574 (0.10)	988 (0.90)	946
	1.0	500(19020)	1098 (0.5)	1098 (0.5)	1098
C480	0.1	271(20946)	75(0.2)	628(0.8)	517
	0.2	325(21900)	102(0.12)	527(0.88)	476
	0.3	335(21700)	465(0.92)	1400(0.08)	540
	0.4	380(21590)	450(0.86)	1400(0.15)	582
	0.5	354(21520)	480(0.75)	1350(0.25)	698
	0.55	279(21385)	572(0.7)	2000(0.3)	924
	0.6	258(21325)	627(0.55)	1400(0.45)	974
	0.65	432(21436)	466(0.5)	1300(0.5)	883
	0.7	368(21378)	55(0.21)	760(0.79)	612
	0.75	465(21375)	328(0.4)	1064(0.6)	769
	0.8	486(21367)	700(0.84)	1500(0.16)	828
	0.85	526(21424)	44(0.04)	733(0.96)	707
	0.9	533(21471)	45(0.11)	755(0.89)	677
	0.95	530(21410)	39(0.3)	1059(0.7)	753
	1	736(21500)	823(0.5)	823(0.5)	823
C343	0.05	143(20687)	370 (0.08)	25000 (0.92)	23030
	0.1	135(20690)	82 (0.28)	23000 (0.72)	16700
	0.2	127(20703)	144 (0.29)	20585 (0.71)	14657
	0.3	203(20716)	231 (0.25)	23260 (0.75)	17502
	0.4	176(20560)	144 (0.42)	16344 (0.58)	9540
	0.5	190(20750)	284 (0.67)	9300 (0.33)	3260
	0.6	300(20682)	417 (0.55)	12700 (0.45)	5945
	0.7	245(20680)	413 (0.71)	7183 (0.29)	2376
	0.8	274(20800)	467 (0.80)	8610 (0.20)	2130
	0.9	300(20930)	480 (0.5)	5000 (0.5)	2740
1.0	575(21010)	247 (0.61)	1406 (0.39)	699	

GLY binary mixture. ^a $\pm 50\text{cm}^{-1}$ ^b $\pm 10\%$

The solvation dynamics in bulk DMSO is ultrafast (~ 3 ps)¹³¹ However, the $\langle \tau_{\text{solv}} \rangle$ in the DMSO–GLY binary mixture is at least a few orders of magnitude slower compared to that in neat DMSO. The effect of GLY on the solvation time of C343 in DMSO is much more drastic compared to the other dyes. The solvation times of coumarin dyes in neat DMSO are too fast (< 30 ps) to be detected by our setup with limited time resolution (~ 70 ps). However, the addition of a small amount of GLY to the neat DMSO makes the entire solvent relaxation process substantially slow. The microscopic origin of “slow solvation” in binary mixtures has been the subject of much debate for the last few decades. The addition of an insignificant amount of GLY to the neat DMSO abruptly slows down the solvation dynamics of C343 to a longer time ($\langle \tau_{\text{solv}} \rangle \sim 23$ ns at $X_{\text{GLY}} \sim 0.05$; Table 3.1). C480 and C153 rather show a much faster solvation dynamics in DMSO–GLY mixtures across the entire GLY concentration range.

The microscopic origin of the 25 ns solvation time of C343 in DMSO–GLY mixture ($X_{\text{GLY}} \sim 0.05$) is not clear to us. Even in a highly viscous neat GLY solvent, C343 is solvated at a much faster timescale (~ 686 ps). The origin of the ultraslow component of C343 in DMSO–GLY could be a reflection of hydrogen bond formation between the –COOH group of C343 with DMSO–GLY complexes within the binary mixture. In a recent study, Dutt and coworkers observed that the hydrogen bond formation between C343 and DMSO causes ~ 2 -fold slower rotation of C343 in neat DMSO compared to the rotational time obtained from a molecule with similar dimensions (with C343) but not hydrogen bonded to the DMSO solvent.¹³⁴ This observation provides an explanation towards the exceptionally slow solvation dynamics of C343 in DMSO–GLY mixture, which could be a reflection of extensive hydrogen formation between C343 and the solvent molecules. Nevertheless, this piece of information could not provide a satisfactory explanation to the question as to why the solvent relaxation in neat GLY is faster than the DMSO–GLY mixtures, even though the probability of hydrogen bond formation of C343 with GLY is the same as with the DMSO–GLY

mixture. The solvent relaxation around the excited state dipole involves a rupturing of the hydrogen bonds predominantly formed between C343 with the GLY molecules in the first solvation shell and is followed by an exchange of less polar GLY molecules from the GLY-rich first solvation shell with the more polar DMSO molecules in the periphery of the first solvation shell.¹⁵⁶ Using the relation, $\langle Z^2 \rangle = 2Dt$, and the diffusion coefficient of glycerol, which is $1.77 \times 10^{-12} \text{ m}^2 \text{ s}^{-1}$ (~ 1400 -fold lower than water),¹³⁵ we find that in a ~ 25 ns timescale, a molecule can diffuse a length of $\sim 2.8 \text{ \AA}$, which is about the thickness of a solvation shell.⁵⁰ Another useful model proposed by Nandi-Bagchi, which shows a possible origin of the slow solvation component in the binary mixture, could be a reflection of the dynamical exchange of “bound” and “free” solvent molecules around the excited dipole.¹³⁶ The “bound” molecules are solvent molecules that are completely immobilized and attached to a surface by hydrogen bonds, while “free” molecules are the bulk solvent molecules. At a high binding energy, the slow component (τ_{slow}) can be approximated as follows:¹³⁶

$$\tau_{\text{slow}}^{-1} = k_{\text{bf}} = \left(\frac{k_{\text{B}}T}{h} \right) \exp\left(\frac{-\Delta G}{RT} \right) \dots\dots\dots (3.2)$$

where ΔG is the activation energy for the solvent relaxation process, and k_{bf} represents the bound-to-free rate constant. From equation, ΔG values corresponding to ~ 250 – 5000 ps (τ_{slow} of C153 and C480 in DMSO–GLY mixtures, Table 3.1) fall in the range of -4.35 to $-6.12 \text{ kcal mol}^{-1}$, which are of the order of hydrogen bond formation energy. The origin of the ultraslow component in case of C343 can be explained by specific-solute solvent interaction which we will describe in the proceeding section.

3.3. Rotational Dynamics Study: Specific Solute-Solvent Interaction

The fluorescence anisotropy decays of coumarin dyes in DMSO–GLY mixtures were recorded across the entire concentration range of GLY ($X_{\text{GLY}} \sim 0$ to 1) at ~ 10 nm in the blue side of their respective emission peaks. A bi-exponential fitting function (equation 3.3) adequately fitted the experimental rotational correlation decay curves.

$$r(t) = r_0 \left[a \exp\left(-\frac{t}{\tau_{\text{slow}}}\right) + (1-a) \exp\left(-\frac{t}{\tau_{\text{fast}}}\right) \right] \dots\dots\dots (3.3)$$

The decay of rotational correlation functions for C153 in some of the compositions in DMSO-GLY binary mixture along with bi-exponential fit have been depicted in figure 3.5. With increasing GLY content in the mixture the rotational correlation function gets slower due to increase in viscosity of the medium. The same observation was obtained for other two dyes also.

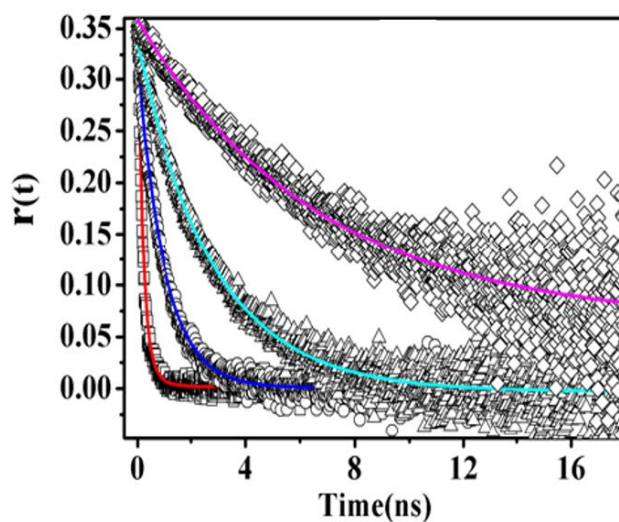


Figure 3.5. Decay of rotational correlation function $r(t)$ of C153 in DMSO-GLY binary mixture with $X_{\text{GLY}}=0.1$ (Red), 0.4(Blue), 0.6(Cyan), 0.8(Magenta).

The rotational dynamics in common solvents were found to be single exponentials, and could be explained by using the Stokes–Einstein–Debye (SED) hydrodynamics theory as follows:¹³⁷

$$\tau_r = \frac{\eta V}{kT} fC \dots\dots\dots (3.4)$$

In the above equation, the shape factor f compensates for any shape deviations (from its spherical geometry) of the solute dipole.¹³⁷ Apart from the other parameters, the solute solvent interaction affects the rotational dynamics of the excited dipole and is accounted for by the solute solvent coupling parameter (C). The value of C varies from zero, for the slip boundary condition, to one for the stick boundary condition.¹³⁴ In the stick boundary condition, the tangential velocity of the solvent molecules at the surface of the rotating dipole vanishes, while in the slip boundary condition, the tangential component of the normal stress is zero at the surface of the solute molecule. The shape factors (f) and the van der Waals volumes (V) of C153 and C343 were reported.¹³⁴ For C480, we assumed f and V would remain the same as for C153, which is reasonable as C480 has a similar structure to C153, except the 4-position $-\text{CH}_3$ group of C480 is replaced by the $-\text{CF}_3$ group in C153. Using the values of f , V , viscosity coefficient (η) and τ_{rot} as the average rotational correlation time in equation, we calculated the C values of coumarin dyes in DMSO–GLY mixtures across all GLY concentrations (Table 3. 2). Fig. 3.6 shows the log–log plots of the average rotational relaxation time ($\langle \tau_{\text{rot}} \rangle$) as a function of the viscosity at unit temperature of the medium (ηT^{-1}) within the slip and stick boundary lines.⁴¹ The slip (or stick) boundary line was obtained by connecting two τ_{rot} values at the complete slip (or stick) boundary condition in DMSO and GLY, respectively.

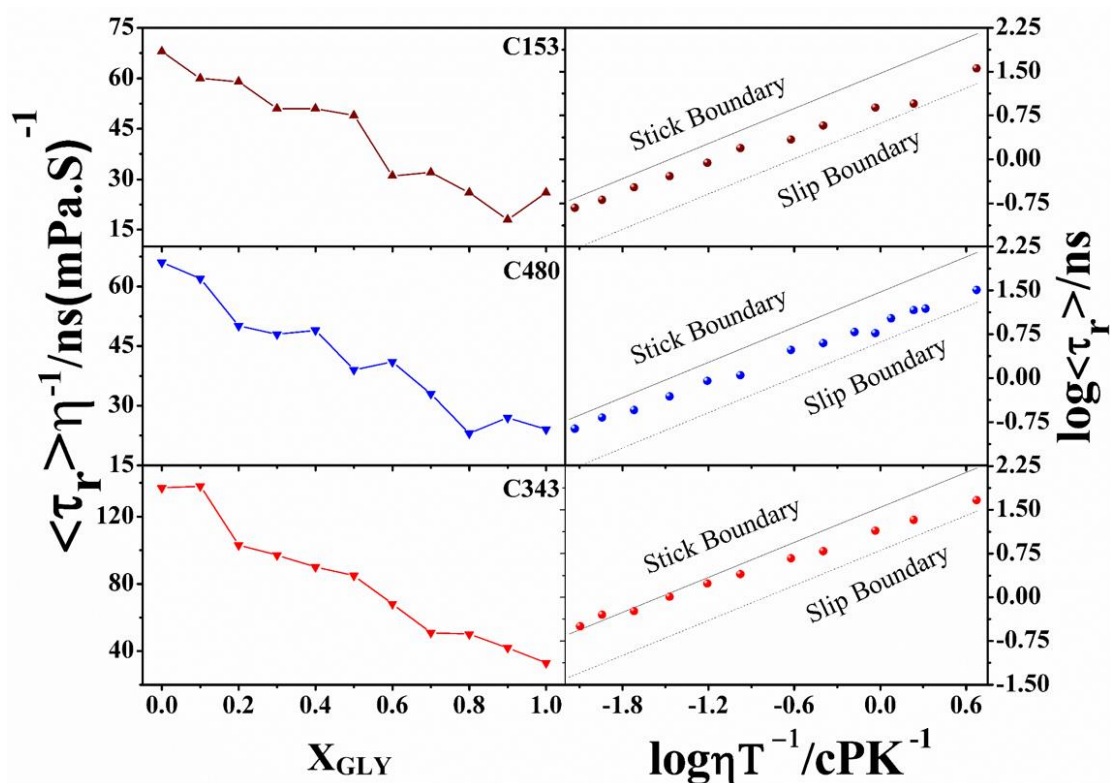


Figure 3.6. The left panel shows the plots of viscosity normalized average rotational times of coumarin dyes as a function of X_{GLY} . The right panel show the log–log plots of the average rotational relaxation times vs medium viscosity at unit temperature of coumarin dyes in DMSO–GLY mixture across the composition under the hydrodynamic boundary conditions.

From Figure 3.6 (and Table 3.2), it is evident that except for C343, solute solvent coupling parameters (C) remain within the two boundary lines across the entire X_{GLY} range in the DMSO–GLY mixtures. In the case of C343, at low GLY concentrations ($X_{\text{GLY}} < 0.2$), the C values appear at the super stick region (above the stick boundary line) with values of more than unity. A high C value is a clear manifestation of a high solvent–solute interaction that hinders the rotation of the excited dipole. This observation is analogous to the anomalous slowdown of the solvation time (~ 23 – 14 ns) within this region ($X_{\text{GLY}} \sim 0.05$ – 0.2 , Table 3.1). Except in this region, the overall trends of C values are the same for all coumarin dyes, the C value decreases monotonically from the near stick boundary values (at low X_{GLY}) to near the slip boundary values (at high X_{GLY}). Similar observations were obtained when we

plotted the viscosity normalized average rotational time ($\langle \tau_{\text{rot}} \rangle / \eta$) as a function of GLY concentration in DMSO–GLY binary mixtures. The value of $\langle \tau_{\text{rot}} \rangle / \eta$ decreases with increases in GLY concentration in the binary mixtures. For instance, the viscosity normalized average rotational time of C153 decreases almost monotonically over ~ 4.2 -fold, from 75 ps in neat DMSO to 18 ps in 90 mole% GLY DMSO–GLY mixture (Table 3.2). The same ($\langle \tau_{\text{rot}} \rangle / \eta$) changes a maximum of ~ 4.2 -fold for C343, from 138 ps (at $X_{\text{GLY}} \sim 0.1$) in the DMSO–GLY mixture to 33 ps in neat GLY ($X_{\text{GLY}} = 1$). On increasing the GLY concentration in the DMSO–GLY binary mixture, the small DMSO molecules are replaced by large GLY molecules. Solvents of small molecules (like DMSO and water) offer good packing inside the solvent cluster compared to the solvents of large molecules (like GLY). In the GLY-rich DMSO–GLY binary mixtures there are many spaces inside the solvent clusters where the dipole can easily rotate. This could be the reason why an excited dipole exhibits a faster rotational relaxation time (viscosity normalized) with increases in the GLY concentration in the DMSO–GLY mixture.

Another interesting observation we noted here is the bi-exponential nature of the rotational dynamics of all the coumarin dyes in the DMSO–GLY mixtures across the entire GLY concentrations. The fast component, which is found to be similar with the rotation time in neat DMSO, remains insensitive to the changes in GLY concentration in DMSO–GLY mixtures. The other component (slow) is highly correlated to the bulk viscosity, and changes linearly with linear changes in the GLY concentration in DMSO–GLY mixtures. We may recall here a recent work of spatially resolved FCS by Bhattacharyya's group, where they reported the presence of a microscopic phase segregation in DMSO–GLY mixtures.⁶⁵

Table 3.2. Rotational relaxation parameters for coumarin dyes in DMSO-GLY mixture

Dye	X _{GLY}	η (cP)	$\tau_1(a_1)$ ps	$\tau_2(a_2)$ ps	$\langle\tau_r\rangle$ ps	$\langle\tau_r\rangle/\eta$	C _{rot}
C153	0	2.2	150(1)	-	150	68	0.68
	0.1	3.4	159(0.83)	415(0.17)	203	60	0.60
	0.2	5.7	175(0.26)	392(0.74)	336	59	0.59
	0.3	10.1	156(0.12)	567(0.88)	518	51	0.51
	0.4	18.5	68(0.13)	997(0.87)	876	47	0.47
	0.5	31.4	140(0.05)	1,609(0.96)	1,552	49	0.49
	0.6	70.8	66(0.22)	2,775(0.78)	2,180	31	0.31
	0.7	119	240(0.06)	4,044(0.94)	3,816	32	0.32
	0.8	275	250(0.05)	8,056(0.95)	7,666	28	0.28
	0.9	510	59(0.20)	11,250(0.8)	9,012	18	0.17
	1	1400	50(0.20)	36,000(0.8)	36,010	25	0.26
C480	0	2.2	145(1)	-	145	66	0.66
	0.1	3.4	179(0.94)	722(0.06)	211	62	0.62
	0.2	5.7	122(0.35)	375(0.65)	286	50	0.50
	0.3	10.1	116(0.2)	579(0.8)	486	48	0.48
	0.4	18.5	317(0.17)	1009(0.83)	892	48	0.48
	0.5	31.4	65(0.24)	1472(0.76)	1127	35	0.36
	0.6	70.8	1724(0.39)	3890(0.61)	3047	43	0.43
	0.7	119	600(0.11)	4,350(0.89)	3950	33	0.33
	0.8	275	88(0.2)	7350(0.8)	5898	21.5	0.21
	0.9	510	904(0.03)	14986(0.97)	14536	28.5	0.28
	1	1400	232(0.05)	34200(0.95)	32260	23	0.23
C343	0	0.35	2.2	302(1)	-	302	137
	0.05	0.35	3.1	193(0.24)	436(0.76)	378	122
	0.1	0.35	3.4	141(0.17)	522(0.83)	458	134
	0.2	0.35	5.7	107(0.16)	672(0.84)	582	102
	0.3	0.35	10.1	800(0.61)	1,357(0.39)	1,017	100
	0.4	0.35	18.5	1,181(0.5)	2,256(0.5)	1,719	93
	0.5	0.35	31.4	54(0.08)	2,695(0.92)	2,538	81
	0.6	0.35	70.8	1,169(0.06)	5,060(0.94)	4,823	68
	0.7	0.35	119	1,031(0.04)	6,280(0.96)	6,070	51
	0.8	0.35	275	1,200(0.03)	14,118(0.97)	13,730	50
	0.9	0.35	510	86(0.11)	23,790(0.89)	21,183	42
1	0.35	1400	291(0.02)	47,411(0.98)	46,468	33	

They observed that two drastically different environments coexisted within this solvent mixture: one with a viscosity coefficient similar to the bulk DMSO, and other that shows a bulk-like viscosity. Our rotational dynamics study also confirms the fact that a large population of DMSO molecules refuse to interact with GLY molecules in DMSO–GLY mixtures, and thus creates neat DMSO-like domains within the solvent clusters of DMSO–GLY mixtures. In summary, for all coumarin dyes, the rotational correlation decays in DMSO–GLY mixtures are best fitted by a bi-exponential fitting function with a DMSO-like time component. The viscosity normalized average rotational time becomes faster with increases in the GLY concentration in the DMSO–GLY mixture. In low GLY concentration regions ($X_{\text{GLY}} \sim 0.05\text{--}0.2$), the solvent–solute interactions increase drastically, and the rotational dynamics of C153 and C480 almost reach the stick boundary limit. This scenario is even more drastic for C343, where we found super stick dynamics within this concentration region of GLY ($X_{\text{GLY}} \sim 0.05\text{--}0.1$) in DMSO–GLY mixtures. This phenomena holds the ultraslow solvation dynamics of C343 at low glycerol containing mixtures. Strong solute–solvent coupling leads to slow reorganization of solvent molecules in the first solvation shell of the probe molecule.

3.4. Conclusion

A solvation dynamics study of three coumarin dyes in DMSO–GLY mixtures (across all the ratios) shows multiple anomalous concentration regions, where the solvation dynamics are significantly slow. The most interesting observation is that the precise locations of these “slow regions” in DMSO–GLY mixtures and the overall feature of the average solvation time *vs.* X_{GLY} curve is also dye dependent. C153 captures only one anomaly (peak at $X_{\text{GLY}} \sim 0.5$) within the DMSO–GLY mixtures across the entire GLY concentration range, while C343 and C480 detected at least three (peaks at $X_{\text{GLY}} \sim 0.05, 0.3$ and 0.6) and two (peaks at $X_{\text{GLY}} \sim 0.6$ and 0.8) anomalous concentration regions in the same binary mixtures. The

solvation dynamics, studied with a moderately hydrophobic dye C480, were found to be diffusion assisted at longer times. The deviation of the stretched exponential parameter (β) from unity remain highly correlated with the average solvation times in anomalous regions, indicating that the slowing down of the solvation dynamics at the anomalous regions is due to the non-exponential nature of the dynamics. The two dyes, C153 and C343, remain strictly confined within the hydrophobic and hydrophilic regions only, and a simple bi-exponential fitting function was able to adequately fit the solvent correlation curves obtained from these two dyes in DMSO–GLY mixtures. In summary, the rotational and solvation dynamics of coumarin dyes in DMSO–GLY mixtures unambiguously establish the presence of microdomains with widely varying polarities within this mixture. The existence of dye specific anomalous regions within the DMSO–GLY mixtures confirms the fact that at particular compositions of DMSO and GLY that produce DMSO–GLY mixtures with inhomogeneous polar domains inside the solvent clusters, the same compositions may not produce the same inhomogeneous nonpolar domains at the same time and *vice versa*.

Study of Microheterogeneity in Acetonitrile –Water Binary Mixture

4.1. Introduction

Protic binary mixtures are of special category among the solvent mixtures for their uses in solubilising biomolecules, cryogenic engineering, chromatographic separations, enzymology and in other numerous applications.²⁹⁻³³ Nonlinear physical (e.g., dielectric constant, viscosity, refractive index, etc) and thermodynamic properties (heat change, entropy etc) are the common features of binary mixtures.³⁴⁻³⁹ The unusual interactions between the cosolvents of a binary mixture lead to an one-to-one or higher order complex formations and in some cases these complexes emerge as a building blocks within an extended hydrogen bond network.⁴⁰ Microheterogeneity is a reflection of these unusual interactions among the solvent molecules within a binary mixture. Amphiphilic aprotic solvents like dimethyl sulfoxide (*DMSO*), acetonitrile (*ACN*), acetone, dimethylformamide (*DMF*) are highly miscible with water at any proportions. Polarity (P) of an ideal binary solvent is the sum of weighted average polarity of the two solvents, e.g., $P = xP_1 + (1-x)P_2$; where P_1 and P_2 are the polarities of the pure solvents and x representing the fraction of the solvent with polarity P_1 . Interestingly, most of the binary solvents are inherently inhomogeneous and behave nonideally towards the static physical (viscosity, refractive index, etc) and dynamical properties (solvation energy, structural transformation, cluster diffusion etc). A dipole within an inhomogeneous binary mixture may experiences a completely different environment from the bulk due to the preferential solvation. Preferential solvation is caused by the active diffusion of the polar solvent molecules to the first solvation shell of the solute dipole. If Y ($=y_N/y_P$) and X ($=x_N/x_P$) be the concentration ratios of nonpolar to polar solvents around the solute dipole and in bulk, they are inter correlated with preferential solvation parameter (Z)

as; $Y = X e^{-Z}$.^{48,55} Z can be further correlated with Onsager's reaction field $F(\epsilon) [=2(\epsilon-1)/2\epsilon+1]$ and solute dipole moment (μ) by the following equation,

$$Z = \frac{1}{4\pi\epsilon_0} \frac{CM\mu^2\Delta F_{N,P}}{2\delta RT r^6} \dots\dots\dots(4.1)$$

Where, $\Delta F_{N,P} = F_p - F_N$

The average molecular weight and density of the solvents are represented by M and δ , respectively. A positive Z value signifies the local concentration of the polar solvent is more around the solute dipole compared to the bulk concentration. Huppert and his coworkers observed a high Z value (~ 1.7) within the hexane-propionitrile binary mixture which they explained by considering a diffusion of the polar propionitrile molecules to the first solvation shell of the C153 dipole.⁴⁸ Apart from the dielectric enrichments and specific solvation, which are relevant to the property of the probe molecule, also the hydrogen bond formation among the cosolvents (irrelevant to dye molecule) largely contributes to the inhomogeneity of these aqueous aprotic binary mixtures.^{34,36-37,39} Fascinating hydrogen bonded clusters formation is a unique feature of an aqueous binary mixture.^{51-52,58,139-140} The efficiency of polar state stabilization of a dye molecule by these mixed solvent clusters is often found to be much higher even compared to its polar cosolvent (neat water). This phenomenon is called *synergistic effect*. In these binary mixtures one can customise the parameters relevant to hydrogen bond formation ability, polarity and protic character to the requisite level by changing the water content and thereby facilitate the desired functionalities; e.g., stabilizing one particular conformation of macromolecules including proteins in an equilibrium process, size selective synthesis of polymer micelles etc.¹⁴¹⁻¹⁴³ A large number of experimental and computational studies have shown the presence of solvent clusters and complex formations within the binary solvents are the key sources of inhomogeneity.⁴²⁻⁴⁵ Slow solvation

dynamics, non linear physical and thermodynamic parameters are the reflections of solvent inhomogeneity, frequently observed within the binary mixtures.

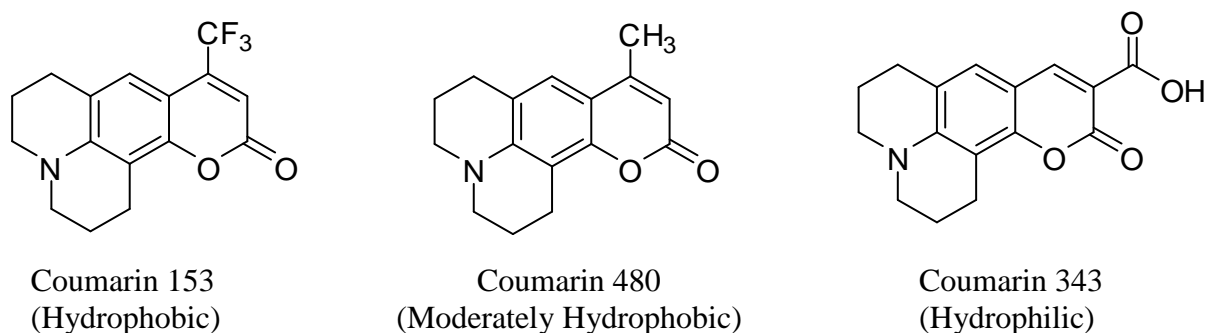
Among several binary solvents, ACN-WT mixture is in special category as it is formed by mixing of highly polar protic and polar aprotic solvents. ACN and WT both are well known as fast solvent for their accelerated solvation properties.^{130,144-145} Therefore one obvious question came to our mind how fast the solvation dynamics would be in a mixture of these two solvents? Needless to say, this piece of information will be helpful for an effective use of ACN-WT mixture in reverse phase chromatography, as a reaction medium and in atmospheric chemistry.¹⁴⁶⁻¹⁴⁸ Efforts have been made for rationalizing the solvent structures of ACN-WT at different stoichiometric ratios. In an early work by Laaksonen and his co-worker studied dynamic simulation and NMR of ACN-WT at different stoichiometric ratios.¹⁴⁹ From simulation they observed enhancement of quasi hydrogen-bonded structures of water within the ACN rich ACN-WT mixtures and that finally break down to produce heterogeneous solvent clusters.¹⁴⁹ Studies of Raman spectroscopy and thermodynamic parameters of water rich ACN-WT mixtures ($x_{ACN} < 0.2$) show ACN molecules barely disturb the water structures and significant tendencies are found among the water molecules to form self-associations in this concentration region.¹⁵⁰⁻¹⁵¹ From the infrared absorption study on ACN-WT mixtures over the entire composition range, Lan and his co-worker observed no enhancement of water structures on addition of ACN to a water rich ACN-WT mixture.¹⁵² Their infrared absorption spectroscopy study detected a slight increase of fraction hydrogen-bonded OH groups within the low ACN content ($X_{ACN} < 0.05$) samples, this is followed by a significant decrease in population of the hydrogen-bonded ACN molecules as ACN concentration (X_{ACN}) reaches to ~ 0.3 . At an even higher concentration of ACN, nearly 90% water molecules form hydrogen bonds to ACN molecules which are solvated by other ACN molecules.¹⁵²

In the list of recent studies on binary solvents polar-nonpolar combinations are mostly dominated while polar –polar or nonpolar-nonpolar combinations are largely neglected.¹⁵³⁻¹⁵⁸ Polar solvents are in general considered as “good solvent”, exhibit a very fast response (~1 ps) for achieving the solvated state of an excited dipole. Therefore solvation dynamics in a mixture of nonpolar solvent (bad solvator) and polar solvent (good solvator) must be diffusion assisted; during solvation, replacement of the nonpolar solvent molecules by polar solvent molecules in the first solvation shell of the excited dipole is a well expected. This slow diffusion may be one major source of the slow kinetics that appears in binary mixtures but absent within the pure solvents. In this study we purposely used a binary solvent of two highly polar solvents acetonitrile and water, both are known as good solvator. In this chapter we plan to study the mode of interaction and dynamics in ACN-WT binary mixture by various spectroscopic methods.

4.2. Results and Discussions

4.2.1 Polarity Resolved Study

In this approach we have probed three coumarin dyes of widely differing polarity through the composition range in this mixture to understand the heterogeneity due to variation of micropolarity (Scheme 4.1). We have analyzed our polarity resolved data by studying the steady state spectra, solvation dynamics and rotational dynamics study.



Scheme 4.1. Chemical Structure of the coumarin dyes used in this study

4.2.1.1. Steady State Spectra and Preferential Solvation Analysis

Among the three dyes used, moderately polar dye C480 exhibits the largest absorption and emission peak shifts in ACN-WT mixture on changing the ACN concentration across the entire range (Figure 4.1). Absorption peak of C480 in ACN-WT mixture shows ~15 nm bathochromic shift from 383 nm in neat ACN ($X_{ACN}=1$) to 398 nm at $X_{ACN}\sim 0.1$. However, for an ACN deficit sample ($X_{ACN}\sim 0-0.1$) we observed a gradual blue shifting (~6 nm) of the C480 absorption peak position on addition of water. This is in contrast to the emission peak, which only shows a monotonous red shift when a less polar ACN rich sample or neat ACN ($\epsilon_{ACN}=35.8$) was diluted with highly polar solvent water ($\epsilon_{WT}=80$) throughout the entire concentration region.

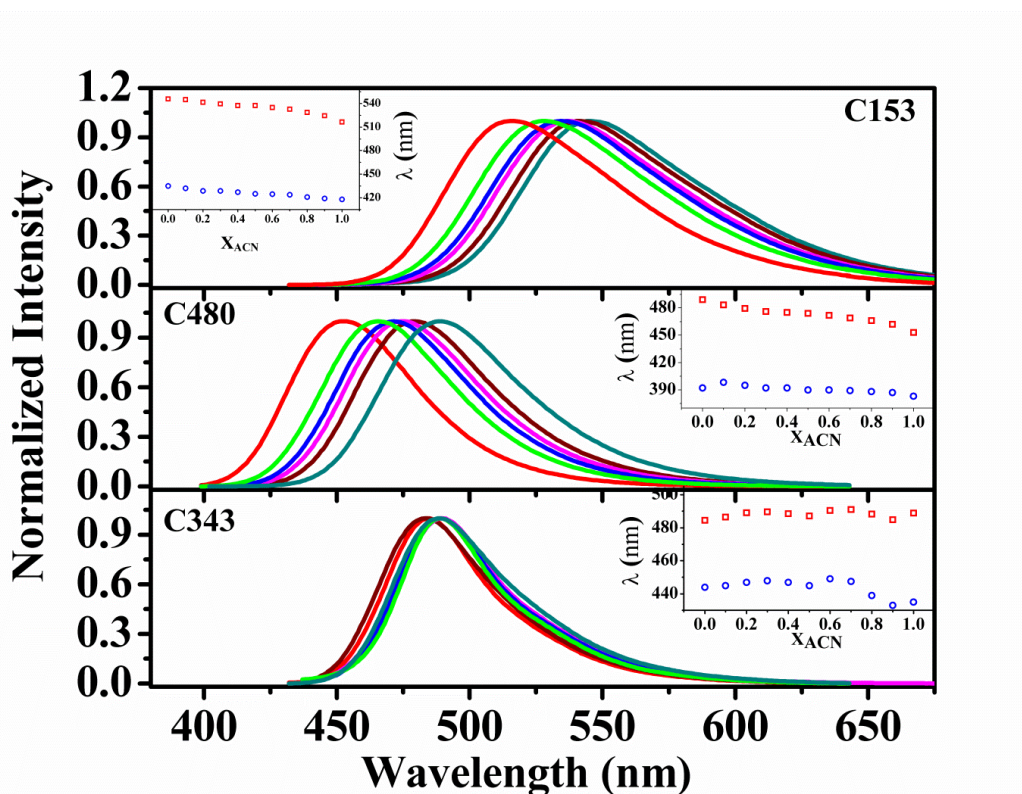


Figure 4.1. Steady state emission spectra of three coumarin dyes in ACN-WT binary mixtures of different mole fraction of ACN in the binary mixture (cyan-0, wine-0.2, magenta-

0.4, blue-0.6, green 0.8 and red- 1.0). The inset shows the plot of absorption and emission maxima as a function of ACN mole fraction.

Solvatochromic peak shift is sometime nicely explained by dielectric continuum model. In this model Onsager reaction field factor $F(\epsilon)$ [$F(\epsilon)=2(\epsilon-1)/(2\epsilon+1)$] is used instead of polarity as a linear function of absorption/emission peak shift. Inset in the figure 4.1 shows the plot of absorption and emission maxima as a function of ACN mole fraction. We have checked the change in $F(\epsilon)$ as a function of ACN mole fraction and found a linear relationship. So, we can infer that none of the dyes shows linear correlation with $F(\epsilon)$, indicating apart from non ideal polarity some other factors like hydrogen bond formation, dielectric enrichment or preferential solvation are contributing to the steady state spectrum. Suppan correlated the preferential solvation index (Z_{PS}) with an experimental non-linearity ratio ρ_{exp} obtained from the spectral shifts using the following equation,¹⁵⁸

$$\rho_{exp} = \frac{2 \int_0^1 (v_{exp} - v_{lin,bulk}) dx_p}{\Delta v_{p-n}} \dots\dots\dots(4.2)$$

Where v_{exp} is the emission peak energy within a binary mixture with polar mole fraction x_p and $v_{lin,bulk}$ is the same within an ideal solvent mixture. Δv_{p-n} is representing the Stokes shift between polar and nonpolar solvents. Nonideality in a solvent mixture (ρ_{exp}) arises from both preferential solvation (ρ_{ps}) as well as dielectric nonideality (ρ_{dn}).¹⁵⁷⁻¹⁵⁸ ρ_{dn} is calculated in a similar manner as we calculated ρ_{exp} using equation (4.2); except the terms v and ρ_{exp} are replaced with Onsager's polarity parameters and ρ_{dn} , respectively.⁶⁶ Using our experimental steady state parameters ρ_{exp} was calculated and found to be ~0.12 for an excited state of C480. Dielectric nonideality (ρ_{dn} ~0.06) was calculated from the reported values of Onsager's polarity parameters [$F(\epsilon)$] in ACN-WT mixture at different stoichiometric ratios.¹⁵⁹ The

experimentally observed ρ_{exp} value (~ 0.12) for the excited state C480 is much higher compared to the dielectric nonideality ($\rho_{dn} \sim 0.06$). This is indicating a second source of nonideality is present in the medium and that likely to be the preferential solvation (ρ_{ps}). We obtained Z_{ps} for the excited state dipole solvation of C480 using the linear relation $Z_{ps} = 3.2\rho_{ps}$ ($\rho_{ps} = \rho_{exp} - \rho_{dn}$) and found to be ~ 0.19 .¹⁵⁸ We also calculated Z_{ps} for other two dyes (C153 and C343) in a similar manner. The most hydrophobic dye C153 experiences a subtle contribution of preferential solvation ($Z_{ps} = 0.09$) in excited state solvation, whereas the most hydrophilic dye C343 displays a maximum involvement ($Z_{ps} = 0.39$) of the specific solvation in its excited state solvation (Table 4.1). Huppert and his coworker measured the contribution of specific solvation in dioxane-water mixture, their results show except the dielectric nonideality no additional sources of

Table 4.1. Parameters of preferential solvation of all three coumarin dyes in ACN-WT binary mixture

Probe	ρ_{exp}	ρ_{dn}	ρ_{ps}	Z_{ps}
C153	0.09	0.06	0.03	0.09
C480	0.12	0.06	0.06	0.19
C343	0.19	0.06	0.39	0.39

inhomogeneity are present within the medium.¹⁶⁰ However the same group reported a high value of Z_{ps} (~ 1.7) of the excited state C153 in hexane-propionitrile mixture, which they explained by assuming a diffusion of polar propionitrile molecules to the first solvation shell of C153 during the excited state solvation.¹⁵⁸ In summary, the values of Z_{ps} obtained from the three coumarin dyes in ACN-WT binary mixture reveal a substantial contribution of preferential solvation exists in the excited state solvation of all the three dyes, the magnitude

of these contributions follows an ascending order from least hydrophilic dye to the most hydrophilic dye ($Z_{PS,C153} < Z_{PS,C480} < Z_{PS,C343}$, Table 4.1). The maximum involvement of specific solvation ($Z_{ps}=0.39$) at the excited state C343 is a major reason of the remarkably slow solvation dynamics of C343 in any composition as compared to the other two dyes (Table 4.1).

4.2.1.2. Time Dependent Dynamic Stokes Shift and Solvation Dynamics Study

Solvation dynamics were measured using a TCSPC setup with ~ 70 ps temporal resolution as discussed in the chapter 2. We probably have missed a substantial part of the kinetics which appears in the ultrafast region (< 70 ps).¹⁶¹ Solvent correlation function $C(t) [= (v_t - v_\infty) / (v_0 - v_\infty)]$ was obtained by measuring the energies (ν) of the time resolved emission spectra (*TRES*) at different times (0 , t and ∞) following the procedure stated in chapter 2. As we discussed in the previous chapter, fluorescence lifetime fittings at the red wavelengths (solvated state), show a rise at the initial time due to the excited state solvation which is followed by the excited state population depletion (decay) at the longer delay time. This wavelength dependent lifetime was mostly observed at intermediate ACN concentration range ($X_{ACN} \sim 0.2-0.8$) where kinetics is substantially slow. At very high ($X_{ACN} > 0.9$) and very low ($X_{ACN} < 0.1$) ACN concentrations, none of the coumarin dyes shows any detectable rise component in their red end lifetime decays. From the fitted values of $C(t)$ we plotted the average solvation time as a function of ACN concentration for all the three coumarin dyes (Figure 4.2). A common feature from the three dyes is that the solvation dynamics remain ultrafast (< 70 ps) within the ACN deficit ($X_{ACN} \sim < 0.2$) and ACN rich ($X_{ACN} > 0.8$) samples. At intermediate ACN concentrations ($X_{ACN} \sim 0.2-0.8$) solvation dynamics from all the three dyes became abnormally slow and easily detected by our setup. Solvation dynamics in this concentration region show abysmal diversities and several dissimilar trends were observed when we compared among the different coumarin dyes. Solvation dynamics in the hydrophobic (probed with C153) and

moderately hydrophobic (probed with C480) regions within the ACN-WT mixture show one anomalous point at $X_{ACN} \sim 0.2$, where the average solvation time climbed to 229 ps (for C153) and 512 ps (for C480), respectively from <70 ps (for C153 and C480) at $X_{ACN} = 0.1$. However the first anomalous point of the hydrophilic domain (probed with C343) was obtained at $X_{ACN} \sim 0.4$ ($\langle \tau \rangle \sim 17,315$ ps), which is followed by a dip at $X_{ACN} \sim 0.5$ ($\langle \tau \rangle \sim 2,595$ ps) and makes a new peak at $X_{ACN} \sim 0.8$ (36,570 ps). The composition dependent slowdown of solvation times has been reported in other binary mixtures by several groups.^{51-52,58} The slowdown was mainly attributed to the formation of 1:2 or 2:1 complex formation and clustering among the solvent molecules. In our case we also obtained similar slowdowns in average solvation times from all the three coumarin dyes across the entire concentration range of ACN. Interestingly in present study we have observed at $X_{ACN} \sim 0.5$ the hydrophobic part (probed by C153) of the ACN-WT mixture shows a maximum non-exponential kinetics with an abruptly slow average solvation time ($\langle \tau \rangle \sim 290$ ps, Figure 4.2). However the hydrophilic domains at same stoichiometric mixture ($X_{ACN} \sim 0.5$) produce the most homogeneous environment with a relatively fast dynamics ($\langle \tau \rangle \sim 2,595$ ps). In summary, solvation dynamics of all the three coumarin dyes unambiguously detected a microscopic inhomogeneous environment at moderate to high concentration range of ACN ($X_{ACN} \sim 0.2-0.8$) within the ACN-WT mixture. In this concentration range the kinetic behaviours of the polar and the nonpolar domains are completely different. However, at very high ($X_{ACN} > 0.8$) or very low ($X_{ACN} < 0.2$) ACN concentrations, the solvent mixtures are relatively homogeneous in nature (Figure 4.2).

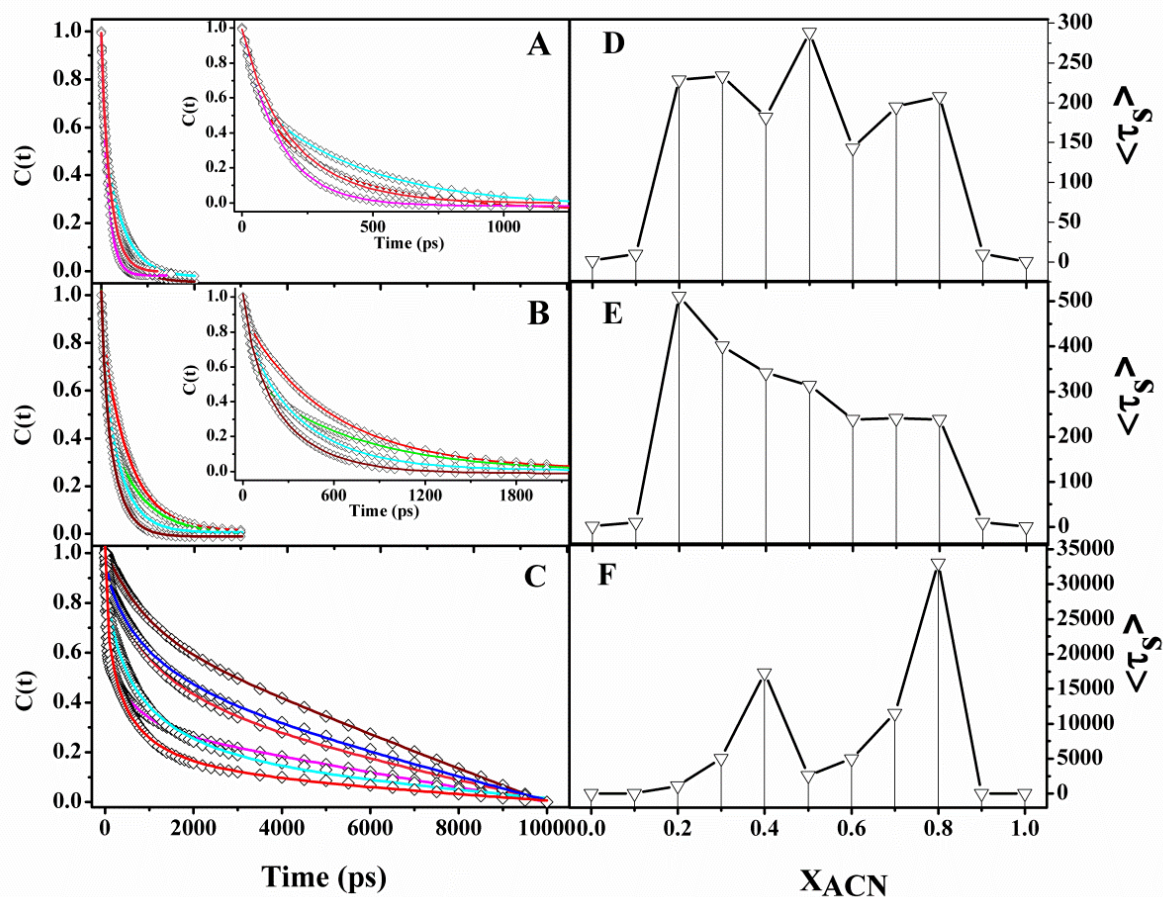


Figure 4.2. The left panel represents the decay of solvent correlation function $C(t)$ for (A) C153, (B) C480 and (C) C343 in ACN-WT binary mixtures with $X_{ACN}=0.2$ (red line), $X_{ACN}=0.3$ (green line), $X_{ACN}=0.4$ (blue line), $X_{ACN}=0.5$ (cyan line), $X_{ACN}=0.6$ (magenta line), $X_{ACN}=0.7$ (pink line), and $X_{ACN}=0.8$ (wine line). The right panel shows the plots of average solvation time $\langle \tau_s \rangle$ as a function of X_{ACN} for (D) C153, (E) C480, (F) C343, respectively. The vertical for clear understanding of the mole fraction values.

Table 4.2. Decay parameters of C(t) of coumarin dyes in ACN-WT binary mixtures at different mole fractions of acetonitrile (X_{ACN}).

Probe	X_{ACN}	$\Delta\nu^a$ (ν_0) cm^{-1}	Decay parameters of C(t)		$\langle\tau_s\rangle$ ps
			τ_1^b (a_1) (ps)	τ_2^b (a_2) (ps)	
C153 (λ_{ex} =405nm)	0				$\sim 1^c$
	0.1				$<70\text{ps}^\dagger$
	0.2	85 (18469)	69 (0.44)	355 (0.56)	229
	0.3	127 (18617)	163 (0.49)	302 (0.51)	234
	0.4	128 (18678)	-	182 (1.0)	182
	0.5	95 (18668)	45 (0.33)	410 (0.67)	289
	0.6	167 (18812)	-	143 (1.0)	143
	0.7	130 (18869)	45 (0.08)	208 (0.92)	195
	0.8	142 (18891)	54 (0.10)	225 (0.90)	208
	0.9				$<70\text{ps}^\dagger$
	1.0				$\sim 1^d$
C480 (λ_{ex} =375nm)	0				$\sim 1^c$
	0.1				$<70\text{ps}^\dagger$
	0.2	250 (20873)	45 (0.12)	577 (0.88)	512
	0.3	135 (21106)	60 (0.45)	680 (0.55)	401
	0.4	150 (21207)	50 (0.40)	535 (0.60)	341
	0.5	134 (21254)	67 (0.24)	392 (0.76)	314
	0.6	155 (21380)	54 (0.15)	272 (0.85)	239
	0.7	130 (21620)	-	241 (1.0)	241
	0.8	150 (21590)	76 (0.29)	306 (0.71)	239
	0.9				$<70\text{ps}^\dagger$
	1.0				$\sim 1^d$
C343 (λ_{ex} =405nm)	0				$\sim 1^c$
	0.1				$<70\text{ps}^\dagger$
	0.2	56 (20722)	226 (0.76)	3951 (0.24)	1120
	0.3	156 (20479)	208 (0.50)	9968 (0.50)	5088
	0.4	75 (20486)	571 (0.20)	21501 (0.80)	17315
	0.5	105 (20618)	505 (0.66)	6654 (0.34)	2595
	0.6	148 (20558)	107 (0.56)	11272 (0.44)	5019
	0.7	109 (20530)	779 (0.32)	16582 (0.68)	11525
	0.8	127 (20487)	934 (0.10)	36570 (0.90)	33006
	0.9				$<70\text{ps}^\dagger$
	1.0				$\sim 1^d$

^a $\pm 15 \text{ cm}^{-1}$, ^b $\pm 10\%$, ^cRef. 145, ^dRef. 130, [†]below our IRF.

ACN and WT both are known as fast solvent. Average solvation times in these two solvents are extraordinarily fast (~ 1 ps).¹²⁹⁻¹³¹ The observation of an ultraslow component in ACN-WT mixture is indeed a striking feature. C343 is hydrogen bond donor as well as acceptor, which can easily accept hydrogen bonds from water molecules and donates to the ACN molecules (Scheme. 4.1). Therefore more number of hydrogen bonds is required to be ruptured to solvate C343 that slows down the overall dynamics. In the case of C153 and C480, being hydrogen bond acceptor only, a lesser number of hydrogen bonds are involved during solvation, and hence, solvated at a faster rate. By virtue of simultaneous hydrogen bond donating and accepting ability, C343 creates more inhomogeneous environment by holding both the solvents (ACN and Water) in its first solvation shell. This is in contrast to the other two dyes, they can only form hydrogen bonds with the water molecules. Hence, the first solvation shells of C153 and C480 are dominated with water molecules only, giving a relatively faster solvation dynamics as compared to C343 (Table 4.2).

To gain further inside into the unnatural slow solvation component of C343, we studied the time evolution of the full width of half maximum (FWHM) of TRES (Γ curve) in ACN-WT mixtures (Figure 4.3). Narrowing of the spectral width of TRES with time is a clear indication of translational movement of the excited dipole from an inhomogeneous environment to a relatively homogeneous environment.¹⁶²⁻¹⁶³ Ground state of a dye molecule is less polar, therefore it can easily spread out over the entire polarity regions within the solvent mixture. Once the dye molecules are excited, electron gets into the highly polar π^* orbital that causes either the translational diffusion of the excited dipole itself toward the more polar environment or excited dipole attracts the polar solvent molecules into its first solvation shell. One can quantify translational diffusion using an exponential fitting function to fit the Γ curve.¹⁶³ We compared the fitted values of the Γ curves for all the three coumarin dyes at different ACN concentrations corresponding to their solvation times (Table 4.3).

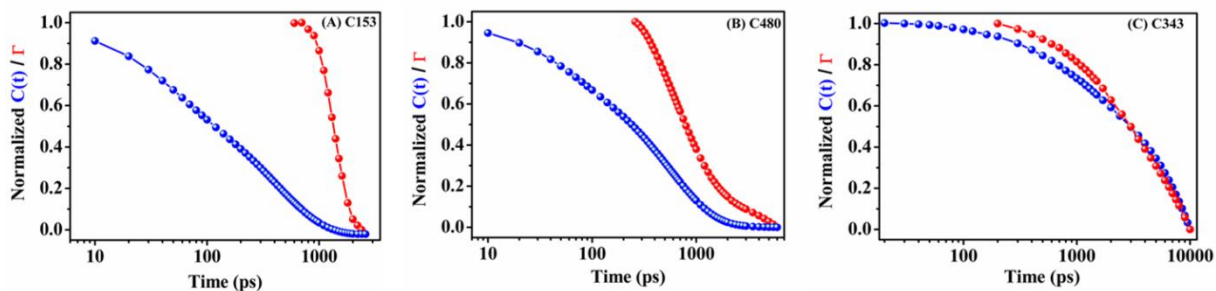


Figure 4.3. Comparison of the decay curve of solvent correlation function $C(t)$ with time evolution of fwhm of TRES (Γ curve) in ACN-WT mixture for (A) C153 at $X_{ACN}=0.5$, (B) C480 at $X_{ACN}=0.2$ and (C) C343 at $X_{ACN}=0.8$. For better comparison, we normalised the Γ curve [$\Gamma(t) = \frac{fwhm(t) - fwhm(\infty)}{fwhm(0) - fwhm(\infty)}$] in a similar manner of normalising $C(t)$ [$= (v_t - v_\infty) / (v_0 - v_\infty)$] curve. Good correlation between long components of Γ curve and $C(t)$ curve was found only in the case of C343, indicating a diffusion assisted solvation kinetics for this dye.

Table 4.3. Comparison of the long component obtained from the solvent correlation function i.e. $C(t)$ and that from the decay of FWHM of TRES i.e. Γ in case of C343 in some of the ACN-WT mixtures.

Mixture Composition	τ_{long} (ps) obtained from	
	Longer decay component of $C(t)$	Longer decay component of Γ curve
$X_{ACN}= 0.6$	11272	11100
$X_{ACN}= 0.7$	16582	16900
$X_{ACN}= 0.8$	36570	36980

However, we found only C343 shows a nice correlation of the longer solvation components with the diffusion times as obtained from the exponential fittings of the Γ curves at all compositions (Table 4.3, Figure 4.3). For example, at $X_{ACN} = 0.8$, the slower component of solvation dynamics of C343 is $\sim 36,570$ ps, which is in good agreement with the excited state translational diffusion time ($\sim 36,980$ ps) of this dye. Therefore remarkably slow solvation

dynamics of C343 in ACN-WT mixture is likely to be a reflection of the following two processes occurring simultaneously; a diffusion assisted solvation process and a significant involvement of specific solvation as discussed earlier. However, the origin of relatively fast kinetics of the other two dyes (C153 and C480) can be well explained by assuming a nearly homogeneous environment of the first solvation shells of these two dyes by forming hydrogen bond with WT molecules only.

4.2.1.3. Time Resolved Fluorescence Anisotropy Study

Time resolved fluorescence anisotropy of all the three coumarin dyes were studied in the ACN-WT binary mixture across the entire concentration region. The details of this technique are provided in the chapter 2. The rotational depolarisation times (τ_{rot}) of all the coumarin dyes are tabulated in Table 4.4. We employed Stokes-Einstein-Debye (SED) theory for the rational understanding of dye-to-solvent interactions within the binary mixtures. The τ_{rot} may be correlated with the shape factor (f), coupling parameter (C_{rot} , $0 < C_{rot} < 1$), medium viscosity (η), hydrodynamics volume (V) using the following relation,^{[9-10], [50-51]}

$$\tau_{rot} = \frac{\eta V}{kT} f C_{rot} \dots \dots \dots (4.3)$$

The above equation can be employed within the framework of stick ($C_{rot}=1$) and slip ($C_{rot}=0$) boundary conditions. Stick boundary assumes a bigger size of the solute molecules compared to the solvent molecules and gives a maximum solute-to-solvent interaction. This is in contrast to the slip boundary, where no theoretical interactions between solvent and solute are actually occurred. f , V , C_{slip} , and C_{stick} values of coumarin dyes were obtained from the literatures.^{66, 138} In Figure 4.4, we compared the average rotational diffusion times of C480 and C343 as a function of viscosity of the medium with the slip and stick boundary lines. C153 shows almost similar trend with C480, we have not included C153 data in the figure for

better clarity. In all the cases the C values obtained from the different coumarin dyes in different compositions appear at the superstick region ($C_{rot}>1$, Table 4.4), indicating an unusual solvent to solute coupling.

Table 4.4. Fitting parameters of time resolved fluorescence anisotropy decays of coumarin dyes in ACN-WT mixtures at different mole fractions of acetonitrile (X_{ACN}).

Probe	X_{ACN}	r_0	τ_{rot}^a	$\frac{\tau_{rot}}{\eta}$	C_{rot}
C153 ($\lambda_{ex}=405nm$)	0.1	0.25	120	133	1.32
	0.2	0.25	118	128	1.28
	0.3	0.24	109	145	1.45
	0.4	0.22	101	155	1.55
	0.5	0.23	97	176	1.76
	0.6	0.24	87	174	1.74
	0.7	0.22	81	184	1.84
	0.8	0.20	72	189	1.89
	0.9	0.19	69	191	1.91
	1.0	0.20	63	175	1.75
C480 ($\lambda_{ex}=375nm$)	0	0.28	110	123	1.22
	0.1	0.25	108	113	1.13
	0.2	0.26	105	114	1.15
	0.3	0.25	113	150	1.51
	0.4	0.26	110	169	1.70
	0.5	0.22	95	172	1.73
	0.6	0.21	90	180	1.81
	0.7	0.19	76	172	1.73
	0.8	0.20	75	197	1.97
	0.9	0.21	71	196	1.96
1.0	0.21	65	180	1.80	
C343 ($\lambda_{ex}=405nm$)	0	0.29	139	154	1.32
	0.1	0.24	145	152	1.31
	0.2	0.25	158	171	1.46
	0.3	0.22	121	161	1.37
	0.4	0.20	135	207	1.76
	0.5	0.24	119	216	1.84
	0.6	0.21	104	208	1.76
	0.7	0.19	92	209	1.77
	0.8	0.18	78	206	1.75
	0.9	0.19	77	211	1.79
1.0	0.20	75	208	1.76	

^a $\pm 10\%$

Interestingly, in all compositions, C343 shows a higher C_{rot} compared to the other two dyes, which is a clear indication of a better interaction between C343 and solvent molecules through hydrogen bond formations as compared to the other dyes. Similar trend was found when we plotted viscosity normalised average rotational time (τ_{rot}/η) of all the three coumarin dyes as a function of ACN concentration within the mixtures (Figure 4.4). C_{rot} of C343 always appears at the higher value in contrast to the other two dyes, due to a more interaction of C343 with solvent molecules. Strong solute-solvent interaction makes the solvent rearrangement around the excited C343 dipole sluggish, which may be the reason for remarkable slowing down of solvation time of C343 as compared to the other dyes in any composition of ACN-WT mixture.

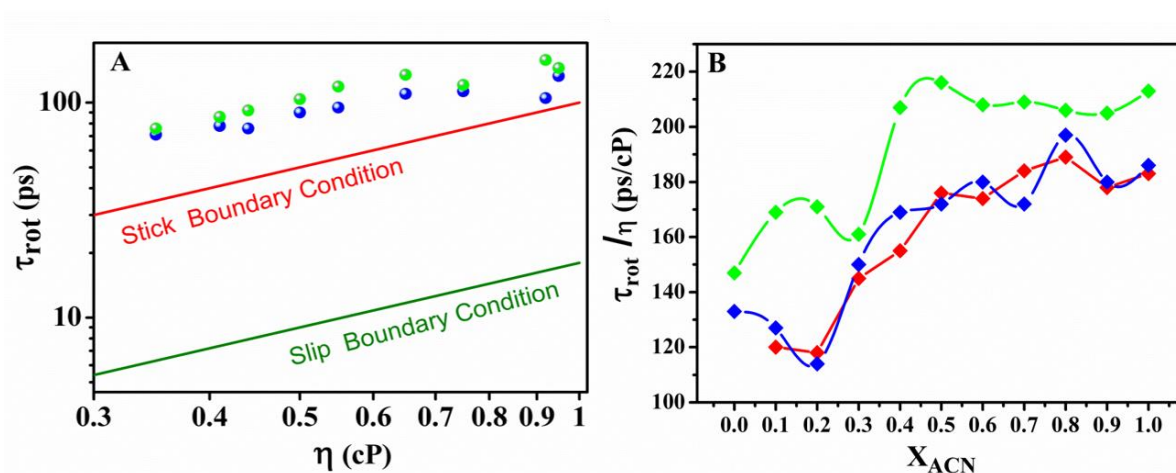


Figure 4.4. (A) log-log plot of rotational relaxation time (τ_{rot}) of C480 (blue) and C343 (green) in ACN-WT binary mixture as a function of medium viscosity within slip and stick boundary condition. C153 exhibited same trend as C480 and hence not shown for clarity. (B) Plot of viscosity normalized rotational time (τ_{rot}/η) of C153 (red), C480 (blue) and C343 (green) as a function of X_{ACN} within the binary mixture.

4.2.2. Nonexponential relaxation of C343: Powerlaw dependence and Simultaneous Stabilization of two forms in the binary mixture

We found nonexponential nature of solvation dynamics for *C343* in *ACN-WT* mixture which unambiguously confirms the inhomogeneous nature of the medium.⁵¹ A power law fitting is much more comprehensive compared to a stretch exponential fitting for a diffusion assisted process like solvation dynamics.¹⁶⁴⁻¹⁷² Power law fitting has been successfully applied in many inhomogeneous systems like protein, DNA, and in other bio-macro molecular assemblies.¹⁶⁴⁻¹⁷¹ Berg and his co-workers observed power law dependency in solvation dynamics from the interior of DNA; a native base pair of DNA was replaced by coumarin 102.¹⁶⁷ Their power law fitting enabled them to observe a ~5 ps time component due to the rapid component of “fraying” when they placed the reporter dye molecule near the end of the oligonucleotide.^{165,167} Recently Fayer and his co-workers have shown proton transfers of a fluorescent photoacid *8-hydroxypyrene-1,3,6-trisulfonate (HPTS)*, inside an ionic reverse micelle (*Aerosol OT*) and within the bulk water follow a power law kinetics.¹⁷² However they observed power law exponent is twice bigger in magnitude in the bulk water (~-1.1) as compared to that (~-0.55) observed inside an ionic reverse micelle.¹⁷² In bulk water the power law $t^{-1.1}$ is assigned to a diffusion controlled recombination process and well correlated with the theoretically predicted power law of $t^{-1.5}$. In our study, using a power law fitting to the $C(t)$ obtained from the reporter dye *C343* is well justified not only due to solvation in binary mixture is a diffusion controlled process, also the dissociated form of *C343* is negatively charged and this electric field in addition to the inhomogeneous nature of the *ACN-WT* mixture can essentially mimic the DNA interior solvation, where power law kinetics is evident.¹⁶⁹ Following power law fitting equation was used for the fitting of solvent correlation function obtained from *C343*.¹⁶⁸

$$S_t = S_\infty \left[1 - \left(1 + \frac{t}{t_0} \right)^{-n} (a_1 e^{-t/\tau_1} + a_2 e^{-t/\tau_2}) \right] \dots\dots\dots(4.4)$$

Where t_0 is the cut off time, S_∞ is the total Stokes shift (obtained by extrapolating the fitting curve), n is the power law exponent and other parameters have their usual meanings.¹⁶⁸ Due to the non-converging nature of $C(t)$ even in the time window extended up to ~ 3 times longer than the lifetime (~ 3.6 ns) of the *C343*, has restricted us from observing the dynamics at longer time (>10 ns) with an appropriate reliability. Conversely, shorter time dynamics is also truncated by the limited time resolution of our TCSPC setup which allows reliable data measurement only after ~ 30 ps time at the shorter end. Therefore, we fitted from 30 ps to 10 ns window to our experimentally observed Stokes shift of *C343* using the power law equation which enabled a comprehensive fitting (Figure 4.5).

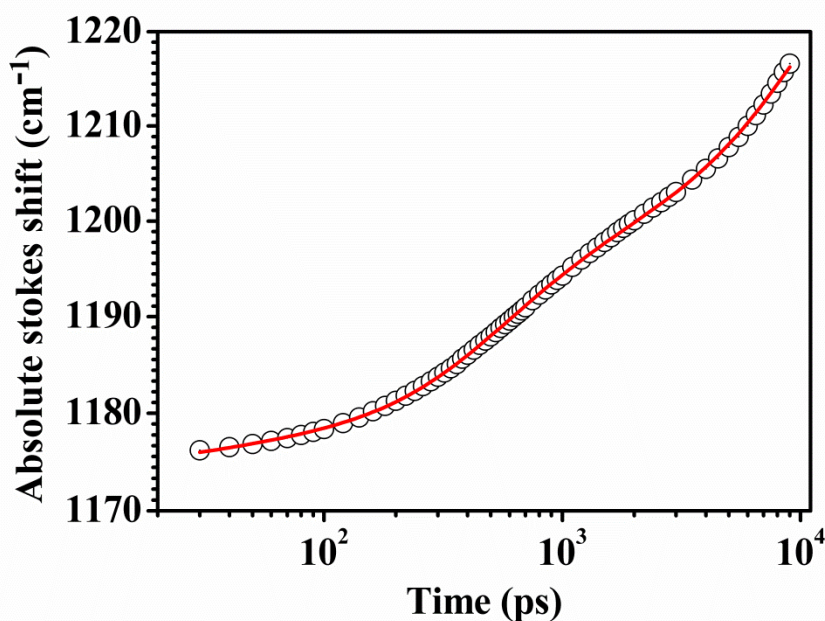


Figure 4.5. Powerlaw fitting to the Stokes Shift data for *C343* in equimolar ACN-WT mixture.

The numeric values of the parameters (of power law fitting of *C343* data) are found to be $t_0=65$ ps, $n=0.45$, $S_\infty=1798$ cm⁻¹, $\tau_1=170$ ps and $\tau_2=6430$ ps, respectively.

Interestingly, the solvation dynamics of the other two dyes *DCM* and *4-AP* did not show any discernible power law dependency and conclusively fitted by a biexponential fitting function. A number of theoretical studies have predicted an exponential value of ~ 1.5 in power law fitting of proton transfer/recombination reaction where three dimensional diffusion of proton and deprotonated forms of the photoacid are involved.¹⁷³⁻¹⁷⁵ In these studies, deprotonated forms of photoacid and protons are assumed to be spherical in shape and their charges are accumulated at the centre of the sphere. On collision between these two spheres, proton recombination takes place. Entire process here is diffusion controlled and a three dimensional diffusion leads to power law behaviour with an exponent of ~ 1.5 .¹⁷² In an experimental work by Huppert and his co-workers have shown the geminate recombination of dynamics of deprotonated form of a wild-type green fluorescent protein in water follows a power law kinetic at longer time of about $t^{-3/2}$.¹⁷⁵ The exponent of $3/2$, representing to a random three dimensional diffusion assisted process, obtained from equal contributions ($1/2$) from each dimensions.¹⁷⁵ In our case also, the exponent value of ~ 0.45 certainly representing a modified or rather restricted diffusion process closely associated to the solvation process of *C343* in *ACN-WT* mixture. Interestingly the power law exponent value 0.45 in our study is close to $1/2$, the exponential contribution from one dimensional diffusion. Therefore, it may be possible that the excited state *C343* dipole diffuses through a one dimensional highly polar micro-channel inside the *ACN-WT* mixture during solvation. This is only possible if different micro-regions with varying polarities are present within the *ACN-WT* mixture and they are delineated in one dimensional array. *C343* being the most hydrophilic dye would prefer to diffuse through the most polar micro-channels only. Among the other possibilities of origin of power law kinetics in solvation dynamics of *C343* in *ACN-WT* mixture can be due to a

geminate recombination process. For *HPTS* molecule, the geminate recombination between *PTS*⁻ and *H*⁺ is well explained by using a power law fitting model and this is already reported in several literatures.¹⁷² Similarly *C343*, bearing *-COOH* group, is also acidic in nature (pKa~ 4.65)¹⁷⁶ and one can expect an excited state recombination process between deprotonated form of *C343* (bearing *-COO*⁻) and *H*⁺. The power law kinetics in our study can also be a reflection for this recombination process. The exponent value of ~0.45 indicating recombination is highly controlled by a one dimensional diffusion of the ion pair, which is obvious, as collision of *H*⁺ only to a specific face of *C343* (bearing *-COO*⁻) would yield the protonated form of *C343*. If recombination causes a power law behaviour, one can expect to see an equilibrium between neutral and deprotonated forms of *C343* in excited state within the *ACN-WT* mixture. An in depth analysis of time resolved area normalized emission spectra (*TRANES*) unambiguously confirms the emission of *C343* consists of emissions from two species (equilibrated through an isoemissive point), arguably from neutral and deprotonated forms of *C343* (Figure 4.6).

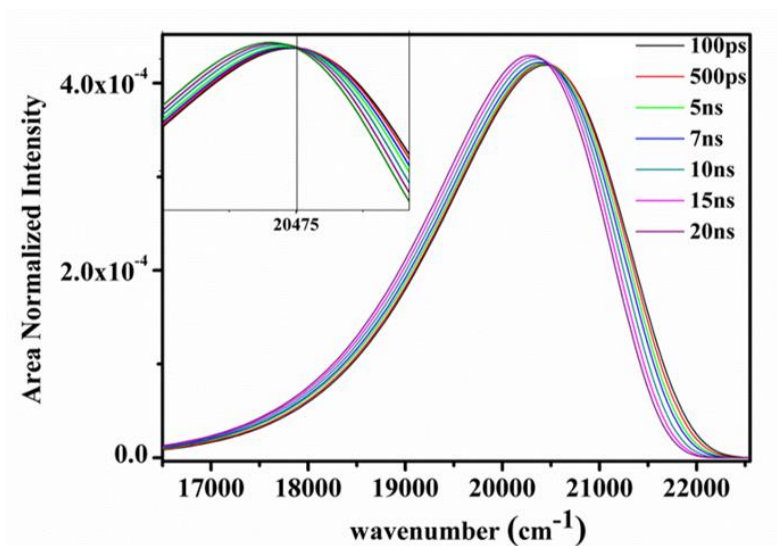


Figure 4.6. Time resolved area normalized emission spectra (*TRANES*) of *C343* in *ACN-WT* ($X_{WT} \sim 0.5$) binary mixture. An isoemissive point at 20475 cm^{-1} is clearly visible as shown in the inset of the figure.

TRANES are the area normalised *TRES*. Periasamy and his co-workers demonstrated the existence of an isoemissive point in *TRANES* is an indication that the observed emission is due to two species, no matter of their origins or dynamics involved to it.¹⁷⁷ Existence of similar isoemissive point in *TRANES* has also been reported within the inhomogeneous lipid bilayer by the same group.¹⁷⁸ Congruent to our present study, existence of an equilibrium between neutral and basic forms of *C343* ($pK_a=4.65$)¹⁷⁶ within the silver nanoparticle containing sodium dioctylsulfosuccinate reverse micelle by *TRANES* study has been reported recently by Sahu and his co-workers.¹⁷⁶ Therefore the power law behaviour of dipole solvation of *C343* is may be due to a strong coupling of the recombination process with the solvent reorganisation process within the *ACN-WT* mixture.

4.2.3. Fluorescence correlation spectroscopy (FCS) study of translational diffusion

We substantiated the fact of coexisting of different polarity regions within *ACN-WT* mixture from the study of translational diffusion coefficient of the dye molecules within this solvent mixture using *FCS* study. The details of the method have been given in chapter 2. It is worth mentioning in this context that Bhattacharyya and coworkers measured the diffusion coefficient of several coumarin dyes in DMSO-GLY binary mixture. They have found a bimodal distribution of diffusion coefficients and concluded that there exist two distinct types of environment are present. We have measured the translational diffusion coefficient (D_t) of two dyes; first one is highly hydrophobic dye *DCM* and second one is highly hydrophilic dye *R6G*, dissolved in *ACN-WT* mixture and diffusion constants were measured in two different sets of experiments. We collected a large number of D_t values from each dye molecule within the *ACN-WT* mixture by moving the microscope objective at least 5-10 μm between the two points of measurement. Eventually a statistical histogram was constructed with D_t values in the X-axis and corresponding numbers of molecules in the Y-axis (Figure 4.7). The autocorrelation curves in every case in this study were convincingly fitted with one

D_t component. However, unlike neat solvents (with a single D_t value irrespective of different X-Y-Z positions), a broad distribution was observed among the D_t values from a single dye molecule within the ACN-WT mixture (Figures 4.7.A and 4.7.C). Within the neat cosolvents (ACN or WT), the statistical distribution of D_t values from a single dye molecule was found to be extremely narrow (Figures 4.7.B and 4.7.D). For an instance, D_t values of DCM in ACN-WT mixture are scattered in a wide window from 50 $\mu\text{m}^2/\text{s}$ to 625 $\mu\text{m}^2/\text{s}$ with a peak at 285 $\mu\text{m}^2/\text{s}$ within the histogram (Figure 4.7.A). However within neat ACN, the D_t values of DCM from different locations are found to be same ($970 \pm 50 \mu\text{m}^2/\text{s}$) within the experimental error range (Figure 4.7.B). A similar broad distribution of D_t values from R6G was also observed in ACN-WT mixture (Figure 4.7.C). However, within neat water, diffusion of R6G is well characterized by a fixed diffusion time irrespective of the different positions of measurements.

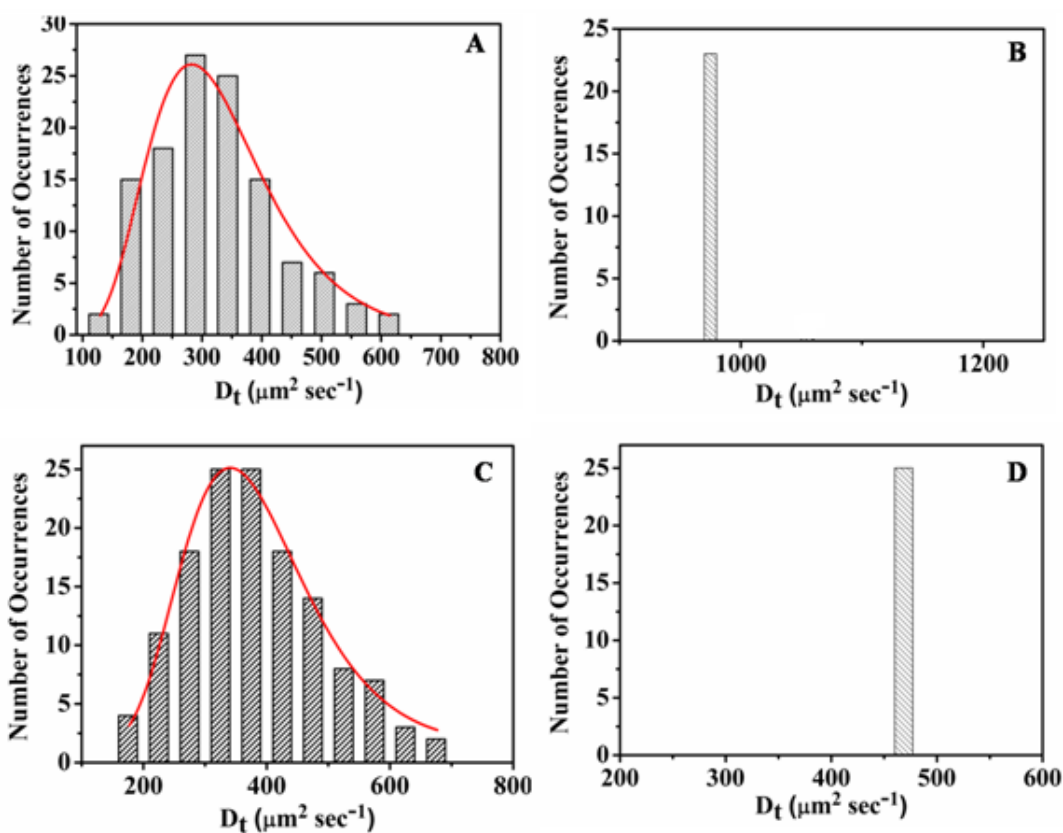


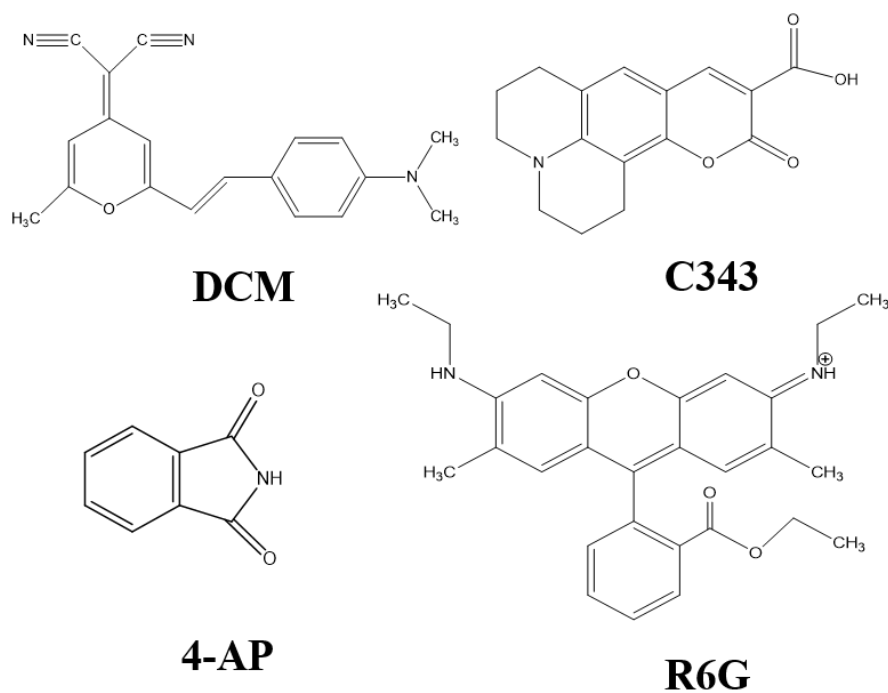
Figure 4.7. Distributions of diffusion coefficients as obtained from FCS measurements for (A) *DCM* in *ACN-WT* ($X_{WT} = 0.51$) binary mixture; (B) *DCM* in neat *ACN*; (C) *R6G* in *ACN-WT* ($X_{WT} = 0.51$) binary mixture and (D) *R6G* in neat *WT*.

A broad distribution of D_t values of a dye molecule in *ACN-WT* mixture is a clear signature of the presence of intrinsic inhomogeneity. The mobility inside the individual micro-domains is significantly different which has been reflected by the broad distribution among the D_t values obtained from the different locations within the mixture which is absent in neat solvents.

4.2.4. Synergistic Solvation behaviour in *ACN-WT* Binary Mixture

We employed *4-aminophthalimide* (*4-AP*) and *coumarin 343* (*C343*) dyes for steady-state measurements. Spectral properties of *4-AP* and *C343* are highly sensitive to the hydrogen bond parameters and the polarity of the medium.⁵⁵⁻¹⁷⁹ Using a regression fitting of *Kamlet-Taft* parameters, Bhattacharyya and his co-workers have shown the hydrogen bond acidity parameter (α) along with hydrogen bond basicity parameter (β) of the *DMSO-WT* binary mixture constitutes a total $\sim 62\%$ contribution for the ground state *4-AP*, which is much higher as compared to the contribution ($\sim 38\%$) earned from the polarity parameter (π^*) only.⁵⁵ Most interestingly they observed nearly 5 folds jump of α value in the excited state *4-AP* which they explained due to a much stronger hydrogen bond formation of amino and imino protons (of *4-AP*) with the solvent molecules. However the coumarin dye displayed just an opposite result to the *4-AP*, with a more contribution of polarity parameter (π^*) over the hydrogen bond parameters ($\alpha&\beta$).⁵⁵ Therefore in this study we used *4-AP* and *C343* for an in-depth investigation on the origins of inhomogeneity in *ACN-WT* binary mixture which are relevant to the polarity as well as to hydrogen bond formation abilities of the medium. Apart from these two dyes, we also studied steady state spectral properties of an extremely

hydrophobic dye 4-(dicyanomethylene)-2-methyl-6-(4-dimethylaminostyryl)-4H-pyran (*DCM*) and an extremely hydrophilic dye *rhodamine 6G* (*R6G*) for their very high (~ 20.7 D) and very low (~ 1.85 D) values of transition dipole moment change ($\Delta\mu_{g-e}$) upon photo excitation (Table 4.5). This will help us further to study the effect of transition dipole moment change of the dye molecule on apparent inhomogeneity of this binary mixture. A high $\Delta\mu_{g-e}$ value of *DCM* is likely to perturb the solvent clusters greatly in the excited state while *R6G* (with lower $\Delta\mu_{g-e}$ value) would cause the minimum damages to the solvent clusters around the excited *R6G* dipole. Steady state absorption spectra, emission spectra and molar transition energies of the dye molecules in *DMSO-WT* mixture as a function of *WT* concentration are depicted in Figures 1-4. A common feature we observed from the “absorption peak wavelength vs. *WT* concentration” curves from all the dye molecules is the presence of *synergistic* solvated states at one or more compositions within the binary mixture where absorption energy is found to be much lower compared to that obtained either in neat *ACN* or in neat *WT*. The variation of absorption or emission peak maxima with composition in a binary mixture generally represented as a function of “Onsager reaction field function” from which the quantitative idea about dielectric enrichment around a solute dipole can be achieved. However in *ACN-WT* binary mixture the calculated “Onsager reaction field function” $F(\epsilon)$ shows a linear dependence with mole fraction of water.



Scheme 4.3. Chemical structure of the dyes used for synergism analysis

Table 4.5. Ground (μ_g) and excited state (μ_e) dipole moments and their differences ($\Delta\mu_{g-e}$) for the dye molecules used in this study.¹⁷⁹⁻¹⁸²

Dye molecule	μ_g (D)	μ_e (D)	$\Delta\mu_{g-e}$ (D)
DCM	5.6	26.3	20.7
4-AP	5.0	10.6	5.6
C343	9.8	12.7	2.9
R6G	11.7 ^a		1.85

^a Obtained from *DFT* [B3LYP/6-31G+ (d,p)] calculations.

A term called molar electronic energy E_T ($=28591/\lambda_{\max}$ kcal mole⁻¹), inversely proportional to the absorption maximum (λ_{\max}) of the dye molecule, whose value provides the extent of ground state stabilization of a dye molecule in a quantitative sense.^{49,183} Extra ground state stabilization due to solvent-solvent interactions or cluster formations (“*synergistic effect*”) within a binary mixture can be well understood when E_T values within a solvent mixture

(experimentally determined red curve in Figures 4.8.C-4.11.C) are compared with the E_T values predicted from the linear combinations (mole fraction weighted average, blue lines in Figures 4.8.C-4.11.C) of the E_T values within the constituent cosolvents. Any diminishing of observed E_T values from their predicted values is a clear signature of extra stabilization of the ground state energy of the solute dipole due to the *synergistic effects* (i.e., efficient solvent-solvent interactions or hydrogen bond formations).⁴⁹ For all the dyes we used here show a significant amount of ground state stabilization across the entire concentration range of *WT*. A maximum stabilization occurs between 40-80 mole percent of *WT* for most of the dyes. The highest ground state stabilization due to *synergism* of *ACN-WT* binary solvent is observed to be maximum ($\Delta E_T^{max} \sim 1.73$ Kcal/mole at $X_{WT} \sim 0.7$) for *DCM*, and minimum ($\Delta E_T^{max} \sim 0.15$ Kcal/mole at $X_{WT} \sim 0.8$) for *R6G*, respectively. *DCM*, with a lower ground state dipole moment (~ 5.6 D), retains the local solvent structures majorly intact. Here formation of highly interacting and unperturbed hydrogen bonded clusters turns binary mixture to a much better solvating agent as compared to the any of its cosolvents. *R6G* in contrast to *DCM*, exerts a huge local electric field to the nearby solvent structures due to its high ground state dipole moment (~ 11.7 D) that probably ruptures the solvent structures around it. This may cause an inefficient stabilization to the ground state *R6G* by the broken hydrogen bonded clusters. It may be noteworthy that *4-AP*, even with a lesser ground state dipole moment ($\mu_{4-AP} \sim 5$ D) compared to the *DCM* ($\mu_{DCM} \sim 5.6$ D), receives a relatively weaker *synergism* ($\Delta E_T^{max} \sim 1.15$ Kcal/mole at $X_{WT} \sim 0.7$) as compared to *DCM* ($\Delta E_T^{max} \sim 1.73$ Kcal/mole at $X_{WT} \sim 0.7$). This is likely due to the higher affinity of *4-AP* toward hydrogen bond formation that makes ground state stabilization of *4-AP* more amenable to the specific solvation rather than a *synergistic* solvation.⁵⁵ The ground state stabilization of *4-AP* in *ACN-WT* is performed by the specific hydrogen bond interactions between the *4-AP* and *WT* molecules from partially broken solvent clusters rather than interacting with *ACN-WT* cluster as a whole, as in

the case of ground state solvation of *DCM*. The solvent clusters within the *ACN-WT* have emerged as a more efficient energy state stabilizer (due to *synergistic effect*) compared to the *WT* alone, the most polar component of the mixture. *Synergistic effects* of the same four dyes are more interesting in their excited states (Figures 4.8.B-4.11.B), as obtained from their emission properties. From our experimental studies of emission peak shifting of the dye molecules with changing the composition ratio of *ACN-WT* mixtures, we observed a significant loss of *synergism* for *DCM* (throughout the entire composition ratios) and a little or almost no change of *synergism* for the other three dyes when compared to their corresponding ground state *synergism* at same composition ratios (compare between Figures 4.8.A & 4.8.B; 4.9.A & 4.9.B; 4.10.A & 4.10.B and 4.11.A & 4.11.B). A remarkable loss of *synergism* in the excited state of *DCM* is elucidated by a significantly higher value of dipole moment change ($\Delta\mu_{g-e} \sim 20.7$ D) due to the photo-excitation, which destroys the solvent clusters around the excited dipole.⁴⁹ *C343* and *R6G* show a mild change of dipole moment upon photo-excitation ($\Delta\mu_{g-e} \sim 2.9$ D and ~ 1.85 D). This causes the preservation of ground state solvent structures in the excited state and therefore, no significant change in *synergistic effect* is observed upon photo excitation of these dye molecules within the binary mixture. For *4-AP*, although the $\Delta\mu_{g-e}$ is quite high (~ 5.6 D), nevertheless it hardly shows any loss of *synergism* in the excited state. This is may be due to its higher affinity towards hydrogen bond formations and this affinity is even more within the excited state of *4-AP* (as discussed earlier). Therefore, both the ground state and excited state of *4-AP* in *ACN-WT* are stabilized specifically by hydrogen bond formation with *WT* molecules only, rather than a *synergistic* stabilization by the interacting solvent clusters. This is may be the reason for not observing any loss of synergism of *4-AP* in *ACN-WT* mixture upon photo-excitation. Rupturing of solvent structures in the excited state (due to a moderately higher value of $\Delta\mu_{g-e}$) would not

make much difference to the excited state stabilization of *4-AP* from the ground state stabilization, as in both the cases *WT* molecules only stabilize the dipoles.

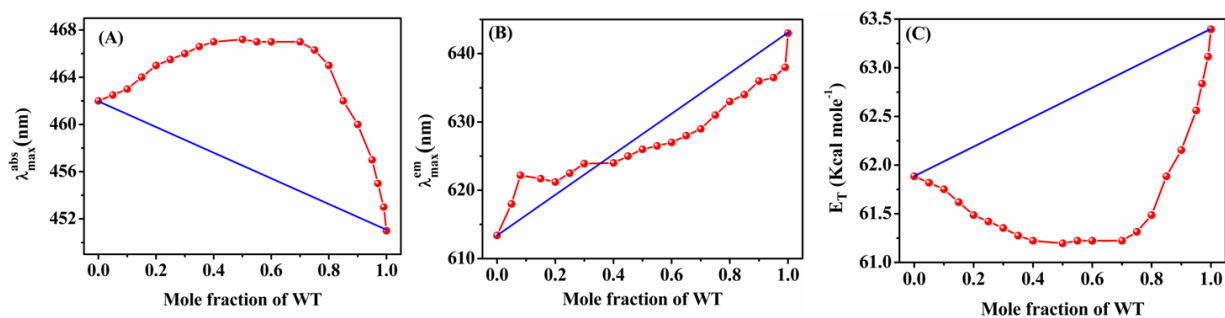


Figure 4.8. Plots of (A) absorption maxima, (B) emission maxima and (C) molar electronic transition energy of *DCM* in *ACN-WT* binary mixture as a function of mole fraction of water.

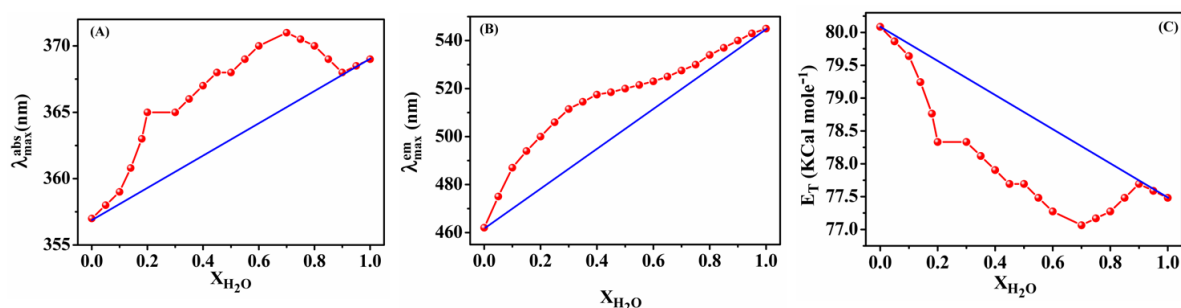


Figure 4.9. Plots of (A) absorption maxima, (B) emission maxima and (C) molar electronic transition energy of *4-AP* in *ACN-WT* binary mixture as a function of mole fraction of water.

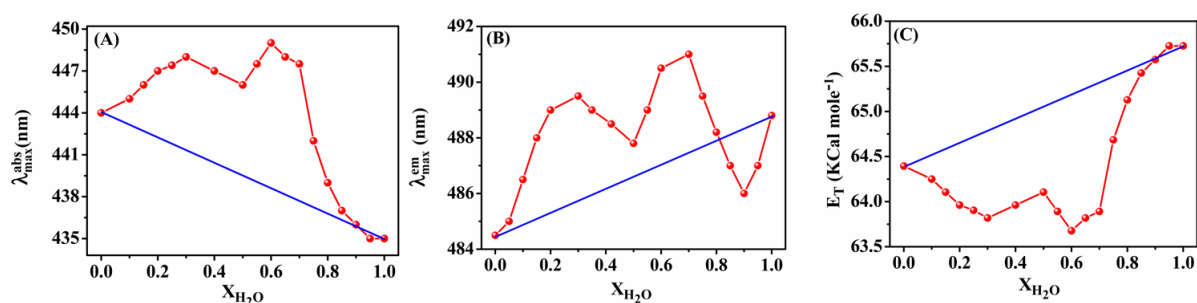


Figure 4.10. Plots of (A) absorption maxima, (B) emission maxima and (C) molar electronic transition energy of *C343* in *ACN-WT* binary mixture as a function of mole fraction of water.

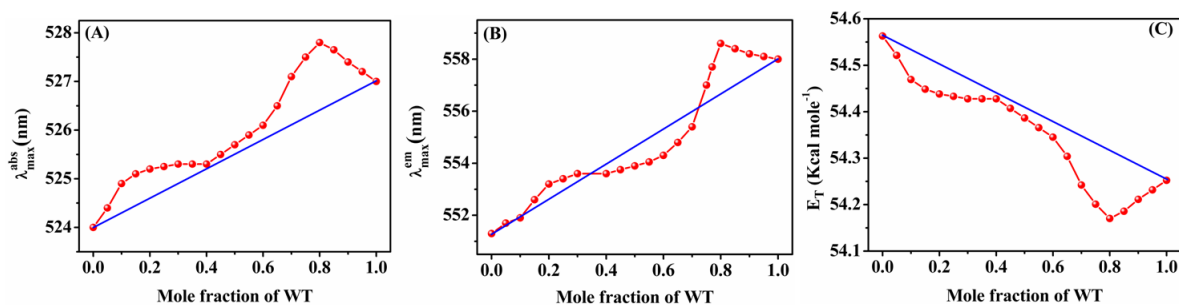


Figure 4.11. Plots of (A) absorption maxima, (B) emission maxima and (C) molar electronic transition energy of *R6G* in *ACN-WT* binary mixture as a function of mole fraction of water.

4.2.5. ^1H NMR study in *ACN-WT* binary mixture

Observing of solvent inhomogeneity using a reporter probe molecule is often refuted by several groups arguing the dye molecule destroys the inherent structures of the solvent clusters; not completely but at least to some extent in most of the cases.¹⁸⁴ We therefore used proton-nuclear-magnetic-resonance (^1H NMR) study for an in-depth analysis of unperturbed heterogeneity of *ACN-WT* mixture. As no external dye is used in NMR study, one can expect that the intrinsic solvent structures of *ACN-WT* can be captured in this study. For NMR study we monitored the observed chemical shift (δ_{obs}) of *C-H* proton of *ACN* as well as *O-H* proton of *WT*; qualitatively both indicated the presence of inter solvent hydrogen bond interactions. Hydrogen bond formation in *ACN-WT* mixture modifies the local electron cloud around the hydrogen bonded *H* atom, which will be reflected by the change of δ_{obs} of the proton of *ACN* and *WT* molecules. The observed chemical shift (δ_{obs}) of *O-H* proton of *WT* exhibited a downfield shift as *WT* content is increased within the *ACN-WT* mixture (Figure 4.12.A). A similar downfield shift (but lower in magnitude) of δ_{obs} of *C-H* proton of *ACN* was also noted in *ACN-WT* mixture as *WT* concentration was increased (Figure 4.12.B); indicating the self aggregated *ACN* molecules (within the *ACN* rich *ACN-WT* mixture) prefer hydrogen bond formation in the presence of *WT* over extending the self aggregations.⁷⁵ The shifting of δ_{obs} of

C-H proton of *ACN* passes through several regimes when plotted against the mole fraction of *ACN* (X_{ACN}); a sharp upfield shift of δ_{obs} was noted with increasing *ACN* concentration at low *ACN* concentration regime ($X_{ACN}<0.2$) which was followed by a plateau in the intermediate concentration regime ($X_{ACN}\sim 0.2-0.7$) and again an upfield shift was observed at higher *ACN* concentration ($X_{ACN}>0.7$) (Figure 9A). In the intermediate concentration regime there is not much change of hydrogen bonded clusters in *ACN-WT* mixture that has probably kept the δ_{obs} value unchanged with the change in composition in this regime (Figure 4.13.A). Interestingly previous reports show the inhomogeneity in *ACN-WT* mixture mostly prevails within this concentration region of *ACN*.^{152, 185-187} Therefore, a stable hydrogen bond network formation in *ACN-WT* binary mixture which remains intact within a broad concentration range of *ACN* ($X_{ACN}\sim 0.2-0.7$) might be the actual reason of the origin of inhomogeneity within this binary mixture.

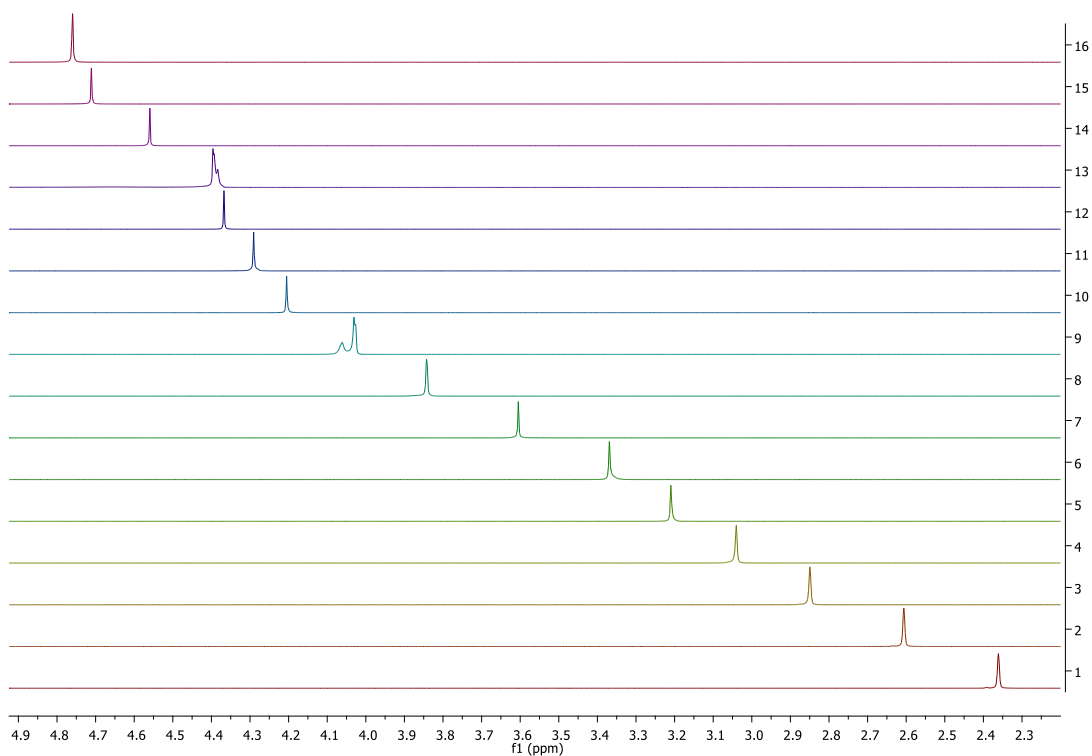
The δ_{obs} of *O-H* proton shows a down field shift with increasing *WT* content within the binary mixture (Figure 4.13.B). As concentration of *ACN* is increased, *WT* molecules start aggregating among themselves to minimize the interaction with *ACN* molecules. This causes the shielding of *O-H* proton of *WT*.⁴⁹ We fitted our experimentally determined “ δ_{obs} of *O-H* proton” as a function of “solvent composition” using a simple model earlier used by Sen and his co-workers.⁴⁹ According to this model the observed chemical shift (δ_{obs}^{O-H}) of *O-H* proton within the binary mixture is the sum of their population weighted chemical shifts due to *WT-WT* hydrogen bond structures (δ_{W-W}) and *ACN-WT* hydrogen bond structure (δ_{A-W}) as,

$$\delta_{obs}^{O-H} = \frac{X_{W-W}^b}{X_W} \delta_{W-W} + \frac{X_{A-W}^b}{X_W} \delta_{A-W} \dots \dots (4.5)$$

Where X_W representing the mole fraction of *WT* present within the binary mixture; out of the total fraction X_W , X_{W-W}^b fraction is bound to the water molecules and X_{A-W}^b fraction is bound to the *ACN* molecules (i.e., $X_W = X_{W-W}^b + X_{A-W}^b$). The δ_{W-W} value can be obtained from the

neat *WT*, where *O-H* protons of *WT* must remain hydrogen bonded to the nearby *WT* molecules. However measuring of δ_{A-W} cannot be obtained from the experiment, which requires performing our experiment at infinitesimally small concentration of *WT* to confirm the *O-H* proton of *WT* is solely hydrogen bonded to *ACN* only. However we can get the value of δ_{A-W} from the fitting of δ_{obs} as a function of *WT* concentration using equation 4.5. Equation 4.5 can be rewritten as,

$$\delta_{obs}^{O-H} = \delta_{A-W} + \frac{X_{W-W}^b}{X_W} (\delta_{W-W} - \delta_{A-W}) \dots \dots \dots (4.6)$$



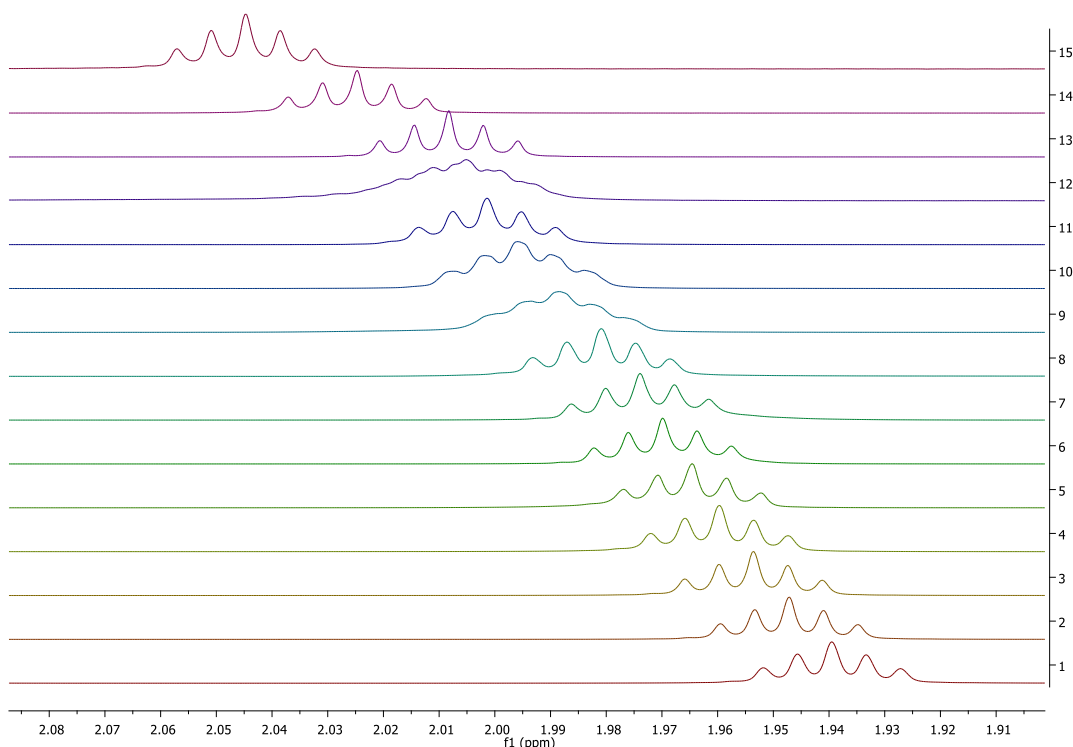


Figure 4.12. (A) Chemical shift data for the O-H proton of water in the binary mixture at different compositions and (B) Chemical shift data for the C-H proton of acetonitrile in the binary mixture at different compositions.

The parameters X_{W-W}^b / X_W in the above equation can be replaced by a following function

$$\frac{X_{W-W}^b}{X_W} = \frac{(-a_1 e^{(-b_1 X_W)} - a_2 e^{(-b_2 X_W)} + a_1 + a_2)}{(-a_1 e^{(-b_1)} - a_2 e^{(-b_2)} + a_1 + a_2)} \dots\dots\dots(4.7)$$

From the fitting of δ_{obs}^{OH} as a function of WT , using equation 4.6 and 4.7 provided the numeric solutions of the unknown parameters δ_{A-W} , a_1 , a_2 , b_1 and b_2 , respectively. Using these values of the parameters and equation 4.7 we can quantitatively measure the fraction of WT bound (X_{W-W}^b) among themselves out of a total X_W fraction of WT within the binary mixture. Knowing the values of X_W and X_{W-W}^b we can easily determine the fraction of WT molecules bind to ACN molecules as well using the relation $X_W = X_{W-W}^b + X_{A-W}^b$. Figure 4.13.C shows the plot of X_{A-W}^b as a function of mole fraction of WT concentration within the

binary mixture. Interestingly this plot clearly indicates the formation of maximum hydrogen bonded structures (i.e., maximum value of X_{A-W}^b) between the two cosolvents are observed at $X_{WT}=0.53$. Notably, either in a very high WT content or in a low WT content $ACN-WT$ mixture, the populations of hydrogen bonded structures (between the cosolvents) are significantly low. This fact is nicely correlating with the observation of composition dependent solvation dynamics study with three coumarin dyes, where we observed a fast solvation dynamics from the low and high WT content samples and slow solvation time from the intermediate WT concentration samples. The slow solvation dynamics of $ACN-WT$ mixture within the intermediate concentration regime of WT is truly due to the hydrogen bonded structures formation among the cosolvents. Extent of hydrogen bond formation or maximum interactions among the cosolvents is found to be maximum at $X_{WT}=0.53$. Therefore, all steady states and dynamics we studied here in nearly equimolar concentration ($X_{WT}=0.51$) of $ACN-WT$ mixture provided us the solvent properties of this mixture when possessing a maximum interactions among the cosolvents.

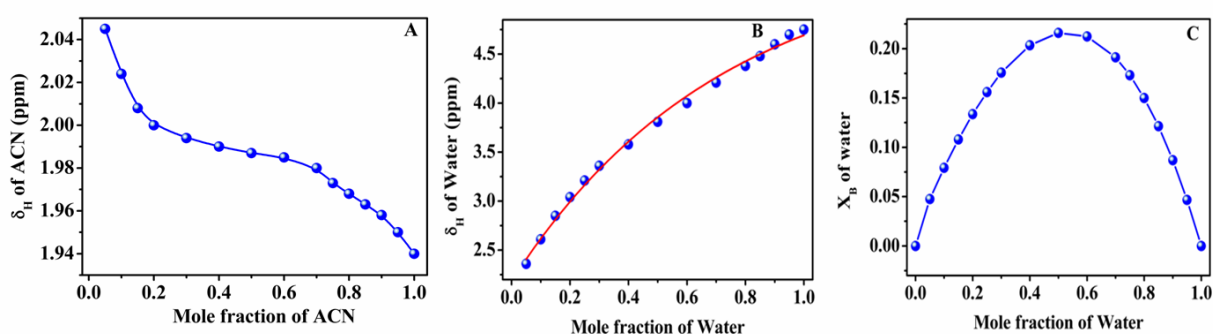


Figure 4.13. Observed chemical shifts of $C-H$ proton of ACN (A) and $O-H$ proton of water (B) as a function of composition ratio in $ACN-WT$ mixture. The red line in figure B represents the best fitting using Eqs 4.6 and 5.7. (C) Plot of fraction of water bound to acetonitrile as a function of water mole fraction within the binary mixture.

4.3. Conclusion

In summary, all these studies presented in this chapter reveal that, at very low ACN concentration ($X_{ACN} < 0.15$), ACN molecules are absorbed within the cavities of the water structures that retains the water clusters close to the neat water. In this region solvation dynamics are facilitated by the water molecules only that justify our observation of the fast solvation time (< 70 ps) from all the three dyes within this region. At a higher concentration, ($X_{ACN} \sim 0.15-0.85$) a large population of ACN molecules do not get enough room within the cavities to get adsorbed; rather they can be absorbed through the formation of hydrogen bond rich structures. Microheterogeneity is dominated in this region. This heterogeneity causes a 2-3 orders of magnitude slowdown in average solvation time for all the three dye molecules. At very high ACN concentrations ($X_{ACN} > 0.85$), clusters of ACN are occasionally disrupted by ACN-water complex molecules. Therefore the observed fast solvation in this region is due to the fast movement of the truncated ACN clusters (or free ACN) molecules around the excited dipole. A power law kinetics of *C343*, in addition to the appearance of an isoemissive point in *TRANES*, univocally confirm the inhomogeneity of *ACN-WT* mixture stabilises both, *C343* and its de-protonated form. *FCS* study has revealed the presence of micro-domains within the *ACN-WT* mixture with widely varying in their local viscosities supports the information obtained from the study of dynamic Stokes shifts as stated above. Inhomogeneity study using 1H *NMR* provides more accurate information on intrinsic inhomogeneity compared to the spectroscopic studies based on fluorescence, as the former technique does not require a dye molecule and therefore solvent clusters remain undisturbed. *NMR* study shows maximum hydrogen bond interaction among the *WT* and *ACN* molecules prevails mostly within the intermediate concentration regime of *WT* in *ACN-WT* mixture and that could be a potential source of intrinsic inhomogeneity of this binary mixture.

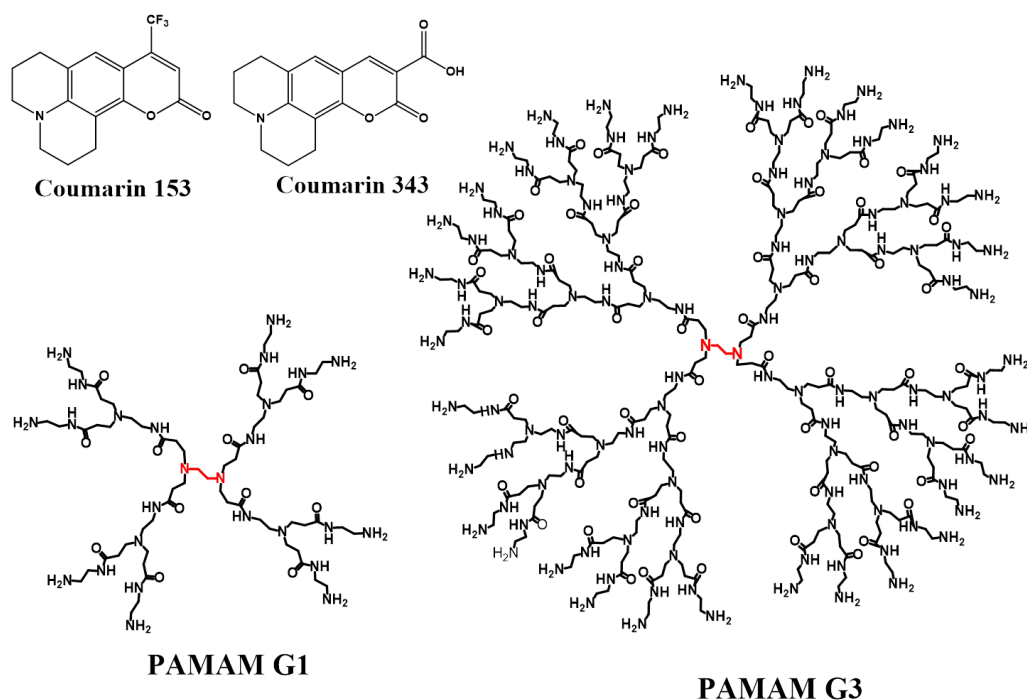
Fluorescence Probing of PAMAM Dendrimer Interior

5.1. Introduction

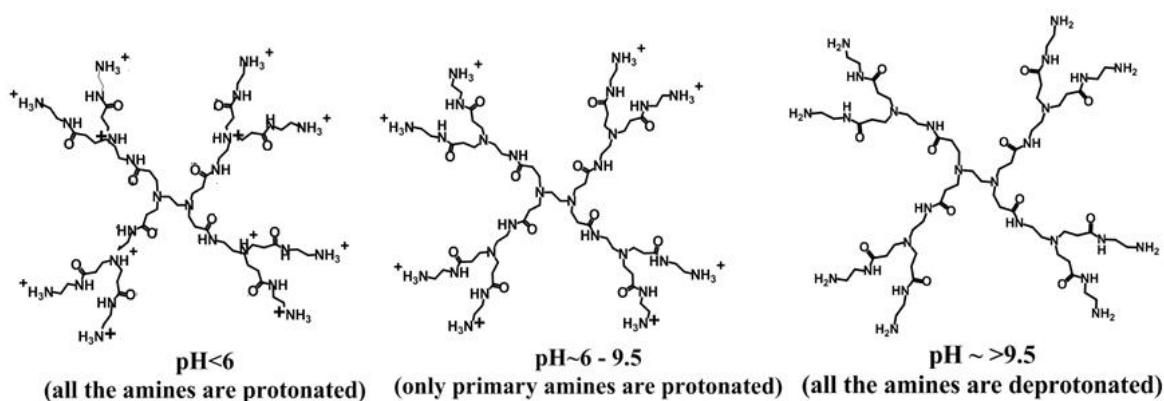
Highly symmetric and hyperbranched dendrimers have received considerable attention from various research fields due to its widespread applications ranging from nanoparticle synthesis to drug delivery and most recently in gene therapy.⁶⁷⁻⁷² Different generation *dendrimers* with various structural scaffoldings are used within the recent reports for various biomedical applications, quantum dot synthesis, optical sensing, mimicking of globular proteins, and optical imaging of cells.^{73-76,188-190} Soft molecular interactions (hydrophobic/hydrophilic, electrostatic and hydrogen bond interactions) between *guest* molecule with dendrimer lead to a stable supramolecular dendritic complex formation.^{68,70} So far there have been a few number of reports which show molecular level insight to a host-guest interaction of a dendrimeric complex.⁸⁹⁻⁹³ Here we studied the interactions between hydrophobic and hydrophilic coumarin dyes with amine terminated first (G1) and third (G3) generation poly-(amidoamine) dendrimers (Scheme 5.1). Amine terminated dendrimer bears two different types of nitrogen centres; primary amines at the periphery and tertiary amines at the interior. These two amine centres behave differently as medium pH is changed.^{81,191} At neutral pH (~7), primary amine (pKa~9.2)¹⁹¹ groups at the exterior of dendrimer remain completely protonated while tertiary amines (pKa~6.3) at dendrimer interior remain partially protonated within the aqueous solution (Scheme 5.2). Stepwise protonation to the primary amines first, and then tertiary amines as pH of the dendrimer solution is lowered, has a close relation with pH dependent fluorescence intensity change of dendrimer molecules.⁸¹ For a G4 amine terminated dendrimer, Imae and her co-worker observed insignificant change of fluorescence intensity when pH was lowered from ~11 to ~6.⁹⁴ This is followed by a dramatic

enhancement of emission intensity (without shifting the emission peak position) on further lowering the medium pH. A maximum intensity they obtained at pH~ 2.5; no change of intensity was noted thereafter. They explained this observation due to a number of facts: e.g., strengthening of hydrogen bonds at low pH; formation of rigid structure of dendrimer in acidic medium due to the electrostatic repulsions among the protonated tertiary amine centres; and formation of new highly fluorescent molecule at low pH medium.¹⁹² Their explanation tacitly assumes fluorescent centre is planted deep inside the dendrimer molecule, as it is mostly influence by the protonation of the interior amines only (at low pH). Intrinsic fluorescence of dendrimer is also modified by several other factors; like aggregation formation among the dendrimer molecules, nature of terminal group (amine, hydroxy or carboxylate) present at exterior surface of dendrimer, and nature of the explicit solvent where dendrimer is dissolved.¹⁹²⁻¹⁹³ Recently Prasad and his co-worker observed dendritic aggregations, formed by the electrostatic interactions among the oppositely charged dendrimers, mostly follow a fascinating dendritic pattern.¹⁹³ Within these patterns, nonradioactive pathways of exciton decay are significantly reduced, which results a considerable appreciation to the intrinsic fluorescence from dendrimer molecules.¹⁹³ Radius of gyration (R_g) of dendrimers, in contrast to the dendrimer fluorescence (which is sensitive to the medium pH), does not change much (<4%) with changing the medium pH (~4-10). Previous studies of small angle neutron scattering (SANS) on G8 and G4 PAMAM dendrimers reveal only ~2% (for G8) and ~4% (for G4) increase of R_g as pH of the medium is changed from ~10.1 to ~4.7.⁸⁷ Findings of these SANS studies are highly congruent to a recent work on atomistic molecular dynamics (MD) simulations by Goddard III and his co-workers.⁸⁸ Goddard III et al observed a subtle swelling (<4%) of G4 PAMAM dendrimer in aqueous solution as pH of the solution was changed from high to low.⁸⁸ They further plotted (solvent accessible surface area)^{1/2} and (solvent excluded volume)^{1/3} of dendrimers as a

function of probe molecule size. From their plots they found probe molecules with size >1.4 nm cannot be placed inside adendrimer molecule. In this chapter we show an extremely hydrophobic dye *C153* strongly interact with dendrimers, leading to a stable dendritic host-guest complex at all *pHs* ($\sim 3-10$). However a similar size hydrophilic dye *C343* does not interact equally with *dendrimer* within the same *pH* range. In *C153*-dendrimer complex, *quasi*-confined water molecules inside the dendrimer act as a better solvator for *C153* compared to the bulk water.¹⁹⁴ However for *C343*, driving force for complex formation is the strong electrostatic interaction, which becomes feasible around *pH* ~ 9 . Apart from noncovalent interactions (hydrophobic/hydrophilic, hydrogen bond, columbic interactions etc), confinement effect on the trapped water inside dendrimer plays a crucial role for dissolving hydrophobic molecule at dendrimer interior.¹⁹⁴



Scheme 5.1. Chemical structures of *PAMAM*dendrimers (*G1* & *G3*)and coumarin dyes used in this study. The ethylenediamine core of the dendrimers has been identified by red colour.



Scheme 5.2. *pH* dependent protonation of primary and tertiary *amine* centers of *dendrimer-G1* in aqueous solution.

5.2. Sample Preparation and Evidence for *Host-Guest* Complex Formation: Among the several methods we tried for the dissolving of *C153* in aqueous *dendrimer* solution, we found solvent evaporation method is the most efficient one. In solvent evaporation method, the host molecules (*dendrimer*) along with the hydrophobic dyes *C153* (guest) are dissolved in a common solvent (*methanol*) where both are equally soluble and the solvent is slowly evaporated to make a thin film at the wall of round bottom flask. This film is hydrated with large excess amount of water and thereby the encapsulated guest molecules within the host are solubilised in *milliQ* water.¹⁹⁵⁻¹⁹⁶ The partitioning of *C153* in aqueous phase in the presence of *dendrimer* was confirmed by checking the UV-Vis spectrum where strong characteristic absorption band of *C153* was observed. Since *C153* is almost insoluble in water, a maximum *OD* of $\sim < 0.02$ can be found from a *C153* saturated water solution. However, *OD* of *C153* increases many-folds (> 14 times) within the aqueous ~ 0.2 mM *dendrimer* solution (Figure 5.2). *C153* saturated water is apparently transparent and almost no emission from *C153* can be found when excited with UV light. However, in the presence of ~ 0.2 mM *dendrimer*, due to higher solubility of *C153*, the resultant solution (*C153* saturated aqueous *dendrimer* solution) turns yellow colored. A strong *C153* fluorescence is observed

from this solution when excited with a UV light (Figure 5.1). This fact confirms that *dendrimer* solubilises the hydrophobic dye *C153* in water through a stable water-soluble *dendrimer-C153* complex formation.

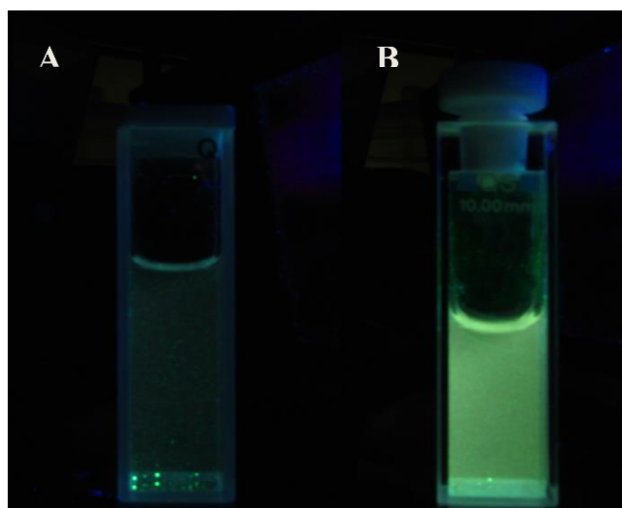


Figure 5.1. Photographs were taken under UV illumination (~ 365 nm) for (A) *C153* in water and (B) *C153* in aqueous solution of *dendrimer-G3* (~ 0.1 mM). A strong fluorescence only from the latter solution was observed under same excitation power.

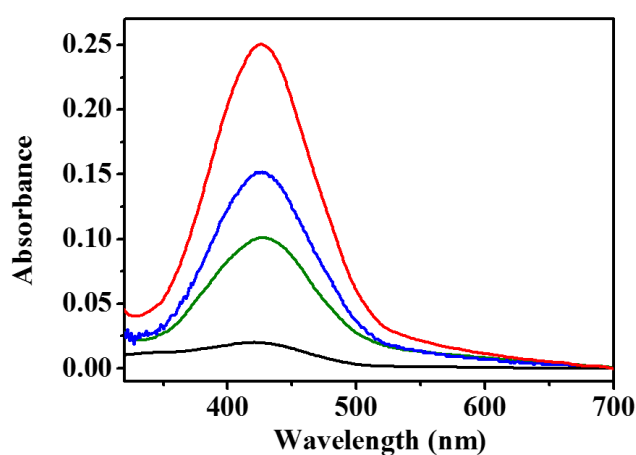


Figure 5.2. Absorption spectra of *C153* saturated water in the absence (black curve) and presence of ~ 0.05 mM (green curve), 0.1 mM (blue curve), and 0.2 mM (red curve) *dendrimer-G3* respectively ($pH \sim 9.6$).

5.3. Results and Discussions

5.3.1. Study of Red Edge Excitation Shift (REES) using Intrinsic Fluorescence of dendrimer

PAMAM dendrimers are intrinsically fluorescent within low *pH* solvents.⁹⁴ In the present work we rigorously studied the intrinsic fluorescence from *generation 1 (G1)* and *generation 3 (G3)* of *PAMAM dendrimer* at natural *pH* only. *pH* dependent fluorescence properties of the same *dendrimer* but different generations (*G2 and G4*) are already reported in a seminal work by Imae and her co-worker.⁹⁴ Imae et al & Crooks et al noted few remarkable spectral properties of *dendrimer* molecules, which are worth mentioning here, before going to our *REES* experiment.^{81,94} (1) Most of the *PAMAM dendrimers* exhibit an absorption peak (λ_{abs}^{max}) within the range of 280-290 nm (figure 5.3; black curve) and excitation at absorption peak (λ_{abs}^{max}) of *dendrimer* produces broad fluorescence spectrum with weak intensity. (2) Excitation spectrum, as obtained from the plotting of emission intensity at emission peak wavelength as a function of excitation wavelength, was found incapable to replicate the actual absorption spectrum. Interestingly these excitation spectra (peaked within ~ 330-400 nm range) are well structured and highly red shifted compared to their corresponding absorption spectra (Figure 5.3; blue and red dotted curves). (3) Excitation at the peak of *excitation spectrum* provides a highly intense and narrower emission spectrum as compared to the emission intensity and width of the emission spectrum obtained through the excitation at absorption peak (Figure 5.3). In *REES* experiment, we therefore studied emission spectra of *dendrimers* by exciting within the range from 310 nm to 405 nm for *dendrimer-G1* and 335 nm to 430 nm for *dendrimer-G3*, with ~5 nm interval between two successive excitation wavelengths (exciting around the excitation spectrum of *G1* and *G3 dendrimers*). The emission peak wavelengths from both the generations are shifted towards red wavelengths

when excitation energies are gradually moved from high energy side to the low energy side. This phenomenon is called red edge excitation shift (*REES*).

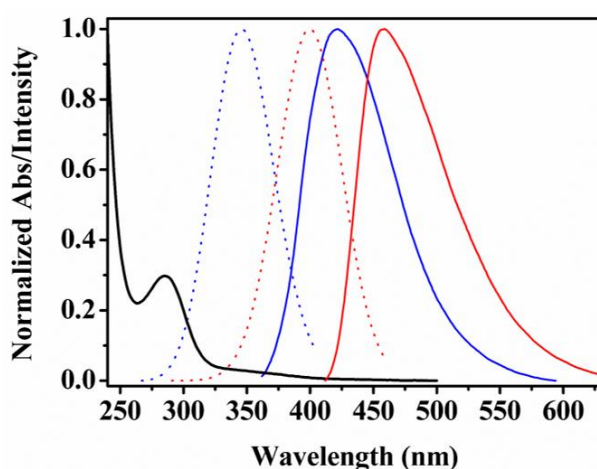


Figure 5.3. Absorption spectrum of *dendrimer-G3* (black) in water. Excitation (dotted lines) and emission (solid lines) spectra of *dendrimer-G1* (blue) and *dendrimer-G3* (red) in water.

REES provides an idea of static inhomogeneity within the medium in a quantitative sense.¹⁹⁷⁻
¹⁹⁸Excitation at extreme blue wavelengths (<300 nm for *dendrimer-G1* & <320 nm for *dendrimer-G3*) leads to a broad and weak emission spectrum with one shoulder-like peak from both the generations, which restricted our excitation wavelengths to ~310 nm (for *dendrimer-G1*) and 335 nm (for *dendrimer-G3*) at higher energy side of excitation. Amount of *REES* is more in *G3-dendrimer* (~78 nm) as compared to that (~65 nm) observed in the case of *dendrimer-G1* (Figure 5.4, Table 5.1).

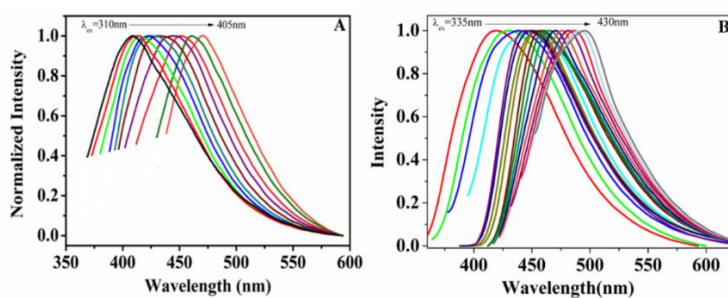


Figure 5.4. Emission spectra of aqueous (A) *dendrimer-G1* and (A) *dendrimer-G3* at different excitation wavelengths.

Table 5.1. Emission maxima (λ_{em}^{max}) for dendrimer intrinsic fluorescence different excitation wavelengths (λ_{ex}) and corresponding of *dendrimer-G1* and *dendrimer-G3* in aqueous solution.

PAMAM-G1		PAMAM-G3	
λ_{ex} (nm)	λ_{em}^{max} (nm)	λ_{ex} (nm)	λ_{em}^{max} (nm)
310	403	335	418
325	407	345	424
335	411	355	432
345	418	365	446
355	422	375	451
365	438	385	461
375	444	395	465
385	454	405	474
395	463	415	482
405	468	430	496

The actual source of inhomogeneity (as indicated by significant amount of *REES*) associated with monodispersed *dendrimer* molecules is not very clear to us. However, several groups have reported the nonideality of the synthesis methods causes implantation of random defect sites within the *dendrimer* molecules.¹⁹⁹⁻²⁰¹ These defect sites, in turn can produce intrinsic inhomogeneity of *dendrimer* molecules.¹⁹¹⁻²⁰¹ A defect site may arise from several components: (1) skeleton defects with missing fragments or formation of unwanted bonds connecting the branches; (2) presence of “*stray fragments*” inside a *dendrimer* molecule; and (3) existence of low generation *dendrimers* obtained from the presence of excess core fragments at the time of growth to a higher *generation* target.²⁰¹ A higher amount of *REES* in *dendrimer-G3* (~ 78 nm) as compared to that (~65 nm) in *dendrimer-G1* is well under our intuitive expectation; a higher generation *dendrimer* with larger number of defect sites will

produce more inhomogeneous environment compared to that in a lower generation *dendrimer* with lesser number of defect sites. Additionally, smaller generation *dendrimers* bear relatively open structures as compared to the structures adopted by higher generation *dendrimers*. As generation of *dendrimer* grows, repulsion among the terminal groups causes significant back-folding of the peripheral subgroups. This back-folding leads to a densely packed inhomogeneous *globular* protein like structure within the higher generations *dendrimer* molecules.^{79,89,202} *REES* within a *globular* like protein is a well-known phenomenon, reported by several groups.¹⁹⁸ Hence, the *globular* like structure of the higher generation *dendrimer* is may be the reason for a larger *REES* from *dendrimer-G3* as compared to that observed for *dendrimer-G1*.

5.3.2. Molecular Recognition Study of *C153-Dendrimer* Complex

In the next step we added a water insoluble hydrophobic dye (*C153*; ~6 μM) to the aqueous *G3-dendrimer* solution (~0.2 mM) through solvent evaporation method. It is worth mentioning here that a high solubility of *C153* within the aqueous *dendrimer* solution, this is in conjunction with a higher quantum yield of *C153* as compared to the quantum yield of *dendrimer* in aqueous solution, cause an overshadowing of weak *dendrimer* emission by the strong *C153* fluorescence of *C153* in aqueous *dendrimer* solution. Moreover, the location of emission peak position of *dendrimer* (in water) is different from the emission peak position of *C153* in aqueous *dendrimer* solution; these factors enabled us to successfully monitor *C153* fluorescence from *C153-dendrimer* complex formed in aqueous solution. Interestingly here we observed no *REES* from *C153* fluorescence when attached to a *dendrimer* molecule. This is may be due to the local homogeneous environment of *C153* within the complex. The emission peak position (~552 nm) and *QY* (~0.08) of *C153* in *dendritic* complex are close to the emission peak position (~549 nm) and *QY* (~0.12) of *C153* in bulk water.²⁰³ This fact ascertains the location of *C153* in *dendritic* complex is within the hydrophilic region; which

iseither at the exterior (*dendrimerperiphery*) or within the internal cavities of *dendrimer*. In both the places *C153* can get a water like environment. Solvation dynamics study utilizing the fluorescence of *C153* (attached to *dendrimer*) can help us revealing the nature of immediate environment of *C153*, within its complex with *dendrimer* molecule.

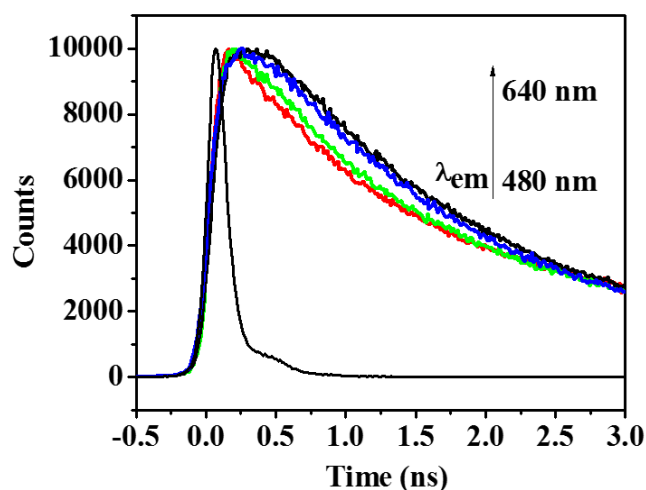


Figure 5.5. Initial portion of the fluorescence lifetime decay profiles of *C153* in aqueous *dendrimer-G1* at different emission wavelengths. No detectable rise component was found at red emission (~640nm) wavelength after reconvolution with excitation lamp profile.

If *C153* resides in a water like environment within the complex, then one can expect to see an ultrafast (~few ps) solvation dynamics (therefore, the ultrafast rise components at red emission wavelengths of *C153*), but that can't be detected by our *TCSPC* set up (*IRF* ~80 ps).¹²⁹ On the other hand, if *C153* binds to a hydrophobic site of *dendrimer*, the rise components at the red emission wavelengths will be slower by several orders of magnitudes, which can easily be detected by our set up. As expected, within the lifetime decay curves of *C153* (in aqueous *dendrimer* solution) at red emission wavelengths, we did not find any detectable rise component using a *TCSPC* set up (Figure 5.5). Therefore this observation also indicates that *C153* resides in a hydrophilic environment within the complex.

5.3.3. Study of *C153* Fluorescence from the *Dendrimer-C153* complex as a Function of the Medium *pH*

Intrinsic fluorescence of *dendrimers* is greatly enhanced with lowering the medium *pH*, especially when tertiary amine centres turn protonated.⁹⁴ In this condition amine centres unable to quench the excited state fluorophore units of *dendrimers* through electron transfer.²⁰⁴ In this work, we studied the effect of medium *pH* on fluorescence property of *C153* attached to a *dendrimer* molecule. Like the intrinsic fluorescence of *dendrimer*, which increases significantly with lowering the medium *pH*, the fluorescence intensity of *C153* attached to *dendrimer* also increases as medium *pH* is lowered. However in latter case intensity change is not that significant. In aqueous *dendrimer* solution (*pH*~ 9.6), only primary amine centres at *dendrimer* exterior remain protonated. *QY* of *C153* in this solution is ~0.075. However, when we lowered the *pH* to ~2 by addition of *HCl*, both primary and tertiary amine centres became protonated.⁹⁰ Within this low *pHdendrimer* solution, *QY* of *C153* was found to be ~0.11, which is very close to the *QY* (~0.12) of *C153* in bulk water (Figure 5.6.A).²⁰³ In former solution (*pH* ~9.6), *C153* fluorescence is quenched by photo-induced electron transfer (*PET*) from non-protonated tertiary *amine* centres, located at *dendrimer* interior, to the excited *C153* molecule.⁹⁰ When *pH* was decreased to ~2 in the latter solution, all *amine* centres became protonated and quenching due to *PET* from *amine* to excited state *C153* is not possible.⁹⁰ Bulk water like *QY* of *C153* from low *pHdendrimer* solution is a clear indication that *C153* is resided within the water like environment inside *dendrimer* molecule. Since protonation of interior *tertiary amine* centres of *dendrimer* causes the fluorescence enhancement of *C153*, this implies that *C153* is also located at the interior of a *dendrimer* molecule; very close to the tertiary amine centres. Imae and her co-worker recently reported a similar observation that the fluorescence intensity of *pyrene* at 446 nm decreases when it binds at interior of a *poly(propyleneimine)(G3)-core:PAMAM(G3)-shell*

dendrimer.⁹⁰ To them, fluorescence quenching of *pyrene* here is due to *PET* from tertiary amine centres of *dendrimer* to the excited *pyrene* molecule.⁹⁰

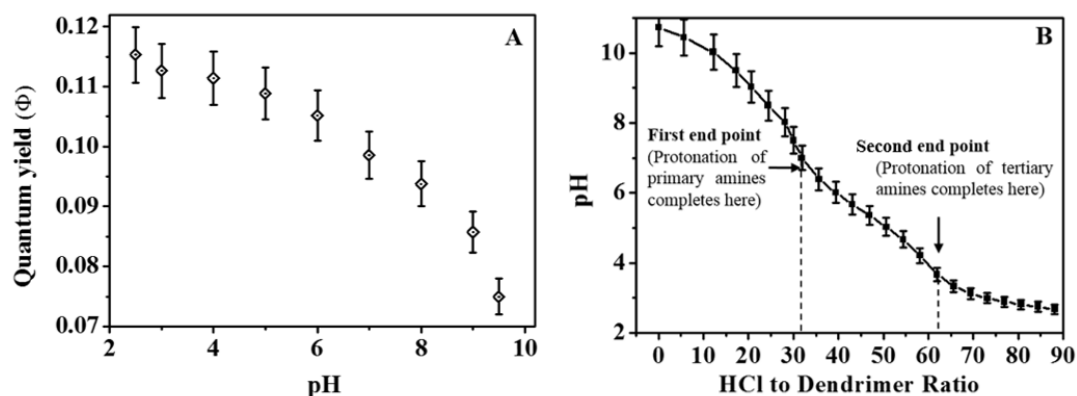


Figure 5.6. (A) Plot of fluorescence quantum yield (ϕ) of *C153* in aqueous *dendrimer-G3* solution as a function of medium *pH*. (B) Plot of *pH* of aqueous *dendrimer-G3* solution as a function of HCl/dendrimer mole ratio. Two end points were detected during the titration due to the stepwise protonation to the primary amine centres first (at HCl/dendrimer ~32) and followed by tertiary amine centres (at HCl/dendrimer ~62). This figure shows a nice correlation of end points with the number of primary and tertiary amines present in *dendrimer-G3*.

Before arriving to our conclusion that at low *pH* protonated tertiary amine unable to take part into *PET* that causes *C153* fluorescence unquenched, a direct evidence showing the tertiary amine centres of *dendrimer* get protonated at low *pH* (<5.5) is highly desirable. For this, we performed quantitative *pH* titration of aqueous *dendrimer-G3* solution by gradual addition of *HCl* (Figure 5.6.B). One mole *dendrimer-G3* contains 32 moles of *primary amine* centres ($pK_a \sim 9.2$) and 30 moles of *tertiary amine* centres ($pK_a \sim 6.3$).⁷⁹ Therefore appearance of two end points in figure 5.6.B (*pH* vs. *HCl/dendrimer* mole ratio curve) is due to a stepwise protonation to the *primary amine* centres first (completed at ~32 molar ratio) and followed by the protonation to the *tertiary amine* centres [completed at ~62 (32+30) mole ratio].

A careful examination of figure 5.6.A and 5.6.B shows a nice correlation; emission *QY* of *C153* (in *aqueousdendrimer* solution) increases upon protonation to the *tertiary amine* centers (with decreasing the medium *pH* from ~8.5 to 4). This fact approves our belief that the fluorescence quenching of *C153* at high *pH* is due to a *PET* from *tertiary amine* center of *dendrimer* to excited *C153*. Therefore, *C153* is located inside the *dendrimer* molecule. When we thought about different binding sites within a *dendrimer* molecule, we found *C153* can possible go to the hydrophobic core (*EDA* core). However, in a seminal work by Tomalia and his co-workers reported that for an *EDA* core *PAMAM dendrimer*, core size is just too small to accommodate a fluorescent dye molecule.⁷² Among the other binding sites, *C153* may enter into the water rich cavities inside *dendrimer* molecule. Goddard III et al and several other authors showed Rose Bengal, which is much bigger in size compared to *C153*, easily fits into the internal cavities of *dendrimer* molecule.²⁰⁵⁻²⁰⁷

To decide the exact location of *C153* inside a *dendrimer* molecule we studied *rotational anisotropy* decay of *C153* within the *dendritic* complex. If *C153* is attached to the *EDA* core of *dendrimer*, we can expect to see an excited state depolarization of the *C153* dipole through the rotation of *C153-attached-dendrimer* assembly as a whole; which would be much slower as compared to the free rotation of *C153* within the water rich cavities of *dendrimer* (if *C153* is resided within the cavity). Interestingly we observed a fast single exponential rotation of *C153* at *dendrimer* interior, which is highly congruent to the rotation *C153* in bulk water. No slow component of rotation was detected, which rules out the possibility of *C153* getting trapped at *EDA* core of *dendrimer*. A detail study of rotational dynamics of *C153* has been discussed in the following section.

5.3.4. Rotational Anisotropy Study of Dendrimers Alone and *C153* attached to the Dendrimer

5.3.4.1. Rotational Diffusions study of Dendrimer using its Intrinsic Fluorescence

Anisotropy decays using the intrinsic fluorescence of *dendrimers* (G1 & G3) in water nicely correlate to their corresponding hydrodynamic radii. Experimental anisotropy decay functions were conclusively fitted with following bi-exponential fitting function,

$$r(\tau)=r_0\{a_1\exp(-t/\tau_{fast}) + a_2\exp(-t/\tau_{slow})\}.....(5.1)$$

The initial anisotropy values ($r_0 \sim 0.3$, at $t=0$; Figure 5.7) from both the generations were found to be close to the limiting value of r_0 ($r_0=0.4$) for the rotation of an one dimensional excited state dipole.¹¹⁷ The actual origin of the two rotational components (τ_{fast} & τ_{slow}) from both the generations of *dendrimer* is not very clear to us. To best of our knowledge, this is the first time investigation on *rotational anisotropy* of *PAMAM dendrimers* utilizing its intrinsic fluorescence. Almost no information on rotational dynamics of *dendrimer* molecules can be found from previous reports. The slow component (τ_{slow}) of rotational decay is nicely correlated to the hydrodynamic radius (r_h) of *dendrimer* molecule, as shown by the following *Stokes-Einstein* relation (equation 5.2).

$$\tau_{slow} = \frac{4\pi r_h^3 \eta}{3kT}(5.2)$$

Therefore the origin of τ_{slow} may be due to the overall rotation of the *dendrimer* molecule. Addition to the overall rotation, a local chain dynamics of non-rigid internal branches at *dendrimer* interior may contribute to the depolarisation of *dendrimer's* intrinsic fluorescence.²⁰⁸ This type of depolarisation is more common for a dye molecule inside a micelle or in a polymer chain.²⁰⁸⁻²¹⁰ For simplicity we assumed the internal movement of the fluorescent centre of *dendrimer* to be a *wobbling* type of motion and apex of it, is fixed to the spherical surface of the *dendrimer*. This *wobbling* motion will produce one cone with a semicone angle of θ .

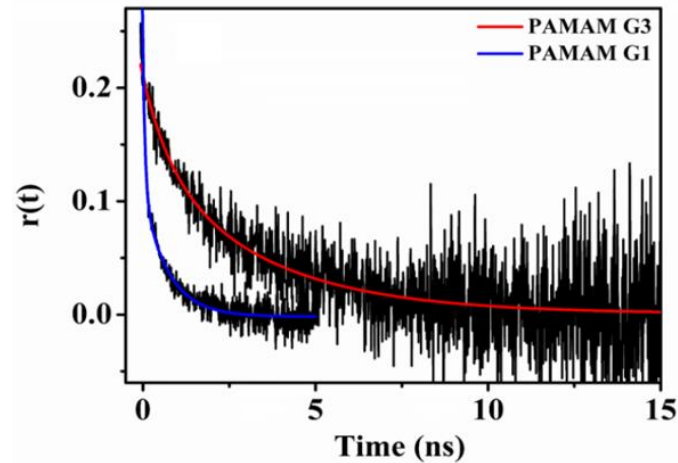


Figure 5.7. Decay of rotational correlation function $r(t)$ with time for *dendrimer-G1* and *dendrimer-G3* in water utilising the intrinsic fluorescence of *dendrimer*. Solid lines represent the fitted curves.

Our proposed model is essentially similar to the popular “*wobbling-in-cone*” model, frequently used within the spherical micellar systems. However, here in contrast to the *wobbling-in-cone* model, we disregarded the translational diffusion of fluorescent centre. If $r(t)$ follows a biexponential decay, as per our proposed model,

$$r(t) = r_0 [\beta \exp(-t/\tau_M) + (1-\beta) \exp\{-t(1/\tau_M + 1/\tau_r)\}] \dots \dots \dots (5.3)$$

Where r_0 is the initial anisotropy (at $t=0$). β represents the fractional contribution to the overall anisotropy decay due to the rotation of *dendrimer* as a whole and τ_M ($=\tau_{Slow}$) is the corresponding rotational correlation time. τ_r be the time coefficient associated with *wobbling* type of motion of the intrinsic fluorescent centre of *dendrimer*. Comparing equation 5.1 and 5.3, we can correlate between experimental fitting parameters with the model parameters as follows.

$$\tau_{Slow} = \tau_M \quad \text{and} \quad \tau_{Fast} = 1/\tau_M + 1/\tau_r \dots \dots \dots (5.4)$$

From the fittings we observed, in all the cases experimental τ_{slow} is nicely correlated to the τ_M as obtained from theoretical prediction using *Stokes-Einstein* equation ($\tau_M = \eta v / kT$). This fact justifies the well acceptability of this model in our case. Rotational diffusion constant (D_w) due to the *wobbling* type motion of the fluorescent centre is given by the following equation.⁵¹

$$D_w = \{\tau_R(1-\beta)\}^{-1}[-x^2(1+x)^2\{\ln[(1+x)/2] + (1-x)/2\}\{2(1-x)\}^{-1} + (1-x)(6+8x-x^2-12x^3-7x^4)/24] \dots (5.5)$$

Where, $x = \cos\theta$; θ is the semicone angle. x is obtained from the coefficient β of biexponential fitting to the experimental anisotropy decay curve using the following equation,

$$\beta = \{0.5x(1+x)\}^2 \dots \dots \dots (5.6)$$

All rotational fitting parameters obtained from the fittings using this model are summarized in Table 5.2. We also studied the *pH* dependency of τ_{slow} component, to get an idea of *dendrimer* size change with changing the medium *pH* (τ_{slow} is directly correlated to the *dendrimer* size). Aqueous *dendrimer* solution is basic in nature (*pH*~9.6), where we obtained $\tau_{slow} \sim 4.12$ ns for *dendrimer-G3*, which represents an overall size of this *dendrimer* is ~ 3.2 nm. However, when *pH* was lowered, we observed τ_{slow} became faster. For instance, at *pH*~2, $\tau_{slow} \sim 2.78$ ns, with a correlating particle size of ~2.8 nm (Table 5.3). The sizes of *dendrimers* obtained here through *rotational anisotropy* studies are highly congruent with previous reports of *dendrimer* sizes.²¹²⁻²¹³

Table 5.2. *Wobbling-in-cone* model parameters obtained from the fittings of *rotational anisotropy* decays of *dendrimer* molecules utilizing their intrinsic fluorescence.

Dendrimer	η (cP)	r_0	β	τ_R (ns)	τ_M (ns)	θ
G1	1.05	0.27	0.47	0.11	0.58	46 ⁰
G3	1.08	0.25	0.57	1.31	3.80	30 ⁰

We also studied dynamic light scattering (*DLS*) for a size estimation of *dendrimer-G3* at various *pHs*. *DLS* study reveals an insignificant change (<5%) of *dendrimer (G3)* size with changing the medium *pH* from ~9.6 (*aqueous dendrimer*) to ~2 (*aqueous dendrimer + HCl*; Figure 5.8). Actual reason of slight shrinking (<10%) of *dendrimer* size at low *pH* is not clear to us. It may be due to the back-folding of *dendrimer*'s peripheral subgroups towards the core at low *pH* which can results shrinking to the overall *dendrimer* size.

Table 5.3. *pH* dependency of fast (τ_{short})& slow (τ_{long}) *rotational anisotropy* decay components and the corresponding sizes of *C153-dendrimer(G3)* complex (as obtained from Stokes Einstein equation assuming τ_{long} originates due to the overall rotation of the complex)

<i>pH</i>	τ_{short} (ns)	τ_{long} (ns)	Hydrodynamic diameter(nm)
2	0.43 (34%)	2.78 (66%)	2.80
3	0.37 (33%)	2.96 (67%)	2.89
5	0.27 (29%)	3.30 (71%)	3.08
7	0.21(35%)	3.90 (65%)	3.16
9.6	0.26(34%)	4.12 (66%)	3.22

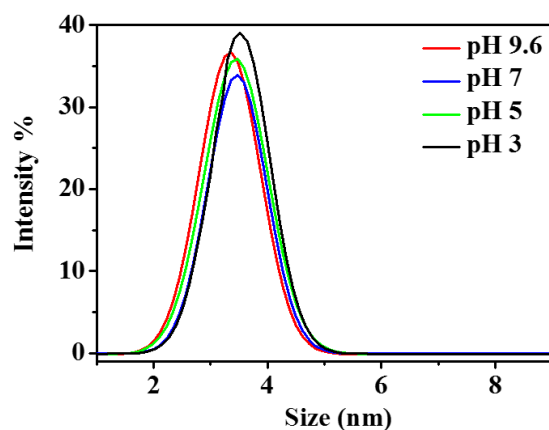


Figure 5.8. Dynamic light scattering (*DLS*) study of sizes of the *dendrimer-G3* complex in water at different *pHs*.

In summary, two components of *rotational anisotropy* decay of *dendrimer* molecules may arise from two independent phenomena: (1) a complete excited state depolarization of fluorescent centre due to the overall rotation of the *dendrimer* and (2) a partial depolarisation through the restricted *wobbling* type motion of the intrinsic fluorescent centre. Dimension of a *dendrimer* molecule in aqueous medium changes slightly with changing the medium *pH*.

5.3.4.2. Rotational Diffusion of C153 Attached to a Dendrimer Molecule

C153 attached to a *dendrimer* molecule shows a fast single exponential rotational diffusion time (~ 150 ps), which is as fast as like rotational diffusion time (~ 100 ps) of *C153* in bulk water (Figure 5.9).²¹¹ Water like rotation of *C153* attached to *dendrimer* is a clear indication that within the complex, *C153* is resided at the water rich regions. This is congruent with our previous observations of similar bulk water like emission peak position (red shifted), and bulk water like low quantum yield of *C153* attached to a *dendrimer* molecule. These facts unanimously confirm the location of *C153* is within the most hydrophilic region of a *dendrimer* molecule.

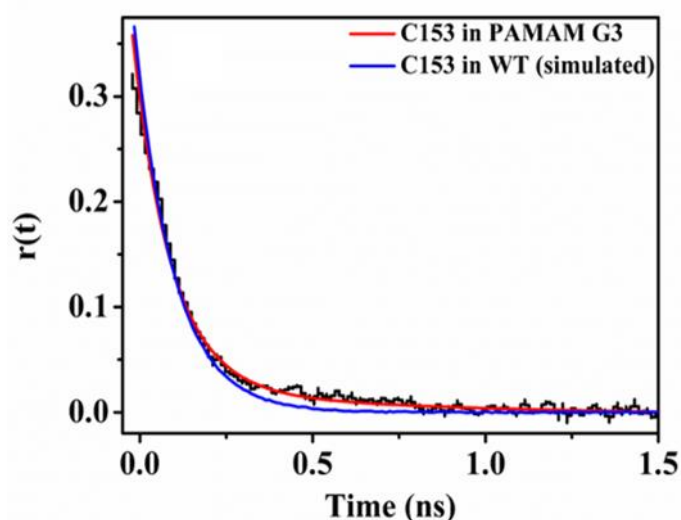
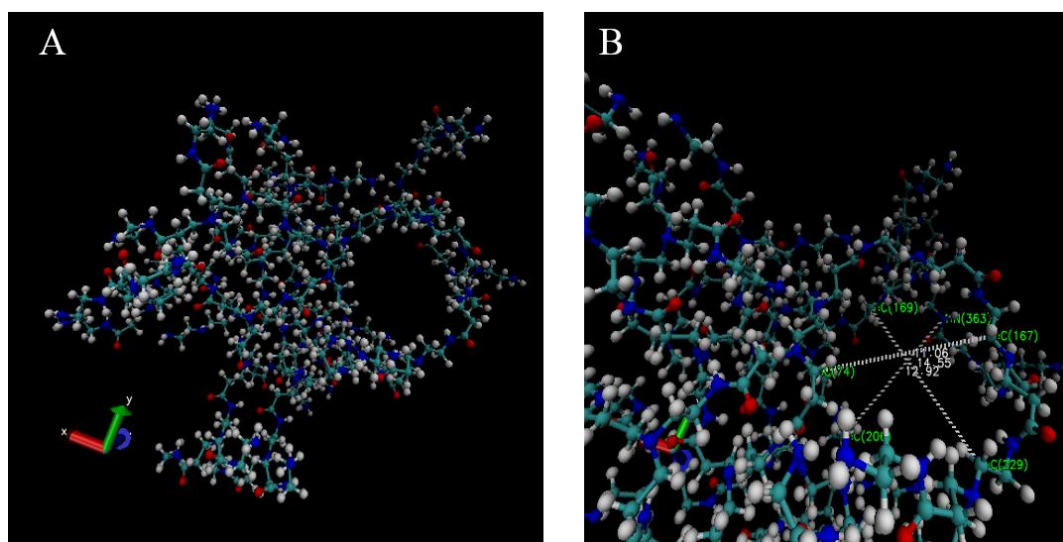


Figure 5.9. Rotational anisotropy decay curves for *C153* in aqueous ~ 0.2 mM *dendrimer-G3* solution (black curve). Red line represents the best fitting to the experimental decay curve.

The blue line has been simulated using the reported rotational correlation time of *C153* in bulk water from Ref 211. The simulated curve is plotted with a viscosity ~ 1.15 times higher (to make a same viscosity with ~ 0.2 mM aqueous *dendrimer-G3* solution) with respect to the viscosity of neat water, to compare these two curves at isoviscous condition.



Scheme 5.3. (A) *MM2* (*molecular mechanics*) optimised structure of *PAMAM dendrimer-G3* in the presence of ~ 200 water molecules.⁷⁹ (B) One cavity of the *dendrimer* has been magnified for the inspection of cavity size, which shows the average diameter of these water rich cavities is ~ 1.3 nm. Therefore *C153* with a size of ~ 0.8 nm can easily be accommodated within the cavity. Water molecules are not shown for clarity.

One may think that water like environment sensed by *C153* in an aqueous *dendrimer* solution could be due to the unbound *C153* present in the solution. However, we are confident that this is not the case here for following reasons: (1) in bulk water saturated *C153* exhibits an *OD* $\sim < 0.02$ at its absorption peak, which increases drastically to > 0.4 in the presence of ~ 0.2 mM *dendrimer*. As mentioned earlier, in the latter case, an intense yellow colour solution is observed, while in the former case resultant solution remained almost transparent (Figure 5.1). (2) *Fluorescence correlation spectroscopy* (*FCS*) study, which will be discussed

elaborately in the succeeding paragraph, shows a significant slowing down of the translation diffusion time of *C153* within the aqueous *dendrimer* solution as compared to the diffusion of *C153* in neat water. These facts provide a direct evidence of strong partitioning of *C153* into the internal cavities of *dendrimer* molecule (Scheme 5.3).

5.3.5. FCS Study of Translational Diffusion of *C153-Dendrimer* Complex

C153 when binds to a *dendrimer* molecule in aqueous solution it exhibits a *QY* of ~0.076 (at *pH*~9.6, Table 5.4). However in bulk water, in absence of *dendrimer*, this value increases to ~0.12.²⁰³ As required by the essential conditions of *FCS* measurement, we used only an insignificant amount (<10 nM) of *C153* with ~0.1 mM aqueous *dendrimer-G3* solution. Such a small amount of *C153* can dissolve into bulk water. Therefore, in this scenario, *C153* will show a partition-equilibrium between bulk water and *dendrimer* in aqueous *dendrimer* solution. As *QY* is different in these two mediums, one should use the following equation for the fitting of *FCS* autocorrelation curve of *C153* from aqueous *dendrimer* solution.¹¹⁷

$$G(\tau) = \frac{f_w Q_w^2 D_w + f_D Q_D^2 D_D}{(f_w Q_w + f_D Q_D)^2} \dots\dots\dots(5.7)$$

Where *f*, *Q* and *D* represent the followings: fraction of *C153* presents in water (*f_w*) and *dendrimer* (*f_D*); *QY* of *C153* in water (*Q_w*) and in *dendrimer* (*Q_D*); and translational diffusion coefficient of *C153* in water (*D_w*) and when attached to a *dendrimer* molecule (*D_D*). We used low excitation power to avoid any triplet state kinetics within the autocorrelation curve. We found two components of translational diffusion of *C153* from aqueous *dendrimer* solution. The fast component (*τ_{D1}*~57-62 μS) is nicely correlated with the size (0.8-0.85 nm) of *C153*. Therefore the source of this component is the diffusion of unbound *C153* in water. The other component (*τ_{D2}*), which appears within the range of ~278 μS to 330 μS (depending on

medium pH), roughly correlates to the size of *dendrimer-G3* (Table 5.4, Figure 10). Therefore we can assign this component due to the translational diffusion of *C153* along with a *dendrimer* molecule. We observed here the size of a *dendrimer (G3)* molecule is not much sensitive to the medium pH . The average size of the *dendrimer-G3* (~3 nm), we obtained from our *FCS* study, is highly congruent with the sizes we obtained from *DLS* and *rotational anisotropy* studies. We also tried to collect autocorrelation curve utilizing the intrinsic fluorescence of *dendrimer*, but unable to detect it (even at low pH) due to its weak fluorescence intensity.

Table 5.4. Parameters obtained from the fittings of *FCS* autocorrelation curves for the translational diffusion of *C153* in aqueous *dendrimer-G3* solution (~0.1 mM) at different pH s.

pH	Q_D	τ_{D1} (μS)	f_w	τ_{D2} (μS)	Size (nm)	f_D
3	0.11	62	0.55	278	3.14	0.45
5	0.10	57	0.45	305	3.40	0.55
7	0.092	55	0.40	282	3.20	0.60
9.6	0.076	58	0.33	330	3.66	0.67

Fraction of bound *C153* with *dendrimer* (f_D) was found to decrease with increasing the medium pH . For an instance, at $pH\sim 9.6$, 67% of *C153* remains attached to *dendrimer*, which falls to ~45% at $pH\sim 3$ (Table 5.4). A similar type of observation was reported earlier by Imae and her co-worker by using a different technique.⁹⁰ For a *poly(propyleneimine)(G3)-core:PAMAM(G3)-shell dendrimer*, Imae et al. observed number of encapsulated *pyrene* molecule per *dendrimer* increases with increasing medium pH , and value of this ratio reaches to maximum (~2.7) at $pH\sim 11$. Autocorrelation curve exhibits an initial fast decay (~ μS time scale) due to an intensity fluctuation arises from

binding/unbinding dynamics between *host* and *guest* molecules for a weak *host-guest* complex.²¹⁴ This fast dynamics is succeeded by a slow (~mS time scale) decay at latter time of the correlation curve due to the translational diffusion of the guest fluorescent molecule.²¹⁴ Generally these two fundamentally different processes happen in two different time regimes without interfering each other within the autocorrelation curve. In our study we did not notice any binding/unbinding dynamics of *C153-dendrimer* complex at the initial time of the autocorrelation curve.

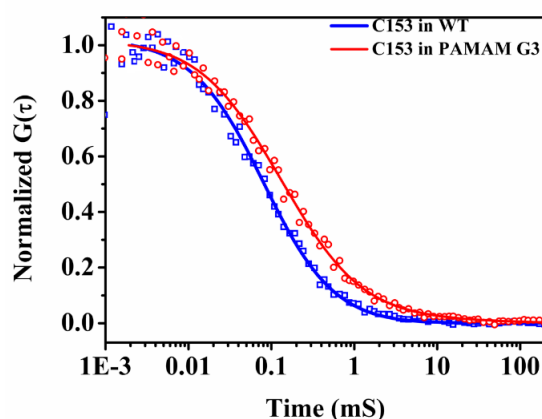


Figure 5.10. Normalized autocorrelation curves for *C153* in water (blue) and *C153* in aqueous *dendrimer-G3* solution (red). *pH* of the aqueous *dendrimer* solution is ~9.6.

5.3.6. Interaction of *Dendrimer* with a Hydrophilic Dye *Coumarin 343*

Interaction of a hydrophilic fluorescent dye *coumarin 343* (*C343*) with *dendrimer* was found to be completely different from the interaction with a hydrophobic dye *C153*. Unlike *C153*, *C343* is highly soluble in water and bears a $-COOH$ functional group with a *pKa* value of ~4.65.⁶¹⁻⁶³ At a sufficiently low *pH* (<3), all the *amine* centres of *dendrimer* turn protonated (Scheme 5.2) and *C343* is also remain protonated at this *pH*. Therefore at low *pH*, neutral form (protonated) of *C343* weakly interacts with a positively charged (protonated) *dendrimer*. Average rotational correlation time of *C343* in aqueous *dendrimer-G3* was found to be ~200 ps at *pH*~2 (Figure 5.11). Rotational correlation time of *C343* in bulk water is

~140 ps.⁶⁴This is clearly indicating that most of the *C343* molecules are resided within the bulk water at this *pH*. At a high *pH* (~9), only the terminal primary amine centres of *dendrimer* remain protonated (positively charged) and *C343* mostly prevails in its deprotonated form (negatively charged). A strong electrostatic interaction between oppositely charged *C343* and *dendrimer* leads to a complex formation which causes a slow rotation of *C343* around *pH*~9.

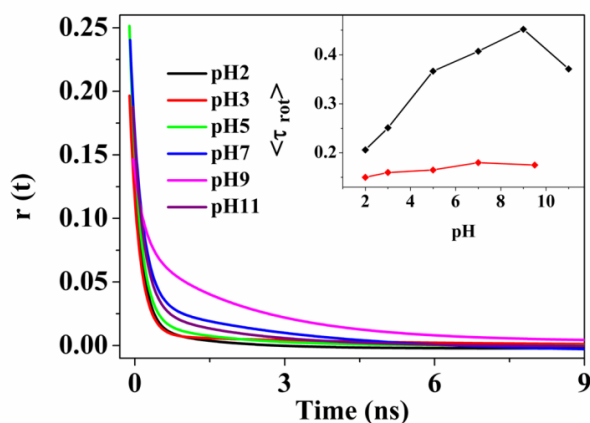


Figure 5.11. Fitted lines of the rotational correlation function $[r(t)]$ of *C343* in ~0.2mM aqueous *dendrimer* solution at different medium *pH*s. The inset depicts the average rotational time of *C343* (black points) and *C153* (red points) as a function of medium *pH*. Samples were excited at 445 nm and emission was collected at the emission peak positions.

We observed almost ~2 times retardation (Figure 5.11) of the rotational correlation time of *C343* in aqueous *dendrimer* solution when *pH* was increased from *pH* ~2 (τ_{rot} ~200 ps) to *pH* ~9 (τ_{rot} ~450 ps). On further increasing of *pH* from ~9 to 11, we observed rotational correlation time of *C343* again became faster to ~370 ps (Figure 5.11). At very high *pH* (≥ 11), all amine centres of *dendrimer* turn deprotonated (*pKa* of tertiary and primary amines are ~6.3 and 9.2, respectively), and *C343* also remains deprotonated at this *pH* (negatively charged). Therefore at very high *pH* negatively charged *C343* does not interact much with a neutral *dendrimer* molecule, which results a recovery of fast rotational time of *C343* within

the highly basic *dendrimer* solution. When we repeated the same experiment using *C153* instead of *C343*, we found there is hardly any change in rotational correlation time with changing the medium *pH* (red points in the inset of Figure 5.11). In all *pHs* *C153* exhibits a fast rotational time similar to the rotation of *C153* in bulk water (Figure 5.11; black curve in the inset). This is a clear indication that *C153* remains within the water filled cavities inside *dendrimer* and interacts equally with *dendrimer* in all *pHs*. For *C153*, we could not go *pH* > 10, as spectral shapes of *C153* get highly distorted at high *pH* medium.

5.4. Conclusion

In this chapter utilizing the spectral properties of *C153* when attached to a *dendrimer* molecule, we show bulk water like environment around the *C153* is highly preserved within the *C153-dendrimer* complex. Several spectroscopic studies have substantiated that the location of *C153* in *C153-dendrimer* complex is most likely within the water rich cavities inside the *dendrimer* molecule. This is a remarkable observation as *C153* is well known for its strong hydrophobic nature. However a big hydrophilic molecule (*Bengal Rose*) can easily get trapped within the water rich cavity of *dendrimer* molecule.²⁰⁵⁻²⁰⁷ Our *MM2* (molecular mechanics) optimised structure of *dendrimer-G3* (in water) shows the average diameter of a water rich cavity inside *dendrimer-G3* is ~1.3 nm; which can easily accommodate one *C153* molecule with a size of ~0.8 nm. We have highlighted the most promising property of *dendrimer* molecule; a stable *host-guest* complex formation with hydrophobic molecule and thereby solubilise the hydrophobic molecules in aqueous phase. For instance, almost water insoluble dye *C153* is found to be greatly soluble in the presence of ~0.2 mM *dendrimer-G3*. The diffusion studies (both translational and rotational) confirmed the location of the dye molecule and explained the water like photophysics of *C153* in *dendrimer*.

Study of Electron Transfer Reactions in a Dendrimeric Assembly: Proper Utilization of Dendrimer Fluorescence

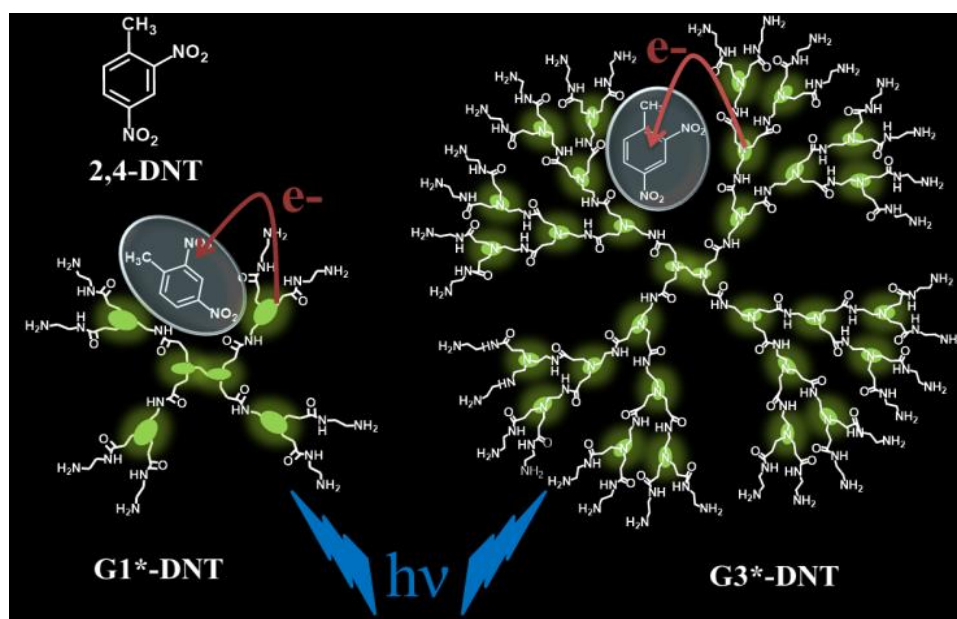
6.1. Introduction

Photo-induced electron transfer (*PET*) is ubiquitous in living biology. Considerable interests of studying *ET* reactions inside a biomimetic assembly are observed within the recent reports as *ET* reactions control several *in-vivo* activities.²¹⁵ Dendrimers have emerged as potential contenders for the formation of bio-mimetic assemblies in many cases due to their globular protein like structures.²¹⁶ The wide spread applications of amphiphilic *PAMAM* dendrimers have eased biosensing, drug delivery process, bio-catalysis reactions, and selective solubilisation of hydrophobic molecules as observed in a number of recent studies.^{71-73,215} Incorporation of metal centres in a fascinating manner produces dendritic redox-architecture that essentially mimics the enzyme activities in many cases.^{73,215} Amphiphilic nature and magnificent branching structures of *dendrimers* are often exploited to obtain supramolecular architecture of host-guest complexes. A dry core at the centre of *PAMAM* dendrimer can easily bind to the hydrophobic molecules. Conversely, amphiphilic peripheral pockets can host the hydrophilic molecules. Interestingly, one can customise the pocket size suitable to the dimension of a specific guest molecule by changing the generation of the dendrimer; a higher generation provides bigger rooms to the guest molecules. Notably the medium pH is another crucial parameter that directly controls the sizes of guest rooms by changing the dendrimer structures.⁹⁴ Dendrimer based fluorescent molecules are often used as pH sensors within the living cells for their harnessing pH dependent optical properties.^{94,217} Dendrimer films are widely used for the detection of nitrated explosive vapours, as dendrimer fluorescence is efficiently quenched through *ET* from dendrimer film to the nitrated

vapour.²¹⁸ *ET* studies within the dendritic assemblies have several other implications with photo-catalytic activities in biological systems.

Nitroaromatic compound *2,4 dinitrotolune (DNT)* is well known as a strong electron scavenger molecule. Earlier *DNT* has been used in *PET* reactions with matched band gap semiconductor molecules like, carbon dot, quantum dots, and polymer molecule poly(iptycenebutadiynylene), etc.²¹⁹⁻²²⁰ The *PAMAM* dendrimers are intrinsically fluorescent, provide nice spectral shapes; though the origin of this fluorescence is a subject of debate.⁹⁴ However most of the reports have predicted the tertiary amine and its repetitive branching (in higher generation) act as an unusual chromophore which is probably responsible for the intrinsic fluorescence of this molecule.⁹⁶⁻⁹⁹

In this chapter we will discuss *PET* from generation 1 (*G1*) and generation 3 (*G3*) *PAMAM* dendrimer to an electron deficient molecule *DNT* by monitoring the intrinsic fluorescence quenching of dendrimer. The work presented in this chapter reveals the sensing application of *PAMAM* dendrimer for nitroaromatic compounds.



Scheme 6.1. Schematic representation of the photoinduced electron transfer from PAMAM dendrimer to 2,4-DNT.

6.2. Results and Discussions

6.2.1. Photophysical Study on PAMAM Dendrimer in Methanol

In the previous chapter we have discussed the photophysical properties of PAMAM dendrimer in water. We have found several interesting properties of PAMAM dendrimer that can be revealed by studying the intrinsic fluorescence. In this chapter we have performed the quenching experiments in methanol. We thoroughly characterised the system (i.e. dendrimer in methanol) through fluorescence spectroscopy before performing the main experiment. Dendrimers exhibit strong excitation bands peaked at ~ 425 nm ($\lambda_{em}=470$ nm) in methanol. Absorption bands of dendrimers are rather weak and unstructured, appear at higher energy side (Figure 6.1).⁹⁴ We excited the dendrimer samples at the at the excitation-band as this leads to a narrower emission spectrum with higher intensity as compared to the emission spectrum obtained when excited at absorption peak.

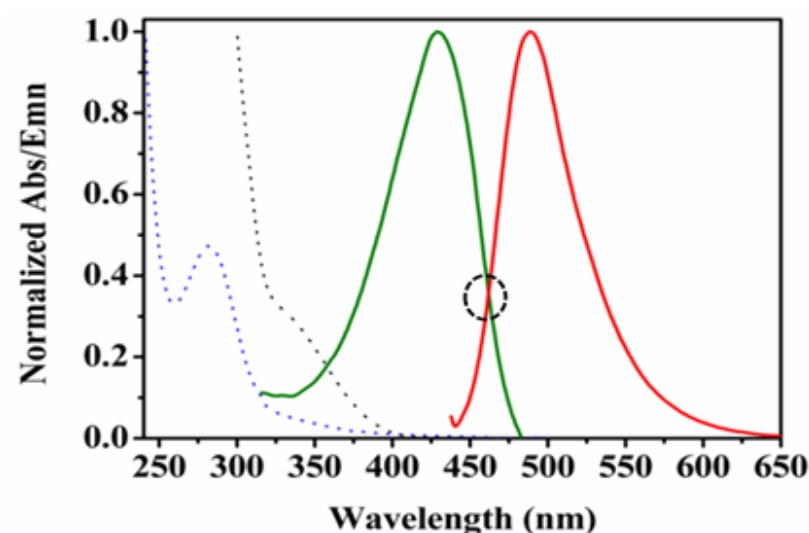


Figure 6.1. Steady state spectra of *PAMAM dendrimer-G3* in methanol: absorption (blue dashed line); excitation (green line, monitored at emission peak); and emission (red line,

excited at excitation spectrum). Black dashed line represents the absorption spectrum of *DNT* in methanol.

We have checked the overlap between the absorption band of DNT molecule and emission band of dendrimers to rule out the possibility of energy transfer that can take part in the quenching process (Figure 6.1). We found no considerable overlap between the donor emission and acceptor absorption. It is also necessary to check at what form the dendrimer molecules remain in the methanol solution for further analysis of ET process. Time resolved rotational anisotropy study utilizing the intrinsic fluorescence of dendrimer provides an estimation of the hydrodynamic radii of *G1* and *G3* dendrimers in methanol which we observed to be nicely correlated with the previous reports on dendrimer sizes by Tomalia and his co-workers (In the previous chapter we provided the details for the dendrimer solution in water; the same method has been followed here).²⁰⁰ Reproducible monomer sizes of dendrimers in methanol solution confirms the absence of any aggregated forms of dendrimers in the present study. From the photophysical studies it is clear that in methanol solution dendrimer monomer emits the fluorescence which we have utilised in the quenching experiment discussed in the next section.

6.2.2. Fluorescence Quenching of Dendrimer in Presence of DNT

Significant quenching of steady state fluorescence and lifetimes of *dendrimers* were observed in presence of *DNT*. We observed an additional steady-state fluorescence quenching of both *G1* and *G3dendrimers* when correlated to their respective lifetime quenching (Figure6.2). This fact suggests a *dendrimer*(host)-to-*DNT*(guest) dark complex formation might have caused an additional quenching of steady-state fluorescence of the *dendrimer* molecules. Fluorescence lifetime of *dendrimer* is truncated by the collisional quenching only; conversely, the steady-state fluorescence quenching is controlled by both static (host-guest

complex formation) as well as collisional quenching. Static quenching is responsible for additional quenching of steady-state fluorescence. Comparing between Figure 6.2.A & Figure 6.2.D, shows lower generation *dendrimer* (*G1*) exhibits a larger steady-state quenching when compared to the higher generation *dendrimer* (*G3*). However, same comparison on lifetime quenching between two *dendrimers* shows almost similar quenching (Figure 6.2.B & Figure 6.2.E). Steady-state and lifetime Stern-Volmer (SV) plots from both the generations are depicted in Figure 6.2.C (for *G1*) and Figure 6.2.F (for *G3*), respectively.

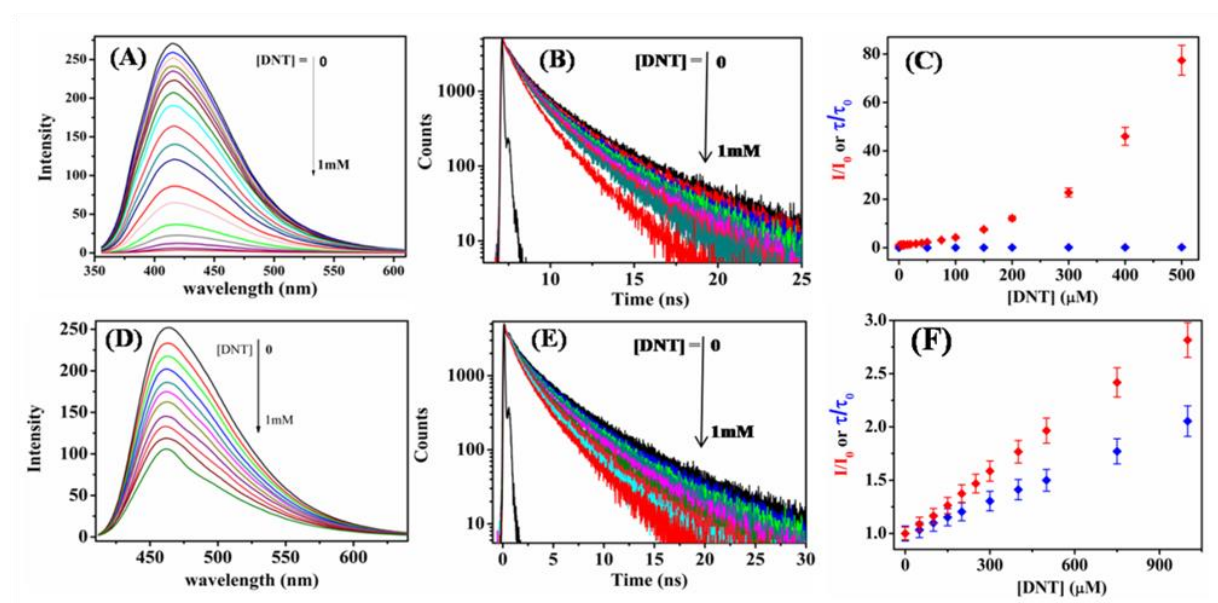


Figure 6.2. Quenching of steady state fluorescence and lifetime of *PAMAMdendrimerG1* (upper panel) and *PAMAMdendrimerG3* (lower panel) in presence of *DNT* in methanol. (C) and (F) represent the lifetime (blue) and steady state (red) SV plots for *G1* and *G3* *PAMAM dendrimers* respectively. $I(\tau)$ & $I_0(\tau_0)$ are the steady state intensities (*lifetimes*) of dendrimers in the presence & absence of quencher molecule.

When we plotted “ $1/\tau - 1/\tau_0$ (of dendrimers)” vs. “quencher concentration” in Figure 6.3, whose slope is a direct measurement of collisional quenching rate (k_{et}), we observed both the generations essentially report the same quenching rates [$\sim 4.7 \times 10^{10} \text{ M}^{-1}\text{S}^{-1}$ (for *G1*) and $\sim 4.5 \times 10^{10} \text{ M}^{-1}\text{S}^{-1}$ (for *G3*)]. However, in this case both the rates have levelled off to the upper

limit of any bimolecular diffusion controlled process in methanol.²²¹ A direct measurement of intrinsic bimolecular quenching rate using lifetime *SV* plot is not possible here as actual electron transfer rate is much faster compared to the bimolecular diffusion rate in methanol. Therefore we used an indirect method to obtain intrinsic *ET* rate within the *dendrimer-DNT* couples where we first obtained the association constant (*K*) of *dendrimer-DNT* complex using isothermal titration calorimetry (ITC) measurement and subsequently we kept *K* value fixed within the steady state *SV* fitting equation (equation 6.1) while fitted the steady state data. We will discuss it more elaborately in the succeeding part of this chapter.

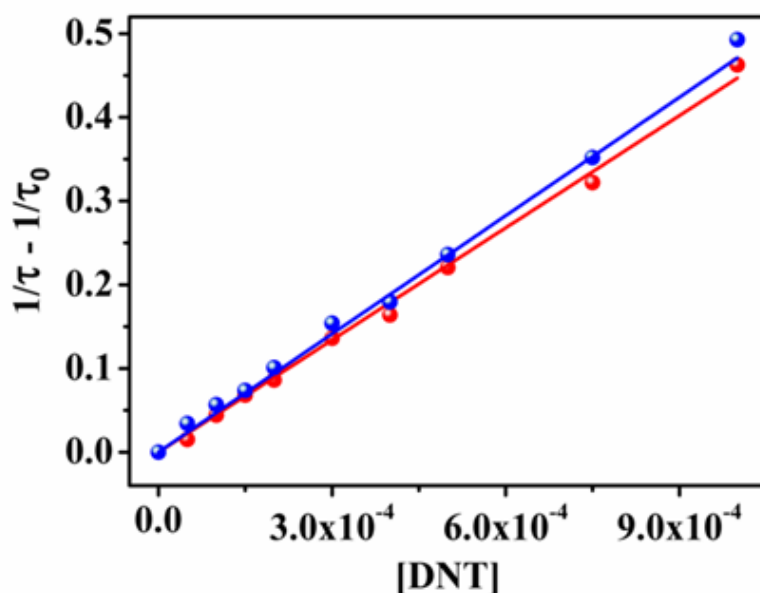


Figure 6.3. *SV* plots of lifetime quenching for *PAMAMdendrimerG1* (blue) and *G3* (red). Solid lines represent linear fit of the experimental data points.

Steady state *SV* plot, which accounts both static and collisional quenching, exhibits a strong upward curvature for *G1 dendrimer* (Figure 6.2.C), but almost linear for *G3 dendrimer* (Figure 6.2.F), particularly at high *DNT* concentration regime. Strong curvature nature of lower generation dendrimer is elucidated by a strong *dendrimer(G1)-to-DNT* complex formation, as an open structure of *G1 dendrimer* provides *DNT* an easy accessible route to the

binding sites. Conversely, a globular like structure and peripheral steric hindrance in higher generation dendrimer (*G3*) create hurdle for an efficient binding with *DNT* molecules (scheme 6.1). In summary, lifetime *SV* plots from both the generations report apparently same collisional *PET* rates though their intrinsic rate might be different. A direct measurement of intrinsic *PET* rate from *SV* plot is not possible as *PET* rate is faster than the diffusion controlled rate. Steady state *SV* plots from *G1 dendrimer* show a strong upward curvature as compared to *G3dendrimer* which is an indication of a stronger host-guest complex formation in former case.

6.2.3. Evidence of Host-Guest Complex Formation: Isothermal Titration Calorimetry Study

To get further insight to a *dendrimer-DNT* complex formation, we directly measured binding constant (*K*) values associated to the complex formations using ITC. ITC provides a quantitative measurement of thermodynamic parameters changes associated with the mixing between host and guest molecules; a further exploitation of these parameters provides a host-guest binding constant value. ²²²⁻²²³Heat change at constant temperature (25⁰C) during the addition of 1 mM of dendrimer solution to 0.2 mM *DNT* in methanol (stirring speed of 600 rpm) were recorded. ITC curves of heat change, when methanolic *DNT* was titrated with *G1* and *G3* dendrimers isothermally, are shown in Figure6.4.A & Figure6.4.C, respectively.

We observed an exothermic (negative ΔH) and spontaneous (negative ΔG) binding for both the cases (Table 1). From ITC measurements, we observed *DNT* has higher affinity of complex formation with lower generation dendrimer ($K_{G1-DNT} \sim 2,380 \text{ M}^{-1}$) as compared to the higher generation dendrimer ($K_{G3-DNT} \sim 1,270 \text{ M}^{-1}$). This is congruent to a larger steady state quenching of *G1* dendrimer compared to *G3* dendrimer as discussed earlier. In fact a large

number of studies have reported greater binding tendency of the lower generation dendrimers.²²⁴⁻²²⁸

Evidence of dendrimer-*DNT* complex formation from ITC study confirms the reason behind greater steady-state quenching of dendrimer fluorescence when compared with their corresponding lifetime quenching is due to a dendrimer-to-*DNT* dark complex formation. Dark complex contributes only to the steady state quenching. As the binding of *DNT* with *G1* dendrimer was found to be more spontaneous compared to *G3* dendrimer (Table 6.1), we observed a larger slope in steady state *SV* plot of *G1* dendrimer compared to *G3* dendrimer (Figure 6.2.C & Figure 6.2.F).

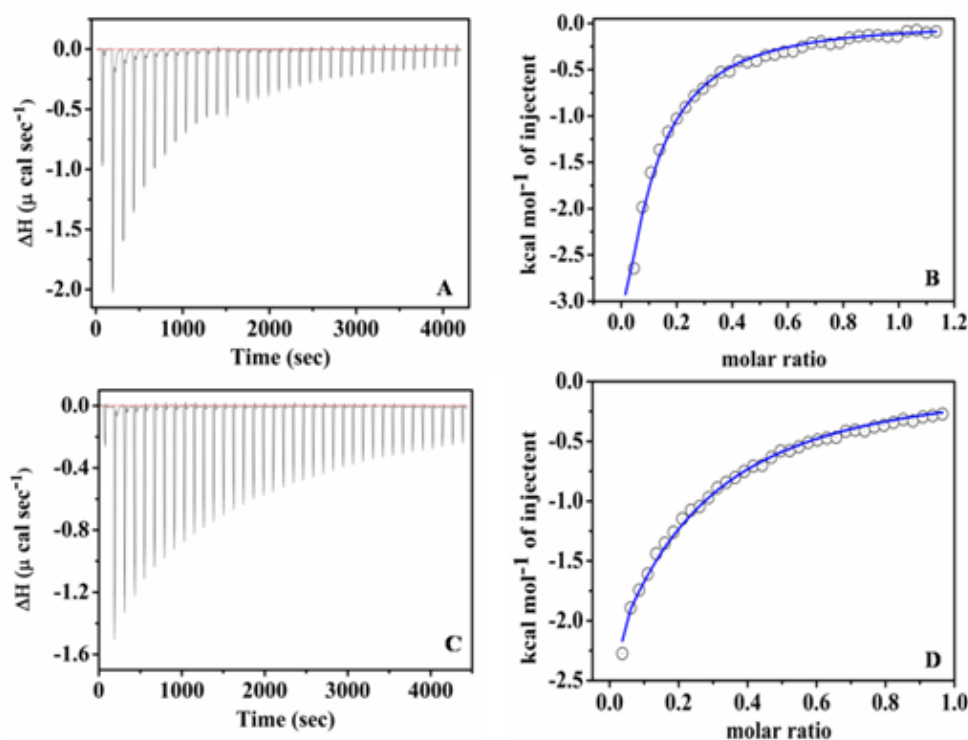


Figure 6.4. ITC raw data of heat change during titration of *DNT* with (A) *G1* and (C) *G3*PAMAM dendrimers in methanol. (B) and (D) are the analysis of the data and blue line represents conclusive fitting with one site binding model.

Table 6.1. Thermodynamic parameters associated to the binding of *DNT* to G1 and G3

System	Binding constant K (M^{-1})	ΔH (Kcal/mol)	ΔS (cal/mol/deg)	ΔG (Kcal/mol)
G1-DNT	2380	-19.1	-52.7	-17.8
G3-DNT	1270	-17.8	-41.5	-16.7

PAMAM dendrimers obtained from ITC measurements.

6.2.4. Electron Transfer Rate and Chemical Driving Force

As we discussed earlier, the actual electron transfer rate is higher than the diffusion controlled rate and hence we could not calculate the intrinsic ET rate directly due to the limitation of our TCSPC setup. So, we have calculated the intrinsic ET rate indirectly from the steady state S-V plot by assuming the contribution of both association constant and electron transfer rate constant. Using the numeric values of binding constant (K of Table 1) from ITC study, we obtained intrinsic *PET* rates (“collisional”) of dendrimer-*DNT* pairs from the fittings of steady state *SV* plots using the following equation.²²⁰

$$I_0/I = (1+K[Q]) (1+k_{et}[Q]) \dots\dots\dots(6.1)$$

Above equation is a modified *SV* equation which assumes steady-state fluorescence quenching is controlled by both, static quenching (due to dark complex formation) as well as collisional quenching. Numeric values of K were taken from ITC measurements for each dendrimer-*DNT* pairs and kept fixed in equation 6.1 while fitted the steady state *SV* curves (Fig. 6.2.C &6.2.F; red curves).

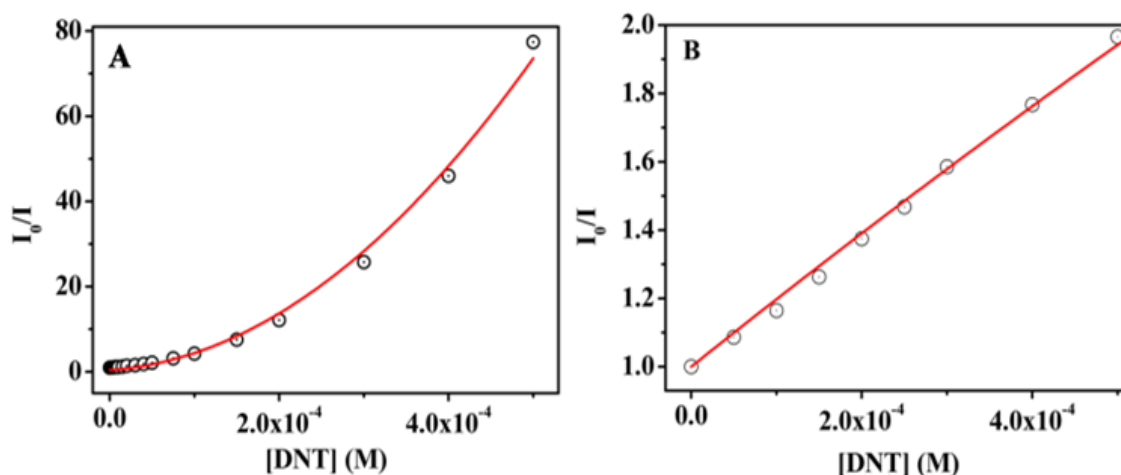


Figure 6.5. Fitting of the steady state S-V plots using equation 6.1 for (A) G1-DNT pair and (B) G3-DNT pair.

Figure 6.5.A & Fig. 6.5.B depict experimental data (same as Fig. 2C & Fig. 2F) of steady state SV plots and corresponding fitted curves using equation 6.1. From the fittings, k_{et} values were found to be $\sim 3.89 \times 10^{12} \text{ M}^{-1} \text{ S}^{-1}$ for G1 dendrimer and $\sim 1.15 \times 10^{11} \text{ M}^{-1} \text{ S}^{-1}$ for G3 dendrimer, respectively (Table 6.2). An accelerated PET rate in G1-DNT redox couple compared to the PET rate in G3-DNT couple is due to a higher chemical driving force (ΔG) associated with PET reaction in former couple. Rehm-Weller equation (equation 6.2) can be used for obtaining ΔG involved in a bimolecular PET process of donor-acceptor couple.

$$\Delta G = (E_{D/D^+}) - (E_{A/A^-}) - E_{00} - e^2 / \epsilon r_{D-A} \dots \dots \dots (6.2)$$

The oxidation potential of dendrimers (E_{D/D^+}) in above equation was obtained from cyclic voltammetry studies (Fig. 6.6). Cyclic voltammetry experiments were performed in a 25ml electrochemical cell with three electrodes configuration. Potentials were recorded with respect to Ag/AgCl electrode in aqueous solution of 0.1 M KCl. Platinum wire electrode and platinum rotating disc working electrode were used for all the measurements. Clear oxidation peaks detected for both the generation of dendrimers. The reduction potential (E_{A/A^-}) of the acceptor molecule DNT was taken from literature²²⁹ and E_{00} [$S_0(v=0)$ to $S_1(v=0)$ transition

energy of dendrimer] was calculated from the intersecting point (indicated with a black circle in Fig. 6.1) between excitation and emission spectra of the dendrimer. Electronic charge (e), dielectric constant (ϵ) were obtained from literature and donor-to-acceptor distance (r_{D-A}) was calculated from the known sizes of dendrimers and *DNT*.

Table 6.2. Calculated parameters associated with the electron transfer in the present system

Pairs	E_{ox} (vs SCE)	E_{red} (vs SCE)	E_{00} (eV)	ΔG_{et} (eV)	K_{et} ($M^{-1}S^{-1}$)
G1-DNT	1.25V	-1.14V	3.26	-1.03	3.89×10^{12}
G3-DNT	1.28V	-1.14V	2.69	-0.41	1.15×10^{11}

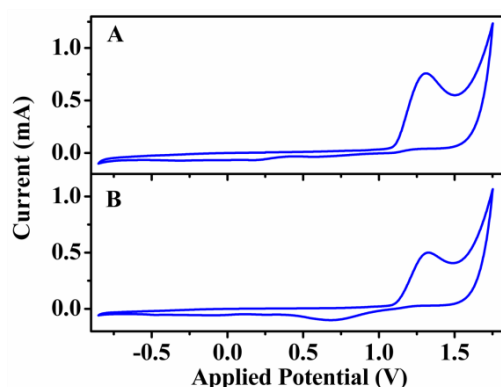


Figure 6.6. Cyclic voltammetry curves for (A) *G1* and (B) *G3PAMAM* dendrimers (represented vs. Ag/AgCl reference electrode).

The calculated $-\Delta G$ for *G1-DNT* couple (~ 1.03 eV) was found to be much higher as compared to 0.41 eV obtained for *G3-DNT* couple (Table 6.2.). Higher $-\Delta G$ causes the faster *PET* rate in *G1-DNT* couple as compared to *G3-DNT* couple.

6.2.5. Understanding the PET Mechanism: Role of Tertiary Amines of Dendrimer

In a comprehensive investigation to understand *PET* mechanism, we further studied *PET* reaction in *G3-DNT* pair in the presence of 1(N) HCl. This study shows available lone pair on

amine nitrogen inside the dendrimer donates electron to the *DNT* molecule at neutral pH (without HCl). When we compared between the lifetimes of *dendrimer* (in methanol) before and after addition of *DNT*, we observed dendrimer lifetime significantly reduced after *DNT* addition which we assigned due to *PET* from *dendrimer* to *DNT* (Figure6.2). However, same study in an acidic methanol solution (1 N HCl) shows no change in dendrimer lifetime after *DNT* addition (Figure 6.7). At low pH, the tertiary amines ($pK_a \sim 6.3$)¹⁹¹ in the interior branches of dendrimer are expected to remain protonated and these amine centres lose electron donating capability. Therefore no *PET* from dendrimer to *DNT* can be possible at low pH. This may be the actual reason for not observing any lifetime quenching of dendrimer on addition of *DNT* in acidic methanol solution. Therefore it may be stated that amine centres of dendrimers act as redox centres in electron transfer reactions. Our study will open the future possibility of using dendrimer based redox couple as a pH sensing agent. Nontoxic dendrimers have already emerged as a wonderful drug delivery agent for an easy injection procedure to a biological system. One can obtain information on local pH inside a living organelle by monitoring the fluorescence from dendrimer based sensors.

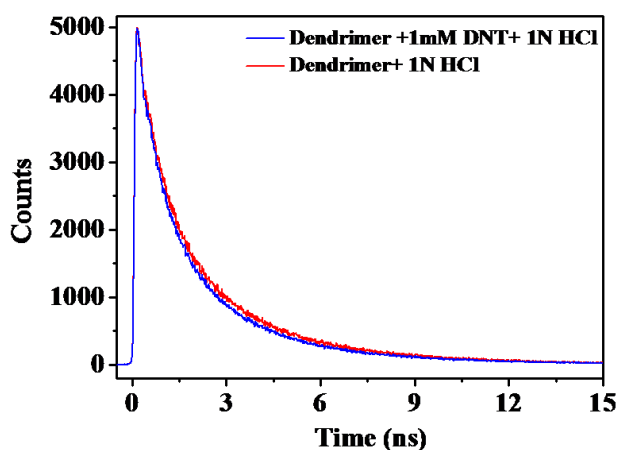


Figure 6.7. Fluorescence lifetime of the dendrimer after addition of 2,4-DNT in presence of 1(N) HCl solution.

6.3. Conclusion

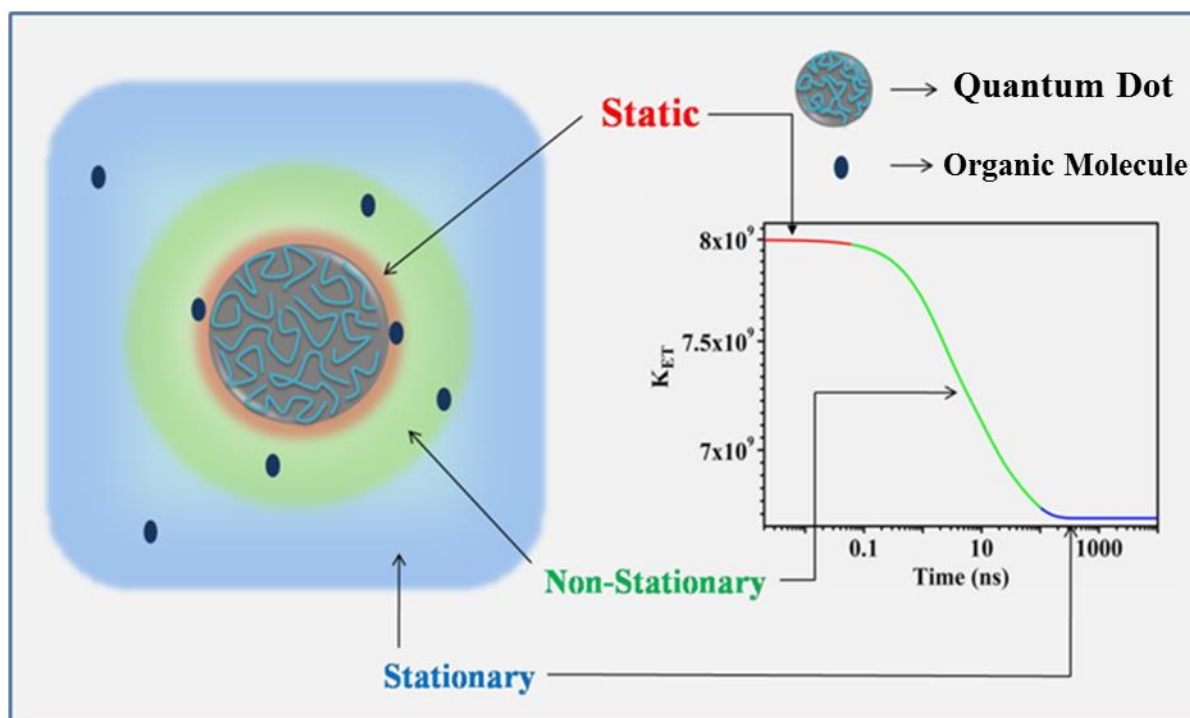
In this chapter we explored a new application of unmodified PAMAM dendrimer. Apart from pH sensing applications, quenching of *PAMAM* dendrimer fluorescence can be exploited for detecting nitroaromatic explosive compounds in solution as dendrimers show an exceptionally high electron transfer rate (and thereby fluorescence quenching rate) in the presence of a nitroaromatic compound. This study in one hand has explored the possibilities of several sensor based applications of *PAMAM dendrimers*, and in other hand this study showcases the novel redox properties of *PAMAM dendrimer* utilizing its intrinsic fluorescence which was hitherto unknown and not reported before. The tertiary amine centres of dendrimers not only responsible for intrinsic fluorescence, also act as an excellent electron donating centre in the presence of an electron deficient molecule. Inner cavities of dendrimers provide adequate rooms to the quencher molecules. A strong host-guest interaction holds the redox centres at proximal distance that causes accelerated electron transfer kinetics for dendrimers-*DNT* couples.

Diffusion Assisted Bimolecular Electron Transfer with Quantum Dots

7.1. Introduction

Electron transfer is a fundamental process in biology and material chemistry.²³⁰⁻²⁴¹ Photo induced electron transfer (ET) in solution is of convenient category to study diffusion assisted bimolecular reaction in solution phase for a number of reasons: reaction can be photo initiated, relatively simple process and temporal profile of fluorescence intensity can be exploited as a probe to study the kinetics.²³²⁻²³⁵ Diffusion controlled bimolecular ET involves three distinct quenching regimes: (1) At early time of the ET, kinetics is dominated by the reactant pairs those are already at proximal distance; no diffusion is required for ET to take place in this regime. This regime is called “static” (red region in scheme 7.1). (2) At a relatively longer time, ET occurs between the reactant pairs that are residing at a little longer separation than the encounter distance and requires diffusion to attain the encounter distance before ET to take place. This non-stationary state continues as long as equilibrium is established between the rates at which reactant pairs are disappearing through ET and the diffusion rate at which the encounter complexes are being formed (green region in scheme 7.1).²³²⁻²³⁵ (3) After sufficiently long time, reaction occurs between the reactant pairs those are separated by a long distance. In this regime ET is stationary in nature and maintains equilibrium with the diffusion rate.²³²⁻²³⁵ The ET here is controlled by the mass transportation rate rather than a kinetically controlled process (blue region in scheme 7.1). Therefore, a complete fitting function of a bimolecular ET reaction should consider all these three regimes. In a seminal work, Fleming and his coworkers studied the ET kinetics in rhodamine B-ferrocyanide reactant couple.²³³ They found Collin Kimball model are unable to reconcile the time resolved with steady state data using a same set of fitting parameter. However when

they added a position dependent intrinsic reaction rate to the Collin Kimball model within the sub-picosecond to sub-nanosecond time window, they obtained a fast ET time of 27.5 ps.



Scheme 7.1. Schematic representation for diffusion assisted bimolecular reaction between quantum dot and organic molecule.

Most commonly used classic Stern-Volmer (*SV*) equation is applicable only to the *stationary* regime of a *PET* reaction, which appears after a long-time where *ET* kinetics is considerably influenced by the mass transportation rate of the solvent rather than a kinetically controlled process.²³⁵ Therefore an intrinsically fast *ET* process may not be detected by classic *SV* plots, rather an apparent diffusion rate will be described within the plot. At an early response of *PET* in solution, electron transfer takes place among the reactant pairs those were already standing to an encounter distance at the time of photoexcitation. No diffusion is required for a bimolecular *ET* to take place in this regime. This regime is called *static*.²³⁵ Here *PET* rate is described by a constant *ET* rate coefficient. Apart from the *static* and *stationary* regimes, a third kind of bimolecular *ET* description in solution is called *nonstationary* which represents

a transition from a purely kinetic *static regime* to a purely diffusive *stationary regime*.⁹ *ET* coefficient is a time dependent parameter here and this *nonstationary* regime continues until the equilibrium is reached between the rates at which reactant pairs are disappearing through *ET* and new encounter complexes are being formed through diffusion. A complete fitting model should consider all these three regimes in a bimolecular *ET* process taking place in solution. Study of fluorescence quenching in solution medium has been considered as a most convenient technique to study bimolecular *ET* process.

Interestingly, in a recent report Burshtein provided statistical analysis based *encounter theory* for explaining bimolecular *ET* in solution which has been successfully confronted several experimental verifications.²⁴² *Encounter theory* enables a bimolecular *ET* reaction to be modelled with a distance dependence *ET* rate coefficient in a much simpler approach.²⁴² Experimental verification of *encounter theory* was performed by Vauthey and his co-workers by studying *ET* from *N,N*-dimethylaniline to 3-cyanoperylene in a highly viscous imidazolium-based room-temperature ionic liquids (*RTIL*).²³⁵ They used reaction probability function $[w(r)]$, reaction pair distribution function $[n(r,t)]$ and inter-reactant distance (r) in fitting equation; the numeric solutions of these functions enabled them a conclusive fitting to their experimental data.²³⁵ In a very recent work, Maroncelli and his co-workers used a spherically symmetric diffusion equation within a framework of a Marcus-type description of *ET* reactions to study *PET* from *DMA* to a photo excited 9,10-dicyanoanthracene molecule in various ionic liquid solvents.²⁴³ Their analysis, resembling to *encounter theory*, showed an apparently faster bimolecular *ET* rate within the high viscous solvents compared to the *ET* rate in low viscous solvents is due to the viscosity effect of the high viscous solvents that appreciates mostly the *static* regime (where apparent *ET* rate is faster for an intrinsically fast *ET* process) of a diffusion-limited *ET* process rather than the *stationary* regime (where *ET* kinetics is apparently slower) as get appreciated mostly within a less viscous solvent.²⁴³

Study of *PET* in inorganic semiconductors is important for improving their wide spread applications in modern devices where *ET* is an integral part of it. Metal chalcogenide (e.g., *CdSe*, *CdS*, *PbSe*, *PbS* etc.) nanocrystals have emerged as a potential contender as building blocks of optoelectrical devices for their harnessing size dependent optical and electrical properties. Therefore desired functionalities within the device can be facilitated by tuning their sizes to the requisite lengths.¹⁰¹ Matched band gap semiconductors in a device either assist charge carriers to recombine (i.e., *LEDs*) or impede the charge recombination by taking away oppositely charged carriers to the appropriate electrodes (i.e., solar cell devices). In both type of devices *ET* is a fundamental part of it. Designing of new semiconductor architectures would consider an accelerated interfacial *ET* from a photo excited nanocrystal to a matched large bandgap semiconductor (desired functionality of solar cells) or an efficient *ET* to an appropriate band (with matched energy) of an electron deficit nanocrystal that would facilitates the electron-hole recombination (desired functionality of *LEDs*). Therefore, study of *PET* in a semiconductor nanocrystal is fundamentally important that will help the rational designing of next generation devices. In a remarkable work, Kamant and his co-workers have demonstrated *PET* at *QD-metal oxide* junction using a series of *CdSe QDs* varying their sizes (~2.8, 3.3, 4.0 and 4.2 nm) coupled to large band gap *metal oxides*. Their study of electron injection to a continuum electron accepting state of metal oxide shows unlike dye-sensitized metal oxide, *ET* reactions in their study does not involve any unthermalized hot-electron.¹¹⁴ They justified their observation by considering a large ratio of *ET* cooling rate to *ET* rate. A number of recent studies have observed an ultrafast *PET* from a photo excited *QD** to an organic dye (or to a semiconductor particle) attached to *QD* in solution. Detection of an ultrafast *PET* in these studies has opened up the possibility toward proper utilization of multiple excitation generation (*MEG*) and thereby enabling a clear roadmap for dramatic improvement of photo current generation efficiency of a device.²⁴⁴ For an instance, Lian and

his co-workers detected an ultrafast (~ 12 ps) *PET* at *CdS QD-Rhodamine B* interface; indicating a further extension of their work would help researches the proper exploitation of *MEG*.¹¹⁵ A similar demonstration of ultrafast (few hundred picoseconds) intrinsic charge transfer from *InSe* to *GaSe* was also reported within the *InSe-GaSe* complex.²⁴⁵ Both these studies obtained *ET* rates from the *donor-to-acceptor* static complex (non-collisional *ET*) in solution, thus *ET* observed here is free from any diffusional characteristic of the solvent.^{115,245} However, in a bimolecular collisional *ET* process in solution, a higher intrinsic *ET* rate gets level off at the solvent's diffusion limit. Therefore, the reliability of collisional *ET* rate obtained in an experimental study is more when intrinsic *ET* kinetics is slower compared to the mass transportation rate of the medium. In a recent work on collisional *ET* study, Wang et al showed an efficient fluorescence quenching of *carbon dot* by electron acceptor molecules *4-nitrotoluene* ($9.5 \times 10^9 \text{ M}^{-1}\text{S}^{-1}$) and *2,4-dinitrotoluene* ($2.1 \times 10^{10} \text{ M}^{-1}\text{S}^{-1}$) within a low viscous solvent.²¹⁹ The rate constant they observed particularly for *2,4-dinitrotoluene* is at the limit of any bimolecular diffusion controlled process in that solution. Assuming *ET* rate to be a time independent parameter below the diffusion limit of a bimolecular quenching reaction in solution, most of the studies show a bimolecular *ET* can be conclusively fitted with conventional Stern-Volmer (*SV*) equation.^{219,236}

Keeping the all facts in mind we have studied diffusion assisted electron transfer involving quantum dots and organic molecules. We have studied two types of quantum dot (core only and core shell type) with organic donor [N-methylaniline (NMA)/acceptor [2,4,-dinitrotoluene (DNT)] molecules. We have fitted our data with diffusion assisted models with certain modifications.

7.2. Results and Discussions

7.2.1. Core Type Quantum Dots

7.2.1.1. Sample Characterization, Optical and Band Properties

Dimensions of CdS QDs were determined from the transmission electron microscopy (TEM) and fluorescence correlation spectroscopy (FCS) measurements which were found to be ~3.8 nm, ~4.5 nm and ~5.4 nm for CdS440, CdS460 and CdS480, respectively. TEM measurement confirms the average particle sizes of CdS440, CdS460 and CdS480 are 3.8 nm, 4.5 nm and 5.4 nm, respectively; nicely agreed with the sizes reported by the supplier Sigma-Aldrich (figure 7.1) Fluorescence correlation spectroscopy (FCS) experiments were performed by using a confocal microscope (Zeiss LSM 780). A diode laser of 405nm has been used to excite the samples. FCS data was used for determining translational diffusion coefficient (D_t) of QDs in toluene. Details of this technique, measurement procedure and instrumental setup are described in chapter 2. D_t of CdS480, CdS460 and CdS440 were found to be 0.9×10^{-6} , 1.45×10^{-6} and 1.97×10^{-6} $\text{cm}^2\text{sec}^{-1}$, respectively, fairly correlating with their respective sizes obtained from TEM measurements (figure 7.2). D_t value of NMA (non fluorescent) in toluene was calculated using the size obtained from DFT calculation and used it in Stokes-Einstein equation. These D_t values were used as a fitting parameters in diffusion equation of electron transfer reaction. NMA and oleic acid capped QD both are hydrophobic in nature. In a hydrophobic medium like toluene both are highly soluble and ET is expected to be collisional in nature. ET from single quantum state NMA (HOMO-level) to the valence band of a photo excited QD* (type II band alignment, Figure 7.3.a) causes significant quenching of the excited state QD lifetime and steady-state emission (Figures 7.4).

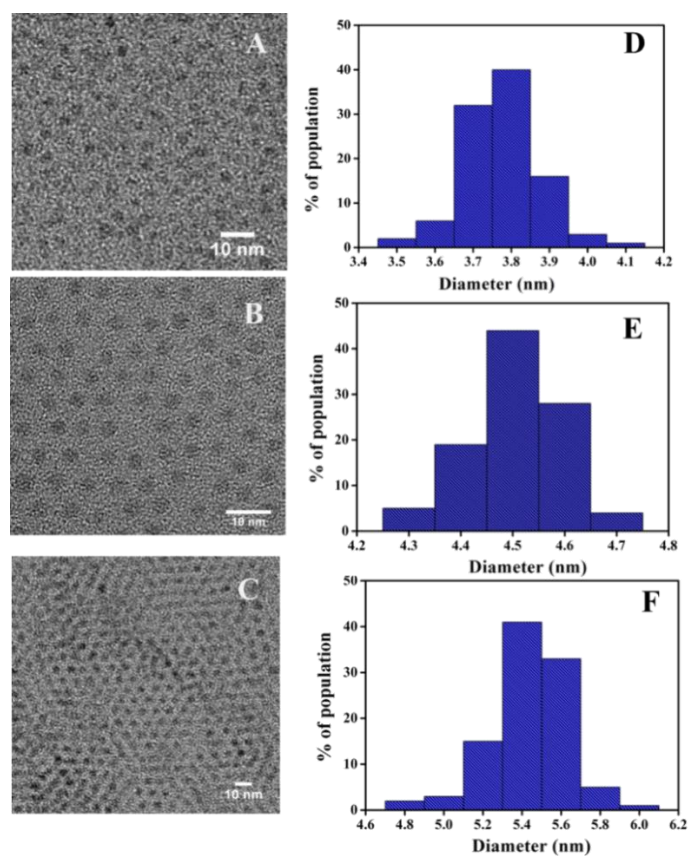


Figure 7.1. Left panel: Transmission electron microscopy images of CdS quantum dots: (A) CdS440, (B) CdS460, and (C) CdS480. Right panel: Corresponding size distribution histograms of (D) CdS440, (E) CdS460 and (F) CdS480.

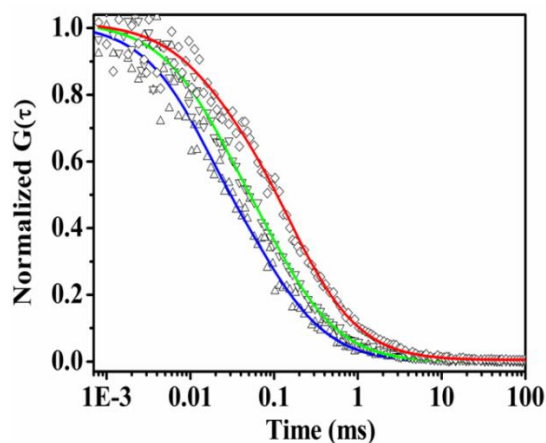


Figure 7.2. Fitted auto correlation curves for CdS440 (blue), CdS460 (green) and CdS480 (red) in toluene.

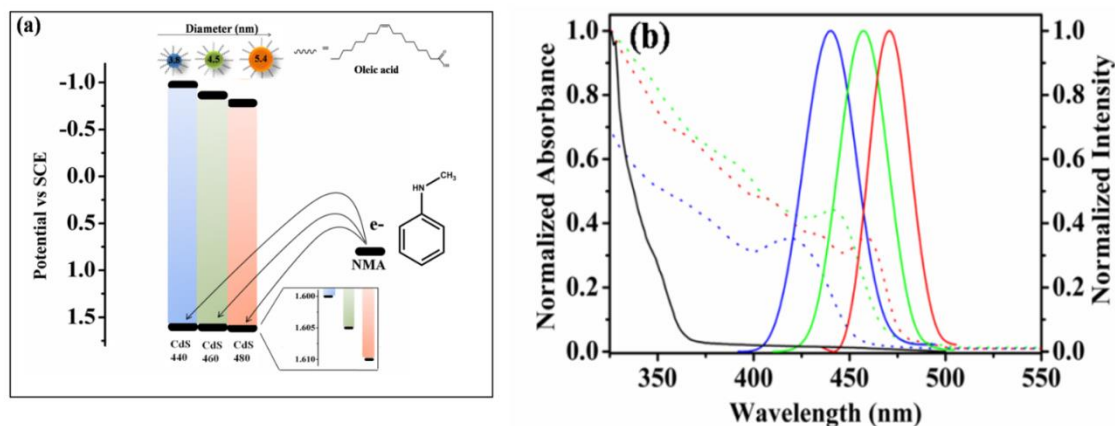


Figure 7.3. (a) Energy band alignment diagram of *QD-NMA* pairs used in this study. (b) Absorption spectra of *NMA* (black solid line), *CdS440* (3.8 nm, blue dotted line), *CdS460* (4.5 nm, green dotted line) and *CdS480* (5.4 nm, red dotted line). Corresponding emission spectra of the *QDs* are shown in solid lines (same colours with absorption spectra).

Excitation (λ_{ex}) at 375 nm used in this study selectively excites only the acceptor molecules (*QD*) within a *QD* and *NMA* mixture. Thus the possibility of ET from LUMO level of *NMA* to the conduction band of *QD* is convincingly ruled out. ET is also not possible to an energetically much higher state (-4.7 eV vs. SCE), LUMO of an unexcited *NMA* from the conduction band of *QD**. A second possibility of quenching is elucidated by the probable energy transfer from *QD** to *NMA*, which is not possible here due to the absence of spectral overlapping between the donor's emission and acceptor's absorption (Figure 7.3.b).

7.2.1.2. Quenching Experiment and Fitting Models

7.2.1.2.1. Fitting to the steady state data

Both excited state lifetime and steady state fluorescence of a series of CdS quantum dots (*QDs*) with different sizes in toluene were quenched by electron donor molecule *N-methyl aniline* (*NMA*). Steady-state Stern-Volmer (S-V) plot was obtained by plotting the steady-state fluorescence intensity ratios of *QD** in the absence (I_0) and presence (I_c) of quencher

molecule (*NMA*) as a function of quencher concentration up to 0.147 M (Figure 2). Two striking features are revealed from the S-V plots in Figure 7.5.: (1) the slope of the curve increases with increasing the *QD* particle size; indicating the overall ET rate increases within the larger size *QD*. (2) All the three curves in Figure 7.5. are straight at low quencher concentrations, however, significantly bent with an upward curvature at high *NMA* concentrations. Overall curvature nature is more prominent within the larger size particles (i.e., CdS480); indicating the mixing of quasi-static states (originated at the initial time of the kinetics and higher quencher concentration) with the transient and stationary states of ET.

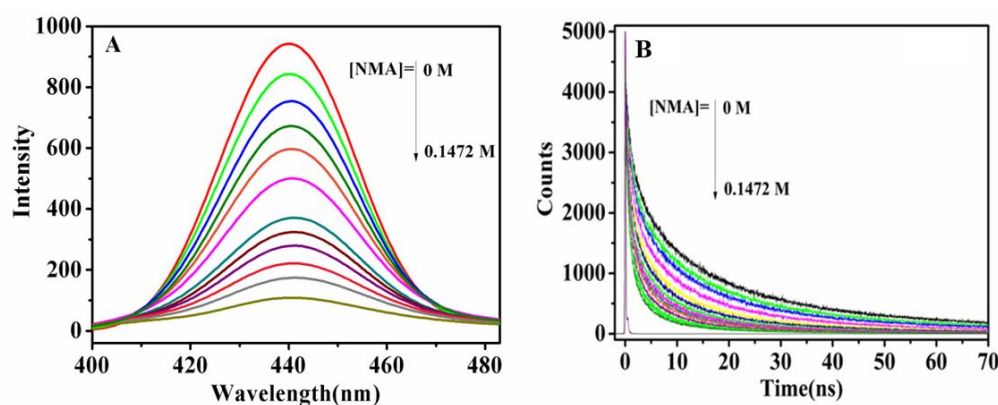


Figure 7.4. (A) Steady state emission spectra and (B) lifetime decay profile of CdS440 in toluene at various NMA concentrations. Excitation wavelength = 375 nm.

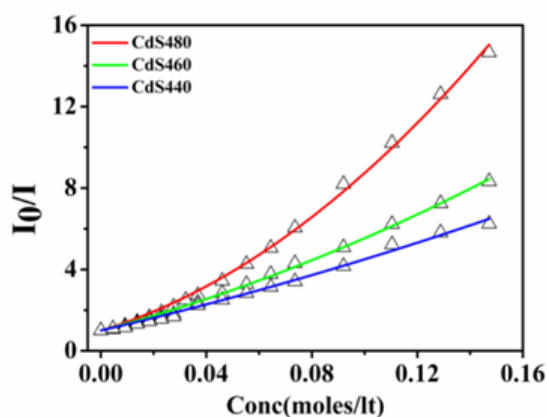


Figure 7.5. Steady state S-V plots of *QD-NMA* pairs. SQCK fittings for CdS440 (blue), CdS460 (green) and CdS480 (red) are shown by the solid lines.

A classical S-V equation only considers the stationary regime of ET kinetics and assumes a linear dependency of fluorescence quenching of QD^* with the quencher concentrations. Thus a special treatment of SQCK diffusion model was employed in this study that considers all the three distinct regimes of a bimolecular ET kinetics.²³²⁻²³³ A valid fitting model should fit both the steady-state and time-resolved data using a same set of fitting parameters, provided no ultrafast component is overlooked in time-resolved study. The functional form of time resolved fluorescence intensity $[I(t)]$ of QD^* in the presence of NMA is obtained by the time integration of the survival probability differential equation $[dS(t)/dt = \{-1/\tau_0 - ck(t)\}S(t)]$ of QD^* in presence of NMA as,²³²⁻²³⁵

$$I(t) = I(0) \exp(-t / \tau_0 - c \int_0^t k(t') dt') \dots \dots \dots (7.1)$$

Where $S(t)$ be the survival probability of QD^* when the excited state depopulation of QD^* is taking place simultaneously by ET as well as natural lifetime decay processes. τ_0 is the excited state lifetime of QD in the absence of NMA (natural lifetime). $k(t)$ be the time dependent ET rate coefficient (or sink term), and c is the bulk concentration of NMA . Unravelling of the ET kinetics from the overall excited state lifetime decay process was strategically made by constructing a survival probability function $[S_q(t)]$ of QD^* in the presence of NMA , whose decay describes the ET process only as²³²

$$S_q(t) = S(0) \exp(-c \int_0^t k(t') dt') = S(t) / \exp(-t / \tau_0) \dots \dots \dots (7.2)$$

Rate coefficient $k(t)$ in the above equation was constructed using Collin Kimball boundary conditions; assuming the quenching rate of a bimolecular reaction is proportional to the probability that a QD^* molecule finds one NMA molecule at a distance between R and

$R + \delta r (\delta r \rightarrow 0)$.²³³ R is the reaction radius or encounter distance. The time dependent rate coefficient is constructed using Collin Kimball model as,²³²⁻²³³

$$k_{CK}(t) = \frac{4\pi DRk_0}{4\pi DR + k_0} \left[1 + \frac{k_0}{4\pi DR} \exp \left\{ \left(\frac{4\pi DR + k_0}{4\pi DR^2} \right)^2 Dt \right\} \operatorname{erfc} \left\{ \left(\frac{4\pi DR + k_0}{4\pi DR^2} \right) \sqrt{tD} \right\} \right] \dots\dots\dots(7.3)$$

Where D is representing the mutual diffusion coefficient between QD^* and NMA ; k_0 is the bimolecular ET rate (intrinsic). Diffusion constant of fluorescent QD^* and non-fluorescent NMA were obtained from FCS measurements and DFT calculation, respectively. D values were found to be $\sim 1.395 \times 10^{-5}$, 1.343×10^{-5} and 1.285×10^{-5} cm^2/sec , respectively, for $CdS440-NMA$, $CdS460-NMA$ and $CdS480-NMA$ pairs. A time integration of equation 7.1 using Collin Kimball sink term [from equation 7.3] provides the theoretical expression of steady-state fluorescence intensity of QD^* [I_C] in the presence of NMA . Which was used for constructing a fitting equation of steady state S-V plot as follows,^{219,237}

$$\left(\frac{I_0}{I_C} \right)_{CK} = 1 + 4\pi RD\tau_0 k_0 \left[\frac{1 + (R / \sqrt{D\tau_0})}{k_0 + 4\pi RD + 4\pi R^2 \sqrt{D / \tau_0}} \right] c + \dots\dots\dots(7.4)$$

The above expression is based on an assumption that ET reaction can takes place only at an encounter distance R and sharply falls to zero at any other separations. This is clearly an unrealistic assumption that could not explain the upper curvature of the steady state S-V plot at higher quencher concentration. Equation 7.4 predicts only a linear dependency of QD^* fluorescence intensity with the quencher concentration. Therefore, in this work we relaxed this assumption by considering bimolecular intrinsic ET can take place in other separations (r) also, as long as r falls within the range $a \leq r \leq R$. Where a is the physical contact distance of QD and NMA in $QD-NMA$ complex.²³² Reaction at $r > R$ is purely diffusion assisted. At $r = a$, reaction is kinetically controlled and at $a < r < R$, reaction dynamics passes through a

transition from purely static regime to a purely diffusion regime. We further introduced a static quenching time parameter $[\tau_q(r)]$, as proposed by Szabo, denoting the position dependent non-radiative lifetime in a bimolecular quenching process.²⁴⁰ $\tau_q(r)$ is correlated to the sink term $[k(r)]$ as, $k(r)=1/\tau_q$.²⁴⁰ Where τ_q describes the kinetic portion of an ET reaction. Solution of steady-state Collin Kimball diffusion equation using the position dependent sink term $[k(r)]$ provides an expression for steady-state fluorescence intensity ratio containing intrinsic ET rate coefficient (k_0) same as equation 7.4; where τ_q is correlated to k_0 as,

$$k_0 = 4\pi DR \frac{(R-a)\lambda \cosh \lambda - [(R-a) - \{\lambda^2 aR / (R-a)\}] \sinh \lambda}{a\lambda \cosh \lambda + (R-a) \sinh \lambda} \dots\dots\dots(7.5)$$

where, $\lambda=(R-a)/\sqrt{(\tau_q D)}$

A more realistic expression of equation 4, that can conclusively fits the upper curvatures of S-V plots was obtained by considering Szabo's assumption of a position dependent sink term and subsequently making the encounter distance less restrictive (assuming $a \leq r \leq R$) in Collin Kimball model as,

$$\left(\frac{I_0}{I_C} \right)_{SQCK} = \left[1 + 4\pi R D \tau_0 k_0 \left\{ \frac{1 + (R/\sqrt{D\tau_0})}{k_0 + 4\pi R D + 4\pi R^2 \sqrt{D/\tau_0}} \right\} c + \dots \right] \exp(\nu c) \dots\dots\dots(7.6)$$

$$\nu = (4/3)\pi(R^3 - a^3)$$

The above equation is similar with equation 7.4; except the additional exponential term $[\exp(\nu c)]$, which nicely reproduces the upward curvatures of S-V plots in Figure 7.5. Therefore using this modified fitting equation, we can take the wealth of static quenching phenomenon of a bimolecular ET reaction taking place in a solution medium.

7.2.1.2.2. Fitting to the time resolved data

Following the recipe of Fleming and his coworkers, static quenching rate constant term [$k_{SQ}(t)$] was incorporated within the time dependent fluorescence intensity expression also (equation 7.1); assuming overall time dependent ET rate coefficient [$k(t)$] is a sum of static and diffusion rates [$k(t)=k_{SQ}(t)+k_D(t)$] as,²³²

$$I(t) = I(0) \exp \left[-\frac{t}{\tau_0} - c\nu \left\{ 1 - \frac{\tau_q}{\nu} k_{SQ}(t) \right\} - c \int_0^t k_D(t') dt' \right] \dots\dots\dots(7.7)$$

$k_D=k_{CK}$

Above equation, elucidating the excited state depopulation kinetics of QD^* in the presence of NMA , can also provide a theoretical expression of $S_q(t)$ when normalised with the excited state lifetime profile of QD^* in absence of quencher as,

$$S_q(t) = I(t) / I(0) \exp(-t/\tau_0) = \exp \left[-c\nu \left\{ 1 - \frac{\tau_q}{\nu} k_{SQ}(t) \right\} - c \int_0^t k_D(t') dt' \right] \dots\dots\dots(7.8)$$

This equation was used to fit the experimental $S_q(t)$ curves in Figure 7.6, however, provided inadequate fittings. Our constructed fitting function (equation 7.8) essentially considers two fundamentally different ET processes: (1) within the reaction sphere ($a \leq r \leq R$) ET is static and a strong distance dependence of $1/\tau_q$ is expected [$k_{SQ}(t)=(\nu/\tau_q)\exp(-t/\tau_q)$]. (2) Outside this volume ($r > R$) reaction is purely diffusive in nature; Collin Kimball diffusion rate equation (equation 7.3) could nicely explains this regime. However, considering these two phenomena inadequately fitted our time resolved data. On further modification to equation 7.7 (and eventually to equation 7.8), we considered another non-radiative decay channel that can cause excited state depopulation of QD^* , and originated from the presence of intrinsic “defect sites” (act as a quencher) statistically distributed over the quantum dot surface.¹¹⁶ This assumption

led to a conclusive fitting to both steady-state (Figure 7.5) and time-resolved data (Figure 7.6) using a same set of fitting parameters; except a slight variation in R values obtained from steady-state and lifetime fittings (Table 7.1). Following Tachiya's formula of poisson type distribution of the quencher sites, we introduced a depopulation channel in equation 7.7 that accounts the defect induced quenching process along with ET as,¹¹⁶

$$I(t) = I(0) \exp \left[-\frac{t}{\tau_0} - cv \left\{ 1 - \frac{\tau_q}{\nu} k_{SQ}(t) \right\} - c \int_0^t k_D(t') dt' - m \left\{ 1 - \exp \left(-\frac{t}{\tau_d} \right) \right\} \right] \dots\dots\dots (7.9)$$

Where m is the average number of defect sites per QD and τ_d is the defect induced quenching time.¹¹⁶ Figure 7.7 shows the static, non-stationary and stationary regimes of electron injection rates for all the three QD - NMA pairs using best fitting parameters. The average number of defect sites per QD was found to increase from ~ 1.05 (CdS440) to ~ 1.53 (CdS480) as QD size is increased from 3.8 to 5.4 nm. This fact rationalizing the descending trend of QDs ' average lifetimes in the absence of NMA from ~ 5.34 ns to ~ 4.16 ns as QD size is increased from ~ 3.8 nm to ~ 5.4 nm.

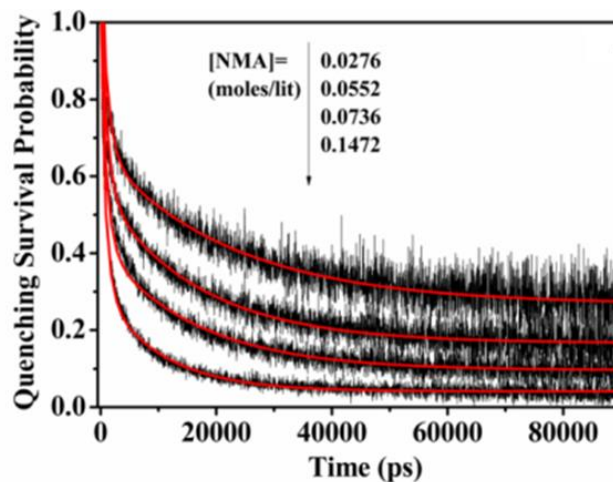


Figure 7.6. Time evolution of experimentally measured survival probability due to ET process only CdS440 at various quencher concentrations. Red lines represent the SQCK fittings.

More quencher sites in larger dimension *QD* (CdS480) drives the defect induced quenching to a relatively faster time ($\tau_d=1.1$ ns) as compared to that ($\tau_d =1.4$ ns) obtained in a smaller size *QD* (CdS440). In this study, we obtained ~3 times faster ET rate ($k_0 \sim 8.3 \times 10^9$ M⁻¹S⁻¹) from larger size *QD* (CdS480) as compared to that ($k_0 \sim 2.74 \times 10^9$ M⁻¹S⁻¹) obtained from a smaller size *QD* (CdS440); nicely correlating with the change in their chemical driving forces (larger *QD* has slightly higher $-\Delta G$ value, Table 7.1).

Table 7.1. SQCK time resolved [$S_q(t)$] and steady-state S-V fitting parameters of *QD-NMA* pairs [using equations 7.6-7.9 with $k_D(t)$ from equation 7.3 & k_0 from equation 7.5]. τ_q^{neat} is the *QD** lifetime in neat *NMA*. $R_{tr}(R_{ss})$ is the reaction radius (R) obtained from time-resolved (steady-state) SQCK fitting. Unit of R and a is nm.

CdS	a	$R_{tr}(R_{ss})$	$\tau_q(\text{ns})$	$\tau_q^{neat}(\text{ns})$	$k_0(\text{M}^{-1}\text{S}^{-1})$	$\Delta G(\text{eV})$
440	2.21	2.23(2.29)	0.70	0.53	2.74×10^9	-0.790
460	2.56	2.57(2.62)	0.45	0.45	4.31×10^9	-0.795
480	3.00	3.02(3.06)	0.25	0.37	8.30×10^9	-0.800

7.2.1.3. The Factors Affecting the ET Kinetics

This observation is indicating that our ET kinetics appears in the normal regime of the Marcus non-adiabatic ET model as (after applying Fermi's golden rule),²⁴⁶⁻²⁴⁷

$$k_{ET} = \left(\frac{\pi}{\hbar^2 \lambda_S k_B T} \right)^{1/2} |V|^2 \exp\left(-\frac{G^*}{k_B T} \right) \dots \dots \dots (7.10)$$

V in the above equation is representing the electronic coupling parameter between reactant and product states. $G^* = [(\Delta G^0 + \lambda_S)^2 / 4\lambda_S]$ and λ_S are the activation energy and solvent reorganisation energy, respectively. In a recent work by Vauthey and his co-workers have shown that two fluorescent dye molecules with same intrinsic ET rates against a quencher molecule can possibly give two different ET rates (apparent) when there is a significant difference in the excited-state lifetimes (τ_0) among the dye molecules.²⁴⁸ A short-lived dye can survive mostly in static regime where ET rate is high (at initial time of the ET kinetics, Figure 7.7). Whereas, for a long lived dye ET is mainly controlled by slow mass transportation rate at longer time rather than a fast kinetically controlled process. In our case also similar trend was observed: CdS440 ($\tau_0 = 5.34$ ns, $k_0 = 2.74 \times 10^9$ M⁻¹S⁻¹), CdS460 ($\tau_0 = 4.61$ ns, $k_0 = 4.31 \times 10^9$ M⁻¹S⁻¹) and CdS480 ($\tau_0 = 4.16$ ns, $k_0 = 8.3 \times 10^9$ M⁻¹S⁻¹).

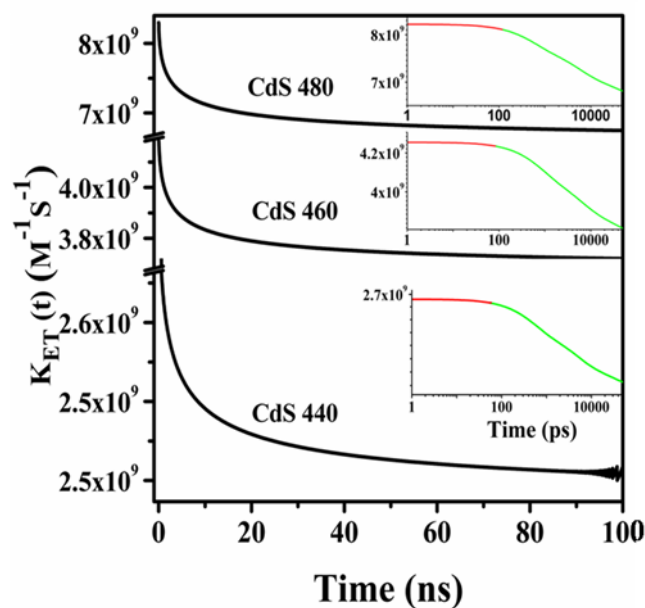


Figure 7.7. Time evolution of the rate coefficient of electron transfer from *NMA* to three different size *QDs* (obtained from SQCK fittings). The insets show the same plots in log scale (time axis): static (red line) and non-stationary (green line) regimes are clearly visible within the plot.

However, by studying ET in neat *NMA* (quencher as solvent) we confirmed that the trend of ET rate (k_0) obtained from SQCK fitting is not due to a fudge factor obtained from dissimilar lifetimes among the *QD* particles. In neat *NMA*, where excited state lifetime (τ_q^{neat} , Table 7.1) of *QD** is solely determined by the intrinsic ET rate (diffusion independent), we observed a similar trend of τ_q^{neat} with static quenching time (τ_q , Table 7.1) obtained from SQCK fitting of *QD-NMA* pair in toluene. This observation also rules out the possibility of more local concentration of *NMA* around a bigger size *QD* in toluene to become a probable reason of getting higher ET rate as compared to the smaller size *QD* in toluene. On a further investigation, we studied the temperature response of ET rates from all the three *QDs* in toluene using Arrhenius type plot of Marcus non-adiabatic ET equation (Table 7.2 and Figure 7.8). From the slope, we obtained a lesser activation barrier for CdS480 (~6.54 kJ/mole) as compared to CdS460 (~6.73 kJ/mole) or CdS440 (~6.93 kJ/mole).

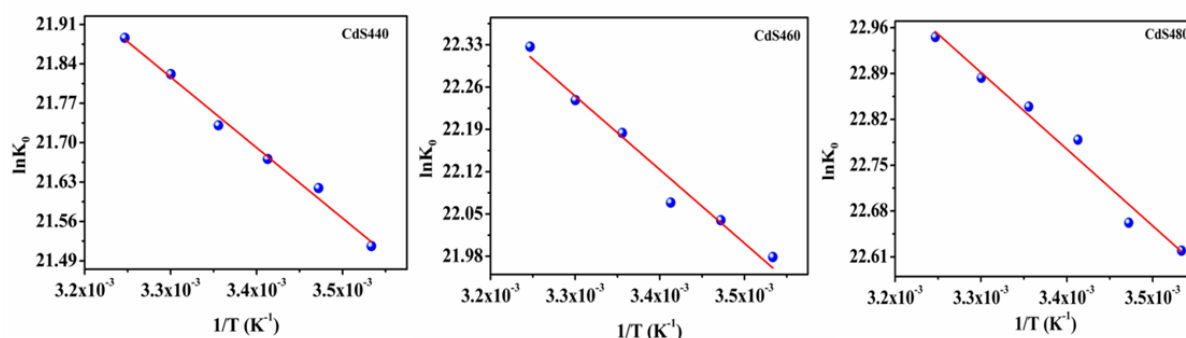


Figure 7.8. Plot of $\ln k_{ET}$ as a function of $1/T$ (Arrhenius plot) for the three *QD-NMA* pairs. Red lines are the linear fit to the experimental data (blue solid balls). Activation energies were calculated from the slope of the fitted lines and equation 7.10.

Table 7.2. Temperature dependent electron transfer rate constants and calculated activation energy for the three quantum dots in toluene. $k_{ET}=k_0$ in SQCK fittings.

QD	Temperature(K)	$k_{ET} (\times 10^9 M^{-1}S^{-1})$	Activation Energy (KJ/mole)
CdS 440	283	2.21	10.43
	293	2.45	
	303	2.58	
	313	2.74	
	323	3.01	
	333	3.20	
CdS 460	283	3.51	10.12
	293	3.73	
	303	3.84	
	313	4.31	
	323	4.55	
	333	4.97	
CdS 480	283	6.66	9.7
	293	6.95	
	303	7.89	
	313	8.30	
	323	8.67	
	333	9.23	

This observation nicely correlates with the sequence of their ET rates. In this study, same ET rate was reproduced from steady state and time resolved fittings of experimental data using a same set of fitting parameters. This can only be possible when no ultrafast ET component is

overlooked. ET rates observed from all the three *QD-NMA* pairs in this study are significantly lower than the diffusion controlled limit ($\sim 1.1 \times 10^{10} \text{ M}^{-1}\text{S}^{-1}$) of any bimolecular process in toluene. Therefore, the ET rates reported in this study are truly kinetically controlled rather than a diffusion limited process.

7.2.2. Core-Shell Type Quantum Dot

In this section we describe the electron transfer phenomena involving two CdSe/ZnS core/shell type quantum dots of different sizes. We have modelled the electron transfer phenomena where the quantum dot acts as both electron donor and acceptor. We have chosen N-methyl aniline (NMA) for the electron injection to the valance band of the photoexcited quantum dot and 2,4-dinitrotoluene (DNT) as an electron acceptor from the conduction band of the quantum dot.

7.2.2.1. Sample characterizations

Overall sizes and core diameters of CdSe/ZnS core shell QDs were obtained from the specification sheet provided by the supplier (*Sigma-Aldrich*). We confirmed the integrity of the QD samples just before commencing the experiments by measuring their sizes using fluorescence correlation spectroscopy (FCS) study [Figure 7.9]. Overall dimensions (including capping ligands) obtained from the FCS studies nicely correlated with the reported values as provided by the supplier ($\sim 6 \text{ nm}$ and $\sim 4.4 \text{ nm}$, respectively for QD560 and QD480). D_t of QD480 and QD560 were found to be $\sim 1.72 \times 10^{-6}$ and $1.02 \times 10^{-6} \text{ cm}^2 \text{ sec}^{-1}$, respectively. Since NMA and DNT are non fluorescent, we could not use FCS technique to determine the diffusion coefficients. The D_t values of NMA and DNT in toluene were calculated by using Stokes-Einstein equation using the sizes of the molecules obtained from DFT calculations. These D_t values were used as a fitting parameters in diffusion equation of electron transfer reaction.

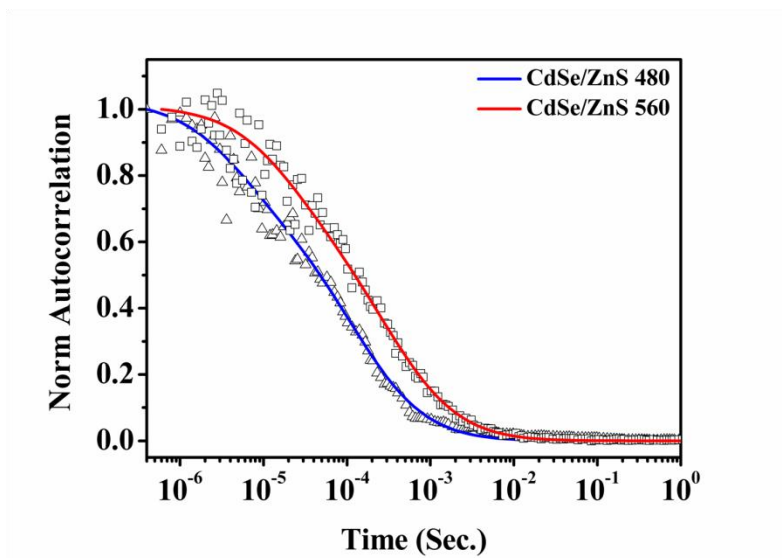


Figure 7.9. Fitted auto correlation curves for *CdSe/ZnS480* (blue) and *CdSe/ZnS560* (red) in toluene.

7.2.2.2. Calculation of Band Positions and Free Energy

In order to get a quantification for the driving force for the electron/hole transfer from the semiconductor quantum dot to organic acceptor/donor, the free energy was calculated by using the redox potential values. The first exciton energy ($E_{CdSe^*}[1S_e, 1S_h]$) of QD^* was calculated by using a formula proposed by Brus (equation 7.11).²⁴¹ Bulk band gap (E_g) of *CdSe* in equation 7.11 was used from reported value (1.7 eV vs.SCE).¹¹⁵ The radius of the QD, R was taken from the value obtained from *FCS* measurement.

$$E_{CdSe^*}[1S_e, 1S_h] = E_g + \frac{h^2 \pi^2}{2R^2 m_e^*} + \frac{h^2 \pi^2}{2R^2 m_h^*} - \frac{1.8e^2}{4\pi \epsilon_0 \epsilon R} \dots\dots\dots(7.11)$$

Values of the other parameters were taken from ref 115 and 4. m_e^* and m_h^* are the effective mass of the electron and hole, respectively. For *CdSe*; $m_e^* = 0.13 m_0$, $m_h^* = 1.14 m_0$ (m_0 is the rest mass of a free electron) and $\epsilon = 5.8$. The second and the third terms of equation 7.11 are representing the confinement energies of electron and hole, respectively. The last term is due to electron hole coulombic attraction force. For the reaction $QD^*[1S_e, 1S_h] + NMA \rightarrow QD^*$

$[1S_e,] + NMA^+$, the free energy change was calculated from a linear equation²³⁹ and using the oxidation potential value of NMA (+0.81 V vs. SCE) and reduction potential value of QD^* .

For the reaction $QD^*[1S_e, 1S_h] + 2,4-DNT \rightarrow QD^+[1S_h,] + 2,4-DNT^-$; ΔG^0 was calculated utilizing a similar procedure as used for $QD-NMA$ couple and an elaborate description of which has been provided by Lian and co-workers.^{115,239}

7.2.2.3. Energy Band Alignments, Steady State Fluorescence and Lifetime Quenching and Stern-Volmer Plots

HOMO-level of NMA [$NMA \rightarrow NMA^+ + e$; 0.81V/vs. SCE] acts as an efficient electron donor state in the presence of an electron deficit valance band of a photo excited QD^* [$CdSe^*(1S_e, 1S_h)/ZnS \rightarrow h + CdSe^-(1S_e)/ZnS$, 0.99 to 1.0 V/vs. SCE; type II band alignment, Figure 7.10.A]. *PET* takes place when this two states are mixed, which is manifested by the significant quenching of steady-state fluorescence as well as excited state lifetimes of QDs^* (Figures 7.11). Similar quenching of the QD^* fluorescence (steady state) and lifetime are also observed when QDs^* are mixed with a single quantum electron accepting state of DNT . In this case *PET* takes place from a quasi-continuum state (conductance band) of QD^* [$CdSe^*(1S_e, 1S_h)/ZnS \rightarrow e + CdSe^+(1S_h)/ZnS$; -2.32 V(for $QD480$) & -1.58 V(for $QD560$) vs. SCE] to the *LUMO-level* of ground state DNT [$DNT \rightarrow DNT^- + h$; -1.14V/vs. SCE]. We studied *PET* in these two cases using two separate sets of experiments. Excitation at 375 nm used in these studies excites the QD only leaving NMA or DNT almost unexcited within the mixture of either QD/NMA or QD/DNT , respectively (Figure 7.10.B). Therefore we can conclusively rule out the possibilities of *PET* either from energetically much higher (\sim -4.7 V/vs. SCE) *LUMO-level* of an excited NMA molecule to the conductance band of an unexcited QD in QD/NMA mixture or from the valance band of an unexcited QD to the ground state of an excited DNT molecule in QD/DNT mixture. A second source of

fluorescence quenching of QD^* in the presence of either *NMA* or *DNT* could be a result of energy transfer from QD^* to the quencher molecules. Certainly this is not the case here; almost no apparent spectral overlapping is evident between the emissions of QDs^* with the absorption spectra of any of the quencher molecules (Figure 7.10.B).

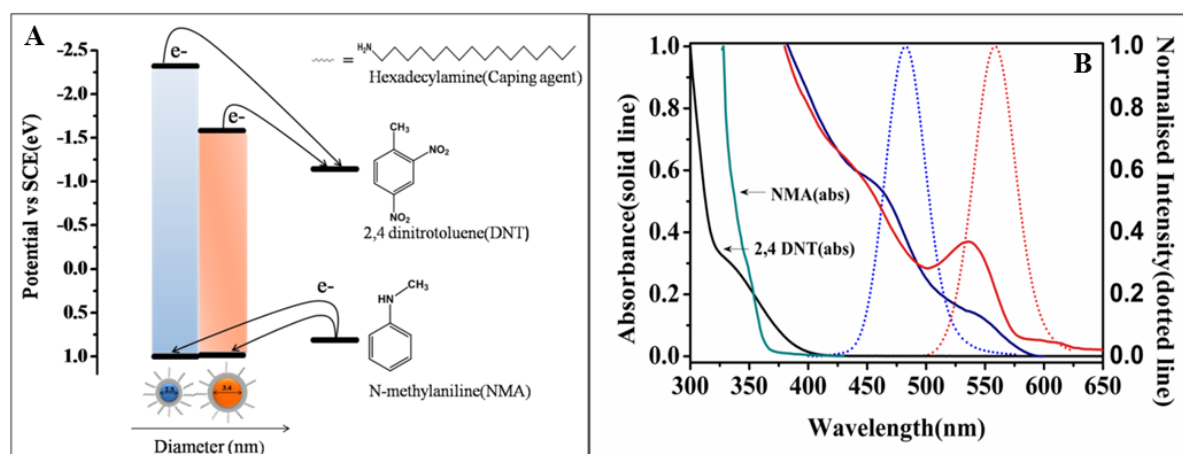


Figure 7.10. (A) Energy band alignment of the *QD-NMA* and *QD-DNT* redox pairs. (B) Absorption spectra (solid lines) for *DNT* (black), *NMA* (cyan), *QD480* (blue), *QD560* (red) and emission spectra (dotted lines) for *QD480* (blue), *QD560* (red).

PET rates in *QD-NMA* pair as well as in *QD-DNT* pair were calculated from both the steady state and time resolved fittings. Though the steady state *SV* plots were considered up to ~ 0.15 M concentration for *NMA*, but for *DNT*, we were able to go only up to ~ 0.007 M concentration (Figures 7.12). We could not go further with quencher concentration for *QD-DNT* pair as steady state fluorescence of *QD* reduces dramatically due to the dark *QD-to-DNT* complex formation, making it difficult to measure *QD* intensity from the samples containing >0.007 M *DNT* concentration. However, the lifetime measurement of the same reactant pair allows us to measure even at much higher (~ 0.04 M) quencher concentration (Figure 7.11). Lifetime, truncated by collisional quenching only, quenched at a much slower rate compared to the steady state fluorescence intensity quenching.

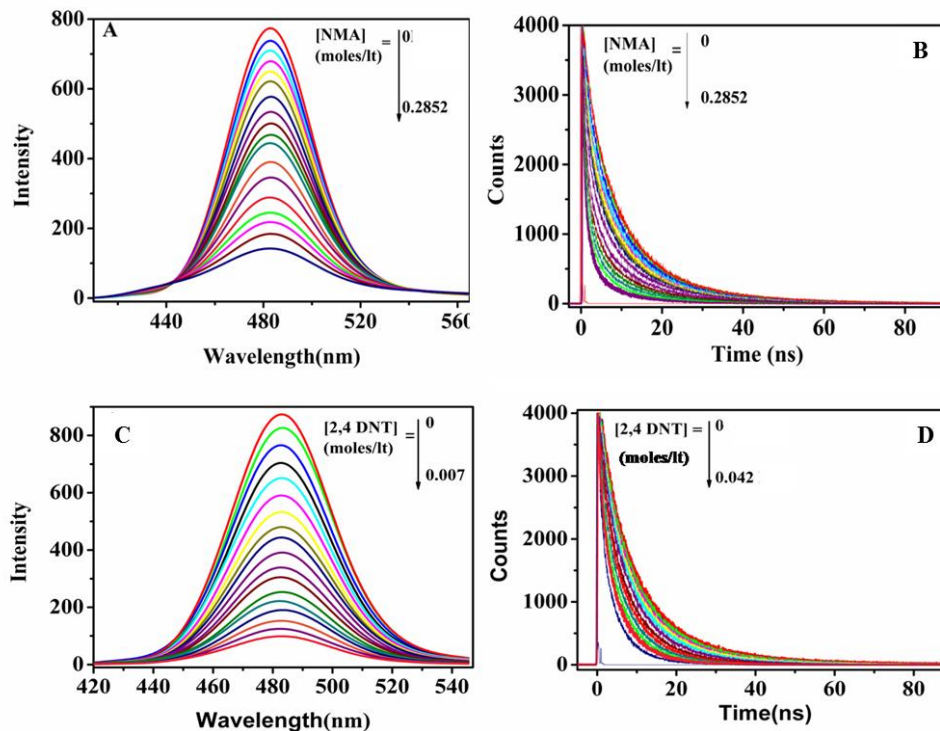


Figure 7.11. Left panel shows steady state emission spectra of *CdSe/ZnS480* in toluene at (A) various *NMA* concentrations and (B) various *DNT* concentrations. Right panel depicts fluorescence lifetime decay profile for *CdSe/ZnS480* in toluene at (C) various *NMA* concentrations and (D) various *DNT* concentrations. Excitation wavelength = 375 nm.

Steady state quenching occurred here mainly due to an efficient *QD-to-DNT* complex formation. When we compared between *SV* plots (of the same *QD-quencher* pair) obtained from steady state and lifetime data, we observed a large discrepancy among the *SV* curves when *DNT* as a quencher (Figures 7.12.A & 7.12.C). In *QD-NMA* sample difference between the same *SV* plots is not much (Figures 7.12.B & 7.12.D). Steady state *SV* plots of *QD-DNT* show strong upward curvatures whose slope increases with increasing *DNT* concentration (Figure 7.12.A). However, lifetime *SV* plots of the same *QD-DNT* pairs, which represent only the collisional quenching, don't show any bent feature (Figure 7.12.C). This discrepancy between steady state and lifetime *SV* plots is a clear signature of dark complex formation between *QD* and *DNT* molecules. Swager and his co-worker observed a similar complex

formation between *poly(iptycenebutadiynylene)* polymer and *DNT* molecule and that cause a significant higher rate of steady state intensity quenching of the polymer when compared to its lifetime quenching.²²⁰

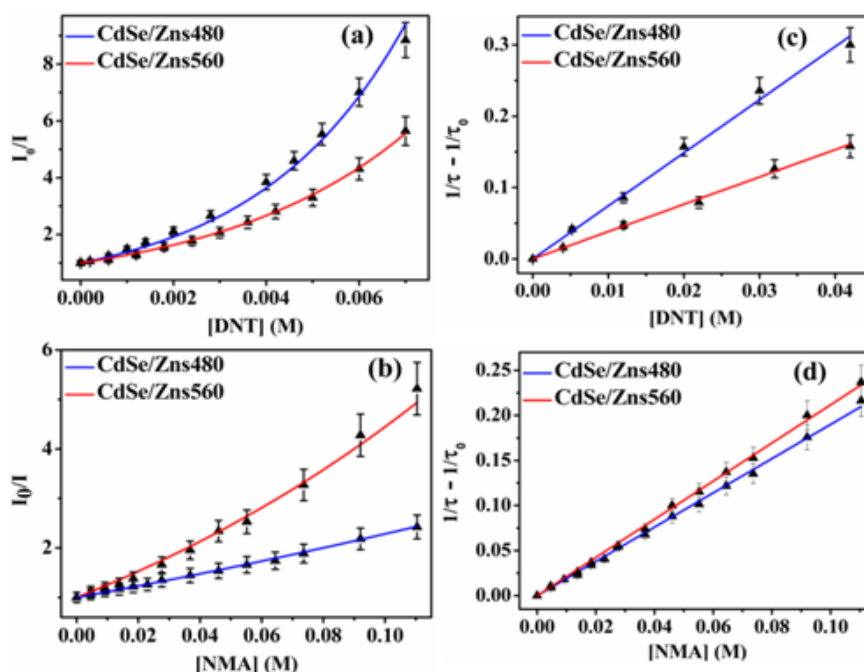


Figure 7.12. Left panel shows the steady state Stern-Volmer plots for (a) *QD-DNT* pairs (the solid lines showing the best fits by eq. 7) and (b) *QD-NMA* pairs (the solid lines showing SQCK fittings). Right panel represents the corresponding time resolved SV plots for (c) *QD-DNT* pair and (d) *QD-NMA* pair, respectively. Solid lines represent linear fit of the data and the error bar represents the error limit in the experimental data points.

PET kinetics in other couple *QD-NMA* is purely collisional in nature and one can expect it to be modelled either with a classic *SV* approximations (for stationary *ET* process); i.e., linear dependency of steady state *SV* plot with quencher concentration or using an advanced level theory that considers presence of a time independent rate coefficient for describing *ET* in deferent regimes (*static*, *non-stationary* and *stationary*). Interestingly, *PET* from *NMA* to *QD*, at lower *NMA* concentration and even with a *PET* rate much lower than the diffusion limit

($\sim 1.1 \times 10^{10} \text{ M}^{-1}\text{S}^{-1}$) of any bimolecular process in toluene, the steady state *SV* plots show an upward curvature instead of a straight line as predicted by a classic *SV* approximations (Figure 7.12.B). The curvature nature is more within the larger size *QD* (*QD560*) as compared to the smaller size *QD* (*QD480*) at higher *NMA* concentrations; here both the *QDs* act as an electron scavenger in the presence of *NMA*. Larger *QD* counts a faster *PET* rate here in the presence of *NMA* (Figures 7.12.B & 7.12.D). However just an opposite trends in curvature and rate are observed when *QDs* act as hole scavenger in the presence of *DNT* (i.e., smaller *QD* has higher curvature and faster *PET* rate compared to bigger size *QD*, Figures 7.12.A & 7.12.C). *PET* from *NMA* to *QDs* in this study is congruent with the study on *PET* from *NMA* to the different size *CdSQDs* as described in the previous section. The upward curvature of *SV* plot (of *QD-NMA*) in the present study is a clear manifestation of the significant mixing of non-stationary state with either static state or stationary state or with both the states of the *ET* kinetics.^{235,248} Classic *SV* assumptions only consider the pure stationary regime of the *ET* kinetics; leading to a linear relationship between steady state intensity ratio of the fluorescent molecule [in the absence (I_0) and presence (I_c) of quencher] with the quencher concentration. Therefore a classic *SV* fitting equation can't provide a conclusive fitting to *QD-NMA* data and a much advanced fitting model (*SQCK*) with a nonadiabatic sink term has been employed in this study for the fitting of *QD-NMA* pairs (to be discussed elaborately in the succeeding paragraph). Quenching due to *donor-to-acceptor* complex formation is the prevailing mechanism of fluorescence quenching in *QD-DNT* pair that leads to a bent feature (upward) in steady state *SV* plot (Figure 7.12.A) but a straight curve (Figure 2C) in lifetime *SV* plot; as latter is controlled by the collisional quenching only. Therefore, for the fitting of *QD-DNT* quenching data, we employed a modified *SV* equation, containing both, collisional quenching constant as well as *donor-to-acceptor* association constant

7.2.2.4. Fitting of QD-NMA quenching data using SQCK model

The previously used model (SQCK model) adequately fitted the PET kinetics of QD-NMA pair. The details of the fitting to the data has been described in previous section in case of CdS-NMA pair. Time evolution curve of *PET* coefficient for *QD* (acceptor)-*NMA*(donor) couple shows different regimes of *ET* kinetics (Figure 7.13). A continuous fall of *PET* coefficients with time at an intermediate time regime was observed, which is due to the falling apart of the donor molecule from acceptor molecule from their contact distance. This regime is called *non-stationary*, which is preceded by a *static* regime at the early response of the kinetics (Figure 7.13). In static regime, donor and acceptor molecules remain at physical contact distance. *PET* rate here is kinetically controlled and intrinsic in nature. At a longer time of the kinetics, *PET* reaction is again becomes stationary and highly influenced by the mass transport rate of the medium. From our fittings, we observed the average number (*m*) of inherit quencher site on *QD* surface increases with increasing the particle size: *m*=0.80 for *CdS480* (~4.4 nm) and *m*=1.00 for *CdS560* (~6 nm); this fact is further correlating to the difference in their natural excited state lifetimes. More quencher sites on bigger particle (*QD560*) causes almost ~2 times shorter fluorescence lifetime (~3.8 ns) of *QD560* as compared to ~7.4 ns observed in smaller size particle *QD480*. Defect site induced quenching time (τ_d) was found to get faster (~700 ps) within bigger size *QD* with a more number of defect sites as compared to that (~1200 ps) obtained in a smaller size *QD* with a lesser number of defect sites (Table 7.3). Figure 4 shows the simulated curve of the time description of *PET* rate coefficient using the numerical values of the parameters of *SQCK* fitting of the experimental quenching data of *QD-NMA* pairs. At early response of *PET* kinetic, *PET* coefficient is *static* and described by Szabo's non-adiabatic sink term [$k(r)$] which is inversely proportional to a non-radiative lifetime [$\tau_q(r)$], appearing due to the

quenching process within the reaction sphere.²⁴⁰ This *static* region is succeeded immediately by a *non-stationary* regime at a relatively longer time and a *stationary* regime at latter time.

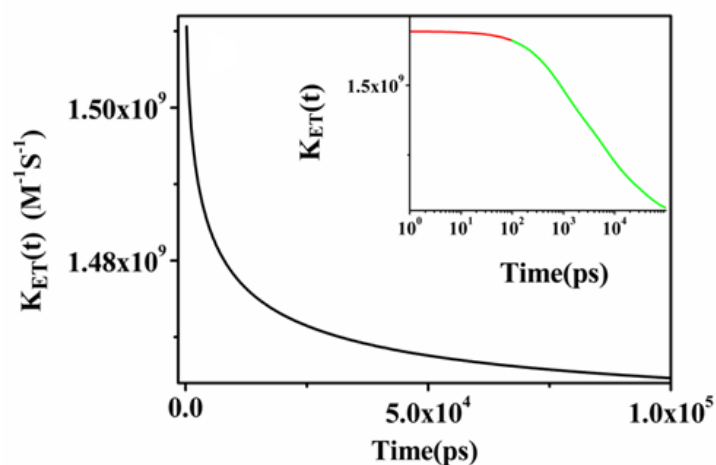


Figure 7.13. Time evolution of the rate coefficient [$k(t)$] for QD-NMA pair. As both the QDs (QD480 & QD560) exhibited similar kind of dependency of ET rate with time, therefore only one data has been shown. Inset shows the different regimes (red- *stationary* and green- non-stationary) of the electron transfer process.

It may be worth mentioning that although in this study we observed bimolecular *PET* reactions in *QD-NMA* couple with a much slower rates ($\sim 1.55 \times 10^9 \text{ M}^{-1} \text{ S}^{-1}$) as compared to the diffusion controlled limit ($\sim 1.1 \times 10^{10} \text{ M}^{-1} \text{ S}^{-1}$) of any bimolecular process in toluene, nevertheless a time independent *ET* rate coefficient was found inadequate for describing the entire kinetics. We also tried to fit quenching data from the other redox pair *QD-DNT* using *SQCK* model first, however, we could not match steady-state and time resolved data with a same rate coefficient only after severely compromising on accuracy of encounter distance (R) as obtained from steady state and time resolved data (Table 7.3). R is a very sensitive parameter in *SQCK* fitting, even a little change among the R values obtained from steady state and time resolved data is a clear indication of inadequacy of the model. This is in addition to a huge difference between the slopes of *SV* plots from steady-state (Figure 7.12.A)

and time-resolved (Figure 7.12.C) data (steady-state has more slope) for a same *QD-DNT* pair clearly indicating the *donor-to-acceptor* dark complex formation. We therefore used a different fitting equation, an extended form of classic *SV* equation for the fittings of quenching data from *QD-DNT* pair. The fitting model for *QD-DNT* has been discussed elaborately in the next paragraph.

Table 7.3. *SQCK* fitting parameters of time resolved $S_q(t)$ and steady-state *SV* plots of *QD-NMA* and *QD-DNT* pairs.

$^{\S}R_{tr}(R_{ss})$ is the reaction radius (R) obtained from time-resolved (steady-state) *SQCK* fitting. ‡ A large discrepancy between the values of R_{tr} and R_{ss} is indicating the breakdown of *SQCK* model for *QD-DNT* pairs, which is due to the *QD-to-DNT* complex formation. $^{\pm}$ *PET* rate coefficients obtained using *SQCK* model for *QD-DNT* couples are not correct due to inconclusive fittings. Accurate rate coefficients were obtained using modified *SV* fittings and

System	a (nm)	$R_{tr}(R_{ss})^{\S}$ (nm)	τ_q (ns)	m	τ_d (ns)	$k_0 \times 10^9$ ($M^{-1}S^{-1}$)
<i>QD480-NMA</i>	2.51	2.53 (2.53)	0.92	0.80	1.2	1.50
<i>QD480-DNT</i>	2.60	2.63 (4.00) ‡	0.43	0.55	1.5	3.29 $^{\pm}$
<i>QD560-NMA</i>	3.31	3.32 (3.35)	0.58	1.00	0.7	1.60
<i>QD560-DNT</i>	3.40	3.42 (4.38) ‡	0.81	0.85	1.2	1.61 $^{\pm}$

values of are given in Table 2. The data represented in the table are within $\pm 5\%$ error limit.

7.2.2.5. Fitting of *QD-DNT* quenching data using modified *SV* equation

The most possible reason of non-linear *SV* plots of *QD-DNT* pairs from steady state data is due to a combine process of collisional quenching and *donor-to-acceptor* complex formation (static quenching). The most straight forward fitting equation, which carries *SV*

approximations of dynamic quenching as well as a static quenching phenomenon assuming a donor-to-acceptor complex formation as follows,²²⁰

$$I_0/I_c = (1+k_D[C])\exp(K_S[C]) \dots\dots\dots(7.12)$$

Where k_D is the collisional rate coefficient; K_S denotes the association constant between *QD* and *DNT*. Other terms have their usual meanings. As the lifetime is truncated by the collisional quenching only, therefore, we used the classic *SV* equation [$\tau_0/\tau_c = (1+k_D[C])$]; τ_0 and τ_c are the lifetimes of *QD* in the absence and presence of *C* moles/litre *DNT*] for the fitting of lifetime *SV* curve of *QD-DNT* pair (Figure 7.12.C). k_D value obtained from this fitting was kept fixed in steady-state fitting equation (Equation 7.12) and the value of the association constants (K_D) was obtained from the steady-state *SV* fitting using equation 6. From the fittings, we observed collisional quenching rate decreases from $7.0 \times 10^9 \text{ M}^{-1}\text{s}^{-1}$ (*QD480-DNT*) to $3.7 \times 10^9 \text{ M}^{-1}\text{s}^{-1}$ (*QD560-DNT*) as size of the *QD* is increased (Figure 7.12.A & 7.12.C, Table 7.4).

Table 7.4. Rate coefficients (k_D) and association constants (K_S) of *QD-DNT* pairs. The value of K_S obtained from the fitting of steady state *SV* plot using Eq 7 (where k_D value was obtained from lifetime *SV* fitting and kept fixed in Eq 7)

System	$k_D \text{ (M}^{-1}\text{S}^{-1})^\S$	$K_S \text{ (M}^{-1})^\ddagger$	$\Delta G \text{ (eV)}$
QD480-DNT	7×10^9	275	-1.18
QD560-DNT	3.7×10^9	230	-0.44

[§]ET rate coefficient for collisional quenching; [‡]*QD-to-DNT* association constant

This observation is completely congruent to the fact that *ET* within the latter reactant couple occurs with lesser chemical driving force ($\sim -0.44 \text{ eV}$), compared to the driving force ($\sim -1.18 \text{ eV}$) in the former reactant couple. The static quenching or *QD-to-DNT* association constant

(K_S) values we obtained here not very different between the two couples ($K_S \sim 275 \text{ M}^{-1}$ and 230 M^{-1} , respectively for *QD480-DNT* and *QD560-DNT*). A moderately higher K_S values in both the cases indicating a strong interaction between *DNT* and *HDA* capping ligand has led to an efficient complex formation. It may be worth mentioning, while fitting the steady state quenching data we first tried with a more commonly used *SV* fitting equation (Equation 7.13) that predicts a linear dependency between the relative fluorescence intensity (I_0/I_c) and the static quenching constant (as in the case of collisional quenching), however, could not enable a conclusive fitting.²²⁰

$$I_0/I_c = (1+k_D[C])(1+K_S[C]) \dots\dots\dots(7.13)$$

In fact the above equation is an approximated form of equation no 7.12, when K_S or C is significantly small. This approximated equation with a linear relationship of fluorescence quenching with the K_S is only applicable when *one-to-one* dark complex is formed with a relatively lower value of K_S . If this is the case, one can always expect a linear relationship between $(I_0/I_c)/(1+k_D[C])$ with $[C]$ as shown in equation no 7.13.

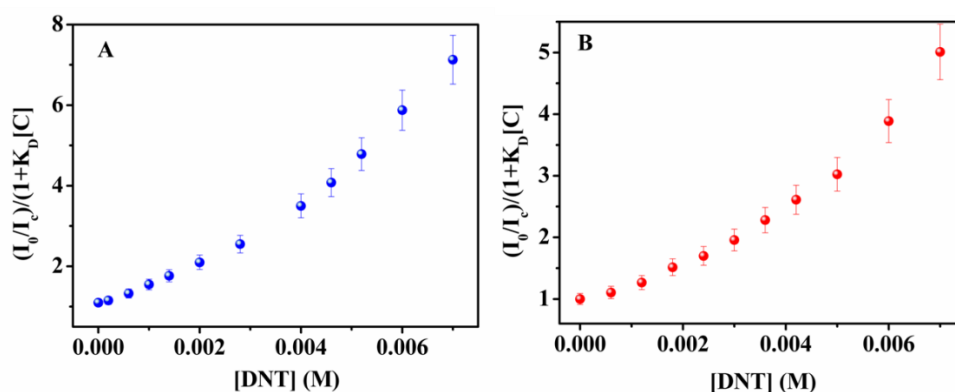


Figure 7.14. Plot of $(I_0/I_c)/(1+k_D[C])$ as a function of quencher concentration $[C]$ for (A) CdSe/ZnS480-DNT pair and (B) CdSe/ZnS560-DNT pair.

However, in our study none of the *QD-DNT* pairs exhibited a linear dependency (Figure 7.14). Therefore we used a more complicated fitting equation (equation no 7.12) that

considers a nonlinear relationship of fluorescence quenching with the quencher concentration due to the complex formation. The discussions stated above explains the breakdown of SQCK model in case of QD-DNT pair.

7.3. Conclusion

In this schapter, we show the electron transfer kinetics in core type CdS and *CdSe/ZnS* core shell quantum dot are diffusion assisted. For the electron injection in the valance band of the quantum dot, a fast ET rate is observed, where *QD* acts as an electron scavenger in the presence of an electron rich molecule *NMA*. *SQCK* fitting model that considers only collisional quenching by relying on concept of sphere of action, can only fits the *QD-NMA* data. However for the fitting of *QD-DNT*, we observed a complete breakdown of *SQCK* model, a *SV* fitting equation with a linear and nonlinear relationship of fluorescence quenching with quencher concentration due to the *dynamic* and *static* quenchings was employed for the fitting. Quenching mechanism in *QD-NMA* is completely collisional in nature, the time evolution of the *ET* rate coefficient here shows distinct regimes: *static*, *non-stationary* and *stationary*, respectively. *QD-DNT* pair, in contrast to *QD-NMA* pair which exhibits only collisional quenching, shows a quenching mechanism comprises with both static (dark *QD-to-DNT* complex formation) and collisional (dynamic) quenchings taking place simultaneously.

REFERENCES

1. Chandler, D. *Nature***2005**, *437*, 640.
2. Tanford, C. *Science* **1978**, *200*, 1012.
3. Bagchi, B. *Chem. Rev.***2005**, *105*, 3197.
4. Bhattacharyya, K. *Chem. Commun.***2008**, 2848.
5. Huang, D. M.; Chandler, D. *J. Phys. Chem. B.* **2002**,*106*, 2047.
6. Wang, L.; Yu, X.; Hu, P.; Broyde ,S.; Zhang, Y. *J. Am. Chem. Soc.***2007**, *129*, 4731.
7. Jayaram, B.; *Annu. Rev. Biophys. Biomol. Struct.***2006**,*33*, 343.
8. Yamasaki, K.; Akiba, T.; Yamasaki, T.; Harata, K. *Nucleic Acids Res.***2007**, *35*, 5073.
9. Winterburn ,T. J.; Wyatt ,D. M.; Phylip L. H.; Bur, D.; Harrison, R. J.; Berry, C. ; Kay, J. *Biol. Chem.***2007**, *282*, 6508.
10. Migliore, A.; Corni, S.; Felice, R. D.; Molinary, E. *J. Phys. Chem. B* **2007**, *111*, 3774
11. Friedman, R.; Fischer, S.; Nacliel, E.; Scheiner, S.; Gutman, M. *J. Phys. Chem. B* **2007**, *111*, 6059.
12. Jordanides, X.J.; Lang, M.J.; Song, X.;Fleming, G.R. *J. Phys. Chem. B* **1999**, *103*,7995.
13. Sykora, J.; Kapusta, P.; Fidler, V.; Hof, M. *Langmuir* **2002**, *18*, 571.
14. Shirota, H.; Castner Jr., E. W. *J. Am. Chem. Soc.* **2001**, *123*, 12877.
15. Brauns, E. B.; Madaras, M. L.; Coleman, R. S.; Murphy, C. J.; Berg, M. A. *Phys.Rev. Lett.* **2002**, *88*, 158101.
16. Datta, A.; Das, S.; Mandal, D.; Pal, S. K.; Bhattacharyya, K. *Langmuir* **1997**, *13*, 6922.
17. Balasubramanian, S.; Bagchi, B. *J. Phys. Chem. B***2001**, *105*, 12529.
18. Balasubramanian, S.; Bagchi, B. *J. Phys. Chem. B* **2002**, *106*, 3668.
19. Faeder, J.; Ladanyi, B. M. *J. Phys. Chem. B***2001**, *105*, 11148.

20. Senapathy, S.; Chandra, S. *J. Phys. Chem. B* **2001**, *105*, 5106.
21. Hansen, J. E.; Pines, E.; Fleming, G. R. *J. Phys. Chem.* **1992**, *96*, 6904.
22. Dutta, P.; Halder, A.; Mukherjee, S.; Sen, P.; Sen, S.; Bhattacharyya, K. *Langmuir* **2002**, *18*, 7867.
23. Cohen, B.; Huppert, D.; Solnsteve, K. M.; Tsfadia, Y.; Nachliel, E.; Gutman, M. *J. Am. Chem. Soc.* **2002**, *124*, 7539.
24. Vajda, S.; Jimenez, R.; Rosenthal, S. J.; Fidler, V.; Fleming G. R.; Castner Jr., E. W.; *J. Chem. Soc., Faraday Trans.* **1995**, *91*, 867.
25. Nandi N.; and Bagchi, B.; *J. Phys. Chem.* **1996**, *100*, 13914.
26. Roy, D.; Mondal, S. K.; Sahu, K.; Ghosh, S.; Sen P.; Bhattacharyya, K. *J. Phys. Chem. A* **2005**, *109*, 7359.
27. Mitra, R. K.; Sinha, S. S.; Pal, S. K.; *J. Phys. Chem. B* **2007**, *111*, 7577.
28. Kuhn H.; Försterling H.D.; Waldeck, D. H. *Principles of Physical Chemistry 2nd Edition, Wiley, Hoboken* **2009**.
29. Chin, J. T.; Wheeler S. L.; Klibanov, A. M. *Biotech. Bioeng.* **1994**, *44*, 140.
30. Ramírez-Silva, L.; Oria-Hernandez J.; Uribe, S. *Proteins in' Water–Cosolvent Binary Systems: Function and Structure. In Encyclopedia of Surface and Colloid Science;* Somasundaran, P., 2nd Ed.; Taylor and Francis: Boca Raton, FL, 2006; Vol. **7**, pp 5299–5313.
31. Tan K. H.; Lovrien, R. *J. Biol. Chem.* **1972**, *247*, 3278.
32. Han, B.; Choi, J. H.; Dantzig J. A.; Bischof, J. C. *Cryobiology* **2006**, *52*, 146.
33. Melnikov, S. M.; Hölzel, A.; Seidel-Morgenstern A.; Tallarek, U. *J. Phys. Chem. C* **2015**, *119*, 512.
34. Marcus, Y. *Solvent Mixtures: Properties and Selective Solvation; CRC Press* **2002**.
35. Filippa M. A.; Gasull, E. I. *J. Mol. Liq.* **2014**, *198*, 78.

36. Kaatze, U.; Brai, M.; Sholle F. D.; Pottel R. *J. Mol. Liq.* **1990**, *44*, 197.
37. Zhang , S.; Li , X.; Chen , H.; Wang , J.; Zhang , J.; Zhang, M. *J. Chem. Eng. Data* **2004**, *49*, 760.
38. Mukherjee,A.; Bagchi, B. *J. Phys. Chem. B* **2001**, *105*, 9581.
39. Luzar, A.; *J. Chem. Phys.* **1989**, *91*, 3603.
40. Srinivas, G.; Mukherjee A.; Bagchi, B. *J. Chem. Phys.* **2001**, *114*, 6220.
41. Reis, J. C. R.; Douheret, G.; Davis, M. I.; Fjellanger I. J.; Hoiland, H. *Phys. Chem. Chem. Phys.*, **2008**, *10*, 561.
42. Catalán, J.; Díaz C.; García-Blanco, F. *J. Org. Chem.* **2001**, *66*, 5846.
43. Roy, S.; Banerjee, S.; Biyani, N.; Jana B.; Bagchi, B. *J. Phys. Chem. B* **2011**, *115*, 685.
44. Ghosh, R.; Banerjee, S.; Chakrabarty S.; Bagchi, B. *J. Phys. Chem. B* **2011**, *115*, 7612.
45. Shin, D. N.; Wijnen, J. W.; Engberts J. B. F. N.; Wakisaka, A.; *J. Phys. Chem. B* **2002**, *106*, 6014.
46. Reichardt, C. *Chem. Rev.* **1994**, *94*, 2319.
47. Krolicki, R.; Jarzęba, W.; Mostafavi, M.; Lampre, I. *J. Phys. Chem. A* **2002**, *106*, 1708.
48. Molotsky, T.; Huppert, D. *J. Phys. Chem. A* **2002**, *106*, 8525.
49. Gupta, S.; Rafiq, S.; Kundu M.; Sen, P. *J. Phys. Chem. B* **2012**, *116*, 1345.
50. Zhang, X.; Zhu, Y.; Granick, S. *Science* **2002**, 295,663.
51. Roy, S.; Bagchi, B. *J. Chem. Phys.* **2013**. *139*,.034308.
52. Banik, D.; Roy, A.; Kundu, N.; Sarkar, N. *J. Phys. Chem. B* **2015**, *119*, 9905.
53. Safford, G.J.; Schaffer, P.C.; Leung, P.S.; Doebbler, G.F.; Brady, G.W.; Lyden, E.F.X. *J. Chem. Phys.* **1969**, *50*, 2140.
54. Roy, S.; Banerjee, S.; Biyani, N.; Jana, B.; Bagchi, B. *J. Phys. Chem. B* **2010**, *115*, 685.
55. Mukherjee, S.; Sahu, K.; Roy, D.; Mondal, S.K.; Bhattacharyya, K. *Chem. Phys. Lett.* **2004**, *384*, 128.

56. Bagchi, B.; Jana, B. *Chem. Soc. Rev.* **2010**, *39*, 1936.
57. Martins, L.R.; Tamashiro, A.; Laria, D.; Skaf, M.S. *J. Chem. Phys.* **2003**, *118*, 5955.
58. Banik, D.; Kundu, N.; Kuchlyan, J.; Roy, A.; Banerjee, C.; Ghosh, S.; Sarkar, N. *J. Chem. Phys.* **2015**, *142*, 054505 (1)–054505 (10).
59. Roy, S.; Jana, B.; Bagchi, B. *J. Chem. Phys.* **2012**, *136*, 03B608.
60. Ghosh, S.; Chattoraj, S.; Chowdhury, R.; Bhattacharyya, K.; *RSC Advances*, **2014**, *4*, 14378.
61. Guo, J.H.; Luo, Y.; Augustsson, A.; Kashtanov, S.; Rubensson, J.E.; Shuh, D.K.; Ågren, H.; Nordgren, J. *Phys. Rev. Lett* **2003**, *91*, 157401.
62. Angulo, G.; Kattnig, D. R.; Rosspeintner, A.; Grampp, G.; Vauthey, E. *Chem. – Eur. J.* **2010**, *16*, 2291.
63. Angulo, G., Brucka, M., Gerecke, M., Grampp, G., Jeannerat, D., Milkiewicz, J., Mitrev, Y., Radzewicz, C., Rosspeintner, A., Vauthey, E.; Wnuk, P. *Phys. Chem. Chem. Phys.* **2016**, *18*, 18460.
64. Rasul, Z.; Ahmed, N.; Anzar, M. *Theriogenology* **2007**, *68*, 813.
65. Chattoraj, S.; Chowdhury, R.; Ghosh, S.; Bhattacharyya, K. *J. Chem. Phys.* **2013**, *138*, 214507.
66. Kaur, H.; Koley, S.; Ghosh, S. *J. Phys. Chem. B* **2014**, *118*, 7577.
67. Tomalia, D. A.; Baker, H.; Dewald, J.; Hall, M.; Kallos, G.; Martin, S.; Roeck, J.; Ryder, J.; Smith, P. *A New Class of Polymers: Starburst-Dendritic. Polym. J.* **1985**, *17*, 117.
68. Khandare, J. J.; Jayant, S.; Singh, A.; Chandna, P.; Wang, Y.; Vorsa, N.; Minko, T. *Bioconjugate chem.* **2006**, *17*, 1464.
69. Abbasi, E.; Aval, S. F.; Akbarzadeh, A.; Milani, M.; Nasrabadi, H. T.; Joo, S. W.; Hanifehpour, Y.; Nejati-Koshki, K.; Pashaei-Asl, R. *Nanoscale Res. Lett.* **2014**, *9*, 1.

70. Nanjwade, B. K.; Bechra, H. M.; Derkar, G. K.; Manvi, F. V.; Nanjwade, V. K. *Eur. J. Pharm. Sci.* **2009**, *38*, 185.
71. Esfand, R.; Tomalia, D. A. *Drug Discov. Today* **2001**, *6*, 427.
72. Watkins, D.M.; Sayed-Sweet, Y.; Klimash, J.W.; Turro, N.J.; Tomalia, D.A. *Langmuir* **1997**, *13*,3136.
73. Zhao, M.; Sun, L.; Crooks, R.M. *J. Am. Chem. Soc* **1998**, *120*,4877.
74. Crooks, R. M.; Zhao, M.; Sun, L.; Chechik, V.; Yeung, L. K. *Acc. Chem. Res.* **2001**, *34*, 181.
75. Astruc, D. *Tetrahedron: Asymmetry* **2010**,*21*, 1041.
76. Dandliker, P. J.; Diederich, F.; Gisselbrecht, J- P.; Louati, A.; Gross, M. *Angew. Chem. Int. Ed. Engl.* **1995**,*34*, 2725.
77. Gorman, C. B. *et al. J. Am. Chem. Soc.***1999**,*121*, 9958.
78. Pollak, K. W.; Leon, J. W.; Fréchet, J. M. J.; Maskus, M. ; Abruña, H. D. *Chem. Mater.* **1998**,*10*, 30.
79. Maiti, P. K.; Cagin, T.; Lin, S. T.; Goddard, W. A. *Macromolecules* ,*38*, 979.
80. Maiti, P. K.; Cagin, T.; Wang, G.; Goddard, W. A. *Macromolecules* **2004**, *37*, 6236.
81. Pande, S.; Crooks, R. M. *Langmuir***2011**, *27*, 9609.
82. Shao, N.; Su, Y.; Hu, J.; Zhang, J.; Zhang, H.; Cheng, Y. *Int. J. Nanomed.* **2011**, *6*, 3361.
83. Porcar, L.; Liu, Y.; Verduzco, R.; Hong, K.; Butler, P. D.; Magid, L. J.; Smith, G. S.; Chen, W. R. *J. Phys. Chem. B* **2008**, *112*, 14772.
84. Welch, P.; Muthukumar, M. *Macromolecules* **1998**, *31*, 5892.
85. Chen, W.; Tomalia, D. A.; Thomas, J. L. *Macromolecules* **2000**, *33*, 9169.
86. Porcar, L.; Liu, Y.; Verduzco, R.; Hong, K.; Butler, P. D.; Magid, L. J.; Smith, G. S.; Chen, W. R. *J. Phys. Chem. B* **2008**, *112*, 14772.

87. Chen, W. R.; Porcar, L.; Liu, Y.; Butler, P. D.; Magid, L. J. *Macromolecules* **2007**, *40*, 5887.
88. Liu, Y.; Bryantsev, V. S.; Diallo, M. S.; Goddard III, W. A. *J. Am. Chem. Soc.* **2009**, *131*, 2798.
89. Pistolis, G.; Malliaris, A.; Paleos, C. M.; Tsiourvas, D. *Langmuir* **1997**, *13*, 5870.
90. Kannaiyan, D.; Imae, T. *Langmuir* **2009**, *25*, 5282.
91. Kleinman, M. H.; Flory, J. H.; Tomalia, D. A.; Turro, N. J. *J. Phys. Chem. B* **2000**, *104*, 11472.
92. Shcharbin, D.; Klajnert, B.; Mazhul, V.; Bryszewska, M. *J. Fluorescence* **2003**, *13*, 519.
93. Paulo, P. M.; Gronheid, R.; De Schryver, F.C.; Costa, S. M. *Macromolecules* **2003**, *36*, 9135.
94. Wang, D.; Imae, T. *J. Am. Chem. Soc.* **2004**, *126*, 13204.
95. Larson, C. L.; Tucker, S. A. *Appl. Spectrosc.* **2001**, *55*, 679.
96. Sun, M.; Hong, C.-Y.; Pan, C.-Y. *J. Am. Chem. Soc.* **2012**, *134*, 20581.
97. Saravanan, G.; Imae, T. *J. Nanosci. Nanotechnol.* **2011**, *11*, 4838.
98. Chu, C. C.; Imae, T. *Macromol. Rapid Commun.* **2009**, *30*, 89.
99. Lu, H.; Feng, L.; Li, S.; Zhang, J.; Lu, H.; Feng, S. *Macromolecules* **2015**, *48*, 476.
100. Lee, W. I.; Bae, Y.; Bard, A. J. *J. Am. Chem. Soc.* **2004**, *126*, 8358.
101. Kamat, P. V. *Acc. Chem. Res.* **2012**, *45*, 1906.
102. Konstantatos, G.; Howard, I.; Fischer, A.; Hoogland, S.; Clifford, J.; Klem, E.; Levina, L.; Sargent, E. H. *Nature* **2006**, *442*, 180.
103. Huang, L.; Tu, C.-C.; Lin, L. Y. *Appl. Phys. Lett.* **2011**, *98*, 113110.
104. Carey, G.H.; Abdelhady, A.L.; Ning, Z.; Thon, S.M.; Bakr, O.M.; Sargent, E.H. *Chemical reviews* **2015**, *115*, 12732.

105. Murray, C.B.; Kagan, C.R.; Bawendi, M.G. *Annual Review of Materials Science*, **2000**, *30*, 545.
106. Brus, L.E., *Chemistry and physics of semiconductor nanocrystals*. Columbia University. , **2007**.
107. Moreels, I.; Justo, Y.; De Geyter, B.; Hastraete, K.; Martins, J. C.; Hens, Z. *ACS Nano* **2011**, *5*, 2004.
108. Bawendi, M. C.; Steigerwald, M. L.; Brus, L. E. *Annual Review of Physical Chemistry* **1990**, *41*, 477
109. Smith, A. M.; Nie, S. *Nature Biotechnology* **2009**, *27*, 732.
110. Vastola, G.; Zhang, Y.-W.; Shenoy, V. B. *Current Opinion in Solid State & Materials Science* **2012**, *16*, 64.
111. Nirmal, M.; Brus, L. *Acc. Chem. Res.* **1999**, *32*, 407.
112. Sargent, E. H. *Nature Photonics* **2012**, *6*, 133.
113. Zhao, Y.; Burda, C. *Energy & Environmental Science* **2012**, *5*, 5564.
114. Tvrdy, K.; Frantsuzov, P. A.; Kamat, P. V. *Proc. Natl. Acad. Sci. U. S. A.* **2011**, *108*, 29.
115. Boulesbaa, A.; Issac, A.; Stockwell, D.; Huang, Z.; Huang, J.; Guo, J.; Lian, T. *J. Am. Chem. Soc.* **2007**, *129*, 15132.
116. Sadhu, S.; Tachiya M.; Patra, A. *J. Phys. Chem. C* **2009**, *113*, 19488.
117. Lakowicz, J. R. *Principles of Fluorescence Spectroscopy*, 3rd editon; Springer: New York **2006**.
118. Becker, W. *Advanced Time Correlated Single Photon Counting Technique*; Springer: New York **2005**.
119. Maroncelli, M.; Fleming, G. R. *J. Chem. Phys.* **1987**, *86*, 6221.

120. Gell, C.; Brockwell, D.; Smith, A. *Handbook of Single Molecule Fluorescence Spectroscopy*, Oxford University Press, **2006**.
121. Haustein, E. ; Schwille, P.; *Annu. Rev. Biophys. Biomol. Struct.* **2007**, 36,151.
122. Elson, E.L.; Magde, D. *Biopolymers* **1974** , 13,1.
123. Reichardt, C.; Welton,T.; *Solvents and Solvent Effects in Organic Chemistry*, Wiley-VCH, 4th edn**2010**.
124. Roy, S.; Jana, B. ; Bagchi, B. *J. Chem. Phys.* **2012** ,136, 03B608.
125. Bhattacharjya, S.; Balaram,P. *Proteins***1997**, 29, 492.
126. Johnson, M. E. ; Malardier-Jugrootd ,C.; Head-Gordon, T. *Phys. Chem. Chem. Phys.***2010**, 12, 393.
127. Gögelein.,C.; Wagner,D.; Cardinaux,F.; Nägele,G.; Egelhaaf,S. U. *J. Chem. Phys.***2012**, 136, 015102.
128. Chakraborty,A.; Seth,D.; Setua,P.; Sarkar,N. *J. Phys. Chem. B* **2006**, 110, 5359.
129. Jimenez, R.; Fleming,G. R.; Kumar,P. V.; Maroncelli, M. *Nature***1994**, 369, 471.
130. Jarzebz,W.; Walker,G. C.; Johnson, A. E. ; Kahlow, M. A;. Barbara,P. F. *J. Phys. Chem.***1988**, 92, 7039.
131. Castner Jr., E. W.; Maroncelli,M. ; Fleming,G. R. *J. Chem. Phys.*, **1987**, 86, 1090.
132. Bagchi, B. ; Oxtoby,D. W. ; Fleaming,G. R.; *Chem. Phys.***1984**, 86, 257.
133. Banerjee,S.; Roy,S. ; Bagchi,B. *J. Phys. Chem. B* **2010**, 114, 12875.
134. Dutt G. B.; Ghanty, T. K. *J. Phys. Chem. B***2003**, 107, 3257.
135. Roy, S.; Bagchi, B. *J. Chem. Phys.***1993**, 99, 9938.
136. Nandi, N.; Bagchi, B. *J. Phys. Chem. B***1997**, 101, 10954.
137. Perrin, F. *J. Phys. Radium***1934**, 5, 497.
138. Dutt,G. B.; Ghanty,T. K. *J. Phys. Chem B* **2003**, 107, 3257.

139. Kirchner, B. ; Reiher, M. *J. Am. Chem. Soc.* **2002**, *124*, 6206.
140. Wong, D. B.; Sokolowsky, K. P.; El-Barghouthi, M. I. ; Fenn, E. E. ; Giammanco, C. H.; Sturlaugson, A. L. ; Fayer, M. D. *J. Phys. Chem. B* **2012**, *116*, 5479.
141. Cubberley, M. S. ; Iverson, B. L. *J. Am. Chem. Soc.* **2001**, *123*, 7560.
142. Hill, D. J. ; Moore, J. S. *Proc. Natl. Acad. Sci. USA* **2002**, *99*, 5053.
143. La, S. B. ; Okano, T. ; Kataoka, K. *J. Pharm. Sci.* **1996**, *85*, 85.
144. Rosenthal, S. J. ; Xie, X. ; Du, M. ; Fleming, G. R. *J. Chem. Phys.* **1991**, *95*, 4715.
145. Rey, R. ; Hynes, J. T. *J. Phys. Chem. B* DOI: 10.1021/jp5113922.
146. Aveldano, M. I.; VanRollins, M. L. Horrocks, A. *J. Lipid Res.* **1983**, *24*, 83.
147. Sanli, S. ; Altun, Y. ; Sanli, N. ; Alsancak, G. ; Beltran, J. L. *J. Chem. Eng. Data* **2009**, *54*, 3014.
148. Sanhueza, E. ; Holzinger, R. ; Kleiss, B. ; Donoso, L. ; Crutzen, P. J. *Atmos. Chem. Phys.* **2004**, *4*, 275.
149. Kovacs, H. ; Laaksonen, A. *J. Am. Chem. Soc.* **1991**, *113*, 5596.
150. Douhéret, G. ; Moreau, C. ; Viallard, A. *Fluid Phase Equilib.* **1985**, *22*, 277.
151. Kabisch, V. ; *Z. Phys Chem. (Leipzig)* **1982**, *263*, 48.
152. Bertie, J. E. ; Lan, Z. *J. Phys. Chem. B* **1997**, *101*, 4111.
153. Bakó, I. ; Megyes, T. ; Pa'linka's, G. *Chem. Phys.* **2005**, *316*, 235.
154. Ladanyi, B. M. ; Perng, B. C. *J. Phys. Chem. A* **2002**, *106*, 6922.
155. Chicos, F. ; Brown, R. ; Rempel, U.; von Borczyskowski, C. *J. Phys. Chem. A* **1999**, *103*, 2506.
156. Chicos, F. ; Wilert, A. ; Rempel, U. ; von Borczyskowski, C. *J. Phys. Chem. A* **1997**, *101*, 8179.
157. Chandra, A. *Chem. Phys. Lett.* **1995**, *235*, 133.
158. Suppan, P. J. *J. Chem. Soc. Faraday Trans.* **1987**, *83*, 495.

159. Cunningham, G. P. ; Vidulich, G. A.; Kay, R. L. *J. Chem. Eng. Data***1967**, *12*, 336.
160. Molotsky, T. ;Huppert, D. *J. Phys. Chem. A* **2003**,*107*,8449.
161. Fee,R. S. ; Maroncelli, M. *Chem. Phys.***1994**, *183*, 235.
162. Majumder,P. ; Sarkar, R. ; Shaw, A. K. ; Chakraborty,A. ; Pal, S. K. *J. Colloid Interface Sci.* **2005**, *290*,462.
163. Dutta,P. ; Sen,P. ; Mukherjee,S. ; Halder,A. ; Bhattacharyya,K. *J. Phys. Chem. B* **2003**, *107*, 10815.
164. Andreatta,D. ; Lustres,J. L. ; Kovalenko,P. S. A. ; Ernsting, N. P. ; Murphy, C. J. ;Coleman, R. S. ; Berg, M. A. *J. Am. Chem. Soc.* **2005**, *127*, 7270.
165. Brauns,E. B. ; Madaras, M. L. ; Coleman, R. S. ; MurphyC. J. ; Berg, M. A. *Phys. Rev. Lett.* **2002**, *88*, 158101.
166. Andreatta,D. ; Sen,S. ; Perez Lustres,J. L. ; Kovalenko,S. A. ; Ernsting,N. P. ; Murphy,C. J. ; Coleman, R. S. ; Berg, M. A. *J. Am. Chem. Soc.***2006**, *128*, 6885.
167. Pal, N. ; Verma, S. D. ; Sen,S. *J. Am. Chem. Soc.***2010**, *132*, 9277.
168. Verma, S. D.; Pal,N.; Singh ,M. K. ; Sen,S. *J. Phys. Chem. Lett.***2012**, *3*, 2621.
169. Sen,S.; Gearheart, L.; Rivers, E.; Lui,H. ; Coleman,R. S. ; Murphy,C. J. ; Berg,M. A. *J. Phys. Chem. B* **2006**, *110*, 13248.
170. Roy,S. ; Yashonath, S. ; Bagchi, B. *J. Chem. Phys.***2015**, *142*, 124502 .
171. Lawler,C. ; Fayer, M. D. *J. Phys. Chem. B* **2015**, *119*, 6024.
172. Hong, K. M. ; Noolandi, J. *J. Chem. Phys.***1978**, *68*, 5163.
173. Pines, E. ; Huppert, D. ; Agmon,N. *J. Chem. Phys.***1988**, *88*, 5620.
174. Debye, P. *Trans. Electrochem. Soc.* **1942**, *82*, 265.
175. Leiderman,P.; Ben-Ziv, M.; Genosar, L.; Huppert, D.; Solntsev, K. M. ; Tolbert, L. M. *J. Phys. Chem. B* **2004**,*108*, 8043.
176. Singha,D. ; Barman,N. ; Phukon, A. ; Sahu,K. *J. Phys. Chem. C***2014**, *118*, 10366.

177. Koti, A.S. R.; Krishna, M. M. G.; Periasamy, N. *J. Phys. Chem. A* **2001**, *105*, 1767.
178. Ira.; Koti, A.S. R.; Krishnamoorthy, G.; Periasamy, N. *J. Fluorescence* **2003**, *13*, 95.
179. Meyer, M.; Mialocq, J. C.; *Opt. Commun.* **1987**, *64*, 264.
180. Sajadi, M.; Oberhuber, T.; Kovalenko, S. A.; Mosquera, M.; Dick, B.; Ernsting, N. *P. J. Phys. Chem. A* **2009**, *113*, 44.
181. Jiang, L.; Liu, W.; Song, Y.; He, X.; Wang, Y.; Wu H.; Yang, Y. C. *J. Chem. Phys.* **2012**, *25*, 577.
182. Al-Tememe, N. A. A.; Al-Ani, S. K. J.; AbdAlfahdaw, A. A. *ISESCO J. Sci. Tech.* **2013**, *9*, 34.
183. Bosch E.; Roses, M. *J. Chem. Soc. Faraday Trans.* **1992**, *88*, 3541.
184. Takamuku, T.; Noguchi, Y.; Matsugami, M.; Iwase, H.; Otomo T.; Nagao, M. *J. Mol. Liq.* **2007**, *136*, 147.
185. Marcus, Y. *J. Phys. Org. Chem.* **2012**, *25*, 1072.
186. Marcus, Y.; Migron, Y. *J. Phys. Chem.* **1991**, *95*, 400.
187. Moreau, C.; Douhe´ret, G. *J. Chem. Thermodyn.* **1976**, *8*, 403.
188. Majoros, I. J.; Williams, C. R.; Baker, J. R.; James, R. *Curr. Top. Med. Chem.* **2008**, *8*, 1165.
189. Biswal, B. K.; Kavitha, M.; Verma, R. S.; Prasad, E. *Cytotechnology* **2009**, *61*, 17.
190. Soršak, E.; Valh, J. V.; Urek, Š. K.; Lobnik, A. *Analyst* **2015**, *140*, 976.
191. Niu, Y.; Sun, L.; Crooks, R. M. *Macromolecules* **2003**, *36*, 5725.
192. Jasmine, M. J.; Kavitha, M.; Prasad, E. *J. Lumin.* **2009**, *129*, 506.
193. Jasmine, M. J.; Prasad, E. *J. Phys. Chem. B* **2010**, *114*, 7735.
194. Phukon, A.; Sahu, K. *Chem. Commun.* **2015**, *51*, 14103.
195. Lavasanifar, A.; Samuel, J.; Kwon, G. S. *J. Control. Release* **2001**, *77*, 155.

196. Wang, Y.; Chen, L.; Tan, L.; Zhao, Q.; Luo, F.; Wei, Y.; Qian, Z. *Biomaterials* **2014**, *35*, 6972.
197. Ghosh, S.; Adhikari, A.; Mandal, U.; Dey, S.; Bhattacharyya, K. *J. Phys. Chem. C* **2007**, *111*, 8775.
198. Chattopadhyay, A.; Haldar, S. *Acc. Chem. Res.* **2013**, *47*, 12.
199. Shi, X.; Bányai, I.; Islam, M. T.; Lesniak, W.; Davis, D. Z.; Baker, J. R.; Balogh, L. *P. Polymer* **2005**, *46*, 3022.
200. Tomalia, D. A.; Naylor, A. M.; Goddard, W.A. *Angew. Chem. Int. Ed.* **1990**, *29*, 138.
201. Islam, M. T.; Shi, X.; Balogh, L.; Baker, J. R. *Anal. Chem.* **2005**, *77*, 2063.
202. Prosa, T. J.; Bauer, B. J.; Amis, E. J.; Tomalia, D. A.; Scherrenberg, R. A. *J. Polym. Sci. Polym. Phys.* **1997**, *35*, 2913.
203. Jones, G.; Jackson, W. R.; Choi, C. Y.; Bergmark, W. R. *J. Phys. Chem.* **1985**, *89*, 294.
204. Kumbhakar, M.; Nath, S.; Mukherjee, T.; Pal, H. *J. Chem. Phys.* **2005**, *123*, 034705.
205. Jansen, J. F. G. A.; de Brabander-van den Berg, D. E. M. M.; Meijer, E. W. *Science* **1994**, *266*, 1226.
206. Jansen, J. F. G. A.; Meijer, E. W.; de Brabander-van den Berg, D. E. M. M. *Macromol. Symp.* **1996**, *102*, 27.
207. Miklis, P.; Cag˘in, T.; Goddard, W. A. *J. Am. Chem. Soc.* **1997**, *119*, 7458.
208. Maiti, N. C.; Krishna, M. M. G.; Britto, P. J.; Periasamy, N. *J. Phys. Chem. B* **1997**, *101*, 11051.
209. Aoki, H.; Horinaka, J-I.; Ito, S.; Yamamoto, M.; Katayama, H.; Kamigaito, M.; Sawamoto, M. *Polym. J.* **2001**, *33*, 464.
210. Viovy, J. L.; Monnerie, L.; Merola, F. *Macromolecules* **1985**, *18*, 1130.
211. Seth, D.; Sarkar, S.; Sarkar, N. *Langmuir* **2008**, *24*, 7085.

212. Tomalia, D.A.; Fréchet, J.M. *J. Polym. Sci. A Polym. Chem.***2002**, *40*, 2719.
213. Devarakonda, B.; Hill, R. A.; de Villiers, M. M. *Int. J. Pharm.* **2004**, *284*, 133.
214. Al-Soufi, W.; Reija, B.; Novo, M.; Felekyan, S.; Kühnemuth, R.; Seidel, C. A. *J. Am. Chem. Soc.* **2005**, *127*, 8775.
215. Astruc, D. *Nat. Chem.***2012**, *4*, 255.
216. Matsushita, T.; Nagashima, I.; Fumoto, M.; Ohta, T.; Yamada, K.; Shimizu, H.; Hinou, H.; Naruchi, K.; Ito, T.; Kondo H.; Nishimura, S. I. *J. Am. Chem. Soc.***2010**, *132*, 16651.
217. Albertazzi, L.; Storti, B.; Marchetti L.; Beltram, F. *J. Am. Chem. Soc.***2010**, *132*, 18158.
218. Geng, Y.; Ali, M. A.; Clulow, A. J.; Fan, S.; Burn, P. L.; Gentle, I. R.; Meredith, P.; Shaw, P. E. *Nat. Commun.***2015**, *6*, 8240.
219. Wang, X.; Cao, L.; Lu, F.; Meziani, M. J.; Li, H.; Qi, G.; Zhou, B.; Harruff, B. A.; Kermarrec, F.; Sun, Y-P. *Chem. Commun.***2009**, 3774.
220. Zhao D.; Swager, T. M. *Macromolecules***2005**, *38*, 9377.
221. Paul A.; Samanta, A. *J. Phys. Chem. B***2007**, *111*, 1957.
222. Bhowmick, S.; Chakraborty, S.; Das, A.; Rajamohanan, P. R.; Das, N. *Inorg. Chem.***2015**, *54*, 2543.
223. Liu, X.; He, B.; Xu, Z.; Yin, M.; Yang, W.; Zhang, H.; Caoa J.; Shen, J. *Nanoscale* **2015**, *7*, 445.
224. Jiang, D-L.; Aida, T. *Chem. Commun.***1996**, *13*, 1523.
225. Balzani, V.; Bandmann, H.; Ceroni, P.; Giansante, C.; Hahn, U.; Klärner, F. G.; Müller, U.; Müller, W. M.; Verhaelen, C.; Vicinelli V.; Vögtle, F. *J. Am. Chem. Soc.***2006**, *128*, 637.

226. Tomoyose, Y.; Jiang, D. L.; Jin, R. H.; Aida, T.; Yamashita, T.; Horie, K.; Yashima, E.; Okamoto, Y. *Macromolecules***1996**, *29*, 5236.
227. Imaoka, T.; Kawana, Y.; Kurokawa, T.; Yamamoto, K. *Nat. Commun.***2013**, *4*, 2581.
228. Shinoda, S.; Ohashi, M.; Tsukube, H. *Chem. Eur. J.***2007**, *13*, 81.
229. Sohn, H.; Calhoun, R. M.; Sailor, M. J.; Trogler, W. C. *Angew. Chem., Int. Ed.***2001**, *40*, 2104.
230. Krause, G. H.; Weis, E. *Annu. Rev. Plant Physiol. Plant Mol. Biol.***1991**, *42*, 313.
231. Kumar, A.; Sevilla, M. D. *Chem. Rev.***2010**, *110*, 7002.
232. Eads, D. D.; Dismar B. G.; Fleming, G. R. *J. Chem. Phys.***1990**, *93*, 1136.
233. Shannon, C. F.; Edas, D. D. *J. Chem. Phys.***1995**, *103*, 5208.
234. Song, L.; Dorfman, R. C.; Swallen, S. F.; Fayer, M. D. *J. Phys. Chem.***1991**, *95*, 3454.
235. Koch, M.; Rosspeintner, A.; Angulo, G.; Vauthey, E. *J. Am. Chem. Soc.* **2012**, *134*, 3729.
236. Chakrabarty, S.; Kaur, H.; Pal, T.; Kar, S.; Ghosh, S.; Ghosh, S. *RSC. Adv.***2014**, *4*, 35531.
237. Zang, H.; Routh, P. K.; Alam, R.; Maye, M. M.; Cotlet, M. *Chem. Commun.***2014**, *50*, 5958.
238. Stams, A. J. M.; Plugge, C. M. *Nature Rev. Microbiol.***2009**, *7*, 568.
239. Huang, J.; Stockwell, D.; Huang, Z.; Mohler, D. L.; Lian, T. *J. Am. Chem. Soc.***2008**, *130*, 5632.
240. Szabo, A. *J. Phys. Chem.***1989**, *93*, 6929.
241. Brus, L. E. *J. Chem. Phys.***1984**, *80*, 4403.
242. Burshtein, A. I. *Adv. Chem. Phys.***2004**, *129*, 105.

243. Liang, M.; Kaintz, A.; Baker, G. A.; Maroncelli, M. *J. Phys. Chem. B* **2012**, *116*, 1370.
244. Beard, M. C. *J. Phys. Chem. Lett.* **2011**, *2*, 1282.
245. Tu, H.; Kelley, D. F. *Nano Lett.* **2006**, *6*, 116.
246. Closs, G. L.; Miller, J. R. *Science*, **1988**, *240*, 440.
247. Frauenfelder, H.; Wolynes, P. G. *Science* **1985**, *229*, 337.
248. Rosspeintner, A.; Koch, M.; Angulo, G.; Vauthey, E. *J. Am. Chem. Soc.* **2012**, *134*, 11396.